

Solid-State Growth of PMN-PT Single Crystals Using a Uniaxial Hot Press

Ashleigh Rebecca Buck

Submitted in accordance with the requirements for the degree of
Doctor of Philosophy

The University of Leeds
School of Chemical and Process Engineering
Faculty of Engineering

January 2024

The candidate confirms that the work submitted is her own and that appropriate credit has been given where reference has been made to the work of others.

This copy has been supplied on the understanding that it is copyright material and that no quotation from the thesis may be published without proper acknowledgment.

The right of Ashleigh Rebecca Buck to be identified as Author of this work has been asserted by her in accordance with the Copyright, Designs and Patents act 1988.

© 2024 The University of Leeds and Ashleigh Rebecca Buck

Abstract

Piezoelectric ceramics are used as sensors and actuators by virtue of their ability to convert electrical energy to mechanical energy and vice versa. Lead zirconate titanate (PZT) has historically been the material of choice, PZT has a piezoelectric charge constant d_{33} up to 700 pC/N, is relatively easy to manufacture, inexpensive and has good versatility through doping. More recent generation piezo-ceramics, including relaxor lead magnesium niobate – lead titanate (PMN-PT) are widely credited for their higher piezoelectric charge coefficient. Single crystal PMN-PT has a d_{33} of up to 2000 pC/N but a growth method to economically produce high quality homogeneous PMN-PT is still being sought.

The Bridgman method, conventionally used to grow piezoelectric single crystals, presents two main disadvantages. Firstly, non-homogenous crystals formed due to differences in ionic diffusion coefficients in the solid and liquid phases and secondly capital expense. These problems can be potentially overcome using the solid-state crystal growth method (SSCG), which describes the conversion of a polycrystalline material to single crystal via heat treatment with single crystal seed. Previous attempts at SSCG have proven challenging in terms of controlling microstructural evolution, and particularly suppressing grain growth in the polycrystal during its conversion.

This work details a study of producing highly dense PMN-PT ceramics using a uniaxial hot press, and use of these precursor materials in SSCG trials. A series of SSCG experiments were undertaken to deduce the activation energy for single crystal growth and what effect the addition of excess lead oxide (liquid enhanced growth) in the polycrystalline materials has on the grown single crystals.

A study of the SSCG method applied to manganese doped PMN-PT was also carried out which gave insights to the role of the solute drag mechanism on controlling porosity in the grown single crystal.

Exploratory work was undertaken to determine the feasibility of textured growth of PMN-PT and barium titanate system using the hot press as a means of orientating anisotropic single crystal platelets within the polycrystalline matrix.

Acknowledgements

First and foremost, I would like to thank my supervisor, Professor Andrew Bell, for sharing his expertise in the field, his forthright advice, support, and encouragement. – Thankyou Andy, I have had an incredible experience undertaking this work and am grateful of the opportunity you gave me.

I acknowledge EPSRC and Thales who provided funding for this work. Special thanks to Laura Stoica for her expert guidance, support, and encouragement throughout this process and during my placement at Thales. Laura – Thank you for your support in this thesis work and beyond, I appreciate all your help.

Thanks also to my supervisor Dr Nicole Hondow who has provided me with fantastic support and encouragement throughout the duration of my project but especially when it was most needed. – Thank you, Nicole, you have made this experience a great one.

I am greatly indebted to Rob Simpson for his invaluable technical support, profound knowledge, and unrivalled skill in building of our beloved hot press. – Thank for everything Rob, your friendship has meant a great deal to me and long may it continue.

Thanks also to my friends and colleagues at Leeds: Rob, Faye, Di, Bob, Tom H, Anton, Chloe, Danielle, Tom B, Jon, Harry, Celine and everyone else for the great atmosphere in the office and labs.

I would also like to thank my friends from Leeds and Nottingham, I have leant on you all throughout the duration of this work and you have been my biggest cheerleaders.

Finally, I would like to thank my family for their endless encouragement, my parents and brother especially, for coming along on this journey with me.

Contents

Abstract	ii
Acknowledgements	iii
Contents	iv
List of Figures	x
List of Tables.....	xxii
Abbreviations	xxiii
Chapter 1 Introduction	1
1.1 Background and Motivation.....	1
1.2 Aims and Objectives	2
Chapter 2 Introduction to Piezoelectric Materials	4
2.1 Introduction to Piezoelectricity	4
2.2 Crystallography	5
2.2.1 Crystal Structures	5
2.2.2 The Perovskite Structure	6
2.3 Properties of Piezoelectric Materials	8
2.3.1 Dielectric Materials	8
2.3.2 Polarisation.....	9
2.3.3 Capacitance	10
2.3.4 Relative Permittivity	12
2.3.5 Dielectric Loss	13
2.3.6 Piezoelectricity	14
2.3.7 Piezoelectric Coefficients.....	15
2.3.8 Ferroelectricity	16
2.3.9 Phase Transformations	17
2.3.10 Morphotropic Phase Boundary	17

2.3.11 Curie-Weiss Behaviour	18
2.3.12 Domain Formation	19
2.3.13 Relaxor Ferroelectric Properties	20
2.4 Contributions to Piezoelectric Materials	21
2.4.1 Barium Titanate.....	21
2.4.2 Lead Based Relaxor Ferroelectric Materials.....	23
2.4.3 Summary of Piezoelectric Materials	25
Chapter 3 Introduction to Single Crystal Growth	26
3.1 Introduction	26
3.2 Single Crystal Growth Methods.....	26
3.2.1 Melt Growth Methods	26
3.2.2 Solution Growth Methods	29
3.2.3 Solid-State Crystal Growth	31
3.3 Background Science.....	32
3.3.1 Grain Growth	32
3.3.2 Atomic Diffusion	33
3.3.3 Normal Grain Growth	34
3.3.4 Abnormal Grain Growth	37
3.3.5 Summary of Grain Growth Mechanisms	39
3.4 Contributions to Single Crystal Growth.....	40
3.4.1 Summary of Single Crystal Growth Literature	49
Chapter 4 Materials Synthesis and Experimental Procedure	51
4.1 Introduction	51
4.1.1 Background	52
4.1.2 Pre-Synthesis Steps	53
4.1.3 Choice of composition	53
4.2 Powder Synthesis	54

4.2.1 Raw Materials	55
4.2.2 Drying and Weighing	56
4.2.3 Mixing	56
4.2.4 Drying	56
4.2.5 Calcination	57
4.2.6 Binder Addition.....	58
4.2.7 Pressing	58
4.2.8 Sintering	59
4.3 Hot Pressing Experimental Procedure	59
4.3.1 Hot Pressing Overview	59
4.3.2 Hot Press Die Set-Up	59
4.3.3 Packing Powder.....	60
4.3.4 Crystal Growth Procedure.....	62
4.3.5 Cutting Procedure of Hot-Pressed Samples for Analysis	63
4.4 Texturing Materials Synthesis and Experimental Procedure.....	63
4.4.1 Overview	63
4.4.2 Materials Synthesis	64
4.4.3 Platelets	65
4.4.4 Mixing.....	66
4.5 Characterisation Techniques	67
4.5.1 Density Measurements	67
4.5.2 X-ray Diffraction.....	68
4.5.3 Optical Microscopy	71
4.5.4 Scanning Electron Microscopy	71
4.5.4.1 Overview of Scanning Electron Microscopy	71
4.5.4.2 Polishing Procedure for SEM Samples	72
4.5.4.3 Sample Preparation	74

4.5.4.4 Linear Intercept Model.....	74
4.5.5 Energy Dispersive X-ray Spectroscopy	75
Chapter 5 Design and Build of Uniaxial Hot-Press	76
5.1 Introduction	76
5.2 Background Science.....	76
5.3 Design and Build of Uniaxial Hot Press	78
5.3.1 Operating Conditions	78
5.3.2 Overall Design	78
5.3.3 Hot Press Components	79
5.3.3.1 Furnace.....	79
5.3.3.2 Hydraulic System.....	80
5.3.3.3 Frame	81
5.3.3.4 Bottom Locator Plate and Hydraulic Support.....	83
5.3.3.5 Top Mounting Plate, Mounting Collar and Locator Plate.....	84
5.3.3.6 Alumina Push Rods.....	87
5.3.3.7 Ceramic Die	88
5.3.3.8 End Caps	88
5.3.3.9 Polycarbonate Safety Screens	89
5.4 Equipment Testing	89
5.5 Summary and Conclusions.....	90
Chapter 6 Solid State Crystal Growth.....	92
6.1 Introduction	92
6.2 Experimental Procedure	93
6.2.1 Sample Preparation	93
6.2.2 Sample Loading	93
6.2.3 Further Heat Treatment.....	95
6.2.4 Material Characterisation	95

6.2.5 Particle Size Analysis.....	95
6.2.6 Single Crystal Seed Properties	96
6.3 Results and Discussion.....	97
6.3.1 Hot Press Unseeded Initial Trials.....	97
6.3.1.1 Determining the Optimum Sintering Temperature	98
6.3.1.2 Investigating the Effects of Sintering Pressure on Microstructure ..	105
6.3.1.3 Comparison to Conventionally Sintered Pellet	107
6.3.1.4 Excess Lead Incorporated Into PMN-PT Samples.....	113
6.3.1.5 Annealing Study of Unseeded Compositions	116
6.3.2 Single Crystal Seeding	125
6.3.2.1 Barium Titanate Single Crystal Seeding	126
6.3.2.1.1 Experimental Procedure	126
6.3.2.1.2 Results of Barium Titanate Single Crystal Seeding.....	128
6.3.2.1.3 Conclusions of Barium Titanate Single Crystal Seeding.....	130
6.3.2.2 PMN-PT Single Crystal Seeding	131
6.3.2.2.1 Annealing Time Analysis for SSCG Trials.....	131
6.3.2.2.2 Comparison to Conventional Sinter	134
6.3.3 Solid State Crystal Growth Results.....	135
6.3.3.1 Stoichiometric PMN-PT.....	136
6.3.3.2 PMN-PT with 2% Excess PbO	140
6.3.3.3 PMN-PT with 5% PbO	147
6.3.3.4. Summary and Conclusions of Solid-State Crystal Growth Trials ..	152
6.3.3.5 Arrhenius Calculations of SSCG Experiments	154
6.3.3.5.1 Conclusions and Further Work of Arrhenius Calculations	159
6.3.4 Manganese Doped PMN-PT Solid State Crystal Growth.....	159
6.3.4.1 Introduction to Manganese-Doped PMN-PT Work.....	159
6.3.4.2 XRD manganese doped PMN-PT	160

6.3.4.3. Microstructure of hot-pressed manganese doped PMN-PT	161
6.3.4.4 Solid-State Crystal Growth of Manganese-Doped PMN-PT	162
6.3.4.5 EDX Analysis Manganese Doped PMN-PT	164
6.3.4.6 Conclusions and Future Work of Manganese-Doped PMN-PT	166
6.4 SSCG Summary and Conclusions.....	166
6.5 SSCG Future Work	168
Chapter 7 Texturing of Piezoelectric Ceramics using Uniaxial Hot-Press	170
7.1 Introduction	170
7.2 Experimental Procedure	172
7.2.1 Barium Titanate Platelets	172
7.2.1.1 Platelet Particle Size.....	173
7.2.1.2 XRD Analysis of Barium Titanate Platelets	174
7.2.1.3 Volume Fraction of Platelets.....	175
7.2.2 Material Characterisation	176
7.2.2.1 Lotgering Factor.....	176
7.3 Results and Discussion.....	177
7.3.1 PMN-PT Texturing	177
7.3.1.1 Textured PMN-PT Analysis Using XRD and EDX.....	182
7.3.1.2 Conclusions of PMN-PT Texturing	185
7.3.2 Texturing of Barium Titanate.....	185
7.3.2.1 Conclusion of Barium Titanate Texturing	190
7.4 Texturing Summary and Conclusions.....	190
7.5 Texturing Further Work	191
Summary and Conclusions.....	192
Further Work.....	194
References	195

List of Figures

Figure 1. Diagram of the 14 Bravais Lattices (Hammond, 2009).....	5
Figure 2. Diagram showing relation of crystallographic structure to piezoelectric, pyroelectric and ferroelectric properties.	6
Figure 3. The perovskite structure shown here for PMN-PT systems.	7
Figure 4. Diagram of energy levels and band gap in dielectric material (Bell, 2016).	8
Figure 5. Polarisation of a molecule and electrostriction (Bell, 2016).	9
Figure 6. Series of elementary dipole prisms (Moulson and Herbert, 2003).	10
Figure 7. Capacitor with and without dielectric material (Moulson and Herbert, 2003).	11
Figure 8. Dielectric in alternating electric field (Moulson and Herbert, 2003).	13
Figure 9. Dielectric loss, trigonometry representation (Moulson and Herbert, 2003).	14
Figure 10. Direct (a and b) and indirect (c and d) piezoelectric effects (Moulson and Herbert, 2003).	15
Figure 11. Schematic showing d_{33} (a), d_{31} (b) and d_{15} (c) modes adapted from (Hammond, 2009).	15
Figure 12. Barium titanate unit cell structure.	16
Figure 13. Displacements in the cubic-tetragonal distortion in BaTiO ₃ (Moulson and Herbert, 2003).	16
Figure 14. Phase transformations with temperature of barium titanate unit cell (Moulson and Herbert, 2003).	17
Figure 15. PMN-PT Phase Diagram (Otoničar et al, 2021).	18
Figure 16. Domains in structure that are (a) randomly orientated (b) under an electric field favourable domains grow (c) net polarisation and (d) mechanical stress inducing 90° switching (Moulson and Herbert, 2003).	19
Figure 17. Dielectric response of relaxor PMN shown over a range of temperature and frequencies (Smolensky and Agronovskaya, 1960).	20
Figure 18. Lattice constants of barium titanate as a function of temperature (Jona and Shirane 1962).	21
Figure 19. Phase Diagram of BaO-TiO ₂ (Lee et al, 2009).	22

Figure 20. Strain levels of single crystals and polycrystalline PZT (Park and Shrout, 1997).	24
Figure 21. Property comparisons between three generation of lead-based relaxor single crystals PMN-PT, PIN-PMN-PT and Mn: PIN-PMN-PT showing piezoelectric coefficient, mechanical quality factor and Curie temperature (Baasandorj and Chen, 2021).	25
Figure 22. Schematic diagram of Czochralski method (Bassani, 2005).	27
Figure 23. Schematic of the Bridgman single crystal growth method (Batra and Aggarwal, 2018).	28
Figure 24. Schematic diagrams of other melt growth methods for single crystal growth; Verneuil Method (left) and Floating Zone Method (Right) (Byrappa, 2003).	28
Figure 25. Schematic diagram of flux growth method (Wang and Li, 2012).	30
Figure 26. Schematic diagram of top seeded solution growth method (Sun and Cao 2014).	31
Figure 27. Schematic diagram of solid-state crystal growth technique.	32
Figure 28. Grain Boundary Migration courtesy of Andrew Bell.	33
Figure 29. Schematic showing exaggerated non uniformly shaples polycrystalline grain. Atoms are in positon A: lattice, position B: convex boundary and position C: concave boundary.	35
Figure 30. Two-dimensional view of grain matrix where arrows indicate direction of growth (left) and schematic two-dimensional internal interfaces of solid grains (right).	35
Figure 31. Schematic showing the energy state of atoms on the surface of Grain I and Grain II. Δg^* represents the activation for atom diffusion between the two grains and Δg represents the driving force for atom diffusion.	36
Figure 32. Schematic illustration of the ‘mixed control mechanism’ with rough and faceted boundaries (Kang et al, 2016).	38
Figure 33. Summary of grain growth mechanisms.	39
Figure 34. Polycrystal/grown crystal/seed crystal interfaces of a sample after hot-pressing for 1h at 950°C under 40 MPa, followed by a pressureless annealing 16 hours at 1200 °C (Li et al, 1998).	42

Figure 35. Seed single crystal (centre) of PMN–35 mol% PT grew several millimetres into polycrystalline precursor after annealing at 1150°C for 140 h (Li et al, 1998).	42
Figure 36. Seeded specimen after 1150°C/10 h anneal packed in PMN– 35PT powder in a double crucible: (A) low-magnification light optical micrograph (note that dark spots in matrix are grain pull-outs from polishing, and that seed cracked during processing); (B) higher magnification SEM micrograph of seed/polycrystal region (Khen et al, 1999).....	44
Figure 37. Microstructure of seeded-specimen after annealing at 1150°C for 10 h surrounded by PZ powder in a covered crucible: (A) low magnification SEM micrograph showing considerable single-crystal growth, and higher-magnification SEM micrographs of (B) seed/grown-crystal region, and (C) polycrystalline matrix (Khan et al, 1999).....	45
Figure 38. Microstructures of the single crystal which has grown toward (a) a 8 mol% PbO excess $\text{Pb}(\text{Mg}_{1/3}\text{Nb}_{2/3})\text{O}_3\text{--PbTiO}_3$ (PMN–PT) powder compact, (b) a 1 mol% Li_2O –7 mol% PbO excess PMN–PT powder compact, (c) a 2 mol% Li_2O –6 mol% PbO excess PMN–PT powder compact, and (d) a 4 mol% Li_2O –4 mol% PbO excess PMN–PT powder compact during annealing at 1200°C for 10 h in oxygen (Kim et al, 2006).	46
Figure 39. Light optical micrographs of PMN–35PT single-crystal migration annealed for 5 h at 1150°C for (a) 0.0, (b) 1.5, (c) 3.0, and (d) 5.0 vol% PbO additions (King et al, 2003).....	47
Figure 40. Grown PMN–PT single crystals using $\langle 111 \rangle$ -oriented BaTiO_3 single crystals. The ceramics were hot-pressed before single crystal growth at 900 °C for 30 min at 45 MPa using (a) oxygen and (b) air atmospheres. The hot-pressed pellets were subsequently annealed in air for single crystal growth at 1150 °C for 10 hours (Richterter et al, 2009).	48
Figure 41. PMN-PT unit cell structure and ion placement.	52
Figure 42. PMN-PT Phase Diagram (Otoničar et al, 2021).	54
Figure 43. Flow chart summarising the powder processing route for hot and cold pressed pellets, including characterisation techniques.....	55
Figure 44. Cataracting (a) vs cascading (b) regimes in a tumbling mill (Djordjevic, 2005).	56

Figure 45. Calcination profile for magnesium niobium oxide.....	57
Figure 46. Calcination profile for PMN-PT.	58
Figure 47. Schematic of experimental design for loading samples into the hot press, showing die components and sample packing.	60
Figure 48. Yttria - Zirconia solid solution phase diagram. (Asadikiya et al, 2016)...	61
Figure 49. XRD spectra of yttria stabilised zirconia packing powder.	62
Figure 50. Cutting procedure schematic of sample containing single crystal seed. ..	63
Figure 51. Barium titanate processing route from raw materials, with addition of BaTiO ₃ platelets.	64
Figure 52. BaTiO ₃ platelets used in texturing experiments.	66
Figure 53. Archimedes density measurement set up.....	67
Figure 54. Representation of Bragg's law being applied to a crystal lattice.....	69
Figure 55. XRD spectra of MgNb ₂ O ₆ calcined at 1150 °C for 4 h.	69
Figure 56. XRD spectra of PMN-PT calcined at 850 °C for 4 hours.....	70
Figure 57. XRD spectra of BaTiO ₃ ceramic powder calcined at 1100 °C for 4 hours.	70
Figure 58. Scanning electron microscope schematic (Nanoscience Instruments, 2018)	72
Figure 59. Truncated octahedral shape, model of average shape of polycrystalline grains and equation used in linear intercept method (Mendelson, 1969).	74
Figure 60. Schematic of EDX showing excitation of core-shell electron and subsequent characteristic X-ray emitted.	75
Figure 61. Schematic of paths for transport of matter during neck growth in sintering (left) and table of diffusion paths to which numbers correspond (right) (Atkinson and Davies, 2000).	77
Figure 62. Hot press conceptual design.	79
Figure 63. ENERPAC RC102 10 Ton Hydraulic Cylinder and P392 Hand Pump and CATS12 Tilt Saddle (ENERPAC, 2019).	80
Figure 64. Process control schematic for hydraulic pump.	81
Figure 65. Schematic and likeness of KJN alumina extrusion profile used to form the hot press frame (KJN, 2005).	82
Figure 66. Hot press frame drawn in SolidWorks software.	82

Figure 67. CAD model of bottom mounting plate housing the hydraulic cylinder and casting support (left) and photograph of finished assembly showing hydraulic ram, casting support, tilt saddle, window frame and attached hydraulic hose (right).....	83
Figure 68. CAD drawing of mounting plate enclosed in locator plate (left) and mounting collar (right).....	84
Figure 69. Bespoke mounting components designed in CAD (top) and finished set up showing locator plate, mounting plate, mounting collar, tilt saddle and top support beams of the hot press frame (bottom).....	85
Figure 70. Load simulation on hot press components showing 100 kN load applied to base of tilt saddle and mounting plate as fixed surface.....	85
Figure 71. Finite element analysis modelling of 100kN load through top tilt saddle and mounting collar hot press components.....	86
Figure 72. Finite element analysis results of 100kN load on tilt saddle.	86
Figure 73. Finite element analysis modelling of 100kN load through re-worked mounting collar hot press components.....	87
Figure 74. Ceramic die modified design with recess for push rod.....	88
Figure 75. End cap design in Solid Works and picture of manufactured end cap.	89
Figure 76. Hot press test run monitoring,	90
Figure 77. Picture of hot-press build at the University of Leeds.	91
Figure 78. Hot press experimental set up,.....	94
Figure 79. Particle size analysis of PMN-PT powders that have been prepared and calcined according to Section 4.2.....	96
Figure 80. SEM images of PMN-PT powders that have been prepared and calcined according to Section 4.2.....	96
Figure 81. XRD Spectrum of PMN-PT single crystal seed.	97
Figure 82. Sintering profile of PMN-PT in the hot press, dwelling temperature of 1150 °C.	98
Figure 83. X-ray diffraction patterns of all samples sintered at a range of 1000°C - 1200°C.	99
Figure 84. Density of PMN-PT samples sintered in the hot press at varying temperatures.	100
Figure 85. Scanning electron microscopy pictures showing the microstructure of sintered samples in the hot press at varying temperatures from 1000 °C to 1200 °C	102

Figure 86. Average grain size vs sintering temperature of PMN-PT samples in the hot press.	103
Figure 87. Density and average grain size plotted for hot-pressed PMN-PT samples sintered at varying temperatures.	104
Figure 88. SEM images showing microstructure of sintered pellets of varying applied pressure; 0 MPa, 20.4 MPa and 40.8 MPa.	105
Figure 89. Effect of sintering pressure on average grain size and sample density... 106	
Figure 90. Hot press sample sintered at 61.2 MPa, push rod failure before sample had reached sintering temperature.	107
Figure 91. SEM image of sample sintered in the hot press at 1150 °C with 2% Optapix binder incorporated into PMN-PT powder.....	108
Figure 92. SEM image of conventionally sintered PMN-PT pellet with 2% Optapix binder, sintered at 1150 °C with a binder burnout stage of 650 °C for 2 hours preceding being heated to sintering temperature.	109
Figure 93. XRD spectra of conventionally sintered PMN-PT sample (1150 °C) and hot-pressed sample (1150 °C, 20.4 MPa).....	110
Figure 94. Enlarged (111) and (200) peaks in XRD spectra of conventionally sintered PMN-PT sample (1150 °C) and hot-pressed sample (1150 °C, 10 kN).....	111
Figure 95. Permittivity vs temperature plot of conventionally sintered PMN-PT 1150 °C and hot pressed PMN-PT 1150 °C 20.4 MPa	112
Figure 96. Losses vs temperature plot of conventionally sintered PMN-PT 1150 °C and hot pressed PMN-PT 1150 °C 20.4 MPa.....	112
Figure 97. SEM images of sample matrix of initial lead incorporation trials. Samples were sintered in the hot press as specified, with varying excess lead oxide incorporated into green powder.....	114
Figure 98. Summary of initial trials excess lead incorporated sample matrix and conventional sample comparison showing average grain size and density of each sample.	115
Figure 99, SEM images showing annealing of hot pressed (10kN 1150 °C) PMN-PT samples annealed at 1150 °C for 2, 4, 8 and 16 hours.	117
Figure 100. Annealing study of sample hot pressed at 10 kN, 1500 °C containing no excess PbO.	118
Figure 101, SEM images showing annealing of hot pressed (40.8 MPa, 1150 °C) PMN-PT samples annealed at 1150 °C for 2, 4, 8 and 16 hours.....	119

Figure 102. Annealing study of sample hot pressed at 20 kN, 150 °C containing no excess PbO.	119
Figure 103, SEM images showing annealing of hot pressed (20.4 MPa 1150 °C) PMN-PT samples containing 2% excess PbO annealed at 1150 °C for 2, 4, 8 and 16 hours.	120
Figure 104. Annealing study of sample hot pressed at 20.4 MPa, 1150 °C containing 2% excess PbO.	121
Figure 105, SEM images showing annealing of hot pressed (40.8 MPa 1150 °C) PMN-PT samples containing 2% excess PbO annealed at 1150 °C for 2, 4, 8 and 16 hours.	122
Figure 106. Annealing study of sample hot pressed at 40.8 MPa, 150 °C containing 2% excess PbO.	122
Figure 107. Comparison of all annealing trials carried out on annealing study. Samples show have been hot pressed and then annealed in a conventional furnace at 1150 °C for varying amounts of time, 2h, 4h, 8h and 16 hours.	124
Figure 108. Plot of parabolic growth law for annealing trials.	125
Figure 109. Polycrystalline PMN-PT pellet pre-sintered in the hot press at 40.8 MPa and 1150 °C in contact with BaTiO ₃ single crystal seed. The set up has been annealed at 1150 °C for 50 hours.	127
Figure 110. Polycrystalline PMN-PT pellet pre-sintered in the hot press at 40.8 MPa and 1150 °C showing lack of contact between BaTiO ₃ single crystal seed and polycrystalline matrix. The set up has been annealed at 1150 °C for 50 hours.	127
Figure 111. Barium titanate single crystal seed incorporated into PMN-PT polycrystalline matrix; this sample has been hot pressed at 1150 °C 40.8 MPa.	128
Figure 112. SEM image of microstructure of hot pressed PMN-PT pellet with barium titanate single crystal seed and annealed at 1150 °C for 20 hours. Hot pressing conditions – left 1150 °C 20.4 MPa, right 1150 °C 40.8 MPa.	129
Figure 113. SEM images of for stoichiometric PMN-PT pellets that have a PMN-PT single crystal seed embedded. The powder compacts have been hot pressed at 1150 °C 40.8 MPa for 4 hours and then annealed for varying times at 1150 °C.	132
Figure 114. Average solid-state crystal growth from seed for stoichiometric PMN-PT pellets that have a PMN-PT single crystal seed embedded. The powder compacts have been hot pressed at 1150 °C 20 kN for 4 hours and then annealed for varying times at 1150 °C.	133

Figure 115. Solid-state crystal growth of conventionally sintered PMN-PT pellet with embedded PMN-PT single crystal seed.	134
Figure 116. SEM image of polycrystalline matrix of sample PMN-PT with 0% excess lead oxide, sintered in the hot press at 1150 °C 20 kN/	136
Figure 117. SEM images of single seed growth and polycrystalline matrix of sample PMN-PT with 0% excess lead oxide, sintered in the hot press and annealed for 100 hours at 950 °C.....	137
Figure 118. SEM images of single seed growth and polycrystalline matrix of sample PMN-PT with 0% excess lead oxide, sintered in the hot press and annealed for 100 hours at 1000 °C.....	137
Figure 119. SEM images of single seed growth and polycrystalline matrix of sample PMN-PT with 0% excess lead oxide, sintered in the hot press and annealed for 100 hours at 1050 °C.....	137
Figure 120. SEM images of single seed growth and polycrystalline matrix of sample PMN-PT with 0% excess lead oxide, sintered in the hot press and annealed for 100 hours at 1100 °C.....	138
Figure 121. SEM images of single seed growth and polycrystalline matrix of sample PMN-PT with 2% excess lead oxide, sintered in the hot press and annealed for 100 hours at 1150 °C.....	139
Figure 122. Summary of solid-state crystal growth experiments for stoichiometric PMN-PT. The average growth from seed is recorded for each of the PMN-PT samples with embedded PMN-PT seed. The samples are hot pressed and then annealed in a conventional furnace for 100 hours at varying temperature.	139
Figure 123. Summary of solid-state crystal growth experiments for stoichiometric PMN-PT. The average grain size is recorded for each of the PMN-PT samples with embedded PMN-PT seed. The samples are hot pressed and then annealed in a conventional furnace for 100 hours at varying temperature.	140
Figure 124. Microstructure of PMN-PT hot pressed pellet with 2% excess lead oxide,	141
Figure 125. SEM images of single seed growth and polycrystalline matrix of sample PMN-PT with 2% excess lead oxide, sintered in the hot press and annealed for 100 hours at 950 °C.....	141

Figure 126. SEM images of single seed growth and polycrystalline matrix of sample PMN-PT with 2% excess lead oxide, sintered in the hot press and annealed for 100 hours at 1000 °C.....	142
Figure 127. SEM images of single seed growth and polycrystalline matrix of sample PMN-PT with 2% excess lead oxide, sintered in the hot press and annealed for 100 hours at 1050 °C.....	142
Figure 128. SEM images of single seed growth and polycrystalline matrix of sample PMN-PT with 2% excess lead oxide, sintered in the hot press and annealed for 100 hours at 1100 °C.....	143
Figure 129. SEM images of single seed growth and polycrystalline matrix of sample PMN-PT with 2% excess lead oxide, sintered in the hot press and annealed for 100 hours at 1150 °C.....	143
Figure 130. Summary of solid-state crystal growth experiments for PMN-PT with 2% excess lead oxide. The average growth from the seed is recorded for each of the PMN-PT + 2% PbO samples with embedded PMN-PT seed. The samples are hot pressed and then annealed in a conventional furnace for 100 hours at varying temperature.	144
Figure 131. Summary of solid-state crystal growth experiments for PMN-PT with 2% excess lead oxide. The average grain size is recorded for each of the PMN-PT + 2% PbO samples with embedded PMN-PT seed. The samples are hot pressed and then annealed in a conventional furnace for 100 hours at varying temperature.	145
Figure 132. EDX analysis of single seed growth and polycrystalline matrix of PMN-PT sample with 2 % excess lead oxide, hot pressed and then annealed at 1050 °C for 100 hours.....	146
Figure 133. Microstructure of PMN-PT hot pressed pellet with 5% excess lead oxide,	147
Figure 134. SEM images of single seed growth and polycrystalline matrix of sample PMN-PT with 5% excess lead oxide, sintered in the hot press and annealed for 100 hours at 950 °C.....	148
Figure 135. SEM images of single seed growth and polycrystalline matrix of sample PMN-PT with 5% excess lead oxide, sintered in the hot press and annealed for 100 hours at 1000 °C.....	148

Figure 136. SEM images of single seed growth and polycrystalline matrix of sample PMN-PT with 5% excess lead oxide, sintered in the hot press and annealed for 100 hours at 1050 °C.....	149
Figure 137. SEM images of single seed growth and polycrystalline matrix of sample PMN-PT with 5% excess lead oxide, sintered in the hot press and annealed for 100 hours at 1100 °C.....	149
Figure 138. Summary of solid-state crystal growth experiments for PMN-PT with 5% excess lead oxide. The average grain size is recorded for each of the PMN-PT + 5% PbO samples with embedded PMN-PT seed. The samples are hot pressed and then annealed in a conventional furnace for 100 hours at varying temperature.	150
Figure 139. Summary of solid-state crystal growth experiments for PMN-PT with 5% excess lead oxide. The average grain size is recorded for each of the PMN-PT + 5% PbO samples with embedded PMN-PT seed. The samples are hot pressed and then annealed in a conventional furnace for 100 hours at varying temperature.	150
Figure 140. EDX analysis of single seed growth and polycrystalline matrix of PMN-PT sample with 5 % excess lead oxide, hot pressed and then annealed at 1050 °C for 100 hours.....	151
Figure 141. Summary of SSCG experiments showing growth from seed obtained at varying annealing temperatures for PMN-PT samples containing 0%, 2% and 5% excess PbO.	152
Figure 142. Arrhenius plot of seed growth obtained in stoichiometric PMN-PT solid-state crystal growth experiments.....	155
Figure 143. Arrhenius plot of seed growth obtained in stoichiometric PMN-PT with 2% excess PbO solid-state crystal growth experiments.....	156
Figure 144. Arrhenius plot of seed growth obtained in stoichiometric PMN-PT with 5% excess PbO solid-state crystal growth experiments.....	156
Figure 145. Arrhenius plot of seed growth obtained in PMN-PT with 2% and 5% excess lead oxide solid-state crystal growth experiments.....	157
Figure 146. XD Spectra of PMN-PT with 2% manganese doping.	160
Figure 147. SEM image of polycrystalline matrix of Mn doped PMN-PT sample hot-pressed at 20.4 MPa and 1150 °C.	161
Figure 148. SEM image of polycrystalline matrix of Mn doped PMN-PT sample hot-pressed at 40.8 MPa and 1150 °C.	162

Figure 149. SEM image of solid state crystal growth of Mn doped PMN-PT hot pressed at 20.4 MPa 1150 °C and annealed at 1150 °C for 100h.....	162
Figure 150. SEM image of solid-state crystal growth of Mn doped PMN-PT hot pressed at 40.8 MPa 1150 °C and annealed at 1150 °C for 100h.....	163
Figure 151. EDX analysis of manganese doped PMN-PT.....	165
Figure 152. Schematic of template alignment by tape casting and the texture fraction increase with heating. (Messing et al, 2001).....	171
Figure 153. Barium titanate platelets.	173
Figure 154. SEM image of barium titanate platelets used in texturing process.....	174
Figure 155. XRD spectra of barium titanate platelets.....	175
Figure 156. Calculated templated grain size as a function of template concentration and template size for a 100% textured material.	176
Figure 157. Schematic of pressure axis on textured sample showing cross section view (left) and surface view (right).	177
Figure 158. SEM image of cross section PMN-PT textured sample 10% volume platelets, hot pressed at 20.4 MPa 1150 °C. Pressure applied during sintering is through the top and bottom of the image.....	178
Figure 159. SEM images of cross section PMN-PT textured sample 10% volume platelets, hot pressed at 20.4 MPa 1150 °C. Pressure applied during sintering for all samples is through the top and bottom of the images.	179
Figure 160. SEM image of surface PMN-PT textured sample 10% volume platelets.	180
Figure 161. Schematic of exaggerated platelet orientation expected in cross sectional view and surface view of samples.....	180
Figure 162. SEM images of cross section PMN-PT textured sample 10% volume platelets, hot pressed at 40.8 MPa 1150 °C. Pressure applied during sintering for all samples is through the top and bottom of the images.	181
Figure 163. SEM images of cross section PMN-PT textured sample 10% volume platelets, hot pressed at 40.8 MPa 1150 °C.....	182
Figure 164. XRD spectra of PMN-PT powder used in texturing trials.....	183
Figure 165. PMN-PT with 10% platelet BaTiO ₃ hot-pressed at 1150 °C 20.4 MPa XRD spectra.	183
Figure 166. EDX images of PMN-PT textured sample 10% volume platelets, hot pressed at 20.4 MPa.	184

- Figure 167. XRD spectra of untextured barium titanate. 187
- Figure 168. XRD Spectrum of barium titanate sample with 5% volume of platelets hot pressed at 1200 °C 20.4 MPa. 187
- Figure 169. XRD Spectrum of barium titanate sample with 10% volume of platelets hot pressed at 1200 °C 20.4 MPa. 188
- Figure 170. XRD Spectrum of barium titanate sample with 15% volume of platelets hot pressed at 1200 °C 20.4 MPa. 188
- Figure 171. Lotgering Factor analysis of barium titanate ceramic with varying volumetric content of barium titanate platelets (5, 10 and 15%) annealed at 1330 °C for varying times (0, 5, 10, 15 hours). 189

List of Tables

Table 1. Tabulated summary of literature survey of PMN-PT single crystal growth via SSCG method.....	50
Table 2. Raw materials for PMN-PT synthesis.....	55
Table 3. Raw materials for synthesis of packing powder – yttria stabilised zirconia.	61
Table 4. Raw materials used to produce BaTiO ₃	65
Table 5. Buehler polishing procedure (Buehler. 2021).	73
Table 6. Density of samples sintered in hot press at 10kN pressure for 4hours at varying temperatures.	99
Table 7. Average grain size of hot-pressed samples with varying sinter temperature from 1000 -1200 °C.	104
Table 8. Matrix of samples investigated in hot press initial trials which incorporate addition of 2% excess lead oxide (PbO).	113
Table 9. Summary of initial trials excess lead incorporated sample matrix and conventional sample comparison showing average grain size and density of each sample.	115
Table 10. Growth rate observed in PMN-PT seeded PMN-PT matrix hot-pressed at 1150 °C 40.8 MPa and further annealed at 1150 °C.	133
Table 11. Comparison of solid-state crystal growth achieved from PMN-PT polycrystalline with embedded PMN-PT single crystal seed that have been sintered in the hot press or conventionally sintered.....	135
Table 12. Summary of grain growth from SSCG experiments.	153
Table 13. Calculated activation energy for single crystal growth from the seed for PMN-PT samples containing 0%, 2% and 5% excess PbO.	158
Table 14. Calculated activation energy for polycrystalline grain growth rate for PMN-PT samples containing 0%, 2% and 5% excess PbO.	158
Table 15. Summary of solid-state crystal growth trials for manganese doped PMN-PT samples.....	164
Table 16. Summary of barium titanate platelet properties.	173

Abbreviations

AGG	Abnormal Grain Growth
ABO ₃	General formula for perovskite structure
BaTiO ₃	Barium Titanate
EBS	Electron Back-Scatter Diffraction
EDX	Energy Dispersive X-Ray Diffraction
ICDD	International Centre for Diffraction Data
IPA	Isopropyl Alcohol
MPB	Morphotropic Phase Boundary
PMN-PT	Pb(Mg _{1/3} Nb _{2/3})O ₃ -PbTiO ₃ (Lead Magnesium Niobate - Lead Titanate)
PZT	Lead Zirconate Titanate
SEM	Scanning Electron Microscopy
SSCG	Solid State Crystal Growth
XRD	X-Ray Diffraction

Chapter 1 Introduction

1.1 Background and Motivation

Piezoelectric ceramics are used as sensors and actuators by virtue of their ability to convert electrical energy to mechanical energy and vice versa. Lead zirconate titanate (PZT) has historically been the material of choice, PZT has a piezoelectric charge constant d_{33} up to 700 pC/N, is relatively easy to manufacture, inexpensive and has good versatility through doping. More recent generation piezo-ceramics, including relaxor lead magnesium niobate – lead titanate (PMN-PT) are widely credited for their higher piezoelectric charge coefficient. Single crystal PMN-PT has a d_{33} of up to 2000 pC/N but a growth method to economically produce high quality, homogeneous PMN-PT is still being sought.

The Bridgman method, conventionally used to grow piezoelectric PMN-PT single crystals, presents two main disadvantages. Firstly, as growth is from the melt, single-use precious metal crucibles are typically used, making the process capital intensive. Secondly, discrepancies in ionic diffusion coefficients in the solid and liquid phases result in compositional gradients along the growth direction of the crystal and ultimately non-homogenous crystals formed. These problems can be potentially overcome using the Solid-State Crystal Growth method (SSCG), which describes the conversion of a polycrystalline material to single crystal with the use of a single crystal seed. Previous attempts at SSCG have proven challenging in terms of controlling microstructural evolution, and particularly suppressing grain growth in the polycrystal during its conversion. A uniaxial hot press is therefore used to sinter ceramics under pressure; providing the driving force to eliminate porosity and control grain growth.

1.2 Aims and Objectives

From previous work conducted in this research area, it is clear that controlling the microstructure of polycrystalline ceramics, used as precursors in the SSCG process, proves very challenging. The initial aim of this work is therefore to design and build a uniaxial hot-press with the aims of reducing porosity in the precursor materials. A range of hot-pressing experiments will be undertaken to understand how the temperature, pressure and liquid phase content effects the microstructure of sintered samples.

The next part of this work is to use these hot-pressed materials in solid-state crystal growth trials. The viability of the SSCG process should be examined by investigating the amount of single crystal growth as a function of further heat treatment time and temperature. The presence of liquid phase, in the form of excess lead oxide in the polycrystalline matrix, will also be investigated as an aid to the SSCG process.

There is a significant gap in the literature of SSCG method being carried out on manganese doped PMN-PT samples. The final aim of this process is to determine the feasibility of SSCG in the Mn-PMN-PT system.

Texturing of piezoelectric ceramics is a very similar process to SSCG, where growth is encouraged on seed templates in the matrix. A feasibility study will be carried out to determine whether the hot press can be used as an effective tool for orientating anisometric single crystal seeds and encouraging growth into the matrix from them.

The aims of this work are summarised as follows:

- Design and build of a uniaxial hot press to produce highly dense polycrystalline materials to be used in SSCG trials. Establish hot pressing procedure by investigating optimal conditions of:
 - Temperature
 - Pressure
 - Presence of PbO liquid phase
- Carrying out of SSCG process. A study of factors affecting single crystal growth rate are to be carried out including:
 - Further heat treatment time
 - Further heat treatment temperature
 - Presence of PbO liquid phase
- Exploratory work using knowledge gained above to apply to manganese doped PMN-PT.
- Feasibility study of hot-pressing as a tool for orientating textured ceramics

Chapter 2 Introduction to Piezoelectric Materials

2.1 Introduction to Piezoelectricity

The phenomenon of piezoelectricity was discovered by the Curie brothers in 1880. It was found that when certain naturally occurring materials such as Rochelle salt or quartz are subject to a mechanical force, a voltage is generated, where the polarity changes in agreement with either compression or tension (Holterman and Groen, 2012).

At the onset of their discovery and continuing to this day, piezoelectric materials have received increased attention as they are used across a broad range of applications. The direct piezoelectric effect, where the output is electrical energy, is used in applications such as gas lighters, airbag sensors or microphones. The inverse piezoelectric effect, where mechanical energy is the output, is used in applications such as positioning stages in microscopes, acoustic transducers, or loudspeakers. Applications that employ both the direct and inverse piezoelectric effect are, for example, medical imaging, hearing aids, sonar, parking sensors, wristwatches or microprocessors (Holterman and Groen, 2012).

Barium titanate is one of the most thoroughly studied and widely used ferroelectric materials. This material was discovered independently during WWII by the US, Russia and Japan for its use in capacitors. Another notable material discovery is lead zirconate titanate (PZT) which was developed in the 1950's. PZT shows improved piezoelectric properties to barium titanate and is still used in a wide range of applications. Barium titanate and PZT have the advantage of versatility through doping and so can be easily tailored to specific applications.

More recently, relaxor ferroelectrics of lead-based systems are of interest in this research area. The improved piezoelectric properties over PZT have led to their replacement in medical imaging equipment (Cady, 2018). Relaxor ferroelectrics are discussed in more detail in Section 2.4.2.

2.2 Crystallography

2.2.1 Crystal Structures

The arrangement of atoms in a structure and their associated symmetry are fundamental to the material properties. Crystalline materials are classified into seven crystal systems, within these seven systems there is some variation in the lattice centering types, which gives rise to a total of fourteen unique Bravais lattices as shown in Figure 1.

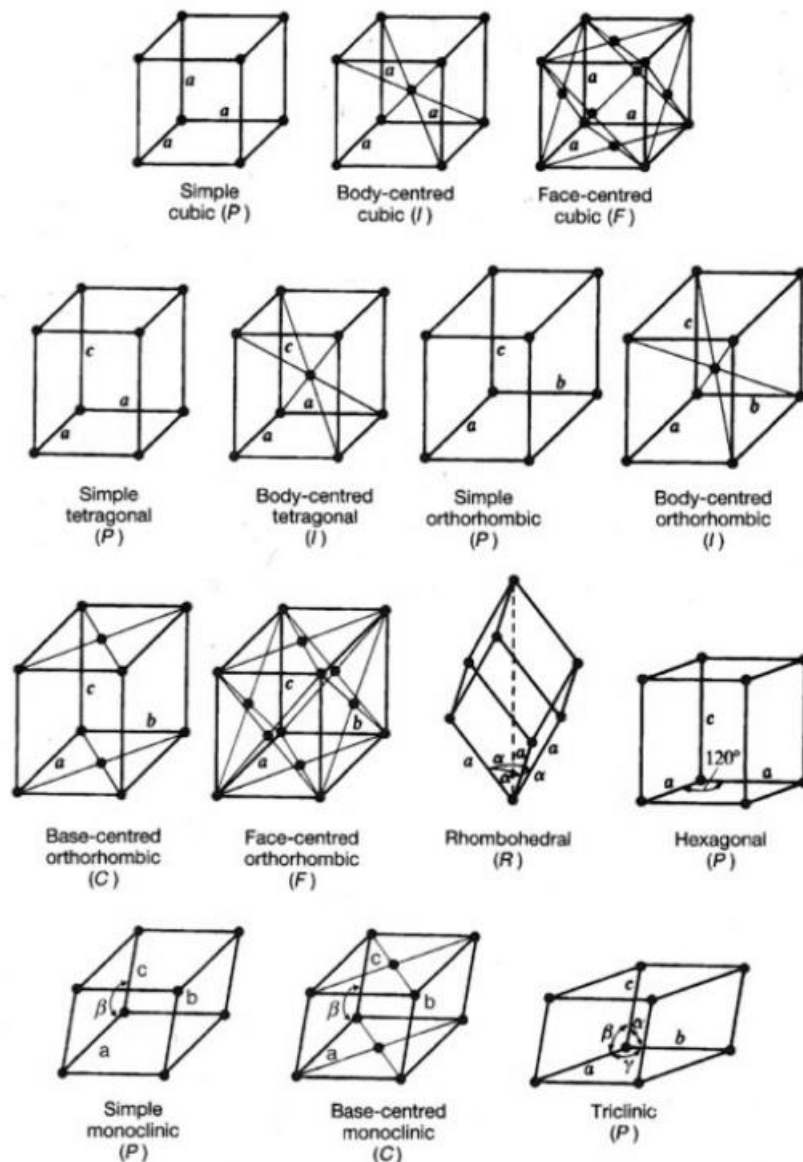


Figure 1. Diagram of the 14 Bravais Lattices (Hammond, 2009).

These 14 Bravais lattices can be further divided by their symmetry into 32 crystal point groups. Of the 32-point groups 21 are non-centrosymmetric, of these 20 are piezoelectric, this is shown in Figure 2. Piezoelectricity is a phenomenon directly related to the symmetry of a crystalline material. The exception is a point group which, although non-centrosymmetric, exhibits other symmetry elements which cancel the occurrence of a dipole (Hammond, 2009).

From those materials that exhibit piezoelectric behaviour, 10 are polar or pyroelectric. These structures exhibit polarity, where the centre of positive charge differs from the centre of negative charge. Pyroelectric crystals generate a voltage upon a change in temperature. In ferroelectric materials, the polarisation may be switched between equivalent stable states by the application of an electric field (Moulson and Herbert, 2003).

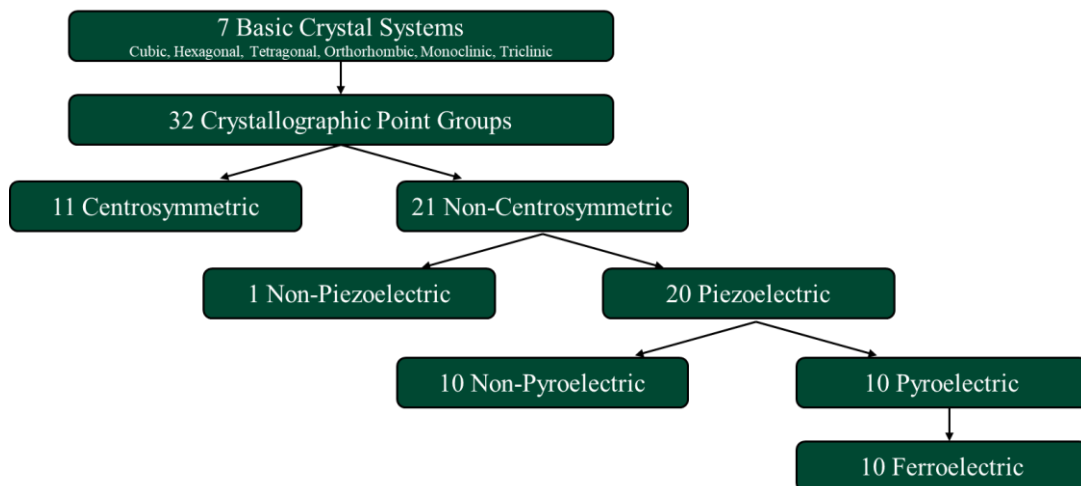


Figure 2. Diagram showing relation of crystallographic structure to piezoelectric, pyroelectric and ferroelectric properties.

2.2.2 The Perovskite Structure

The perovskite structure is shown in Figure 3. Here, the ionic placements are labelled with ions that are present in PMN-PT, as this is the material studied in this work. However, the perovskite structure is generally used to describe a material with the formula ABO_3 . The unit cell is comprised of cation A site on the corners of the unit

cell, smaller cation B sites in the centre of the unit cell, and face centred oxygen anions. A cubic cell is represented here but the perovskite unit cell exists also in the rhombohedral, tetragonal, and orthorhombic configuration. Under certain conditions, the cation on the B site is displaced from its centred position and the structure becomes non-centrosymmetric and therefore may exhibit piezoelectricity.

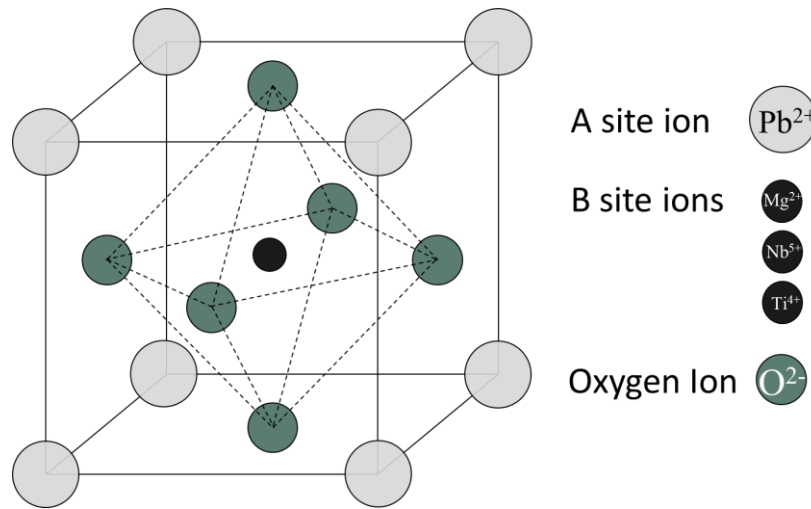


Figure 3. The perovskite structure shown here for PMN-PT systems.

The Goldschmidt tolerance factor is used to describe the relationship of anions and cations in the perovskite structure. This is shown in Equation (1), where the tolerance factor (t) is expressed in terms of the ionic radii (r) of the ions on the A,B and O sites. A wide variety of cations can be accommodated in the perovskite structure, which results in structural distortion to accommodate cation radii. Typically, a tolerance factor of 0.9-1 is associated with an ideal perovskite structure (Hammond, 2009).

$$t = \frac{r_O + r_A}{\sqrt{2} (r_B + r_O)} \quad (1)$$

2.3 Properties of Piezoelectric Materials

2.3.1 Dielectric Materials

A dielectric is an electrically insulating material that experiences a polarised state in the presence of an applied electric field. The structure of electrons within the material governs the insulating properties. Generally, bonding of materials causes electron orbitals in adjacent atoms to overlap; specifically for ceramics this bonding is a combination of ionic and covalent bonding. The overlap of the orbitals causes electrons to occupy a spread of energy levels, the Pauli Exclusion Principle states that no electron can occupy the same discrete energy level as an adjacent electron, hence a band of energies is formed (Moulson and Herbert, 2003). This process is dictated by quantum mechanics; that the sharply defined energy levels of an electron broaden into an energy band when a large number of atoms condense to form a crystal (Moulson and Herbert, 2003). This process is shown in Figure 4.

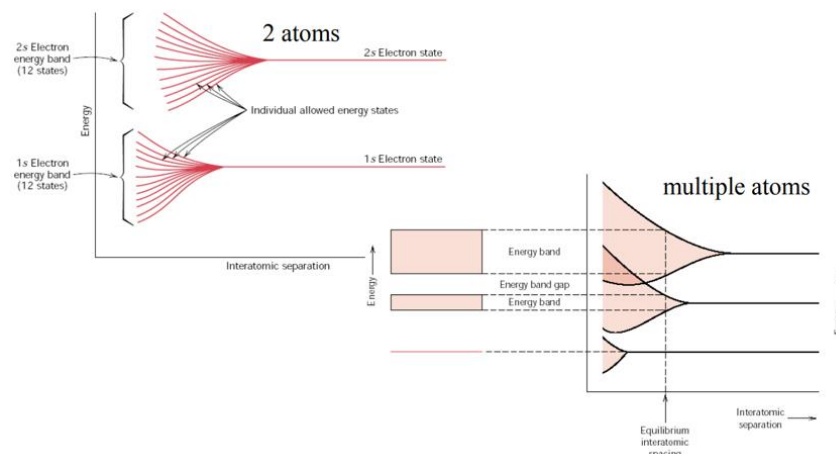


Figure 4. Diagram of energy levels and band gap in dielectric material (Bell, 2016).

The bands created in this way define how the material behaves in an applied electric field. The valence band is highest filled or partially filled band of the structure. The next highest energy band is defined as the conduction band, electrons can be promoted to this band with an input of energy, either thermally or externally through energy

sources such as photons (Moulson and Herbert, 2003). For an insulator the band gap between the valence band and the conduction band is relatively large, typically in excess of 2 eV (Moulson and Herbert, 2003) For a semi-conductor this bad gap is less than 2 eV, implying that with sufficient energy the valence band electrons can be excited and promoted into the conduction band, hence giving the ability to carry an electrical current through the material.

2.3.2 Polarisation

Dielectrics are considered to be insulators: no long-range transport of charge through the structure is exhibited through their structure. There is, however, limited rearrangement of the dielectric structure manifested as a dipole moment. When a charge is applied to a dielectric material, a dipole moment is created in which there is short range polarisation of the material, shown in Figure 5.

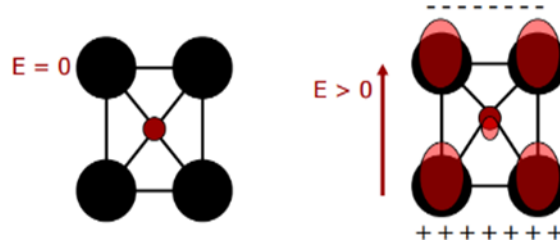


Figure 5. Polarisation of a molecule and electrostriction (Bell, 2016).

Figure 5 shows the deformation of the structure at a polarised state when compared to a neutral state. A dipole moment (p) is considered as two equal point charges at distance x and magnitude of charge (Q), as shown in Equation (2).

$$p = Q dx \quad (2)$$

The dipole moment is considered as a vector directed from the negative to the positive charge. The dipole moment per unit volume is defined as the polarization of the

material. Polarisation can be viewed as a series of elementary dipole prisms as shown in Figure 6.

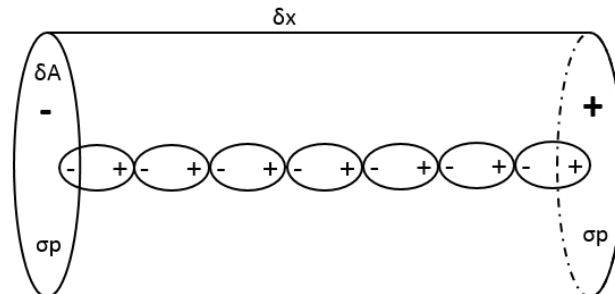


Figure 6. Series of elementary dipole prisms (Moulson and Herbert, 2003).

The polarisation of the material is expressed in Equation (3) (Moulson and Herbert, 2003) where the dipole moment (p) per unit volume (V) is equal to the product of the unit vector normal to the surface of the polarised material directed outwards. (n) and the polarisation (P). This equation shows how the polarization of a material can vary from region to region.

$$\frac{\delta p}{\delta V} = \sigma_p = n P \quad (3)$$

2.3.3 Capacitance

A capacitor is a device that is used to store electrical charge, which comprises of two parallel plates separated by an insulator. As current flows through an electric circuit, charge builds up on one plate but cannot pass through the insulating material, a build-up of opposite charges results on the two plates. Introducing a dielectric into a capacitor decreases the total electric field, which in turn decreases the voltage, this increases the capacitance capability, as shown in Figure 7.

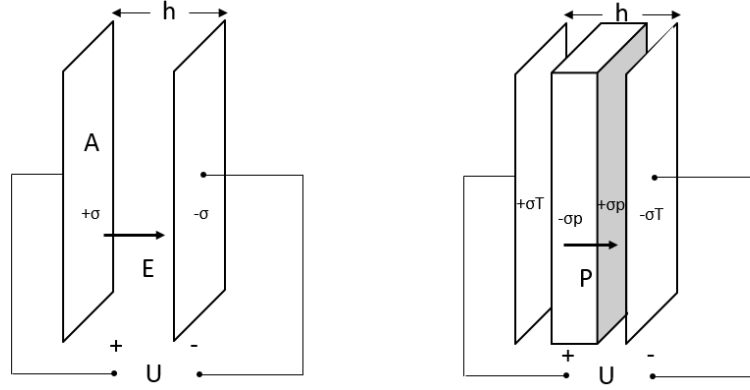


Figure 7. Capacitor with and without dielectric material (Moulson and Herbert, 2003).

Equation (4) shows that the charge density on the surfaces of the dielectric in Figure 7 compensates part of the charge density (Moulson and Herbert, 2003). The electric field is represented by E , total charge density by σ_T , the polarisation charge density appearing on the surface σ_p , and the permittivity of free space ϵ_0 .

$$E = \frac{\sigma_T - \sigma_p}{\epsilon_0} \quad (4)$$

Total charge density is expressed by the product of the field between plates and the permittivity of free space, summed with the dipole moment per unit volume or polarisation (P) (Equation (5)).

$$\sigma_T = \epsilon_0 E + P \quad (5)$$

Polarisation is proportional to the electric field within the material and can be expressed as the product of electric susceptibility (X_e), the permittivity of free space (ϵ_0) and the electric field (E), as shown in Equation (6) (Moulson and Herbert, 2003). X_e is a dimensionless constant which expresses the electric susceptibility, the ability of the material to separate charge under an electric field. $X_e = 1$ in vacuum, but $X_e > 1$ for a dielectric in a capacitor.

$$P = \chi_e \varepsilon_0 E \quad (6)$$

Equations, (4), (5) and (6) may be combined into Equation (7) to express the total charge density as a function of electric susceptibility and electric field.

$$\sigma_T = \varepsilon_0 E + \chi_e \varepsilon_0 E = (1 + \chi_e) \varepsilon_0 E \quad (7)$$

A capacitor is defined by Equation (8) where the capacitance (C) is equal to the total charge on the capacitor plate (Q_T) divided by the voltage between the plates (U) (shown in Figure 7) Combined Equation (8) with Equation (7) derived previously gives the capacitance (C) where the space between the plates is filled with a dielectric material (Equation (9)).

$$C = \frac{Q_T}{U} \quad (8)$$

$$C = (1 + \chi_e) \varepsilon_0 E \frac{A}{h} \quad (9)$$

2.3.4 Relative Permittivity

When comparing a capacitor with a vacuum between the plates and a capacitor with a dielectric material, the capacitance is increased by a factor of $(1+\chi_e)$. The permittivity of a dielectric (ε) is defined in Equation (10).

$$\varepsilon = \varepsilon_0 (1 + \chi_e) \quad (10)$$

The relative permittivity (ε_r) is equal to the permittivity of the dielectric (ε) compared to the permittivity of free space (ε_0) shown in Equation (11) (Moulson and Herbert, 2003).

$$\epsilon_r = \frac{\epsilon}{\epsilon_0} = 1 + \chi_e \quad (11)$$

The relative permittivity is often referred to as the dielectric constant, it gives a direct value of the dielectric properties of the material. The relative permittivity is the extent by which a dielectric material can store charge (and thereby be polarised) by a given voltage.

2.3.5 Dielectric Loss

Capacitors in ordinary circuit applications experience an AC field. As the voltage reaches a maximum value the capacitor plates become saturated with charge, at this point the current drops to zero. The voltage then returns to zero and the charge on the plates is released, resulting in an increase in current to a maximum. During one half cycle the capacitor is charged and the next it reversibly releases its charge without loss of energy maintaining a constant phase difference between the current and voltage of 90° . This process is shown in Figure 8.

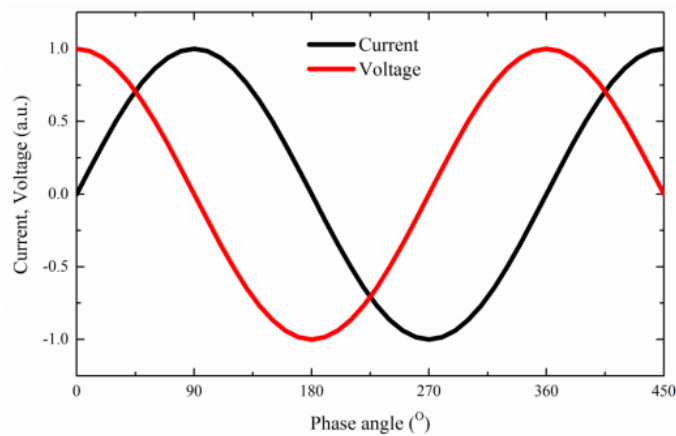


Figure 8. Dielectric in alternating electric field (Moulson and Herbert, 2003).

An ideal dielectric will have a phase difference of 90° between current and voltage. Leakage of current results in losses in the system and a deviation from 90° phase

difference, shown in Figure 9. The ratio of the capacitive and loss components is known as the dissipation factor and is represented as $\tan \delta$ as displayed in Equation (12) (Moulson and Herbert, 2003).

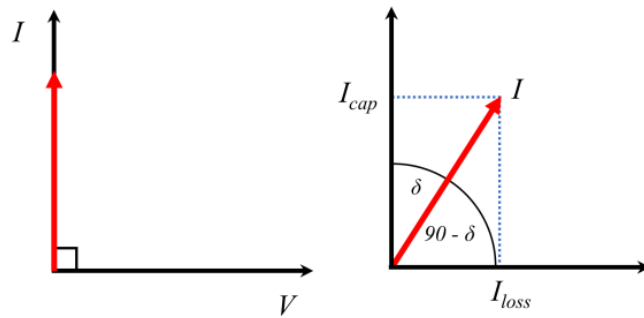


Figure 9. Dielectric loss, trigonometry representation (Moulson and Herbert, 2003).

$$\frac{I \sin \delta}{I \cos \delta} = \tan \delta \quad (12)$$

2.3.6 Piezoelectricity

Piezoelectric materials exhibit polarization on application of mechanical stress. Strain that is developed is directly proportional to the electric field applied to the material. The piezoelectric effect is reversible: materials that exhibit this effect polarise with an applied stress and experience the converse generation of stress when a field is applied (Ye, 2008). This is shown in Figure 10.

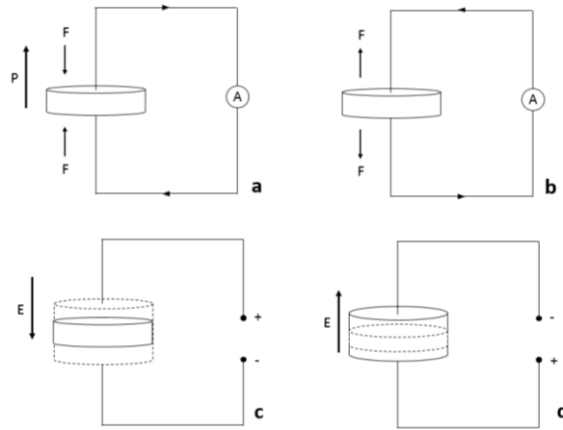


Figure 10. Direct (a and b) and indirect (c and d) piezoelectric effects (Moulson and Herbert, 2003).

Figure 10 shows strain applied to a piezoelectric material and the deformation that follows. Dipoles occur within the material due to the deformation of the unit cell, this manifests as a surface charge of the material (Ikeda, 1996).

2.3.7 Piezoelectric Coefficients

A value of d_{33} is often quoted as a general indicator of piezoelectric performance. This coefficient quantifies the volume change associated when a piezoelectric material is subject to an electric field, or the polarization on the application of stress. The mode of operation is described using tensor notation d_{ij} , commonly d_{33} is quoted but other operating modes are used in different applications, these are shown in Figure 11.

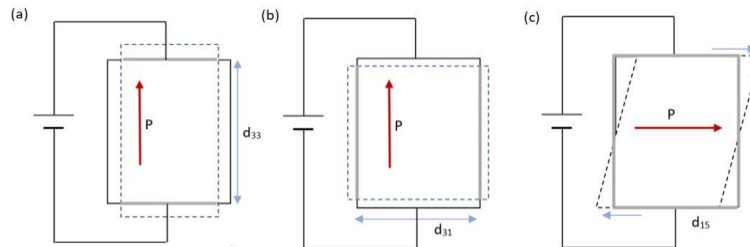


Figure 11. Schematic showing d_{33} (a), d_{31} (b) and d_{15} (c) modes adapted from (Hammond, 2009).

2.3.8 Ferroelectricity

A ferroelectric material has a crystal structure that can exhibit spontaneous polarization which can be reversed when an external electric field is applied. This is exhibited in the perovskite structure with general formula (ABO_3), the unit cell of barium titanate is shown in Figure 12 .

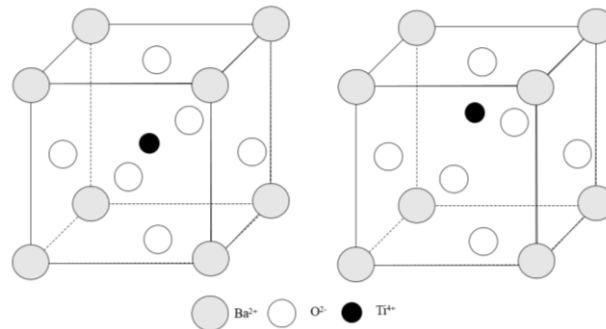


Figure 12. Barium titanate unit cell structure.

The titanium atom in the centre of the unit cell translates towards an oxygen atom as the material experiences polarization. As the titanium moves closer to an oxygen ion, this creates a dipole within the unit cell. A dipole is then induced in the adjacent unit cell, causing titanium atoms adjacent to each other to translate in the same direction. This leads to the formation of domains in the crystal structure (Uchino, 2017). Figure 13 shows the cubic-tetragonal distortions in barium titanate structure.

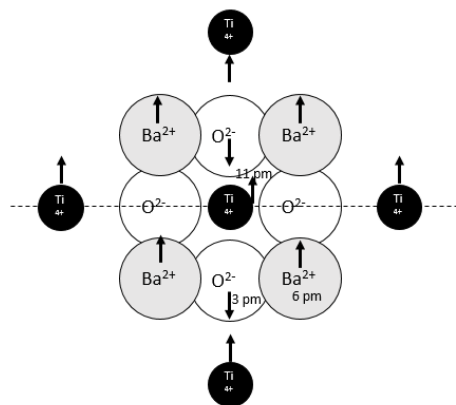


Figure 13. Displacements in the cubic-tetragonal distortion in $BaTiO_3$ (Moulson and Herbert, 2003).

2.3.9 Phase Transformations

Piezoelectric perovskites have temperature dependant polymorphic forms and undergo phase transitions due to temperature. As seen in Figure 14, barium titanate transforms to a tetragonal phase at 130 °C, to an orthorhombic at 0 °C and further to a rhombohedral phase at -90 °C. Phase transformations where the symmetry of the structure is changed which results in a loss of piezoelectric properties are discussed further in Section 2.1.11.

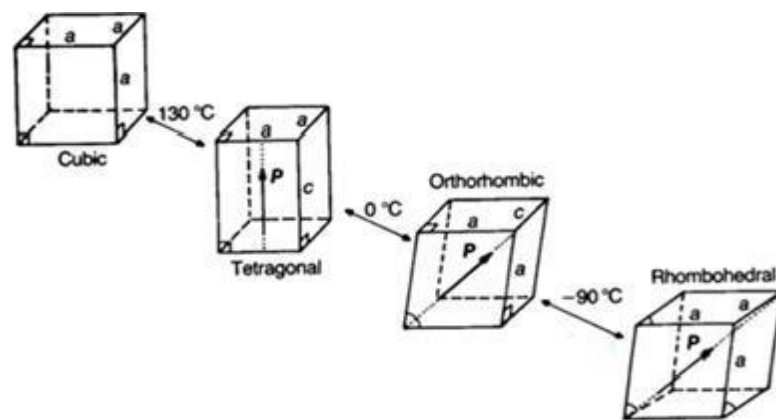


Figure 14. Phase transformations with temperature of barium titanate unit cell (Moulson and Herbert, 2003).

2.3.10 Morphotropic Phase Boundary

Phase changes in a piezoelectric perovskite are also dependent on composition. The morphotropic phase boundary is of particular interest for solid solutions where two or more crystallographic phases may be stable depending on the ratios of the components. The point which a phase transformation, as a result of a change in composition, takes place is defined as Morphotropic Phase Boundary (MPB)

The phase diagram of PMN-PT is shown in Figure 15. PMN-PT compositions are intentionally formulated around the MPB as this gives superior piezoelectric properties compared to other compositions. The origins of these properties at the MPB have been attributed to the polarization rotation that can happen more easily in the area of structural instability which occurs where rhombohedral and tetragonal phases are

in close proximity (near the MPB). When an electric field on the rhombohedral crystal is applied along its off-polar [001] direction, the field-driven rotation of the [111] rhombohedral polarization vector toward the [001] tetragonal direction becomes easier in the proximity of the tetragonal phase, resulting in large piezoelectric coefficients measured in compositions close to the MPB (Rojac, 2023).

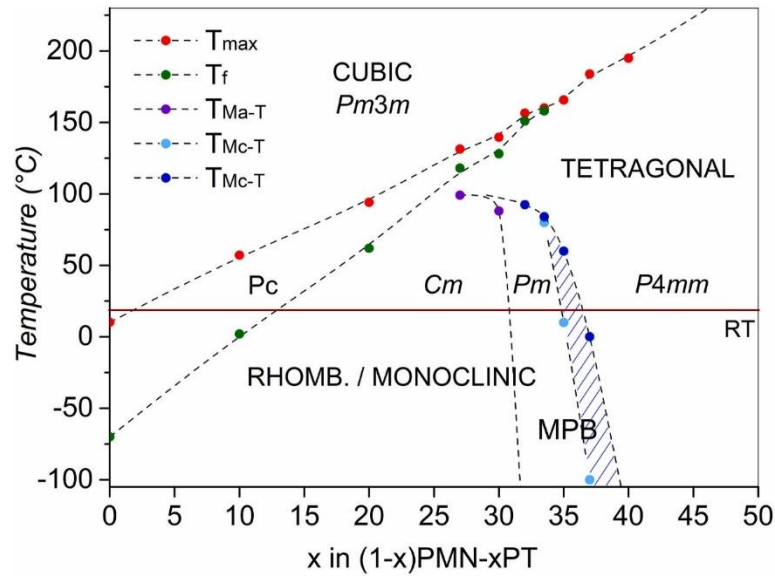


Figure 15. PMN-PT Phase Diagram (Otoničar et al, 2021).

2.3.11 Curie-Weiss Behaviour

The Curie-Weiss Law is given by Equation (13). This law expresses the electric susceptibility as a function as the material specific Curie constant (A) and the temperature of the material (T) compared to the Curie temperature (T_C) (Trainer, 2000). Below the Curie temperature spontaneous polarisation can be exhibited, above this temperature the electrical susceptibility follows the Curie-Weiss Law, the material becoming less susceptible as the temperature deviates further from the Curie temperature.

$$\frac{A}{T - T_C} = \chi_e \quad (13)$$

As a paraelectric material is cooled through its Curie temperature it undergoes a phase transition and becomes ferroelectric. The Curie temperature is an important parameter to consider as upon heating into the paraelectric phase, all piezoelectric properties are lost at this point, and so the operating temperature of piezoelectric ceramics is often limited by this parameter.

2.3.12 Domain Formation

Figure 16 shows that it is energetically favourable for the titanium atoms in a column of neighbouring atoms to be displaced in the same direction. Displacement of the titanium ion from the central position in the unit cell, therefore, falls into two energy wells and hence form 180° domains relative to each other according to Landau theory (Moulson and Herbert, 2003). These 180° domains form to minimise the energy associated with spontaneous polarization. These domains can be switched by applying an electric field in the opposite direction to polarisation that is significant enough to overcome the energy barrier separating the two wells.

90° domains can form via this mechanism also and are accompanied by a dimensional change of the unit cell. 90° switching can be induced by an applied mechanical stress (Moulson and Herbert, 2003). This is demonstrated in Figure 16.

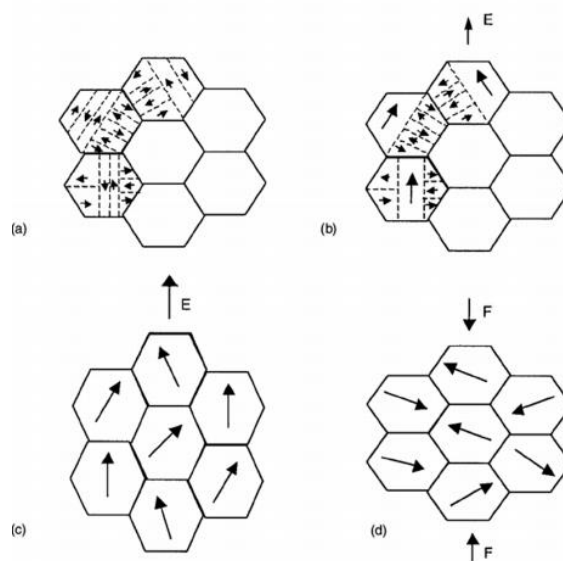


Figure 16. Domains in structure that are (a) randomly orientated (b) under an electric field favourable domains grow (c) net polarisation and (d) mechanical stress inducing 90° switching (Moulson and Herbert, 2003).

2.3.13 Relaxor Ferroelectric Properties

Relaxor ferroelectrics are ferroelectric materials that exhibit high electrostriction. The dielectric response of PMN over a range of frequencies is shown in Figure 17. Contrary to ferroelectrics, where the maximum dielectric permittivity is frequency independent and the temperature at which the maximum occurs is associated with the Curie point T_C , for a relaxor, the temperature of maximum permittivity shows a frequency dependence and is not associated with a structural phase transition.

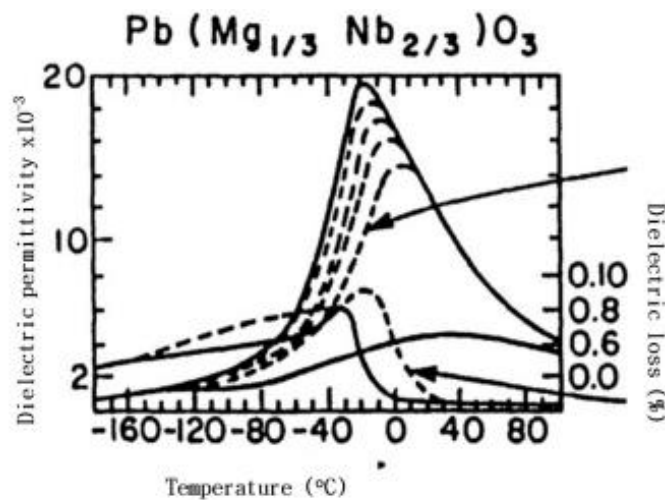


Figure 17. Dielectric response of relaxor PMN shown over a range of temperature and frequencies (Smolensky and Agronovskaya, 1960).

PMN exhibits this behaviour as there is disorder on the cation sites which are occupied by either Mg^{2+} or Nb^{5+} . This disorder leads to formation of polar nano regions which are responsible for the broad dielectric peak. As PMN is cooled, field induced alignment of polar nano regions takes place which causes a relaxation in the polarisation mechanism, the outcome of which is the frequency dependent dielectric peak (Cross, 1994).

2.4 Contributions to Piezoelectric Materials

2.4.1 Barium Titanate

Barium titanate was the first piezoelectric ceramic to be developed and commercialised, initially as an acoustic generator and ultrasonic detector. It is less commonly used now with the discovery of PZT, but is still used in multilayer capacitors due to its high dielectric coefficient. The lead-free formulation of BaTiO_3 is advantageous especially with restrictions on lead use worldwide.

Barium titanate is still of interest today firstly because it is chemically and mechanically very stable, secondly because it exhibits ferroelectric properties at and above room temperature, and finally because it can be easily prepared and used in the form of ceramic polycrystalline samples. Doped barium titanate is used in applications such as semiconductors, thermistors, and piezoelectric devices.

BaTiO_3 has a perovskite structure which is shown in Section 2.2.2. The phase transformations undergone by BaTiO_3 are also previously discussed in Section 2.3.9. The Curie temperature of barium titanate is approximately 120°C . Above this temperature the cubic unit cell is stable up to 1460°C but does not exhibit ferroelectric properties. Crystallographic dimensional changes are a product of temperature as shown in Figure 18.

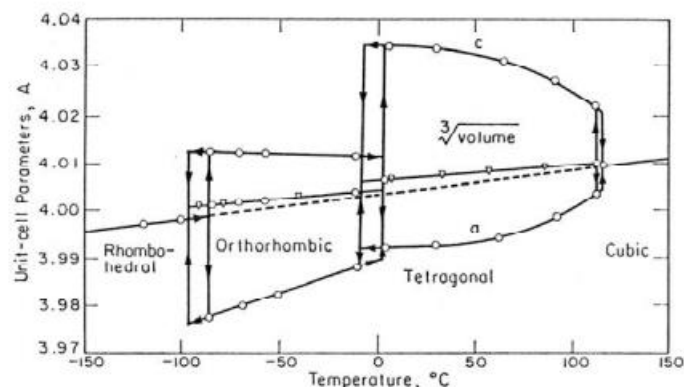


Figure 18. Lattice constants of barium titanate as a function of temperature (Jona and Shirane 1962).

Barium titanate can be prepared by several different methods. Solid state reaction is traditionally used in forming polycrystalline ceramics, some alternatives include sol-gel or hydrothermal method (Moulson and Hebbert, 2003).

Doping of BaTiO₃ is carried out to adjust the properties and microstructure to suit the intended end application. The Curie temperature of barium titanate can be adjusted via A site doping, with substitution of the Ba²⁺ ion for Sr²⁺ or Pb⁺. Domain wall pinning can also be induced with acceptor dopants such as the addition of Co³⁺ in place of Ti⁴⁺(Patil et al, 2020).

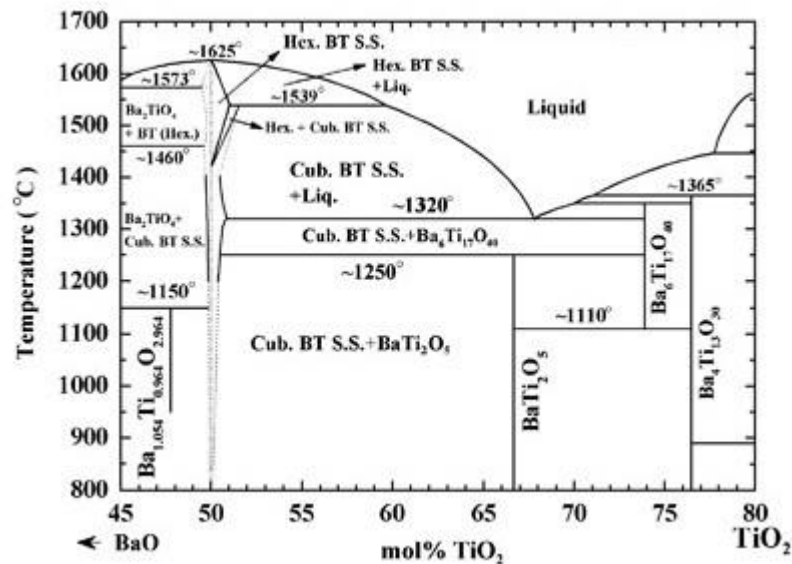


Figure 19. Phase Diagram of BaO-TiO₂ (Lee et al, 2009).

Single crystals barium titanate cannot be obtained from melt growth techniques such as the Bridgman and Czochralski methods due to the existence of a high temperature hexagonal phase. This hexagonal phase is present at 1460°C and can remain in a metastable state during cooling through to room temperature. The BaTiO₃ solidifies at 1618°C and so this process is unsuitable for single crystal growth. Other methods are used instead such as Remeika's method of flux growth (Remeika, and Jackson 1964) and Sasaki's method of melt growth (Sasaki, 1965).

In Remeika's method, the crystals of barium titanate are produced using a small amount 0.2% of iron oxide and 30% BaTiO₃ and covered with potassium fluoride

which is placed into a platinum crucible. This is then heated to 1200°C for 8 hours before being slowly cooled to 900°C (Remeika, and Jackson 1964).

The method developed by Sasaki uses a mixture of 65% TiO₂ and 35% BaTiO₃. The mixture is then heated to 1450°C and then cooled slowly to around the eutectic temperature to enable crystallisation, at which point the cooling can be accelerated. (Sasaki, 1965).

Solid-state crystal growth of barium titanate has been shown to be successful when small amounts of liquid phase are present in the polycrystalline matrix, facilitated by the addition of TiO₂. Single crystals 3 mm x 3 mm x 0.5 mm in size have been obtained by seeding a BaTiO₃ polycrystalline matrix with BaTiO₃ single crystal seeds produced via Remeika method. Samples were annealed at a temperature range between 1250 °C and 1350 °C for 1-30 hours (Yamamoto and Sakuma, 1994).

2.4.2 Lead Based Relaxor Ferroelectric Materials

A true interest in relaxor based ferroelectric single crystals began in 1997 when Park and Shrout (1997) reported on the unusually large piezoelectric response in PZN-PT and PMN-PT single crystal materials. The piezoelectric coefficient was reported up to ~2500 pC/N in the vicinity of the morphotropic phase boundary. The electromechanical coupling coefficient k_{33} was reported at 0.9 with minimal hysteresis. This work prompted more investigation into single crystal growth and other lead based relaxor ferroelectric materials. Three generations of single crystal materials are widely reported in the literature.

The first generation of piezoelectric single crystals are mentioned above, comprised of pseudo-binary compounds such as PZN-PT or PMN-PT. These materials showed a large increase in piezoelectric performance compared to PZT. Figure 20 shows the improved strain properties of Generation I single crystal PZN-PT and PMN-PT compared to various PZT compositions. The enhanced piezoelectric response was observed in rhombohedral PZN-PT and PMN-PT primarily in the (001) orientation. PZT-5H, a 'soft' piezoelectric, has a d_{33} of 590 pC/N and k_{33} of 0.75 (Messing et al, 2004).

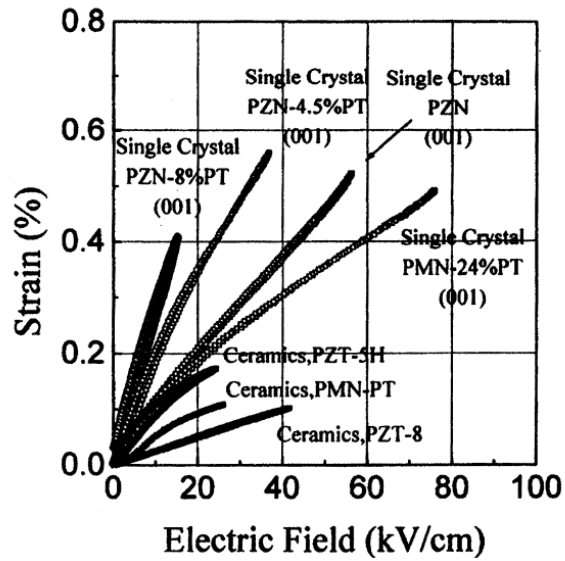


Figure 20. Strain levels of single crystals and polycrystalline PZT (Park and Shrout, 1997).

Generation II saw the introduction of pseudo-ternary systems such as PIN-PMN-PT, the addition of lead indium niobate resulted in improved thermal and field stability. Generation II piezoelectric single crystals however, experience high losses and are therefore unsuitable for high power applications such as transducers.

Generation III are comprised of Mn-doped $\text{Pb}(\text{In}_{1/2}\text{Nb}_{1/2})\text{O}_3$ -PIN-PMN-PT, which has improved the mechanical quality factor for high powder applications while retaining comparable piezoelectric properties to earlier generations (Baasandorj and Chen, 2021).

A summary of the properties observed in the three generations of lead-based relaxor materials is shown in Figure 21.

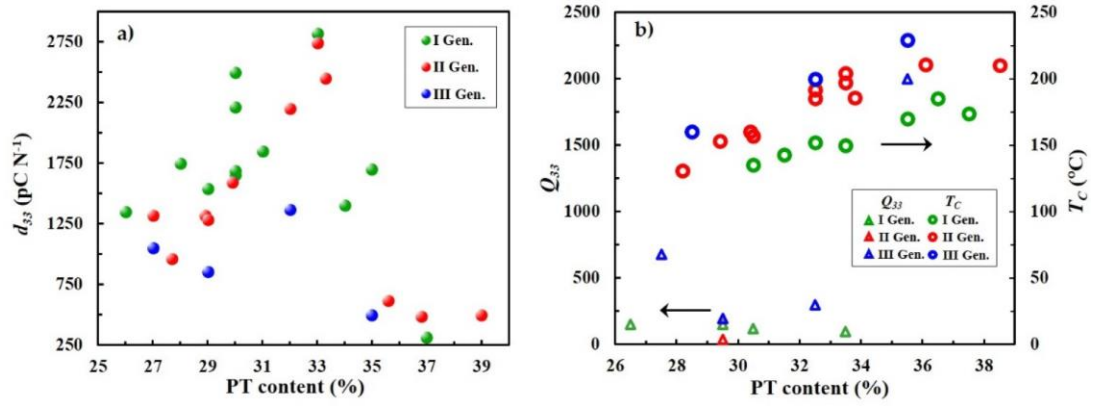


Figure 21. Property comparisons between three generation of lead-based relaxor single crystals PMN-PT, PIN-PMN-PT and Mn: PIN-PMN-PT showing piezoelectric coefficient, mechanical quality factor and Curie temperature (Baasandorj and Chen, 2021).

2.4.3 Summary of Piezoelectric Materials

The materials studied in this work are PMN-PT relaxor ferroelectrics. Single crystal growth of these materials is a topic of much interest due to their exceptional piezoelectric properties compared to PZT. The aim of this work is to establish the SSCG process of PMN-PT first generation materials and apply the knowledge obtained from this to more complex materials, in particular manganese doped PMN-PT for high power applications.

Chapter 3 Introduction to Single Crystal Growth

3.1 Introduction

The benefits of single crystal PMN-PT relaxor piezoelectric materials in applications such as underwater systems and medical devices make establishing a single crystal growth method an interesting and essential topic. This chapter aims to review and discuss the current techniques available for single crystal growth. A thorough analysis of the Solid-State Crystal Growth (SSCG) method is then undertaken as well as a review of the mechanisms underpinning the SSCG process.

Finally, a literature survey is conducted on the current work in single crystal formation of PMN-PT and current work in SSCG of PMN-PT.

3.2 Single Crystal Growth Methods

Single crystal growth methods can be subdivided into three categories; melt growth, solution growth and solid-state growth.

3.2.1 Melt Growth Methods

The Czochralski and Bridgman methods are the two most utilized melt-growth techniques. The Czochralski method is used in the production of single crystals for electronic and optical applications, such as silicon and germanium single crystals, as well as some fluoride and oxide single crystals (Milisavljevic and Wu 2020).

The Czochralski method is shown in Figure 22. The material to be grown is first melted in a controlled atmosphere in a non-reacting crucible. The material is held at that temperature for a period of time before being cooled slowly to slightly above the freezing point. A seed is then inserted into the melt and by pulling and rotating the

seed simultaneously, the crystallisation process occurs. The diameter of the pulled crystal is controlled by manipulating the temperature and pulling rate (Bassani, 2005).

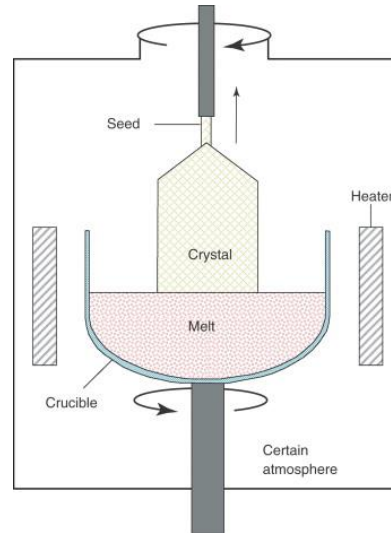


Figure 22. Schematic diagram of Czochralski method (Bassani, 2005).

Single crystal growth from melt allows for the fabrication of large single crystals of excellent quality in a relatively short time when compared to other growth techniques. The melt-growth technique shows some disadvantages however; such as difficulties in maintaining a stable temperature during the crystal growth, achieving chemical homogeneity especially in the case where multiple elements are present in the system, minimising reactivity of the melted material with the crucible, and high costs of production and equipment.

The Bridgman method is also a widely used technique for solid state crystal growth. Similar to the Czochralski method, the Bridgman method employs crystal growth from the melt. The principle of the Bridgman technique is the directional solidification of the material by translating a melt from the hot zone to the cold zone of the furnace. The Bridgman method is shown in Figure 23, here a crucible containing the molten material is translated along the axis of a temperature gradient in the furnace.

Building on this work, the Stockbarger technique, employs the use of distinct temperature zones; high temperature zone, an adiabatic loss zone and a low temperature zone.

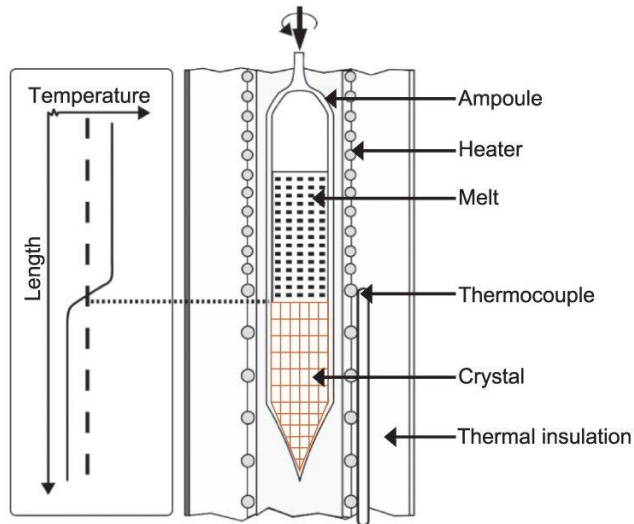


Figure 23. Schematic of the Bridgman single crystal growth method (Batra and Aggarwal, 2018).

Modern Bridgman furnaces are commercially available with separate temperature zones, combined with good control of the lowering mechanism to control growth from the melt. This method is commonly used commercially to produce relaxor-PT single crystals.

Other less commonly used melt techniques are used, the Verneuil method and Floating zone method are shown in Figure 24.

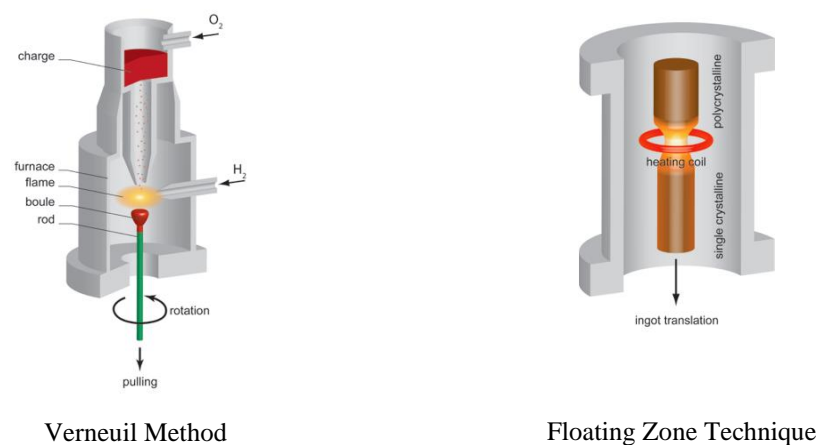


Figure 24. Schematic diagrams of other melt growth methods for single crystal growth; Verneuil Method (left) and Floating Zone Method (Right) (Byrappa, 2003).

The Verneuil method, also known as flame fusion technique, is used in processing of high-quality crystals such as corundum, spinel, rutile and strontium titanate. This technique involves a furnace with oxygen and hydrogen supply, the starting material is a fine powder which is continuously released into the furnace chamber. As the powder passes through the flame in the chamber, it melts into droplets which form on a support rod. As more droplets accumulate, the support rod is lowered away from the flame forming a cylindrical single crystal (Byrappa, 2003).

During the floating zone method, a polycrystalline sample is translated slowly through a heater, where a narrow region will melt. At the solid-liquid interface the impurities diffuse and segregate from solid region to liquid region as the heating zone passes over the whole sample. To grow a single crystal, a seed crystal having a certain orientation needs to be brought into contact with the molten region at the beginning of the process (Byrappa, 2003).

The drawbacks of these methods include very high temperatures for a long period of time, also the use of expensive platinum crucibles which often can't be fully recovered from the process.

Melt grown methods are effective but imperfect at producing completely homogenous single crystals. Relatively large PMN-PT single crystals can be grown by the Bridgman at rates in the order of mm/hour (Messing et al, 2004) However there is still considerable difficulty in precisely controlling the uniformity of titanium concentration in PMN-PT crystals. This is particularly problematic for crystals with composition close to the MPB as a small change in composition can have a large impact on the material properties. The chemical heterogeneity resulting from Bridgman grown crystals renders a large fraction unusable (Messing et al, 2004).

3.2.2 Solution Growth Methods

Solution growth methods are useful for growing crystals that cannot be obtained from the melt growth methods due to factors such as incongruent melting behaviour or materials that undergo phase transitions at temperatures cooler than their melting point. Solution growth methods use starting materials which are dissolved into a

solution, which then becomes supersaturated upon cooling of the solution or evaporation of the solvent.

The flux growth method is shown in Figure 25. This method is based on spontaneous nucleation from a solution upon super-saturation during the cooling process. The starting material along with flux are placed into a platinum crucible within a sealed alumina crucible to prevent loss of volatile components. The crucible arrangement is then placed into a furnace and heated to a suitable temperature. The furnace is then held at this temperature for several hours to ensure complete melting before being slowly cooled. During this cooling process crystallisation occurs, after the material has completely cooled the flux can then be removed with an acidic solution.

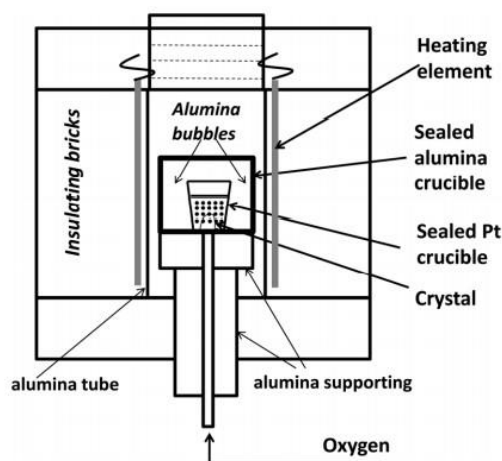


Figure 25. Schematic diagram of flux growth method (Wang and Li, 2012).

This method generates crystal growth at a relatively low temperature compared to melt methods such as Bridgman. However, nucleation can occur at multiple points and variations are seen in impurity and dopant distribution throughout the crystal due to solvent inclusion in the resulting crystal (Wang and Li, 2012).

The Flux Bridgman method is a combination of the conventional Bridgman and flux method where starting materials and flux are contained in a platinum crucible, which after reaching a suitable temperature is cooled through a temperature gradient. An oxygen cooling system is set at the bottom of the crucible to induce nucleation, similar to the conventional flux growth (Wang and Li, 2012). This method is most often used

in manufacture of PZN-PT materials where growth of large crystals has been reported, up to 75 mm in diameter and 55 mm in length.

Top seeded solution growth is also a flux growth method. This again involves melting starting materials and flux in platinum crucible and then placing a seed on the top of the molten mixture. The seed crystal is suspended on a platinum wire as shown in Figure 26.

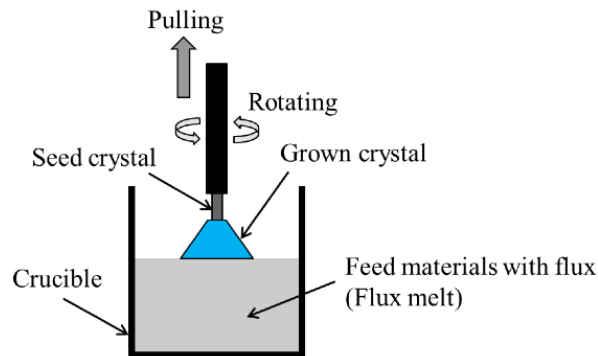


Figure 26. Schematic diagram of top seeded solution growth method (Sun and Cao 2014).

This method offers some advantages in terms of preventing compositional segregation and enabling control of crystallographic growth direction via the seed. However, the growth rate is slower and again this method is costly requiring a specialised furnace, high temperatures and platinum crucibles (Sun and Cao 2014).

3.2.3 Solid-State Crystal Growth

The solid-state crystal growth method utilises the phenomenon of abnormal grain growth in polycrystalline materials. This method is of particular interest because of its simplicity and cost effectiveness. Theoretically with heat treatment one large grain, or the seed crystal, grows at the expense of other grains in the system, resulting in smaller grains being consumed and the ultimate formation of a single crystal material. The principle of the solid-state crystal growth method is shown in Figure 27. This method can take place in a conventional furnace and as such reduces cost implications associated with melt/flux methods.

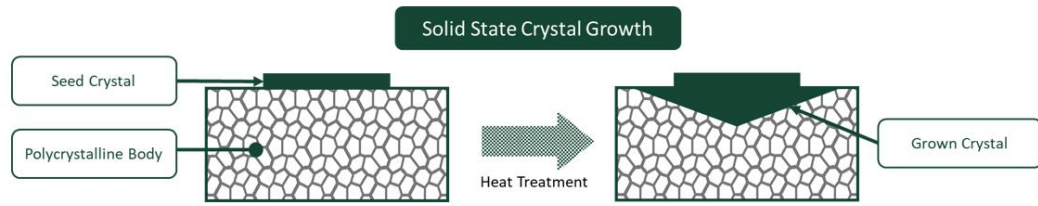


Figure 27. Schematic diagram of solid-state crystal growth technique.

When the SSCG method is successful in fabricating single crystals it has several advantages over conventional growth techniques such as the Bridgman method. The main advantage is homogeneity of grown crystal; for PMN-PT growth particularly, the solubility of the titanium ion is different in the solid and liquid phase which results in a compositional gradient along the grown crystal. In SSCG this problem is mitigated as all growth takes place in the solid state (Lee et al, 2015).

The limitations of this technique are difficulty in achieving control of the microstructure of the polycrystalline ceramic during heat treatment. Growth from the seed and in the grains of the polycrystalline matrix both occur upon heating. Grains that grow within the matrix can impinge on the seed single crystal and inhibit growth rate. A further difficulty that has been identified is control of porosity within the matrix (Lee et al, 2015).

3.3 Background Science

3.3.1 Grain Growth

Grain growth occurs in polycrystalline materials during heating. The growth of grains occurs to enable an overall reduction in grain boundary energy of the polycrystal. The total grain boundary area throughout the polycrystal is reduced as the number of grains is reduced, as shown in Equation (14) (Chiang et al, 1996). ΔG represents the reduction in free energy that occurs when atoms diffuse across boundaries causing grain growth, The grain boundary energy is represented by γ and A_2 and A_1 are the final and initial total grain boundary areas respectively.

$$\Delta G = \int_{A_1}^{A_2} \gamma dA = \gamma(A_2 - A_1) \quad (14)$$

3.3.2 Atomic Diffusion

Diffusion can take place via lattice or grain boundary pathways. The free energy is at a minimum in the centre of a lattice (farthest from the grain boundaries). At concave boundaries the atoms have less neighbours and so the free energy is greater. Convex boundaries have the highest free energy state.

Consequently, as atoms diffuse through the lattice and across boundaries the grain boundary will migrate towards the centre of radius of curvature. Large grains will grow at the expense of smaller grains, which will be consumed.

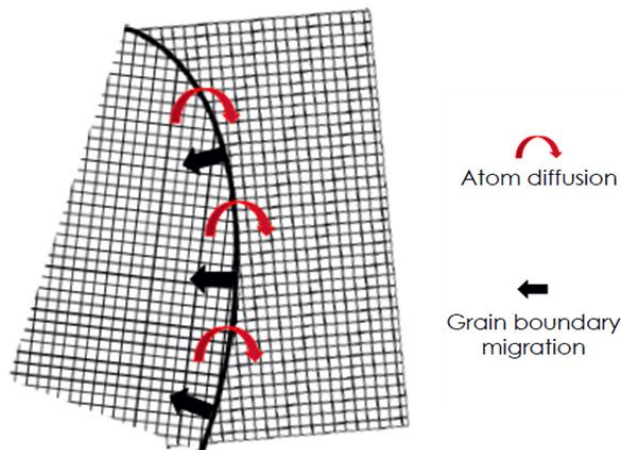


Figure 28. Grain Boundary Migration courtesy of Andrew Bell.

The diffusion constant is temperature dependent. Solid state crystal growth (SSCG) uses a seed crystal, a perfect single crystal, to encourage growth of this large grain which will theoretically consume all the larger grains in the polycrystalline matrix: producing a single crystal.

Atoms diffuse from high concentration to a low concentration according to Fick's First Law, shown in (15). Where the atom flux is represented by J , D is the diffusion coefficient, and dC/dx is the concentration gradient of a material over linear distance.

$$J = -D \frac{dC}{dx} \quad (15)$$

Diffusion is dependent on the species and pathway. The species can vary between cation/anion, interstitial or vacancies. The pathways these can take can be via the lattice, surface, grain boundary or vapour transport.

3.3.3 Normal Grain Growth

In the case of normal grain growth (NGG), the energy difference between two adjacent grains comes from the non-zero curvature of the grain boundary. The diffusion-controlled boundary migration assumes that the energy difference between two atoms is position dependent only.

In Figure 29, atoms are shown in different positions in a polycrystalline grain. Atoms at position A, in the lattice, are at the minimum free energy they can achieve. Atoms in position B, at the convex grain boundary, have fewer neighbours and therefore have a higher free energy than at position A. Atoms at position C, the concave boundary, have the least number of neighbours and therefore the highest free energy. This is expressed in Equation (16) where G represents the free energy of an atom at a given position.

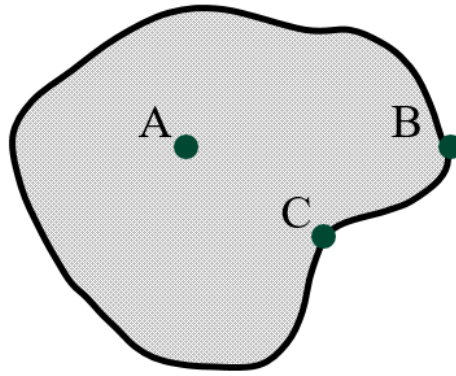


Figure 29. Schematic showing exaggerated non-uniformly shaped polycrystalline grain. Atoms are in position A: lattice, position B: convex boundary and position C: concave boundary.

$$G_A < G_B < G_C \quad (16)$$

Atoms will diffuse to positions of lower energy, therefore atoms at positions B and C will tend to position A to obtain the minimum energy state. When viewing a grain matrix in two dimensions, the direction of growth and subsequent disappearance of neighbouring grains can be predicted from the location of the centre of curvature of the grain boundary, this is shown in Figure 30.

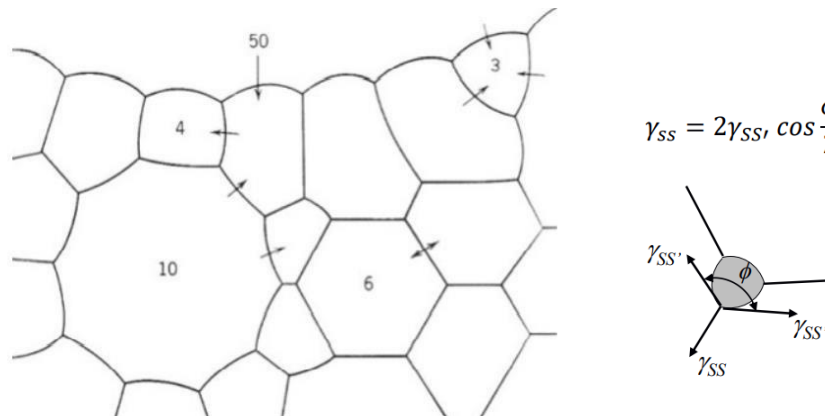


Figure 30. Two-dimensional view of grain matrix where arrows indicate direction of growth (left) and schematic two-dimensional internal interfaces of solid grains (right).

The number of neighbouring grains and therefore number of sides a grain has, determines the curvature of the boundary. Grains with >6 sides have convex boundaries, and these grains are more likely to grow at the expense of their neighbours.

Grains with <6 sides are most likely to be consumed as in all cases grain boundaries migrate towards their centre of radius of curvature. Six sided grains, in this two-dimensional example, are at equilibrium as the grain boundaries in the matrix tend towards dihedral angles that are determined by the interface energies. To maintain an equilibrium at the interface between grains, if both interface energies equal each other, the angle at the boundary must be equal to 120° resulting in 6-sided shape.

In summary of the case of normal grain growth; the driving force for grain growth is the reduction in total grain boundary energy achieved by reduction in grain boundary area. Therefore, larger grains with convex boundaries tend to grow at the expense of smaller grains with concave boundaries.

The grain boundary velocity (v_b) is therefore determined by the driving force (F_b) for resulting from boundary curvature and the grain boundary mobility (M_b) as shown in Equation (17).

$$v_b = M_b F_b \quad (17)$$

Figure 31 shows the free energy state of an atom across a boundary. An energy barrier, shown by Δg^* , represents the activation energy for diffusion. The driving force (Δg), occurs when there is an energy difference of an atom in two different states. The two different states occur when the atom is associated with grain I and grain II. Migration of the boundary occurs when there is a net flux of atoms from one state to another. All atom motion is stochastic but results in a net flux in a particular direction.

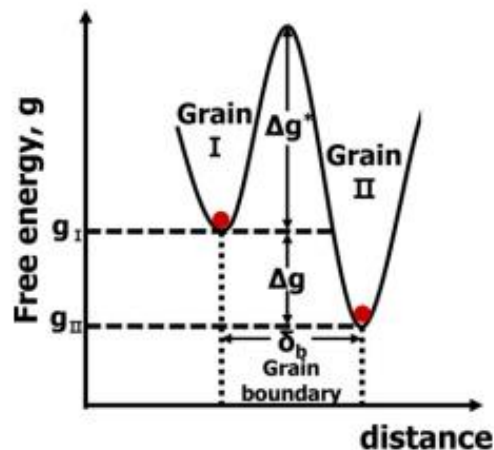


Figure 31. Schematic showing the energy state of atoms on the surface of Grain I and Grain II. Δg^* represents the activation for atom diffusion between the two grains and Δg represents the driving force for atom diffusion.

Normal grain growth obeys the parabolic growth law shown in Equation (18). The difference between the squares of grain size (r) at time (t) and at time = 0 is directly proportional to the product of the interfacial energy and time.

$$r(t)^2 - r(0)^2 \propto \gamma_{SS}t \quad (18)$$

3.3.4 Abnormal Grain Growth

The solid-state crystal growth technique exploits abnormal grain growth (AGG) in the polycrystalline matrix. Grain growth is subdivided into 2 groups: normal grain growth, the idealised case where grain growth is time invariant resulting in unimodal distribution of grain sizes; and abnormal grain growth, referring to certain energetically favourable grains growing rapidly at the expense of other grains, resulting in a bimodal distribution of grain size.

There have been several mechanisms proposed to explain this deviation from normal behaviour. These include second phase particle or pore drag mechanism, the solute drag mechanism and the liquid film enhancement mechanism.

According to the solute drag mechanism, AGG occurs when a pinning force of the secondary phase particles is reduced locally with their coarsening or dissolution. Solute drag occurs with an interaction between a solute and a moving grain boundary. The solute cannot migrate along a grain boundary as easily as the boundary and this causes a drag force on the movement of the grain boundary leading to a reduction of growth for select grains and ultimately development of AGG in the system (Lee et al, 2015).

The principle of the liquid film enhancement mechanism is that mass diffusion facilitated by a liquid film is much faster than diffusion in the lattice or at the boundary. Liquid film enhancement is thought to aid the AGG process. It occurs by a solution segregation process, where larger grain are seen to be less soluble and so smaller grains dissolve more readily. This dissolved material then deposits on the larger grains,

facilitating faster mass transport and more rapid growth of large grains (Lee et al, 2015).

More recently it has been observed that the type of grain boundary has more significance on determining whether AGG will occur. Faceted grain boundaries have been observed to be more likely to undergo AGG. A more recent study by Kang et al. (2016) showed the migration kinetics are not linear with respect to driving force in a faceted system. This result suggests that the migration mechanism of a faceted boundary varies with the driving force. This critical driving force Δg_c was shown to be related to the degree of faceting in the system.

The grain growth here has been observed to be controlled by either by the interface reaction or the diffusion of atoms implying mixed control of the boundary migration. this is shown schematically in Figure 32.

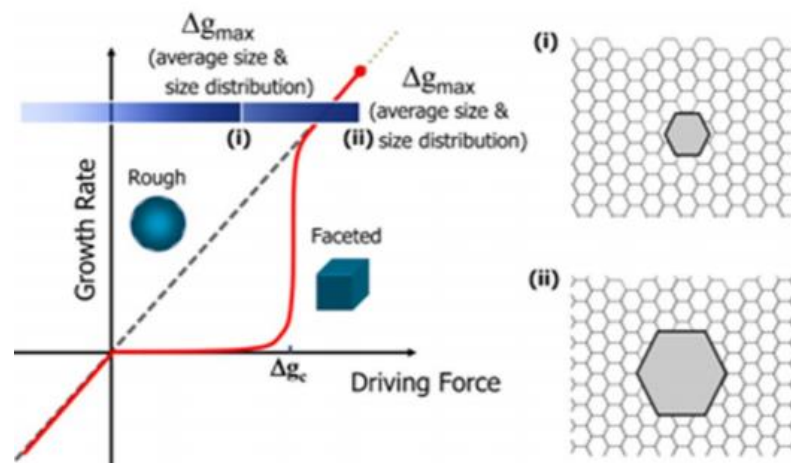


Figure 32. Schematic illustration of the 'mixed control mechanism' with rough and faceted boundaries (Kang et al, 2016).

The growth of faceted single crystals has been shown in this study to be comparable to the abnormal grain growth of faceted grains. The maximum driving force Δg_{max} of the complete system is dependent on grain size distribution and average grain size. The grain growth behaviour of a system can be predicted as follows (Lee et al, 2015):

When $\Delta g_c = 0$	NGG
When $0 < \Delta g_c \ll \Delta g_{max}$	Pseudo NGG
When $\Delta g_c \leq \Delta g_{max}$	AGG
When $\Delta g_{max} \ll \Delta g_c$	Stagnant grain growth

3.3.5 Summary of Grain Growth Mechanisms

Figure 33 shows a visual summary of the grain growth mechanisms discussed in this section, including NGG and the proposed mechanisms of AGG.

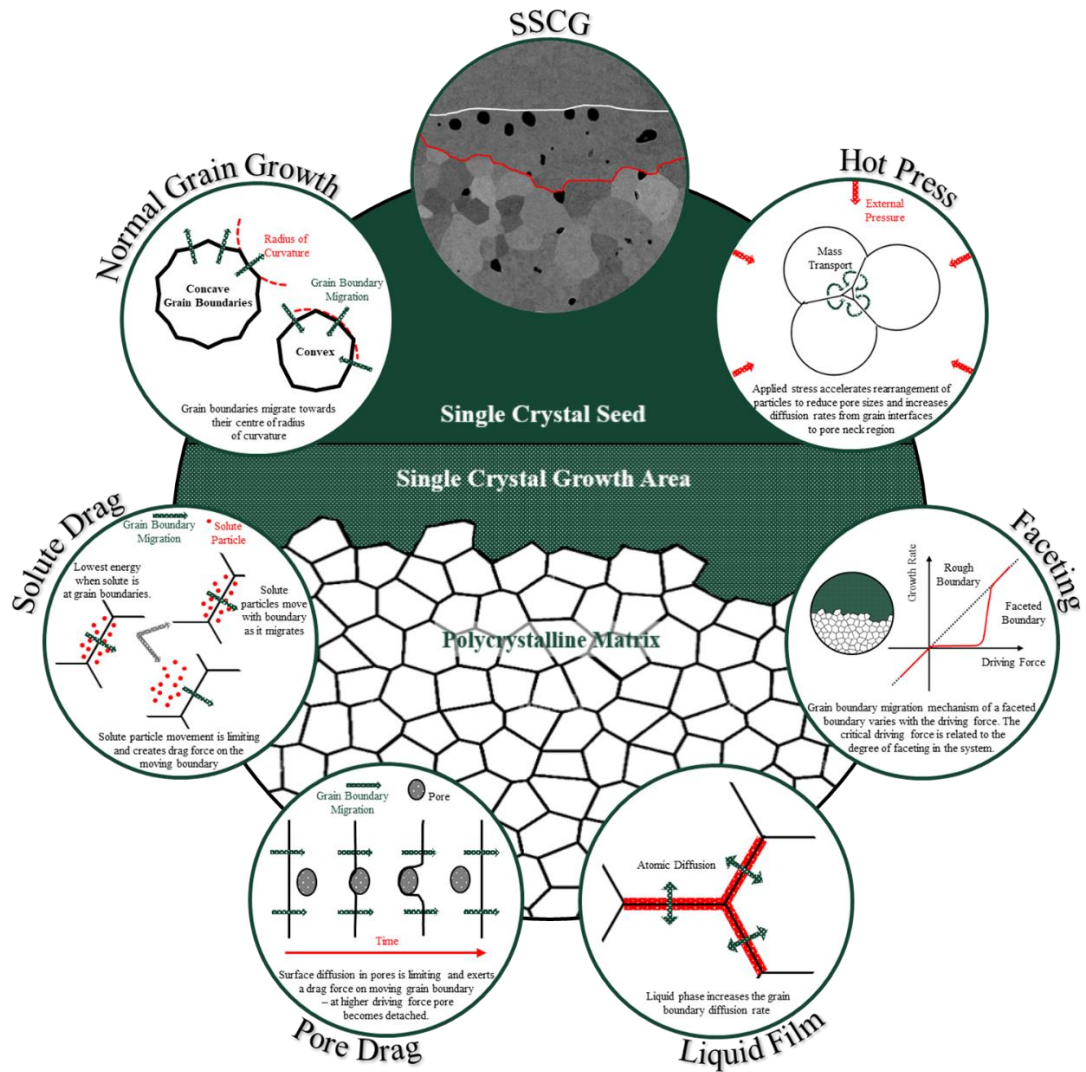


Figure 33. Summary of grain growth mechanisms.

3.4 Contributions to Single Crystal Growth

Growth of PMN-PT crystals has traditionally been conducted by Bridgman method. Shimanuki et al. (1998) grew the first relaxor-PT single crystals using the vertical Bridgman method. In their experiment, the charge was suspended inside the furnace, and it was then moved down to the lower zone to be crystallized. Lim et al. (2005) used the modified Bridgman method to grow PMN-PT single crystals. Relatively large (30 mm diameter \times 150 mm length), lead based relaxor-PbTiO₃ ferroelectric single crystals are grown at mm/h rates by the Bridgman method.

Composition segregation is an unavoidable disadvantage of the Bridgman method for growing solid solution crystals. Grown crystals show segregation of Ti⁴⁺ ion and longitudinal piezoelectric variation along growth direction with three different modified Bridgman methods. A PMN-PT single crystal, 80 mm in diameter and 320 mm in length, was grown using modified Bridgman method by Echizenya and Matsushita (2011); however segregation of the titanium ion resulted in inconsistent properties. The piezoelectric coefficient (d_{33}) ranged from 1300 to 1700 pC/N. The modified Bridgman method used (continuous feeding) reduced the TiO₂ variation in the crystal grown to 6% compared to 20% variation in the conventional Bridgman method.

Zawilski et al. (2003) encounter similar problems stating ‘despite the rapid progress in developing techniques for growing larger single crystals, there is still considerable difficulty in precisely controlling the uniformity of the concentration of Ti in lead-based single crystals’. This is particularly problematic for MPB crystals as the properties are very sensitive to composition. The chemical heterogeneity of Bridgman grown single crystals renders a large fraction of the crystal unusable.

As such research has been undertaken focussing on using the solid-state crystal growth method to produce single crystal PMN-PT. As a general observation, the SSCG method is carried out in similar ways between studies; a composition of PMN-PT is chosen near the MPB, and the polycrystalline is seeded with either barium titanate or PMN-PT single crystal seeds and then further heat treated. Variation occurs on pre-processing such as use of a hot press, or use of excess PbO/liquid phase. Sintering

regimes also differ with variation in time or temperature or sintering in oxygen or other atmospheres.

The use of BaTiO₃ single crystal seed was justified by Messing et al. (2001) as barium titanate is isostructural with PMN-PT, The lattice parameters of Pb(Mg_{1/3}Nb_{2/3})O₃–30 mol% PbTiO₃ (PMN-30PT) and BaTiO₃ are very similar: PMN-30PT has lattice parameter $a = 4.015 \text{ \AA}$ and barium titanate $a = 3.992 \text{ \AA}$, $c = 4.036 \text{ \AA}$. ° From a practical point of view, it is preferable to use PMN-PT crystals but low-cost commercial crystals of BaTiO₃ are easier to obtain. BaTiO₃ was chosen over other perovskite candidates as it is chemically stable at high temperature and in the presence of PbO liquid phase (Messing et al, 2001).

Some initial work on this topic was undertaken by Li et al. (1998) after other studies had shown that the SSCG method had been proven feasible for producing single crystal ferrites (Yamamoto and Matsuzawa, 1988) and the BaTiO₃ system (Yamamoto and T. Sakuma, 1994).

In the work by Li et al. (1998), Pb(Mg_{1/3}Nb_{2/3})O₃–35 mol% PbTiO₃ (PMN–35PT) single crystals were embedded in polycrystalline powders of the same composition and cold isostatically pressed at 340 MPa into pellets. These were then hot-pressed from 900 °C to 1000 °C for 1 h at 40 MPa to obtain a fully dense matrix prior to crystal growth. The sintered pellets were then annealed at temperatures ranging from 900 °C to 1200 °C with a double crucible arrangement and PbZrO₃ packing powder to prevent volatilisation of lead. It was found in this work that pores pinning the boundary between the seed crystal and polycrystalline matrix slowed the growth rate from the seed, and so hot pressing was incorporated into the process to reduce porosity and therefore the pore drag effect and facilitate grain boundary migration of the single crystal.

Figure 34 shows an SEM image of the prepared PMN-35PT samples in the work by Li et al. (1998). There is an area of single crystal growth around the original seed, made obvious by the porosity in the polycrystalline matrix and growth area. It was proposed in this work that the limiting factors of the grain boundary migration were the effects of pore coarsening and compositional degradation during the annealing stage.

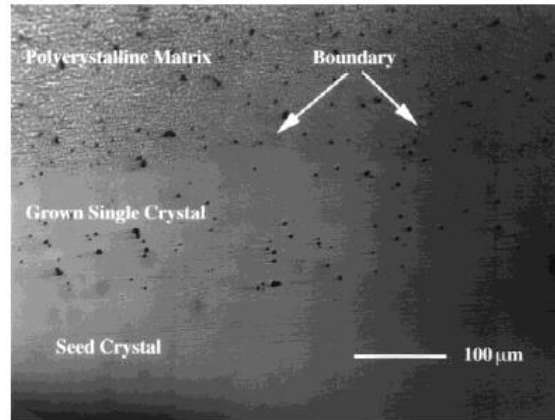


Figure 34. Polycrystal/grown crystal/seed crystal interfaces of a sample after hot-pressing for 1 h at 950°C under 40 MPa, followed by a pressureless annealing 16 hours at 1200 °C (Li et al, 1998).

Figure 35 shows the cross section of a seed single crystal that has grown several millimetres into the polycrystalline matrix after annealing for 140 h at 1150°C in air under pressureless conditions (Li et al, 1998). However, the polycrystalline matrix was much more porous resulting in loss of dielectric properties compared to that of the hot pressed sample. The porosity of the grown crystal decreased from 5.4 vol% by pressureless annealing to 1.8 vol% by hot-pressing and annealing.

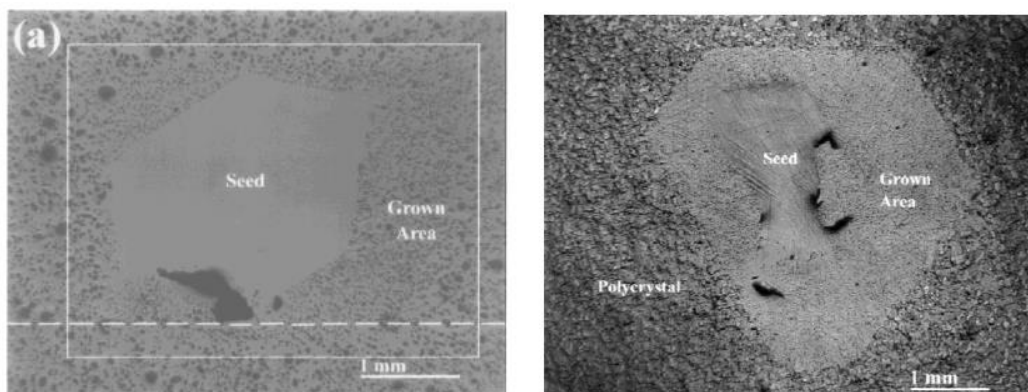


Figure 35. Seed single crystal (centre) of PMN–35 mol% PT grew several millimetres into polycrystalline precursor after annealing at 1150°C for 140 h (Li et al, 1998).

This work by Li et al (1998) was concluded by noting that the work carried out had established the feasibility of growing relaxor-based single crystals from polycrystalline pre-cursors using the new approach of solid-state crystal growth. In

general, the velocity of a grain boundary was found to be directly proportional to both the boundary mobility and the driving force for migration. An increase in either of these would therefore enhance the growth rate of the crystal. It was also stated that hot-pressing a seeded polycrystalline compact of PMN–35PT prior to crystal growth yielded a fully dense matrix and a significant reduction of porosity in the grown single crystal after annealing, with more emphasis to be placed on the effect of grain size and porosity on crystal growth rate in future work.

Khan et al. (1999) also succeeded in growing PMN–35PT single crystals of approximately 0.5 mm size in the presence of a small amount of a PbO liquid with the addition of PbZrO₃ or PbO. In this study, PMN–35PT single crystals were embedded in PMN–35PT powder and uniaxially pressed to shape at 56 MPa. The compacts were then cold-isostatic-pressed at 380 MPa, and finally uniaxially hot-pressed at 20 MPa and 950°C for 30 mins. After hot-pressing, the compacts were then buried in powder of the same nominal composition and annealed for 10 h at 1150°C in a conventional furnace using a double alumina crucible arrangement to minimize PbO loss. The resulting specimens were then polished to be analysed by XRD. The average grain size was then determined by the linear intercept method.

Figure 36 shows the resulting samples produced in the work by Khan et al. (1999) after hot pressing with embedded seed and further annealing at 1150 °C for 10 hours. The average grain size was reported as $0.48 \pm 0.05 \mu\text{m}$, after annealing there was grain coarsening reported with the average grain size increasing to $1.86 \pm 0.20 \mu\text{m}$. It is quoted that ‘negligible single-crystal growth had occurred’ (Khan et al, 1999). It is later suggested that the lack of growth was attributed to the presence of pores and/or second phases at the single crystal to polycrystal interface (shown in Figure 36 (B)). This work suggests that suppression in the growth was caused by grain boundary pinning by such features.

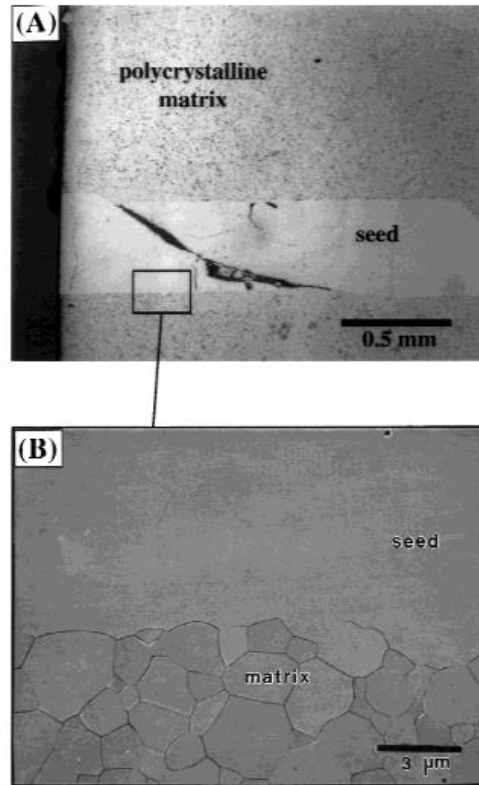


Figure 36. Seeded specimen after 1150°C/10 h anneal packed in PMN–35PT powder in a double crucible: (A) low-magnification light optical micrograph (note that dark spots in matrix are grain pull-outs from polishing, and that seed cracked during processing); (B) higher magnification SEM micrograph of seed/polycrystal region (Khen et al, 1999).

In the experiments carried out in this study (Khan et al, 1999), where the hot-pressed specimens are annealed with atmospheric powder enriched with PbZrO_3 , crystal growth did occur, as shown in Figure 37. There was also matrix grain coarsening reported at $13.3 \pm 0.3 \mu\text{m}$, considerably more than the specimen annealed without the PbZrO_3 enriched atmosphere. The maximum growth of the seed crystal was reported at 1.4 mm. It is worth noting that there were spherical second phase inclusions produced that were dispersed throughout the grown crystal (shown in Figure 37) in the region of grown single crystal. EDX analysis of the second phase particles revealed they were primarily composed of Lead and Oxygen. What appear initially to be large pores in the grown area and polycrystalline matrix are suggested to be the PbO secondary phase pull-outs from polishing. The samples are reported to be fully dense but quantitative density values of the samples are not reported in this paper and so it is unconfirmed whether this is grain pull-out or porosity in the sample.

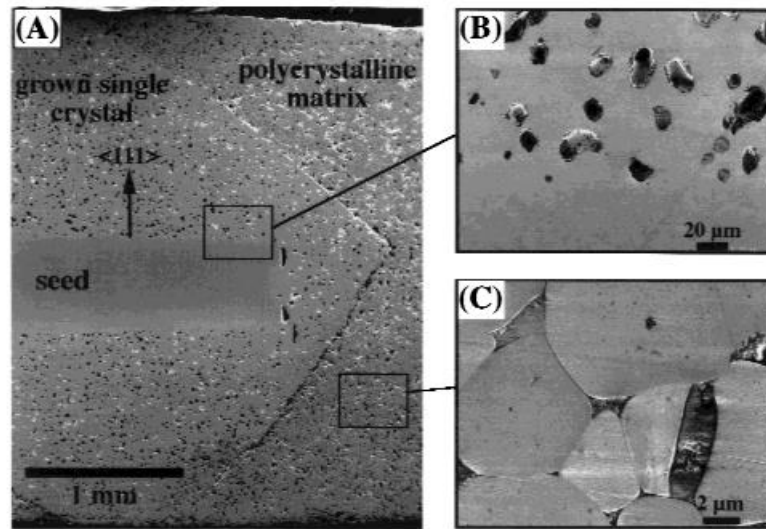


Figure 37. Microstructure of seeded-specimen after annealing at 1150°C for 10 h surrounded by PZ powder in a covered crucible: (A) low magnification SEM micrograph showing considerable single-crystal growth, and higher-magnification SEM micrographs of (B) seed/grown-crystal region, and (C) polycrystalline matrix (Khan et al, 1999).

Khan et al (1999) conclude that the most prominent difference between the two growth experiments is the attendant formation of a wetting PbO-based second phase in the polycrystalline matrix of the specimen annealed surrounded by PbZrO₃ powder. The PbO based second phase was assumed to be liquid at annealing temperature, this is as expected as the temperature of 1150°C used is considerably greater than the melting points of PbO and the PbO rich PbO–PMN and PbO–PT eutectics, 886°, 830° and 838°C respectively. It is reasoned that the liquid PbO-based second phase increased boundary mobility and thus promoted matrix grain growth and single-crystal growth.

The growth kinetics of PMN–PT single crystals was also studied by Kim et al (2006). In this study, single crystal growth of PMN-35PT via the solid-state crystal growth technique was observed with the addition of Li₂O/PbO dopants while using barium titanate single crystal seeds.

The PMN-35PT ceramic powder was prepared using solid state processing method and was incorporated with a ratio of Li₂O/PbO, varying from 1-8mol%. The powders were then cold isostatically pressed at 200 MPa with the BaTiO₃ single crystals embedded in the powder and then annealed at 1200 °C for 10 h in oxygen. The aims of this study was to determine the effect PbO and Li₂O on the microstructure and growth from the seed.

Figure 38 shows the results of single crystal growth published by Kim et al. (2006) where samples have been produced with varying ratios of excess PbO and Li₂O and all annealed at 1200 °C for 10 hours in oxygen. In Figure 38 the samples are as follows: a) 8% mol PbO excess, b) 1% mol Li₂O and 7% mol excess PbO, c) 2% mol Li₂O and 6% mol excess PbO and d) 4% mol Li₂O and 4% mol excess PbO.

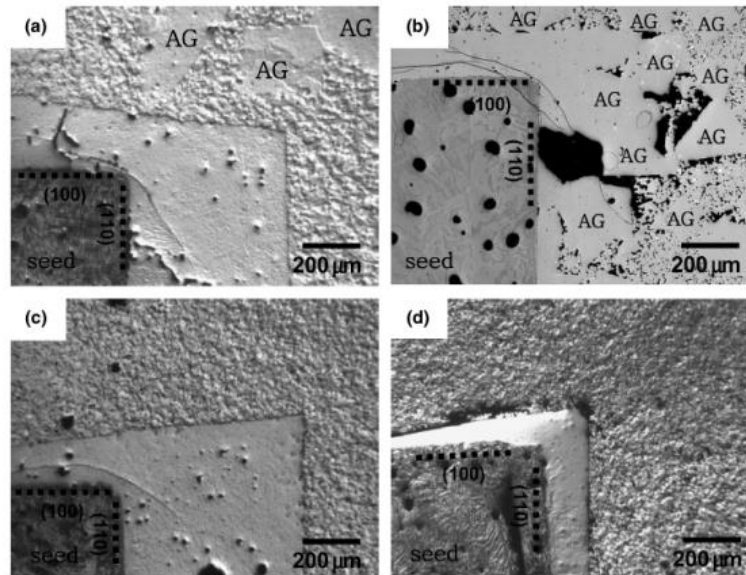


Figure 38. Microstructures of the single crystal which has grown toward (a) a 8 mol% PbO excess $Pb(Mg_{1/3}Nb_{2/3})O_3-PbTiO_3$ (PMN-PT) powder compact, (b) a 1 mol% Li₂O–7 mol% PbO excess PMN-PT powder compact, (c) a 2 mol% Li₂O–6 mol% PbO excess PMN-PT powder compact, and (d) a 4 mol% Li₂O–4 mol% PbO excess PMN-PT powder compact during annealing at 1200°C for 10 h in oxygen (Kim et al, 2006).

From Figure 38, sample (a) shows considerable growth from the seed, and also the formation of abnormal grains in the polycrystalline matrix. In sample (b) the abnormal grains have inhibited crystal growth due to impingement with the seed.

It is summarised in the work by Kim et al (2006) that the driving force of crystal growth is determined by the difference in size between the seed crystal and the matrix grains. When the driving force for crystal growth exceeds the critical driving force, the growth is governed by diffusion.

Although SSCG was shown to be achievable in this work by Kim et al (2006), with grain growth from the seed between 50 – 200 μm over 10 hours, the produced single crystals were not large enough for practical use and contained a considerable fraction of pores of several tens of microns.

King et al (2003) have also studied PMN-PT single crystals grown using the SSCG method. In this study single crystal seed plates were embedded in a matrix of PMN-35PT with varying amounts of liquid phase (PbO) content in the range of 0 to 5 vol%. PMN-PT single crystal seeds were embedded in the PMN-35PT powders and uniaxially pressed at 10 MPa. These pellets were then cold isostatically pressed at 340 MPa and then subsequently hot-pressed at 20 MPa for 30 min. The hot-pressing temperature for samples with 0 vol% excess PbO was 900°C. This temperature was lowered to 880°C for all samples with excess PbO to prevent volatilization of the liquid phase. The sectioned sintered pellets were then annealed in a conventional furnace for 0 – 10 hours at 1150 °C.

The average grain sizes for all samples after the hot-pressing step were found to be approximately 0.7 μm (King et al, 2003). Figure 39 shows the SEM images of the single crystal growth for various liquid-phase volume fractions annealed in this work. The gradient in pore size from the interior to the single-crystal interface is indicative of matrix coarsening during the annealing treatments. Figure 39 shows the grown crystals achieved by King et al (2003). The samples here have been annealed for 5 hours at 1150 °C with increasing excess PbO content; a) 0%, b) 1.5%, c) 3.0% and d) 5.0%. Growth from the seed can be seen to be approximately 100 μm. Again, porosity can be seen in the matrix and the crystal growth area.

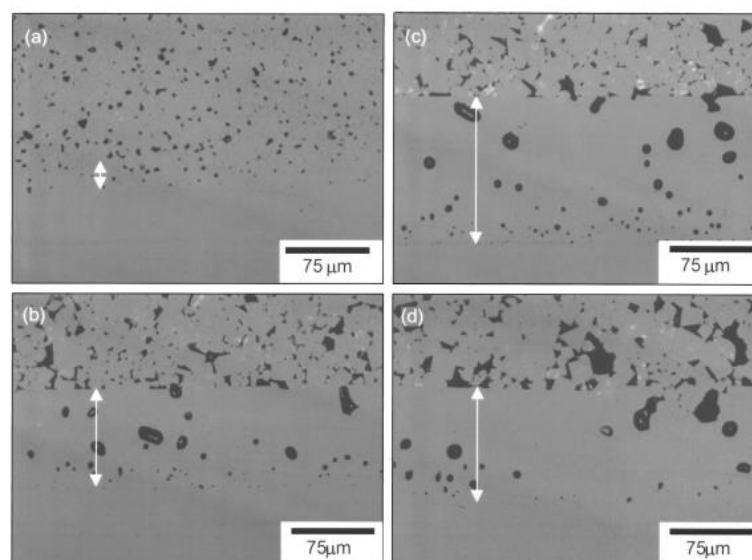


Figure 39. Light optical micrographs of PMN-35PT single-crystal migration annealed for 5 h at 1150°C for (a) 0.0, (b) 1.5, (c) 3.0, and (d) 5.0 vol% PbO additions (King et al, 2003).

In summary of the work carried out by King et al (2003), the growth rate maxima were observed at an excess PbO composition of 3 vol%. For PbO contents from 0 to 3 vol%, both the matrix and single crystal growth constants increased with increasing PbO content, attributed to an increase in pore mobility. For larger PbO volume fractions, the single-crystal growth constant was independent of PbO content, indicative of an interface reaction-controlled mechanism.

Sintering in oxygen atmosphere was explored by Richter et al. (2009) where PMN-PT samples were hot pressed before SSCG at 45 MPa and 900 °C for 30mins, using an oxygen or air atmosphere, this is shown in Figure 40. There is a significant reduction in porosity of the single crystal growth area when using an oxygen annealing atmosphere. This is speculated to be caused by high concentration of O₂, which also is said to be reducing the evolution of O₂ gas during the evaporation of the volatile components by avoiding the loss of liquid PbO phases through the following reaction: $\text{PbO(l)} \leftrightarrow 2\text{Pb(g)} + \text{O}_2\text{(g)}$.

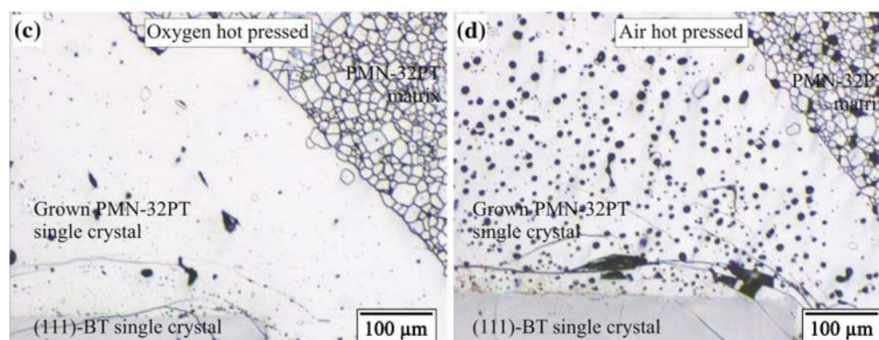


Figure 40. Grown PMN-PT single crystals using $\langle 111 \rangle$ -oriented BaTiO₃ single crystals. The ceramics were hot-pressed before single crystal growth at 900 °C for 30 min at 45 MPa using (a) oxygen and (b) air atmospheres. The hot-pressed pellets were subsequently annealed in air for single crystal growth at 1150 °C for 10 hours (Richter et al, 2009).

Commercial production of lead-containing piezoelectric single crystals by the SSCG method has been recorded. Ceracomp produce PMN-30PT, PMN-PZT and Mn-Doped PMN-PT single crystals using the SSCG process (Lee, 2004). These are made using barium titanate single crystal seeds. There is very little literature pertaining to the process of growing these materials, however mm size single crystals are available

to purchase from Ceracomp, giving an idea of the size of single crystal growth achieved (Lee, 2004).

3.4.1 Summary of Single Crystal Growth Literature

Table 1 shows a summary of the previous work of SSCG in the PMN-PT system.

From the literature survey conducted as part of this work, insights into the preparation and processing of PMN-PT grown via the solid-state crystal growth method have been gained. The main points of interest to be taken from this section are listed below:

- Crystal growth has been seen to be limited by porosity in the matrix, the presence of pores and/or second phases at the single crystal to polycrystal interface is reported to significantly reduce single crystal growth rate (Kim et al, 2006) (Khan et al, 1999).
- Hot pressing has proven to be a valuable tool for producing highly dense precursor materials for SSCG. It is reported in several works that hot-pressing a seeded polycrystalline compact of PMN-PT prior to crystal growth yielded a fully dense matrix with a significant reduction of porosity in the grown single crystal after annealing (King et al, 2003) (Khan et al, 1999) (Li et al, 1998).
- The presence of liquid phase in the system is beneficial, it is reported that the growth rate maxima were observed at an excess PbO composition of 3 vol%. For PbO contents from 0 to 3 vol%, both the matrix and single crystal growth increased with increasing PbO content, which was attributed to an increase in pore mobility (King et al, 2003).
- Hot pressing or annealing in an oxygen atmosphere has a positive effect on single crystal growth, it is reported that there is a significant reduction in porosity of the single crystal growth area when using an oxygen annealing atmosphere (Richter et al, 2009).

It is therefore vital that the first part of this work that is undertaken is to establish the hot-pressing process to maximise density and minimise porosity, to ensure the best possible precursor materials are made to obtain an optimal amount of single crystal growth in the SSCG process.

Table 1. Tabulated summary of literature survey of PMN-PT single crystal growth via SSCG method.

Reference	Li et al. 1998	Li et al. 1998	Khan et al. 1999	Kim et al. 2006	King et al. 2003	Richter et al. 2009
Material	PMN-35PT	PMN-35PT	PMN-35PT	PMN-35PT	PMN-35PT	PMN-35PT
Seed	PMN-35PT	PMN-35PT	PMN-35PT	BaTiO ₃	PMN-PT	BaTiO ₃
Hot Press	900 °C- 1000 °C 1 hour	900 °C- 1000 °C 1 hour	950 °C 20 MPa 30 mins	Not hot pressed	880-900 °C 20 MPa 30 mins	900 °C 45 MPa 30 mins Oxygen/Air
Annealing	1100 °C 16 hours	1100 °C 16 hours Presence of PbZrO ₃	Hot pressed at 950°C and 20 MPa for 30 min. Annealed surrounded by PbZrO ₃ powder.	1200 °C 10 hours Oxygen atmosphere.	1150 °C 0-10 hours	1150 °C 10 hours
Approximate Growth Rate	15 µm/h	6 µm/h	0.14 µm/h	5-20 µm/h	20 µm/h	10-30 µm/h
Comments	High porosity in polycrystalline matrix and growth area.	Slower growth rate though to be caused by pore coarsening, and compositional degradation during the anneal	Secondary PbO rich phase formed in polycrystalline matrix and growth area.	Some abnormal grains formed that limited grain growth by abnormal grains in matrix.	Increasing PbO excess was seen to increase growth rate as it increased pore mobility with presence of liquid film.	Significant reduction in porosity of the single crystal growth area when using oxygen annealing atmosphere.

Chapter 4 Materials Synthesis and Experimental Procedure

4.1 Introduction

This chapter will give a detailed description of the synthesis of materials used in this work. The powder synthesis route to produce PMN-PT is firstly shown, along with the evaluation of processing methods and choice of composition. The hot-pressing experimental method is then detailed, which includes the synthesis procedure of hot pressing-specific supplementary materials. This is then followed by the texturing experimental method and finally a description of the materials characterisation and analysis techniques used in this work. Any deviations from the process outlined here that are used for specific experiments are noted in the appropriate experimental results section.

PMN-PT ceramic powder is prepared via the metal oxide route which is shown in Section 4.2. This method entails mixing stoichiometric quantities of raw oxide powders. The powders are then heated together to enable the constituents to combine in a solid-state reaction. A two-steps procedure is required to produce PMN-PT to avoid forming impurity phases. This method is widely known as the Columbite method, where precursor MgNb_2O_6 is first formed and then used as a reactant in the PMN-PT synthesis step. The composition of PMN-PT can be selected and tailored by changing the amount of raw material used. Generally, researched compositions of PMN-PT are selected near the morphotropic phase boundary which is discussed in Section 4.1.1.3.

This chapter will also review the synthesis for the supplementary materials required for the hot-press and texturing experimental procedure. These are explored in detail in Sections 4.3 and 4.4 respectively. The hot press experimental procedure is outlined here to demonstrate the equipment and materials required for each experiment. The bespoke die that is used to contain the sample is shown along with the processing of inert packing powder used to surround and protect the ceramic sample.

For the texturing section of this work, barium titanate platelets are used. The method of incorporation of the platelets into the ceramic powder is discussed and the formulation of barium titanate later used in this work is also outlined, this is again produced via the solid oxide route.

Finally, the characterisation techniques to analyse the materials are shown. The techniques include; the Archimedes method for density measurements, X-ray diffraction, scanning electron microscopy (SEM) and energy dispersive X ray (EDX) analysis. Specific sample preparation for these characterisation methods are shown in this section.

4.1.1 Background

Lead Magnesium Niobate (PMN) is a relaxor ferroelectric. PMN-PT is a solid solution of PMN and lead titanate PbTiO_3 . It takes the form of an ABO_3 perovskite structure as shown Figure 41, where lead cations occupy the A site coordinated with 12 oxygen anions and a distribution of magnesium, niobium and titanium cations occupy the B sites in the octahedral interstices.

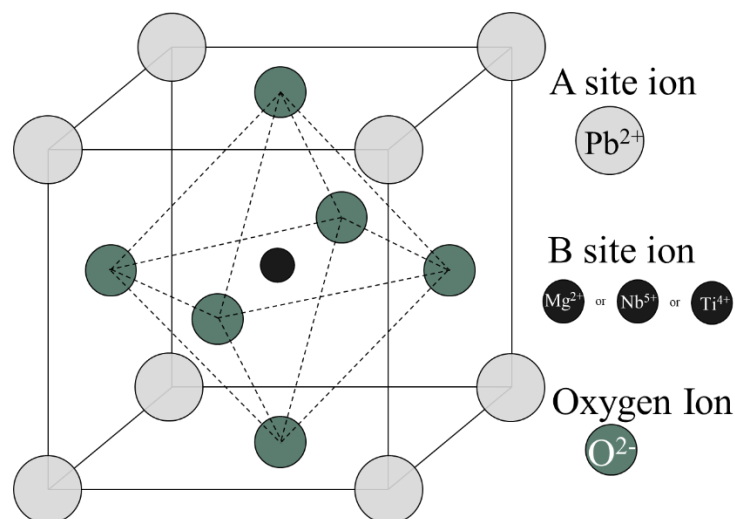
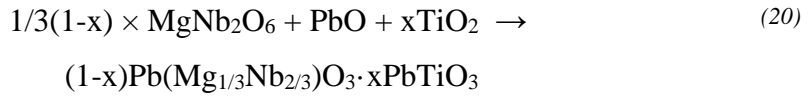
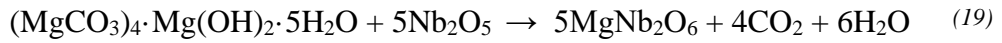


Figure 41. PMN-PT unit cell structure and ion placement.

4.1.2 Pre-Synthesis Steps

To synthesise pure perovskite PMN-PT, the precursor material, MgNb_2O_6 , must first be produced. Swartz and Shrout (1982) first proposed pre synthesis of the Nb_2O_5 and MgO , separately to PbO , to avoid the niobium and lead components reacting together to form a pyrochlore phase. The pyrochlore phase has the general formula $\text{A}_2\text{B}_2\text{O}_7$ and due to its paraelectric nature, significantly degrades the dielectric properties of PMN-PT.

To avoid formation of the pyrochlore phase, MgNb_2O_6 is first produced as shown in Equation (19). Equation (20) then shows the second stage where PMN-PT is produced where 'x' represents the composition of the final PMN-PT.



4.1.3 Choice of composition

PMN-PT is a solid-state solution made up of lead magnesium niobate and lead titanate. The phase diagram of PMN-PT is shown in Figure 42. The composition of the PMN-PT used in this work is $0.7 \text{Pb}(\text{Mg}_{1/3}\text{Nb}_{2/3})\text{O}_3 \cdot 0.3 \text{PbTiO}_3$. This was selected as it is near the rhombohedral-tetragonal morphotropic phase boundary, slightly favourable to the rhombohedral phase. We also initially wanted to follow the structure of work undertaken by Ho Yong Lee's group at Ceracomp who use the same composition of PMN-PT in their solid state crystal growth experiments (Guo, 2012)(Lee et al, 2009).

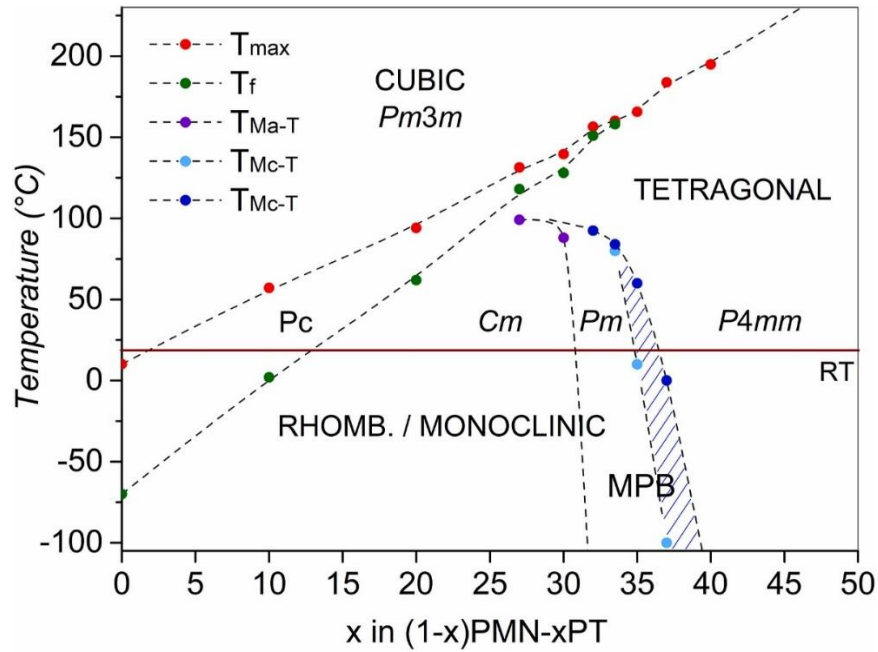


Figure 42. PMN-PT Phase Diagram (Otoničar et al, 2021).

4.2 Powder Synthesis

Each step is shown for the making of the precursor MgNb_2O_6 and subsequent PMN-PT. The analysis techniques used to ensure quality and phase purity at each stage are also highlighted in Figure 43.

The method begins with the addition of dry niobium oxide and magnesium carbonate hydroxide pentahydrate (MCHP), the raw materials are milled, dried and calcined. Lead oxide and titanium dioxide are then added to the formed magnesium niobate to produce PMN-PT. The materials are milled again, dried, and further heat treated. The binder can then be added and pressing takes place to shape the green powder into disc compacts which are then sintered.

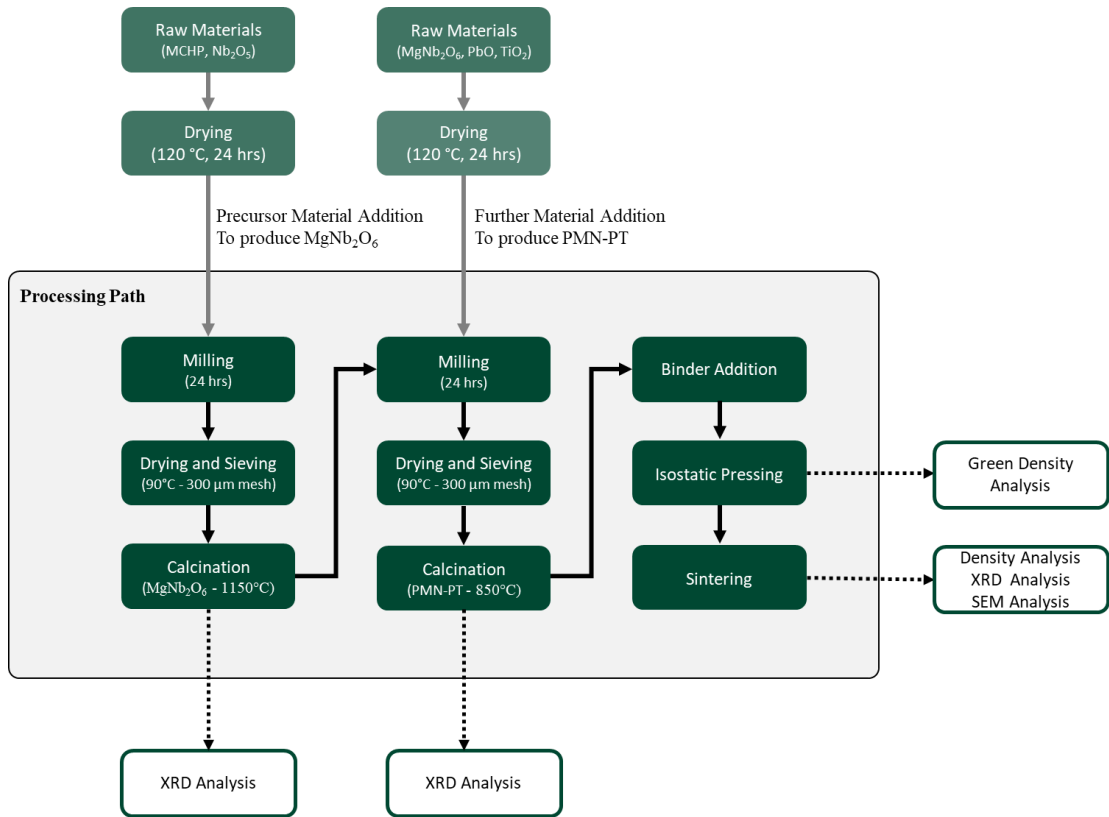


Figure 43. Flow chart summarising the powder processing route for hot and cold pressed pellets, including characterisation techniques.

4.2.1 Raw Materials

The raw materials that are used in this process are summarised in Table 2. The purity and manufacturer of each raw material is provided.

Table 2. Raw materials for PMN-PT synthesis.

Raw Material	Chemical Formula	Manufacturer	Purity
Niobium Oxide	Nb ₂ O ₅	Sigma-Aldrich	> 99.9%
Magnesium carbonate hydroxide pentahydrate (MCHP)	(MgCO ₃) ₄ ·Mg(OH) ₂ ·5H ₂ O	Honeywell	> 99%
Lead Oxide	PbO	Sigma-Aldrich	> 99%
Titanium Dioxide	TiO ₂	Sigma-Aldrich	> 99.9%

4.2.2 Drying and Weighing

The raw powders are first dried at 120 °C for at least 24 hours to remove any moisture. They are then weighed to the desired amounts using a balance accurate to 0.001 g.

4.2.3 Mixing

To ensure a homogenous mixture and uniform particle size, the mixed powders are milled on a ball mill for 24 hours (Model 12 VS CAPCO). The powders are milled in iso-propan-2-ol solvent, which is added to the dry powders gradually until a 'double cream' like consistency is achieved. Zirconia beads with a diameter 10 mm, are used as milling media.

The milling is monitored to ensure the milling media is rolling in a cascading motion rather than cataracting, this is shown in Figure 44. The cascading motion of the milling media forms a compressive zone where particles are broken under compression, the cataracting motion alone is not sufficient for effective grinding (Djordjevic, 2005).

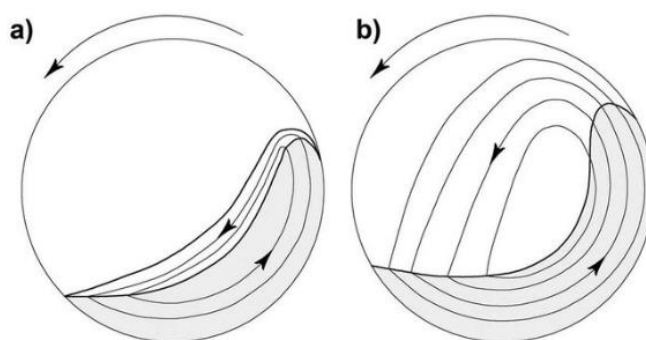


Figure 44. Cataracting (a) vs cascading (b) regimes in a tumbling mill (Djordjevic, 2005).

4.2.4 Drying

The milled powders are thoroughly dried using a Kenwood Cooking Chef KM080 mixer. This enables powdered to be dried via induction heating with constant mixing

throughout the process. The dried powder is then sieved through a 300 μm nylon monofilament mesh to obtain a powder of uniform particle size that is free-flowing.

4.2.5 Calcination

The calcination process involves heat treatment of the dried powders, they are heated but kept below the melting temperature, to facilitate a thermochemical reaction between the mixed oxide constituents.

The first calcination step which produces MgNb_2O_6 is described in Section 4.1.1.2 of this chapter. A conventional furnace is used to heat the powders, which are contained in a sealed crucible, according to the regime shown in Figure 45. The powders are heated to a temperature of 1150 $^\circ\text{C}$ at a rate of 300 $^\circ\text{C}/\text{hour}$, held at temperature for 4 hours and then cooled at 300 $^\circ\text{C}/\text{hour}$ back to room temperature.

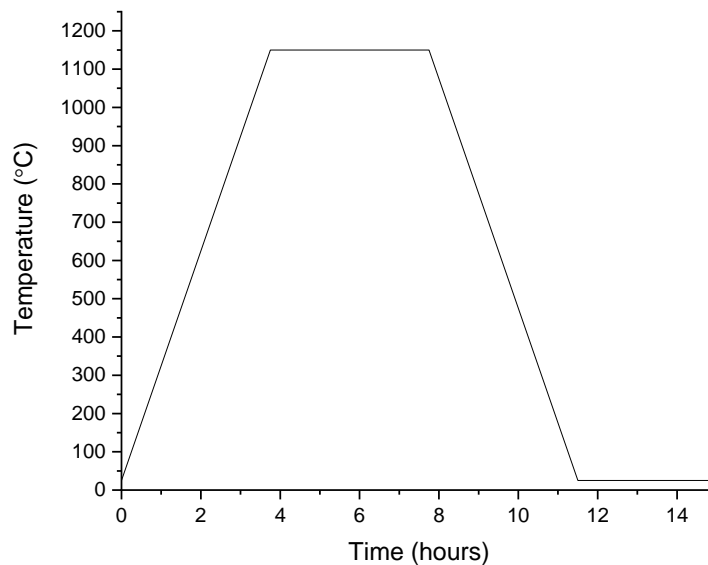


Figure 45. Calcination profile for magnesium niobium oxide.

The second calcination step occurs later in the process, where lead oxide and titanium oxide have been added to precursor MgNb_2O_6 to produce PMN-PT. The furnace regime for this calcination step is shown in Figure 46. The powders are heated to

850 °C at a rate of 300 °C/hour, followed by a 4-hour dwell and then cooling at 300 °C/hour back to room temperature.

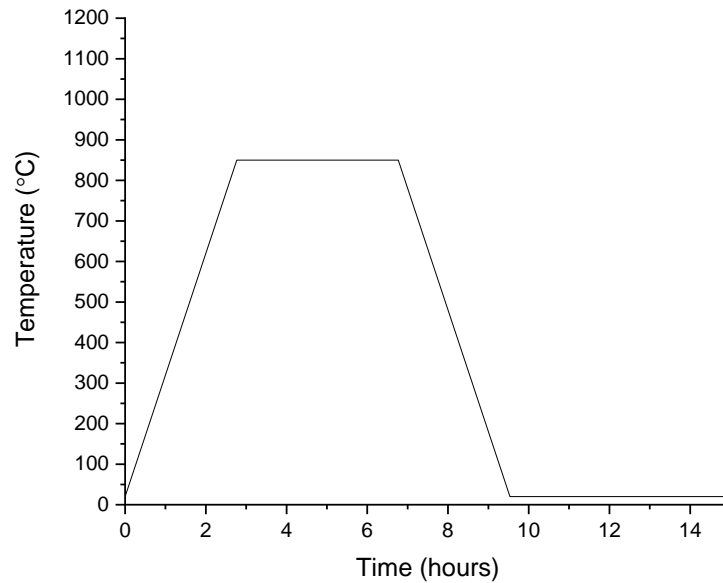


Figure 46. Calcination profile for PMN-PT.

4.2.6 Binder Addition

For some experiments in this work, it is required that a binder be added to the green powders, these experiments are clearly labelled in the text. For binder addition, the calcined powders are milled again with 1% by mass optapix binder and made up with deionised water to form a ‘double cream’ consistency. After ball milling for 24 hours, the powders are dried and sieved again to obtain a free-flowing powder.

4.2.7 Pressing

The green powders are cold pressed into compact discs of 13 mm diameter at a pressure is 20 MPa using an isostatic press. The formed pellets are then further isostatically pressed at 200 MPa for 5 minutes.

4.2.8 Sintering

Sintering involves further heat treatment to densify and compact the materials. The sintering process of the PMN-PT samples is varied in each experiment as part of this work. For each experiment the exact sintering regime will be provided in the text.

4.3 Hot Pressing Experimental Procedure

4.3.1 Hot Pressing Overview

This section describes the general experimental set up of the hot press which includes the design of the die in which samples are contained, packing of the ceramic sample, and production of the inert packing powder. The design of the hot press is discussed in Chapter 5. For each experiment conducted, the specific temperature, pressure and time are given in the text.

4.3.2 Hot Press Die Set-Up

The loading of samples in the hot press is shown in Figure 47. Green ceramic powder is initially cold isostatically pressed at 200 MPa for 5 mins into 13mm diameter pellets with a single crystal seed compacted inside. The dimensions of the seed crystal are approximately 3mm x 3mm x 0.8 mm. The resulting pellet is then placed into the hot press die surrounded by packing powder, as shown schematically in Figure 47.

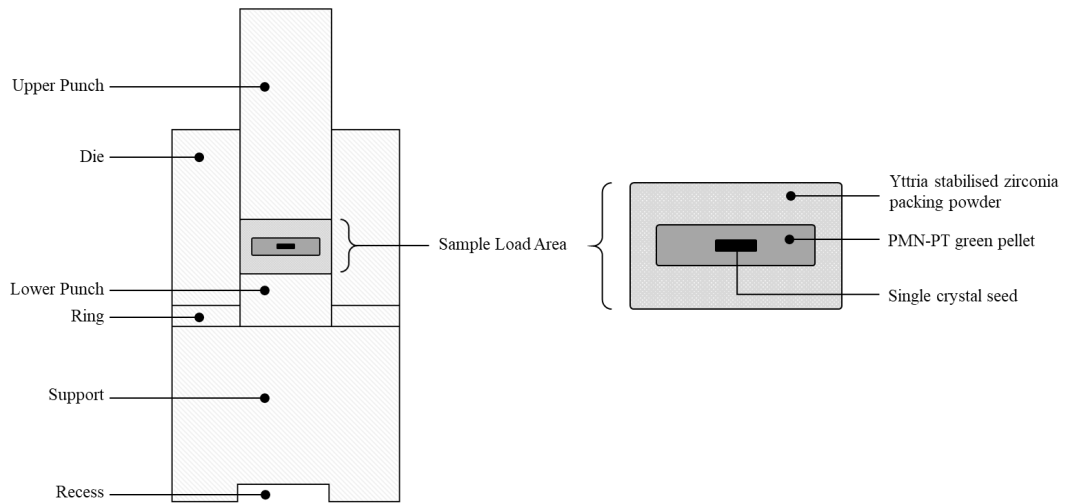


Figure 47. Schematic of experimental design for loading samples into the hot press, showing die components and sample packing.

4.3.3 Packing Powder

The use of packing powder is essential to stop any interaction of the PMN-PT sample and the internal surface of alumina die. It is also used to distribute pressure evenly to the PMN-PT sample. It is important therefore, that the packing powder remains inert and retains the same crystal phase for the entire temperature range of the experiment thus avoiding any volume changes due to phase transitions that could cause regions of increased pressure on the sample. Volume changes of up to 5% can result from shifts between tetragonal and monoclinic phases (Hasanuzzaman et al, 2022). The material selected was yttria stabilised zirconia. The combination of zirconia (ZrO_2) doped with yttria (Y_2O_3) at 19% by mass has a cubic crystal structure. The phase diagram of yttria and zirconia solid solution is shown in Figure 48.

Packing powder was formed at 19% mass yttria, ensuring a consistently cubic phase for the duration all hot press runs where the temperature can be up to 1200°C.

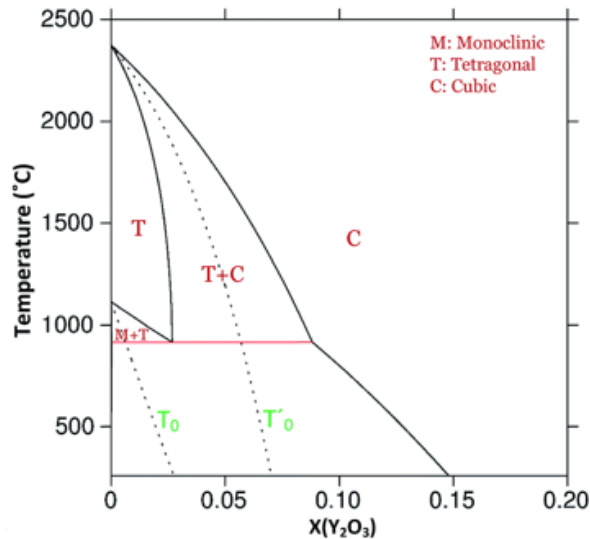


Figure 48. Yttria - Zirconia solid solution phase diagram. (Asadikiya et al, 2016).

The raw materials used to synthesise the yttria stabilised zirconia packing powder are shown in Table 3. This material is synthesised much like the PMN-PT process previously shown in Section 4.2.

The yttrium oxide and zirconium dioxide powders are first dried in an oven at 120 °C for >24 hours to eliminate any moisture. They are then accurately weighed and thoroughly mixed on a ball mill with a ‘double cream’ solution of IPA for 24 hours. Once dried the powders are then screened through a 300 µm mesh to form a free-flowing powder. The combined powders are then heated in a furnace to 1500 °C at a rate of 300 °C/hour and held there at that temperature for 24 hours.

Table 3. Raw materials for synthesis of packing powder – yttria stabilised zirconia.

Raw Material	Chemical Formula	Manufacturer	Purity
Yttrium(III) Oxide	Y ₂ O ₃	Sigma-Aldrich	> 99.99%
Zirconium Dioxide	ZrO ₂	Sigma-Aldrich	> 99%

The powders are then analysed using XRD, an XRD spectrum of yttria stabilised zirconia packing powder used in this work is shown in Figure 49. The spectrum shows

sharp peaks at the labelled peak positions, lack of peak splitting indicates a cubic structure.

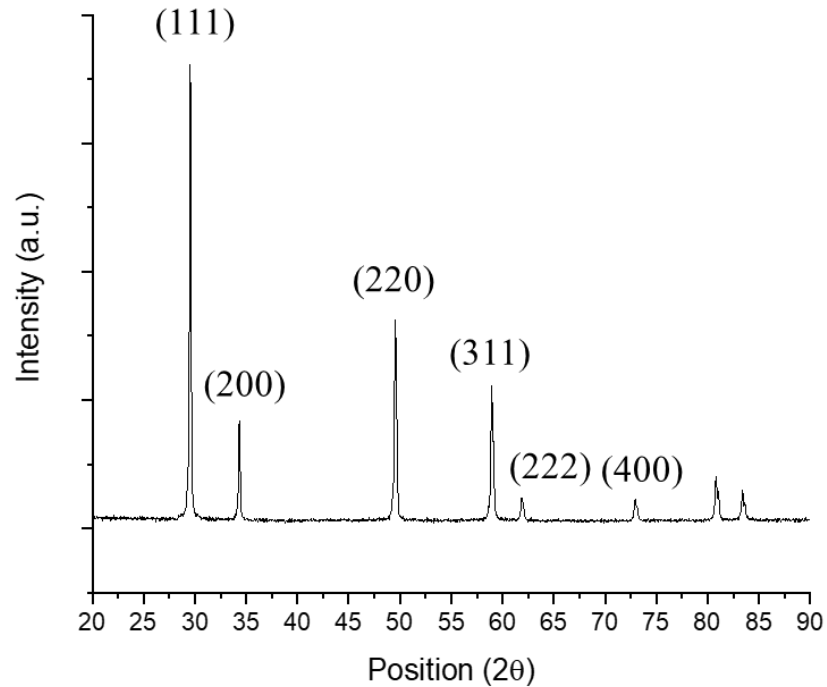


Figure 49. XRD spectra of yttria stabilised zirconia packing powder.

The packing powder was used to surround the PMN-PT powder in the hot press. For every 3 g pellet of PMN-PT used in the experiments, 9 g of packing powder is used to surround the pellet. The packing powder was found to consistently protect the alumina die from degradation that could result from lead vapour escaping from the pellet, and similarly also protected the pellet from interacting with the alumina die.

4.3.4 Crystal Growth Procedure

Further heat treatment is conducted in conventional furnaces. For each experiment conducted the relevant temperatures and times of the annealing process are listed in the text. All samples are further heat treated in a sealed crucible buried in sacrificial powder of the same composition, to limit the loss of lead from the sample.

4.3.5 Cutting Procedure of Hot-Pressed Samples for Analysis

After heat treatment the samples are removed from the furnace/hot press and the surfaces are ground down to remove any packing powder or atmospheric powder. The samples are then examined with optical microscopy. In the case that the sample contains a crystal seed, the optical microscopy is used to determine the exact location of the seed by shining a light through the sample and marking the outline of the seed before cutting. The sample is then mounted on an aluminium substrate for cutting.

As show in Figure 50, the sintered samples are then divided into quarters, this is done using a Struer's Accotom-5 precision cutter. The samples are fed through the cutter at a rate of 0.025 mm/s with the blade rotating at 3000 rpm. This ensured an accurate cut and no breakage of the sample.

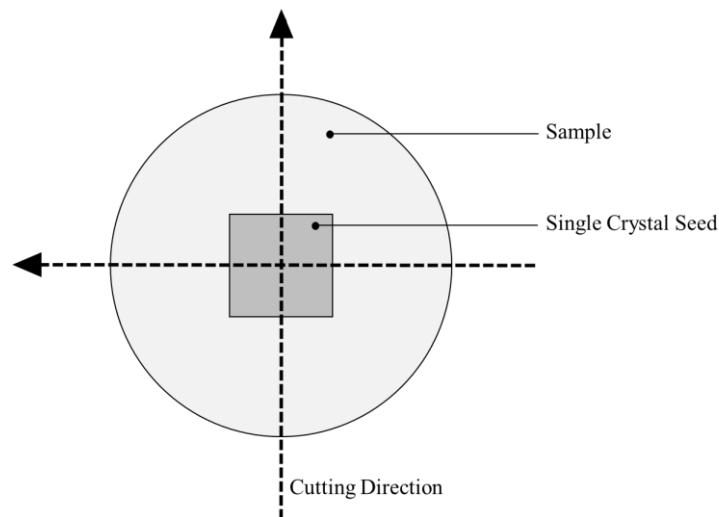


Figure 50. Cutting procedure schematic of sample containing single crystal seed.

4.4 Texturing Materials Synthesis and Experimental Procedure

4.4.1 Overview

In this section of work, it is investigated whether the hot press is an effective stand-alone tool for texturing piezoelectric materials. Barium titanate platelets are used as texturing templates and orientated by the uniaxial pressure applied during sintering in

the hot press. Initially the platelets were added to the same PMN-PT ceramic powder that has been used in the previous section. This work also goes on to look at producing textured barium titanate piezoelectric material with barium titanate platelets. As such, this section will summarise the materials synthesis of barium titanate ceramic powder and the general experimental method of this texturing section of work.

4.4.2 Materials Synthesis

The materials synthesis of the ceramic powders used in this section of work is much like that of the powder synthesis shown in Section 4.2. Once the ceramic powders have been produced and calcined, the platelets are added with a small amount of deionised water acting as binder. The mixture of ceramic powder and pellets is then isostatically cold pressed as before and sintered in the hot press. Stoichiometric barium titanate was prepared according to Figure 51.

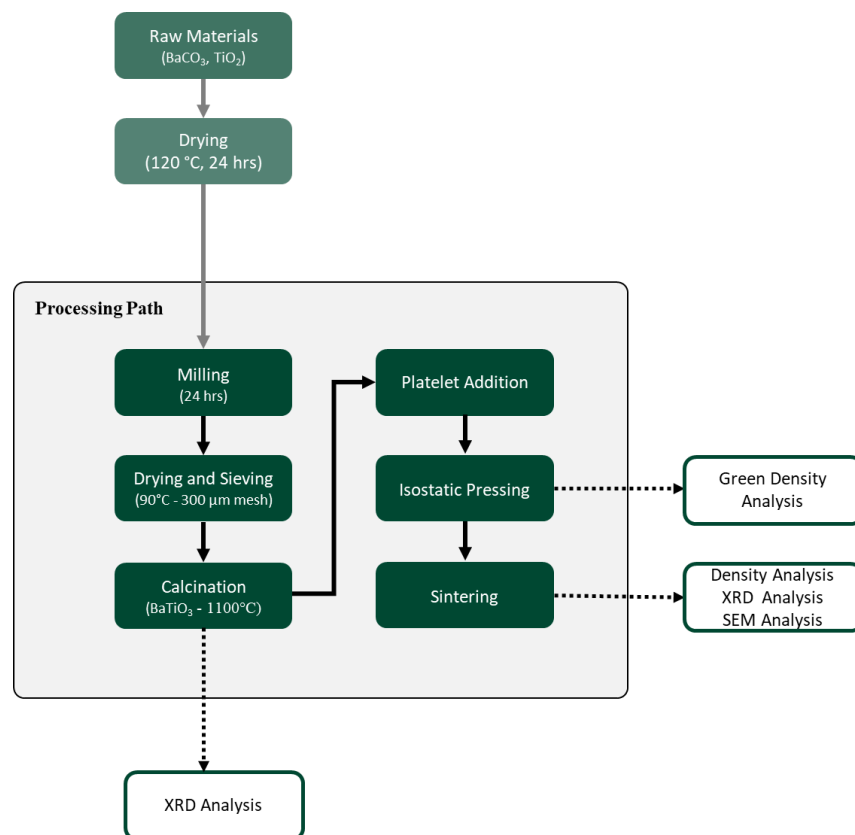


Figure 51. Barium titanate processing route from raw materials, with addition of BaTiO₃ platelets.

The raw materials of barium carbonate and titanium dioxide, listed in Table 4, are first thoroughly dried in an oven (120 °C, 24 hours) to eliminate any moisture. These are then weighed accurately to give a stoichiometric mixture. The mixture is milled with IPA which is added to the dry powder until a ‘double cream’ consistency is achieved. After milling the slurry is milled with 10mm zirconia milling media for 24 hours. The powders are then dried thoroughly and sieved through a 300 µm mesh to form a free-flowing powder. This powder is then sealed in an alumina crucible and heated in a furnace to 1100 °C to calcine and form barium titanate.

Table 4. Raw materials used to produce BaTiO₃.

Raw Material	Chemical Formula	Manufacturer	Purity
Barium Carbonate	BaCO ₃	Alfa Aesar	> 99%
Titanium Dioxide	TiO ₂	Sigma-Aldrich	> 99.9%

For the texturing section of work, barium titanate platelets are then added to the calcined BaTiO₃ powders and mixed mechanically. The incorporated platelets and BaTiO₃ powder are then cold isostatically pressed at 20 MPa for 5 mins before being transferred to the hot press for sintering.

4.4.3 Platelets

Barium titanate platelets with <10% bismuth oxide impurity are used in the texturing section of work. Figure 52 shows the anisometric shape of the platelets, the average size of these is 7.5 µm.

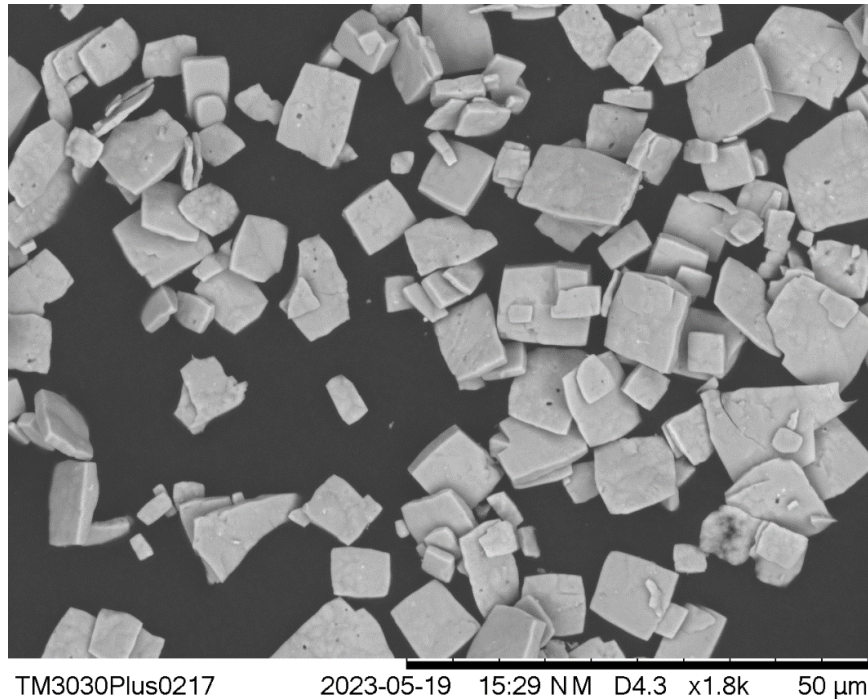


Figure 52. BaTiO₃ platelets used in texturing experiments.

4.4.4 Mixing

Incorporating the barium titanate platelets into the ceramic powder in a uniformly distributed way is challenging due to the large size and mass differences of the platelets and ceramic particles; issues of segregation becoming prevalent. Conventional mixing such as ball milling would cause segregation due to the difference in mass of the tumbling particles and would also cause damage to the platelets. The impact of milling media is likely to break the platelets, as the anisotropic shape is the key to achieving orientation, this mixing method is unsuitable. Other mixing methods that include shaking/falling/tumbling the mix also encourage segregation or breakage.

It was therefore decided that the most effective method to use is manual mixing. This was done in a small inert container, using a spatula as a mixing tool. The process was kept as consistent as possible, with the platelets gently mixing for 5 minutes, this ensured more than enough time was allocated to the mixing process where a uniform colour of powder/platelet mix could be achieved.

4.5 Characterisation Techniques

4.5.1 Density Measurements

For the density determination of sintered samples, the Archimedes method is used. This method is based on the Archimedes principle which states that the upward buoyant force exerted on a body immersed in fluid is equal to the weight of the fluid that the body displaces. Application of this principle gives a simple and reliable method of density measurement. The density of the immersed object relative to the density of the fluid is expressed in Equation (21).

$$\frac{density_{object}}{density_{fluid}} = \frac{mass_{object}}{mass_{object} - mass_{apparent\ immersed}} \quad (21)$$

Weighing of samples is conducted on a set up as shown in Figure 53. A bridge sits on the bench, independent to the balance, and holds the contained deionised water. A sample holder, which is placed with its base on the balance, holds the sample immersed in the water. Multiple readings of the mass and apparent immersed mass are recorded for each sample and an average is taken.

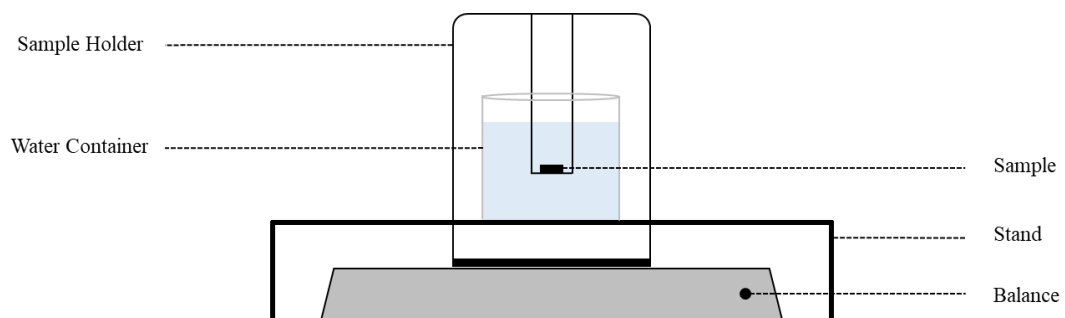


Figure 53. Archimedes density measurement set up.

4.5.2 X-ray Diffraction

X ray Diffraction (XRD) is used to determine the crystalline structure of the materials. The material phase, composition and any impurities can be identified using XRD.

A D8 Bruker diffractometer was used for analysis in this work. X-rays are produced in a cathode ray tube, filtered to monochromatic waves, and directed towards the sample. The X-rays produced have wavelengths characteristic of the target material, copper, and are composed of $K\alpha$ and $K\beta$ x-rays. $K\alpha$ X-rays comprise of two wavelengths $K\alpha_1$ and $K\alpha_2$. Monochromators are then used so the analysis is performed only on $CuK\alpha$ spectra.

Powder samples and pellets are analysed using XRD. In the case of powders, they are compacted into the sample holder, ensuring a flat surface for clear results. For pellets, the surfaces are first ground down to remove any impurities, the pellets are then located into sample holders and levelled to be analysed.

The interaction of incident rays with the sample produces constructive interference when conditions satisfy Bragg's law, given in Equation (22).

$$n\lambda = 2d \sin \theta \quad (22)$$

The beams enter the sample throughout a range of scanning angles. At specific angles, constructive interference occurs as a result of symmetry in the crystal lattice as shown in Figure 54. The diffraction pattern is interpreted and plotted on a spectrum of diffraction angle vs the intensity of the diffracted beam.

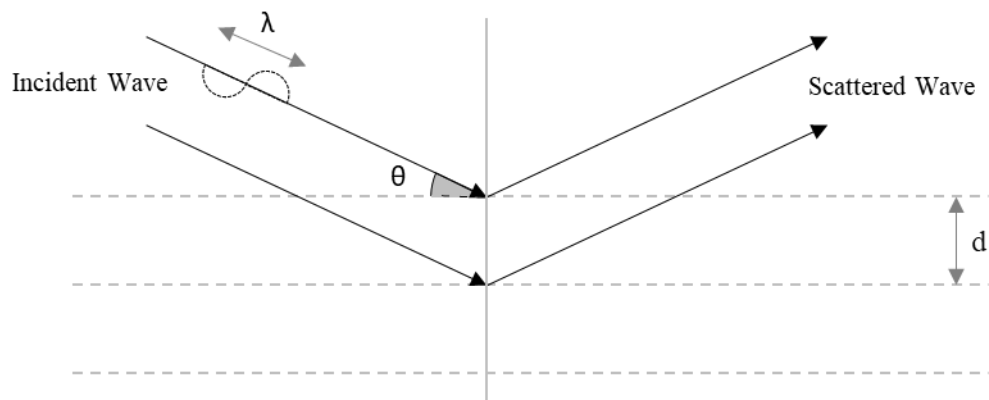


Figure 54. Representation of Bragg's law being applied to a crystal lattice.

The XRD spectra of the key formulated compositions are shown below for precursor MgNb_2O_6 , PMN-PT and BaTiO_3 .

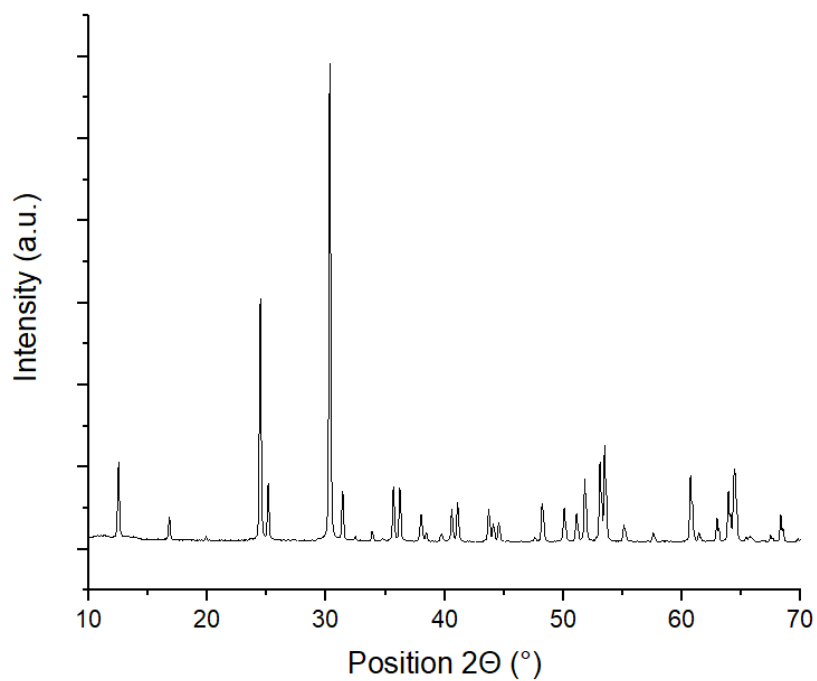


Figure 55. XRD spectra of MgNb_2O_6 calcined at 1150°C for 4 h.

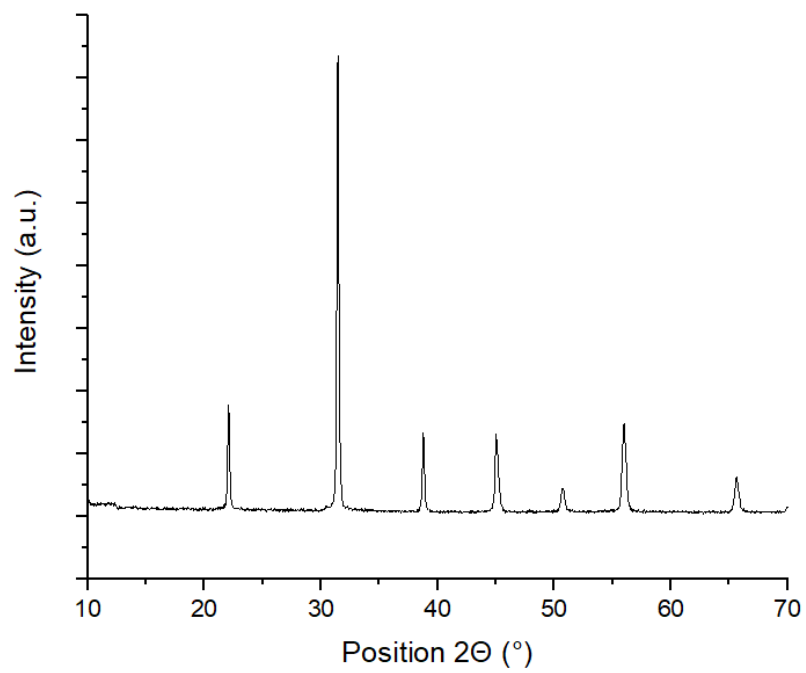


Figure 56. XRD spectra of PMN-PT calcined at 850 °C for 4 hours.

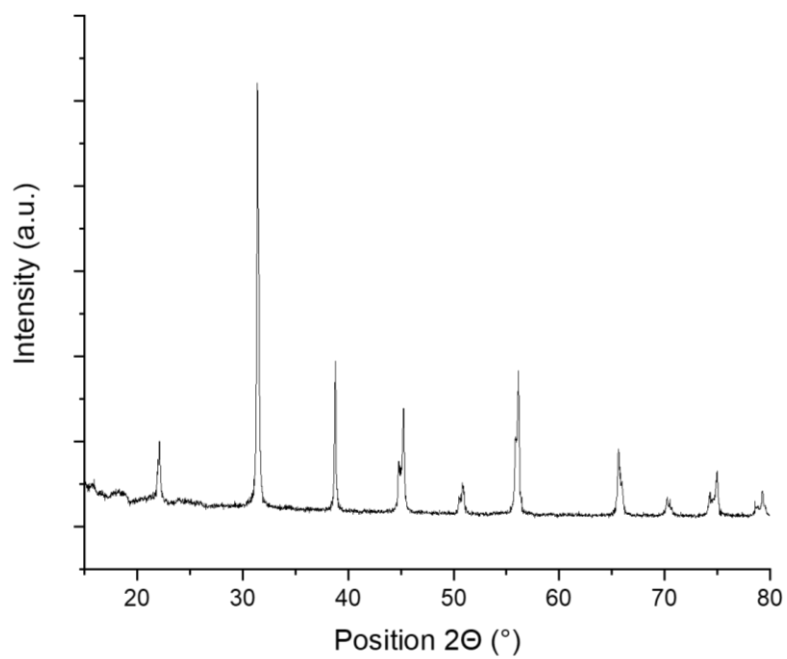


Figure 57. XRD spectra of BaTiO₃ ceramic powder calcined at 1100 °C for 4 hours.

4.5.3 Optical Microscopy

Optical microscopy is used here to view the surface of materials in detail. The specific equipment used is an OLYMPUS OLS4100 optical microscope. This technique is also used at each stage of the sample polishing process for SEM outlined in Section 4.5.4.2 to ensure an even finish and effective polishing is being achieved with each abrasive.

4.5.4 Scanning Electron Microscopy

4.5.4.1 Overview of Scanning Electron Microscopy

Scanning electron microscopy (SEM) is used to observe and analyse the microstructure of the polycrystalline materials. Grain structure can be viewed in sintered samples and particles can be studied in powder form.

The principle of an SEM is to produce images of a sample by studying the interactions of the surface with a focused beam of electrons. A schematic of how a scanning electron microscope operates is shown in Figure 58.

An electron beam is accelerated through a column from the source through a series of lenses to focus on the sample surface. The electron beam interacts with atoms in the sample at the surface through to a depth of a few microns.

Secondary electrons are emitted due to inelastic scattering that transfer energy from the primary electron beam to an atom in the sample. Elastic scattering at high angles $> 90^\circ$ results in the emission of backscattered electrons from the surface of the sample. Where the primary beam approaches the nucleus of an atom in the sample, the positive charge causes a deflection of the fast electron, causing it to be remitted from the surface (Nanoscience Instruments, 2018). The positions of the Secondary Electron (SE) and Back-Scattered Electron (BSE) detector are shown in Figure 58.

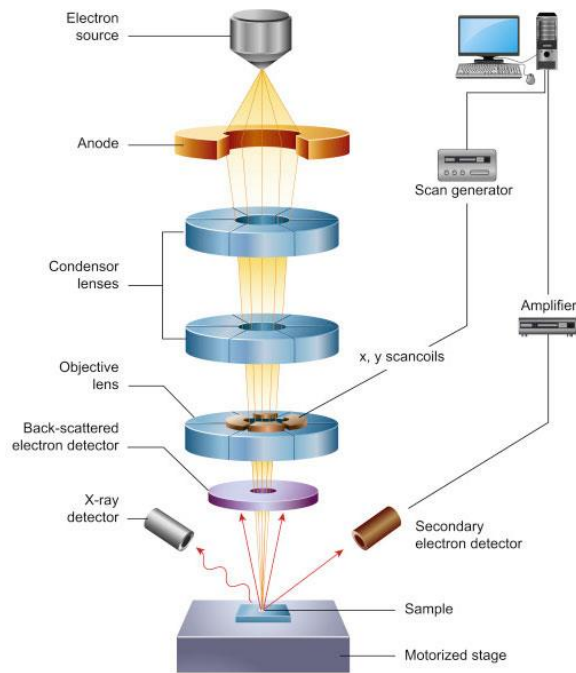


Figure 58. Scanning electron microscope schematic (Nanoscience Instruments, 2018)

The scanning electron microscope used for analysis in this research was a Hitachi SU8230 CFEG SEM (cold-field emission gun scanning electron microscope). The detectors used for secondary electrons were the upper and lower secondary electron detectors (SE(U) and SE(L)) and a plate detector for back scattered electrons (PDBSE).

4.5.4.2 Polishing Procedure for SEM Samples

To examine the samples using a scanning electron microscope, they must be carefully polished. The newly exposed cross sections of the samples are mounted in silicone moulds and set in resin. Beuhler EpoThin 2 epoxy 2 resin was used and mixed in accordance with the manufacturer's instructions with the EpoThin 2 corresponding epoxy hardener. The samples are then left for >8 hours to cure in air. The polishing procedure is listed below in Table 5 from manufacturer Beuhler (2021). This polishing technique was found to give consistent results allowing samples to be examined clearly during SEM..

Table 5. Buehler polishing procedure (Buehler, 2021).

Process Step	Polishing Surface	Abrasive	Force (lbs/sample)	Time (sec)	Platen Speed (rpm)	Head Speed (rpm)	Relative Rotation
1	Silicone Carbide	P600/P400 Water lubricant	4.0	Until Plane	150	60	Comp
2	TexMet P	9 μ m MetaDi Supreme	4.0	300	150	60	Contra
3	TexMet P	3 μ m MetaDi Supreme	4.0	300	150	60	Comp
4	TriDent	1 μ m MetaDi Supreme	4.0	180	150	60	Comp
5	ChemoMet	Colloidal Silica MasterMet	4.0	80	100	60	Contra

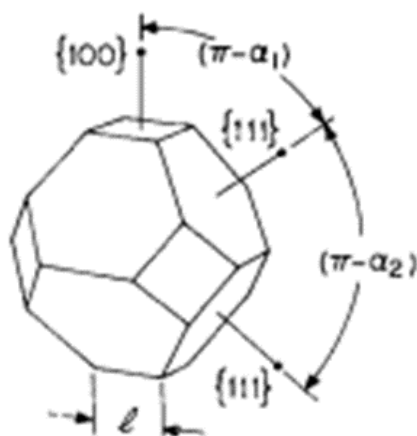
4.5.4.3 Sample Preparation

Samples must be prepared further to be characterised using SEM. First, the ceramic samples are cut, then set in resin and polished according to the polishing procedure in Section 4.5.4.2. They are then attached to a small sample holder compatible with the Hitachi SU8230 CFEG SEM equipment. Carbon paint is then applied to the sample and holder set-up to provide a conductive pathway away from the sample, it is then coated with a nano-layer of carbon via aerosol deposition to reduce charge build up on the sample.

4.5.4.4 Linear Intercept Model

The linear intercept model is used to estimate the grain size of a polycrystalline ceramic. A test line of known length is overlaid on an SEM image of a polished ceramic sample, the intercept length of grain boundaries with the test line is related to the average grain size by a proportionality constant.

To determine the proportionality constant, the average 3D shape of the polycrystal is assumed to be a truncated octahedral (or tetrakaidecahedron), comprised of six $\{100\}$ faces and eight $\{111\}$ octahedral faces. A distribution of polyhedral grains exists in polycrystalline ceramics, during grain growth the average shape of a space-filling polyhedron approaches the truncated octahedron, which is shown in Figure 59.



$$\bar{D} = 1.56\bar{L}$$

Where \bar{D} is equal to the average grain size and \bar{L} is equal to the average length intercept over a large number of grains.

Figure 59. Truncated octahedral shape, model of average shape of polycrystalline grains and equation used in linear intercept method (Mendelson, 1969).

Both the grain size and number of grain boundary intersections per unit area are expressed in terms of surface area/volume ratio of the grain geometry. By defining the grain structure as a truncated octahedral shape and having a log normal distribution, the relation between the average grain size \bar{D} and the average intercept length \bar{L} can be expressed. The equation shown in Figure 59 shows the generalised form of the equation where the proportionality constant is found to be 1.56 for polycrystalline ceramics. This number has also been experimentally verified in Mendelsen's work (Mendelson, 1969).

4.5.5 Energy Dispersive X-ray Spectroscopy

Energy dispersive X-ray spectroscopy (EDX) is a technique used to analyse the elemental composition of a sample. This method is based on the interaction between source energy and the sample. An excited atom dissipates some of the absorbed energy by emitting a core shell electron. A higher energy outer shell electron then fills its place, releasing the difference in energy as an X-ray. The difference of energy states and therefore X-ray released is unique to each element and so can be identified on a spectrum characteristic to the original atom. This process is summarised in Figure 60. This operating principle is based on Moseley's law which states that the square root of the frequency of the emitted X-ray is approximately proportional to the elements atomic number (Atkins and De Paula, 2010).

For elemental mapping carried out here, the excitation source sufficient to eject core shell electrons comes from the electron beam used in the scanning electron microscope equipment described previously in Section 4.5.4. Sample preparation is therefore identical to the SEM procedure.

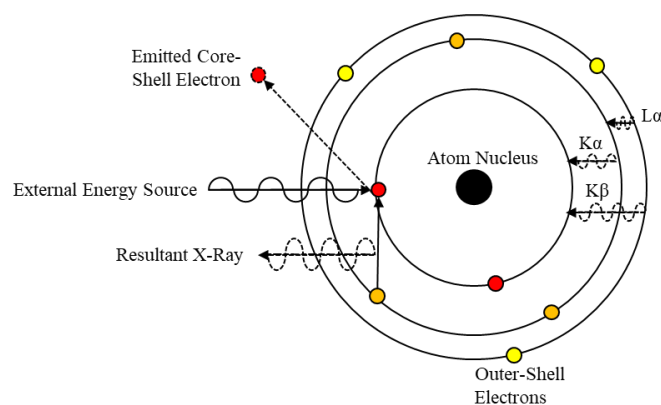


Figure 60. Schematic of EDX showing excitation of core-shell electron and subsequent characteristic X-ray emitted.

Chapter 5 Design and Build of Uniaxial Hot-Press

5.1 Introduction

This chapter documents the design and build of the uniaxial hot press equipment. The equipment was designed for this thesis specifically and the undertaking of design and assembly was a significant part of this research project.

Hot pressing is an established technique used to manufacture high quality piezoelectric ceramics. The process involves applying both heat and pressure simultaneously to green ceramics to shape and consolidate the powder into well-defined sintered components. The use of a hot press, like many other sintering methods, was first developed for metals, such as in production of high-performance turbine blades (Moulson and Herbert, 2003).

Hot-pressing provides several advantages over conventional sintering. Uniaxial hot-pressing enables high density ceramic bodies to be produced without additional sintering aids, so that the desired purity of the finished product is not impaired. With application of higher pressures, it is possible to reduce the sintering temperature and shorten the sintering time considerably, limiting grain growth during the sintering process (Liebertz, 1987).

This section of work will cover the background science of densification and hot-pressing, followed by a review of hot-pressing used in the manufacture of piezoelectric ceramics. Finally, the design and build of the uniaxial hot press used in this work will be discussed.

5.2 Background Science

During the sintering process, a system will try and achieve its minimum energy configuration, for a crystalline material the lowest energy state would contain no defects, pores or boundaries. Thermodynamically it is favourable to reduce energy in the system by eliminating porosity first, as the specific surface energy of a pore is

greater than the grain boundary energy (Atkinson and Davies, 2000). In real systems however, the process of grain boundary elimination or grain growth often occurs before the process of pore elimination is complete.

The mechanisms of diffusion for removal of pores are shown in Figure 61. Matter can be transported to fill a pore at point 'A' from the grain boundary via the grain boundary itself or the crystal lattice. This is shown in Figure 67 as paths 1, 2 and 6, which results in the distance between the centres of the grains decreasing and therefore achieving densification. Paths 3 and 5 however, do not cause densification as matter is transported from an area on the surface of the pore to another, resulting in a change of pore shape but not the overall volume (Atkinson and Davies, 2000). Applied stress during hot-pressing accelerates particle rearrangement to reduce pore sizes and increases diffusion rates from grain interfaces to pore neck region.

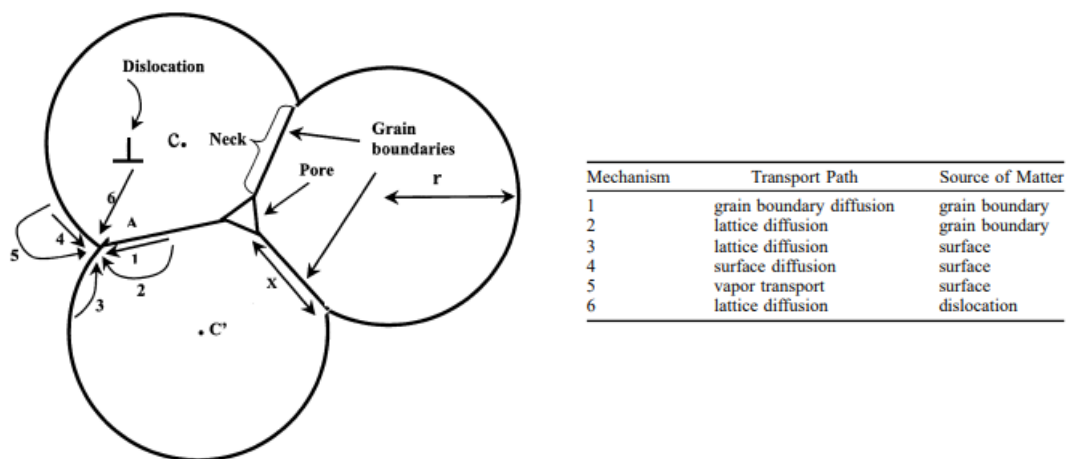


Figure 61. Schematic of paths for transport of matter during neck growth in sintering (left) and table of diffusion paths to which numbers correspond (right) (Atkinson and Davies, 2000).

The surface-energy driving force for pore closure is often opposed by the internal pressure of the gas evolved caused by shrinkage of pores. The gas phase may then tend to dissolve in the matrix or diffuse to a region of lower pressure (usually accumulating in larger pores). The external pressure used in hot-pressing adds to the surface energy driving force for pore closure and overcomes any push-back caused by pore shrinkage. The gas phase then tends to diffuse into the matrix or to the surface of the component rather than to another pore, resulting in densification (Atkinson and Davies, 2000).

The combination of pressure and temperature can be used to achieve a density at lower temperature than would be required for conventional sintering alone. Reducing the sinter temperature limits unfavourable grain growth.

5.3 Design and Build of Uniaxial Hot Press

5.3.1 Operating Conditions

The hot press will be operated at a temperature range of 900 °C – 1200 °C. The amount of pressure applied to the sample will be over an area of ~5 cm² (circular area of 25 mm diameter) at 10-50 MPa. Each experiment using the hot press will typically have a duration of 4-5 hours.

5.3.2 Overall Design

The hot press is designed around a pre-existing vertical tube furnace. The frame surrounds the furnace and supports the hydraulic equipment. The alumina push rods and die components suspend and contain the sample between the top frame support and the hydraulic cylinder located on the bottom frame support. The tube furnace encloses the die components for heat treatment and gives clearance at each end for the push rods to pass unobstructed. Figure 62 shows the general design for the hot press. To give a sense of scale, the hot press footprint covers an area of approximately 1.2 m x 1.0 m and stands at a height of 2.3 m.

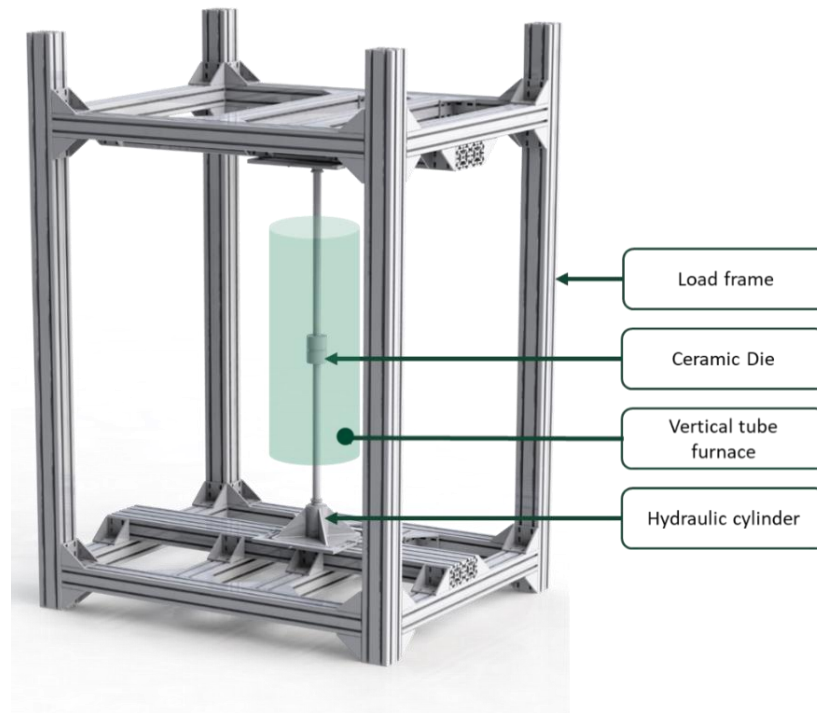


Figure 62. Hot press conceptual design.

Originally it was proposed to purchase an off-the-shelf workshop press. However no combination of press and furnace could be found with compatible dimensions, standard presses had insufficient daylight between the cross members to accommodate a suitable furnace. Instead, an off-the-shelf hydraulic system has been purchased individually which is married to a press frame constructed in-house.

5.3.3 Hot Press Components

5.3.3.1 Furnace

A Carbolite KVT1220600-400TN vertical tube furnace was used as the starting component of the hot press. The furnace is hinged to allow for practical sample set up. The internal diameter of 200 mm allows sufficient working space. The furnace is operated with a standard primary programable temperature controller, and a secondary over-temperature controller.

5.3.3.2 Hydraulic System

An Enerpac RC102 10-ton hydraulic cylinder and P392 hand pump were purchased off-the-shelf, these are shown in Figure 63. A 10-ton cylinder was chosen for its capacity, small size, and short travel. Pressure applied to the samples during hot-pressing experiments will not exceed 70 MPa, which translates to < 3 tons. A casting support for the hydraulic ram, which is fixed to the hot press frame was also purchased directly from Enerpac.



Figure 63. ENERPAC RC102 10 Ton Hydraulic Cylinder and P392 Hand Pump and CATS12 Tilt Saddle (ENERPAC, 2019).

An Enerpac CATS12 tilt saddle was used take up any offset in alignment between the hydraulic ram on the bottom support and mounting plate at the top support. The possibility of incorrect alignment in the components were mitigated as much as possible through careful design and build, however imperfect configuration at contact surfaces such as the die components and push rods could still cause issue, which is exacerbated by the length of the rods (>500 mm). The tilt saddle was therefore seen as a requirement to mitigate this problem (also shown in Figure 63).

As the temperature of the furnace is increased during experimental runs, the push rods begin to expand and increase the amount of pressure applied to the sample. To alleviate this effect, pressure must be monitored throughout the experiment and tapped off via a pressure release valve at regular intervals.

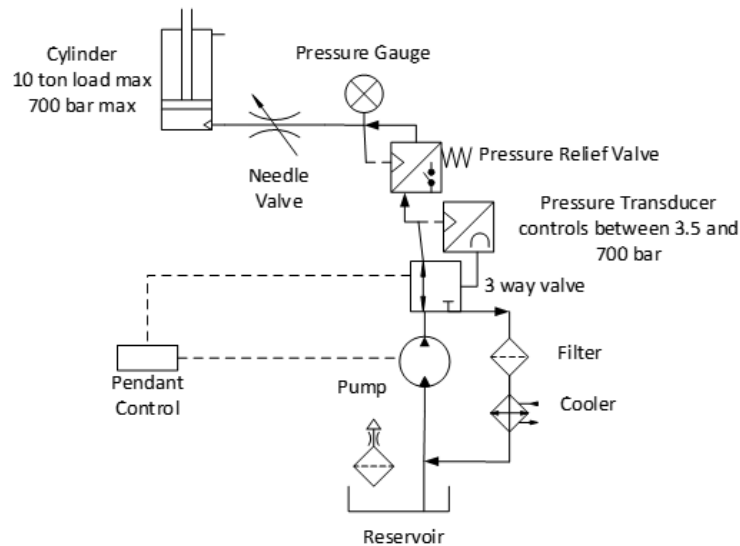


Figure 64. Process control schematic for hydraulic pump.

It was discussed to use an automatic pressure control system, to be incorporated later in the duration in the work. The design is shown in Figure 64. The pump actuates the hydraulic ram from a reservoir at 0.55 l/min via a three-way valve. The needle valve is adjusted to reduce flow rate and ram speed to a maximum of 7mm/s. If the pressure is below transducer set point, the three-way valve will be in open position. If the pressure passes above the set point, the three-way valve is placed in hold position and returns fluid from the pump to the reservoir. Return is via a filter and cooler to keep the hydraulic fluid in good working condition.

To help with the set up, it is possible to switch the pump on and off by handheld pendant, and can also momentarily place three-way valve in open and retract positions. The pump incorporates adjustable relief valve to set a maximum pressure.

5.3.3.3 Frame

The press frame is constructed of high stiffness aluminium extrusion sections purchased off-the-shelf from KJN. Figure 65 shows the 90 mm x 90 mm profiles of the aluminium extrusions used. The extrusions were cut to order by the supplier and assembled in-house as shown in the schematic in Figure 66. All brackets, fasteners and feet are also provided by KJN.

$$y_{max} = \frac{w L^3}{48 E I} \quad (23)$$

The sections of aluminium are fixed together with the corresponding KJN brackets. Each of the 64 brackets is fixed in place by 8 T-bolts, which were all torqued at 25Nm as per the manufacturers' recommendation.

The base ends of the alumina extrusions were tapped in-house to allow levelling foot bases to be fixed. Upon construction the hot press was carefully levelled in the working position.

5.3.3.4 Bottom Locator Plate and Hydraulic Support

To mount the hydraulic cylinder onto the bottom support beams of the hot press frame, a custom window frame was made to locate the cylinder and casting support as shown in Figure 67. The frame is fastened onto the bottom support and is used to align the hydraulic cylinder with locator screws. The casting support was purchased off-the-shelf from Enerpac to house the RC102 10-ton hydraulic cylinder.

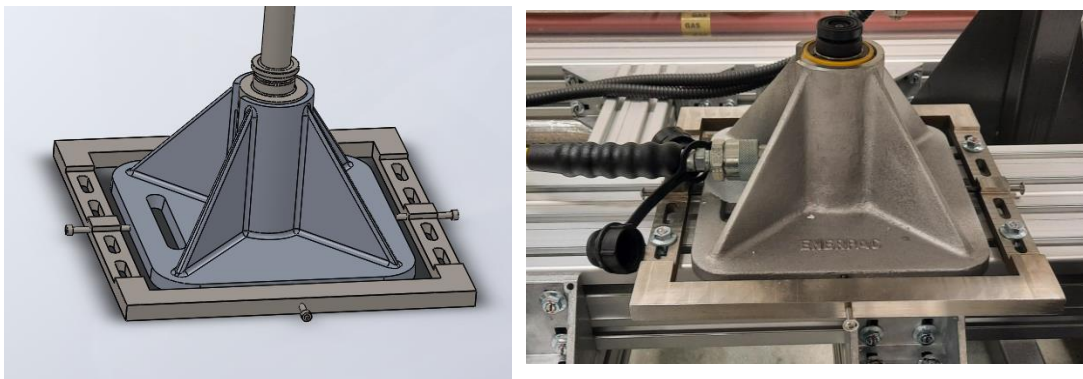


Figure 67. CAD model of bottom mounting plate housing the hydraulic cylinder and casting support (left) and photograph of finished assembly showing hydraulic ram, casting support, tilt saddle, window frame and attached hydraulic hose (right).

5.3.3.5 Top Mounting Plate, Mounting Collar and Locator Plate.

The hot press frame must provide a support for the top tilt saddle used to contact the alumina push rod, to achieve this, custom parts have been designed and produced in-house. The top support section of the hot press is comprised of a mounting plate, mounting collar and locator plate these are shown below in Figure 68.

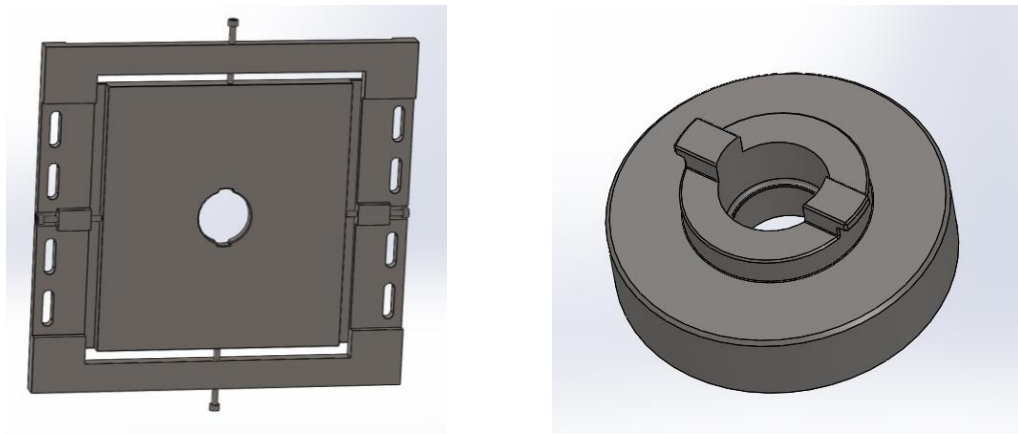


Figure 68. CAD drawing of mounting plate enclosed in locator plate (left) and mounting collar (right).

The locator plate is fastened to the top support beams of the hot press and clamps the mounting plate in place. Locator screws are used to align the mounting plate with the hydraulic cylinder to ensure the axis that pressure is exerted through is completely normal to the top and bottom support. The mounting collar is inserted into the mounting plate and rotated into the bayonet fitting. The upper tilt saddle, shown in Figure 63, is then positioned into the mounting collar with a spring-loaded ball bearing fitting. This combination of components is designed to dissipate pressure from the saddle to a larger area on the top support beams. The complete assembly is shown in Figure 69.

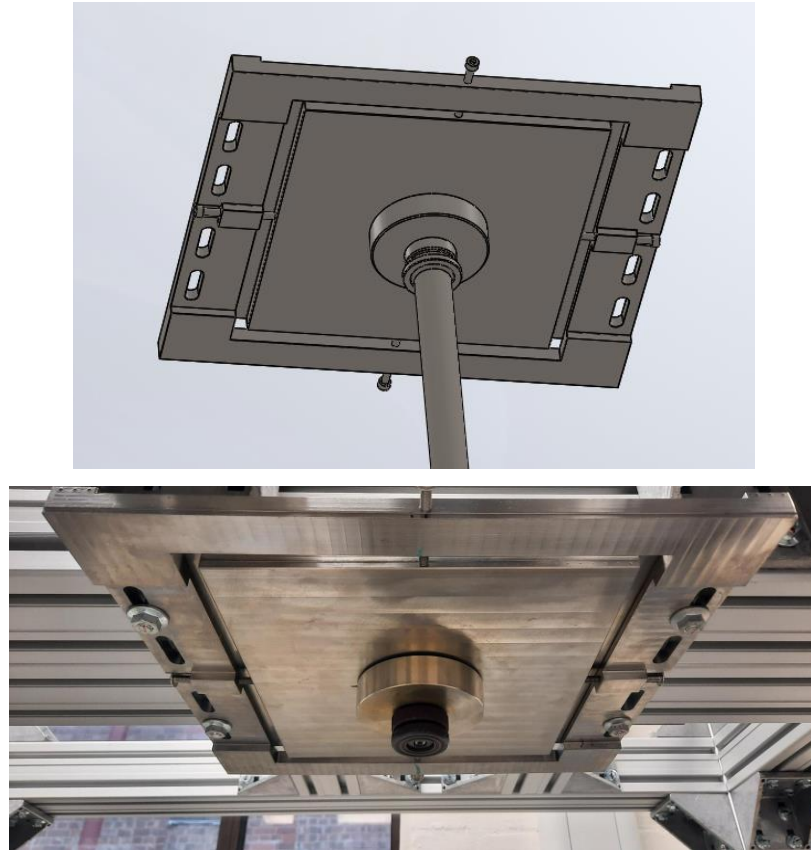


Figure 69. Bespoke mounting components designed in CAD (top) and finished set up showing locator plate, mounting plate, mounting collar, tilt saddle and top support beams of the hot press frame (bottom).

Several iterations of the components were analysed using finite element analysis. The aim of this was to identify if and where there is a build-up of pressure on the components and then reinforce them accordingly. A load of 100 kN was simulated through the base of the tilt saddle as shown in Figure 70 with the top surface of the mounting plate simulated as a fixed surface.

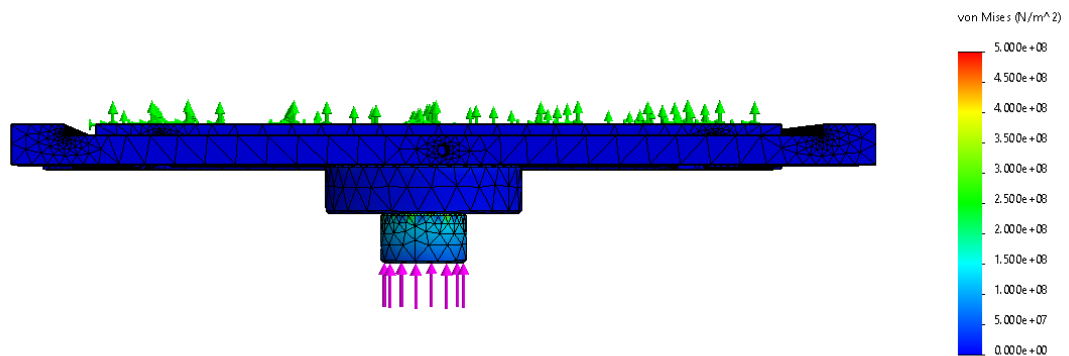


Figure 70. Load simulation on hot press components showing 100 kN load applied to base of tilt saddle and mounting plate as fixed surface.

From inspection of the finite element analysis results, it was clear that the largest amount of induced stress is located on the tilt saddle and radius of the mounting collar. Both these components are simulated together in Figure 71.

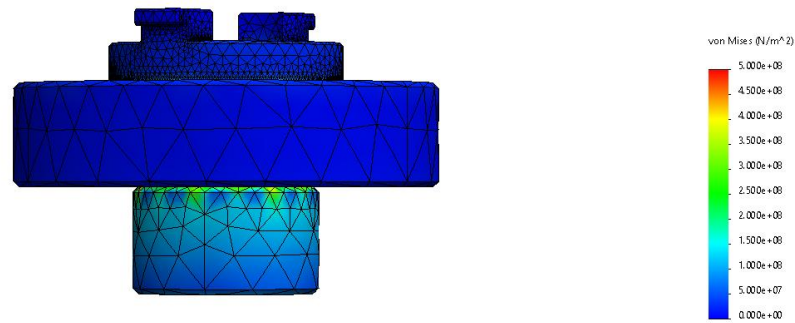


Figure 71. Finite element analysis modelling of 100kN load through top tilt saddle and mounting collar hot press components.

The tilt saddle analysis is shown separately in Figure 72. A maximum value of 496 N/m² von Mises stress is found on the load bearing radius of this component which is in contact with the bore of the mounting collar.

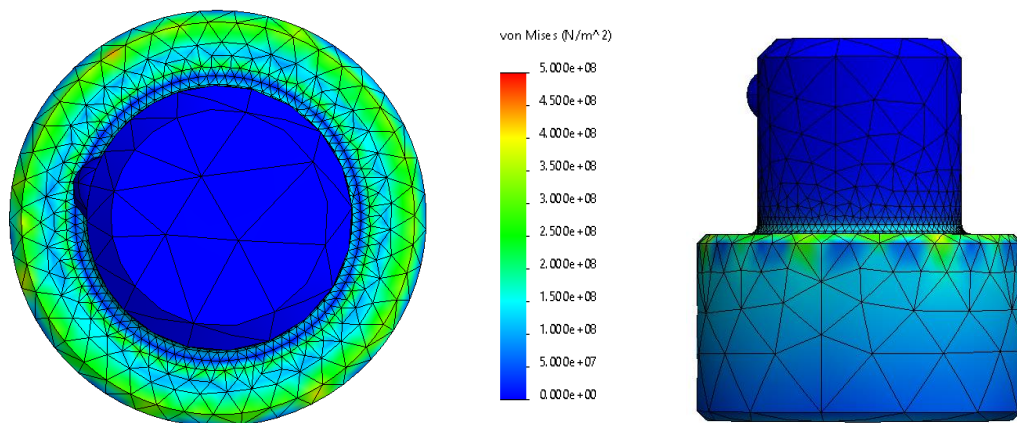


Figure 72. Finite element analysis results of 100kN load on tilt saddle.

As a result of the finite element analysis conducted, the radius of the mounting collar was increased as shown increased from 15 mm to 19.5 mm to reduce overall stress on the component as shown in Figure 72.

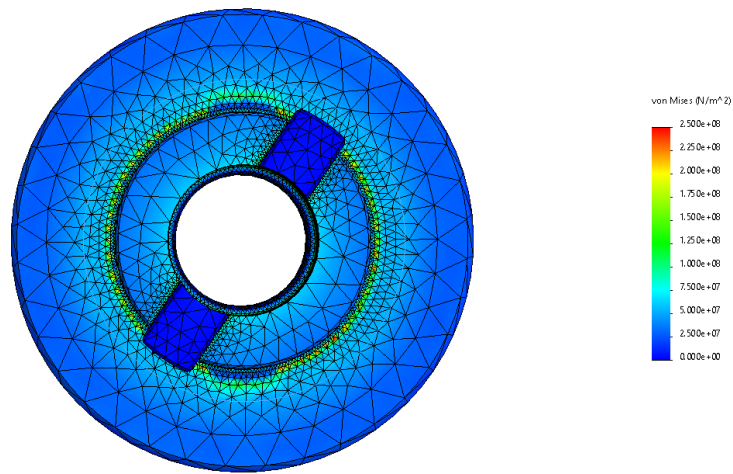


Figure 73. Finite element analysis modelling of 100kN load through re-worked mounting collar hot press components.

5.3.3.6 Alumina Push Rods

Two push rods are required for this set up to translate pressure from the hydraulic ram to the sample and to suspend the sample in the eating zone of the vertical tube furnace. They are specified at 550 mm and 600 mm in length. The push rods need to withstand high pressure and have sufficient thermal stability to endure the hot-pressing experimental conditions. Alumina and zirconia were considered as appropriate materials and after consulting external companies it was decided that alumina rods of 25mm diameter would be used.

It was particularly important that the end surfaces of the rods are completely perpendicular to their length to ensure the axis of pressure was straight through the entire length of die and push rod set-up. The push rods were specified to tolerances that ensured no more than 1 mm variation in the total run-out. The company Almath were able to meet these specification and rods were purchased from them.

5.3.3.7 Ceramic Die

The ceramic die was manufactured from high-density alumina ceramic. The die is custom manufactured by Nanoker. The original concept was to have a floating die arrangement where the uniaxial pressure on the sample is converted to radial pressure from the sample into the interior surface of the die. The associated friction maintains the position of the die. However, this system was replaced by a support arrangement to allow ease of set-up.

The die is used to contain the sample and surrounding packing powder. It is made of highly dense alumina to withstand the high pressures. The die has been sourced from the company Nanoker and has been tried and tested by the company. The bottom support of the die was adjusted to accommodate the alumina push rods, a recess of 5mm height and 26mm diameter was incorporated into the original die and is shown in Figure 74.

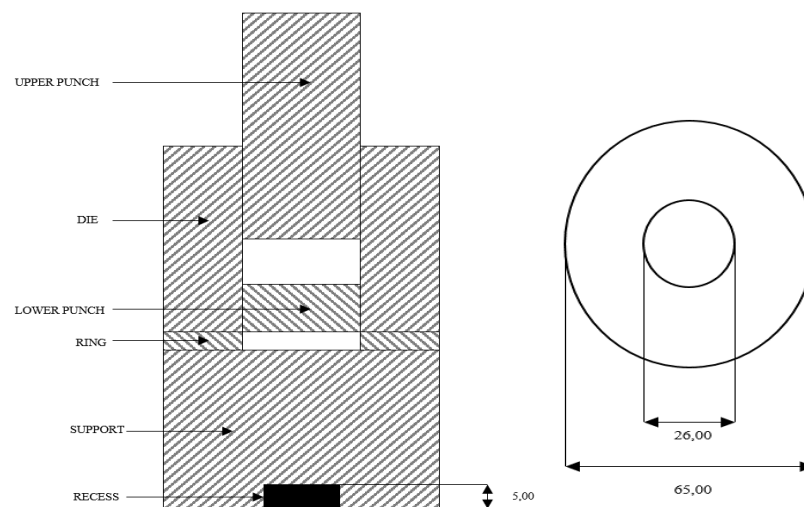


Figure 74. Ceramic die modified design with recess for push rod.

5.3.3.8 End Caps

The final manufactured component of the hot press are the end caps, these are used to buffer the interface between the alumina push rods and the hardened steel tilt saddles.

The end caps are simple discs 5mm thick made of stainless steel. They are intended to be slightly malleable to allow them to mould to the ridged shape of the saddle and dissipate pressure evenly to the surface of the alumina rods. Other materials such as bronze or copper were considered but were assessed as too ductile for this application.

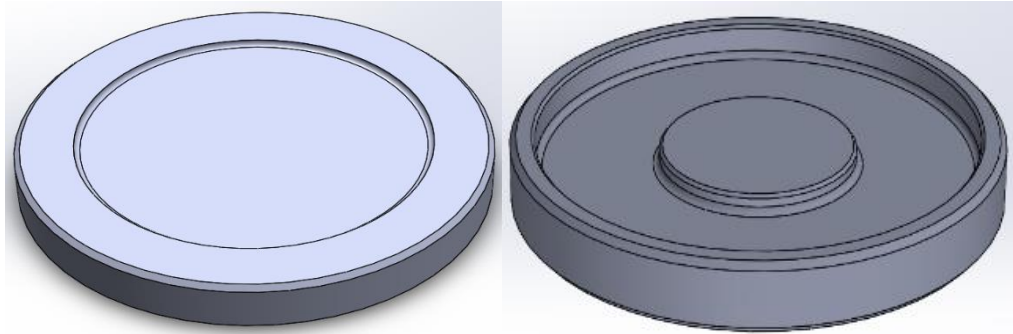


Figure 75. End cap design in Solid Works and picture of manufactured end cap.

5.3.3.9 Polycarbonate Safety Screens

As an additional safety measure, polycarbonate screens were fixed to the hot press frame to enclose the equipment during experimental runs. This was to ensure that in the event of failure, any fragments of alumina push rods that are exposed outside of furnace are contained. The shields are transparent to allow experiment monitoring. The front panels are removeable for access to load/unload samples.

5.4 Equipment Testing

The initial testing was conducted to ensure that the alumina rods and die would withstand a load of 60 kN applied by the hydraulic press (equal to 6 tons or 122 MPa). The furnace was then heated gradually to 900 °C to observe to what extent thermal expansion would cause lengthening of the push rods and how this translated to increased pressure in the system. The deflection was also monitored closely using a dial gauge indicator mounted on the bottom support beam of the hot press frame.

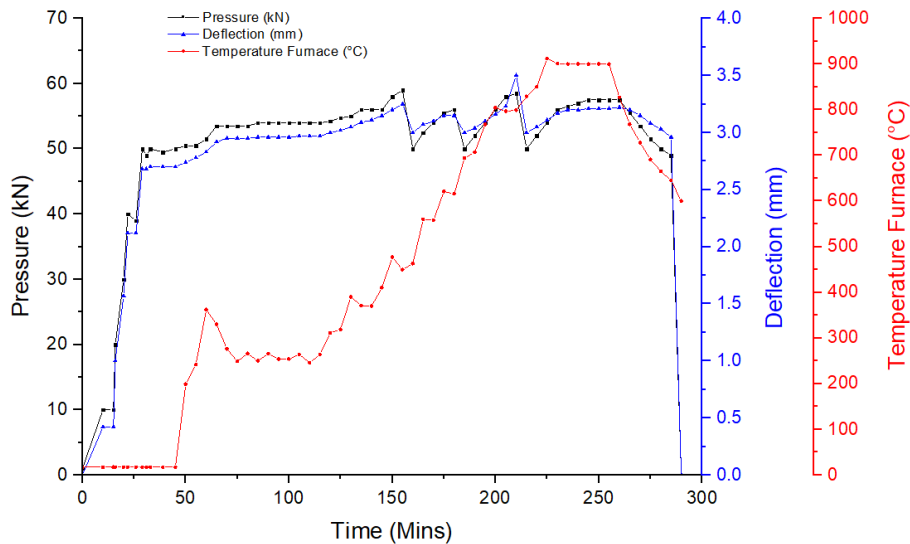


Figure 76. Hot press test run monitoring.

Figure 76 shows that the increased pressure results in an increased deflection of which a maximum of 3.5 mm is recorded at 60 kN load. This is in line with what was expected when performing the safety calculations for the deflection of the beams. As the temperature rises there is an increase in the overall pressure measured, at temperatures above 80 °C this becomes more apparent. When the temperature decreases and the rods begin to cool, the pressure and deflection both also decrease. The onset of the decrease in pressure occurs approximately 5 minutes after the furnace has reached its dwell point. The pressure falls rapidly to zero as the furnace temperature slowly decreases back to room temperature.

5.5 Summary and Conclusions

The hot-press was designed to be able to conduct experiments of sintering piezoelectric ceramics under pressure for this work, with the overall aim to drive densification and reduce porosity in sintered samples.

The hot press has been designed to operate in the following experimental conditions, a temperature range of 900 °C – 1200 °C and pressure up to 122 MPa. It has been shown in the testing phase that the built equipment is indeed capable of these operating conditions. The final hot-press build is shown in Figure 77.



Figure 77. Picture of hot-press build at the University of Leeds.

Chapter 6 Solid State Crystal Growth

6.1 Introduction

The aim of this section of work is to understand the effect hot-pressing has on the microstructure of PMN-PT samples, and then using this knowledge to incorporate single crystal seeding and solid-state crystal growth trials. It is first necessary to develop understanding of how the hot-pressing process varies from that of traditional sintering, and how best to adapt this process to produce ideal precursor material candidates for the solid-state crystal growth process.

Initially a series of experiments were undertaken to establish the optimal sintering conditions of PMN-PT in the hot press by varying temperature and pressure. This is followed by an annealing study to understand how the grains evolve with time upon further heat treatment. To further increase the density of sintered samples, trials were undertaken with the use of polymer binders to aid the densification process. Liquid phase sintering was then explored, where the addition of excess lead oxide (PbO) was used to promote formation of a liquid film at the grain boundaries to facilitate more efficient mass diffusion and therefore greater grain boundary mobility.

Using the knowledge gained from the preliminary set of experiments, solid state crystal growth experiments were then carried out. Firstly, barium titanate single crystal seeds were incorporated into the PMN-PT polycrystalline green powder to stimulate heterogeneous abnormal grain growth from the seed. Following this, PMN-PT single crystals were used to seed SSCG trials.

A further annealing stage is required after the hot-pressing to initiate crystal growth from the seed. A study of the annealing time and temperature and the effects observed in the microstructure of grown single crystals is carried out later in this section. The addition of a liquid phase is also explored in this section where PMN-PT samples are produced firstly stoichiometrically, then with 2% mol addition PbO and further 5% mol addition PbO.

From the data gathered in the solid-state crystal growth trials with varying excess lead oxide content, Arrhenius plots have been generated to determine the activation energy for single

crystal growth and compared to the activation energy required for grain growth in the polycrystalline matrix.

Finally, the effectiveness of the solid-state crystal growth method is used to produce manganese doped PMN-PT samples. The single crystal growth obtained from these samples is analysed and compare to that of stoichiometric PMN-PT samples.

6.2 Experimental Procedure

This section will give an overview of the equipment and procedures followed in the hot-pressing and subsequent solid state crystal growth experiments. Production of the piezoelectric ceramic materials and supplementary packing powder are outlined in Chapter 4.

6.2.1 Sample Preparation

PMN-PT samples that are sintered in the hot press are produced from the raw materials according to Section 4.2. The green powders are cold uniaxially pressed at 20 MPa into 3 g pellets of 13 mm diameter, with deionised water added to aid green strength. The pellets are then isostatically pressed at 200 MPa for 5 minutes. The pressed pellets can then be transferred to the hot press for sintering.

The single crystal seeds used in this work require some pre-processing. Single crystal seed samples were obtained from MaTeck (2013). The single crystals from MaTeck are [001] orientated 10x10x1 mm squares. These are first polished to a mirror finish as outlined in Section 4.5.3.2 and cut into 9 smaller pieces, in a 3x3 grid, using a precision saw (detailed in Section 6.2.5). Both barium titanate and PMN-PT single crystal seeds have been used in this set of experiments.

6.2.2 Sample Loading

The hot press experimental set up is shown in Figure 78. The sample pellet loaded into the hot press die is surrounded by yttria stabilised zirconia packing powder, which is produced according to Section 4.3.3. This is used to evenly distribute pressure to the sample and eliminate direct contact of the alumina die and PMN-PT pellet which could cause damage or unwanted interaction between the two materials. The packing powder is first loaded into the bore of the die and compressed to form a flat surface, the sample pellet is then placed on top of the yttria stabilised zirconia layer, and the remaining packing powder is then used to fill the voids between pellet and die wall and to cover the exposed top surface of the sample pellet. It was found that 9 g of packing powder is sufficient to completely enclose and protect the sample pellet.

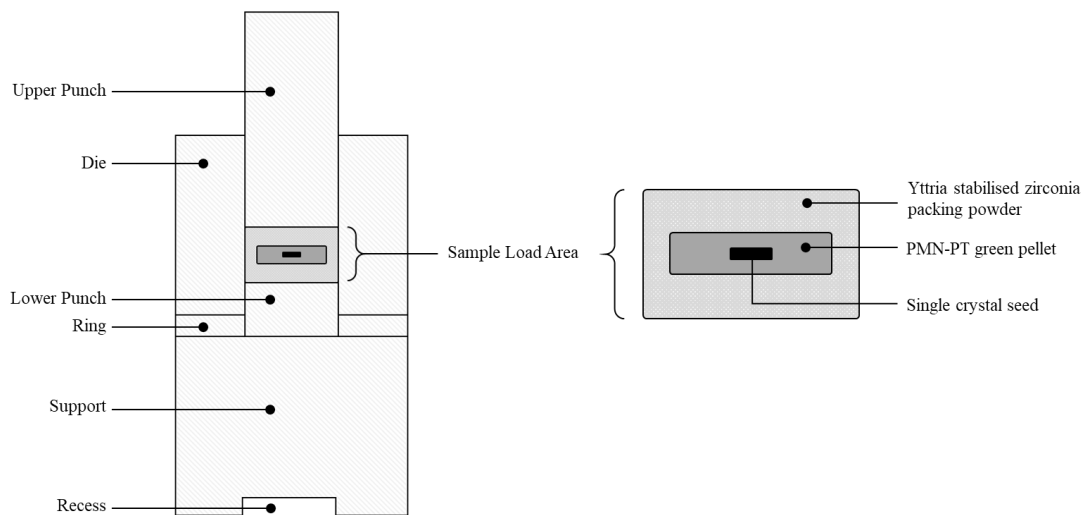


Figure 78. Hot press experimental set up,

The die is then loaded into the hot press and pressure is manually applied through the hydraulic pump. As the temperature of the furnace increases, the alumina rods begin to expand, increasing the total amount of pressure on the sample. It is therefore necessary to monitor the pressure accumulating in the system as the rods undergo thermal expansion. Pressure is tapped off from the hydraulic equipment periodically to maintain as constant pressure as possible on the sample. It was found during initial safety runs of the hot press, that as the temperature stabilises when the experimental dwell temperature is reached, thermal expansion of the push rods can be seen to plateau around 20 minutes after this point (Section 5.5).

6.2.3 Further Heat Treatment

After sintering in the hot press, the samples are further annealed to promote single crystal growth. Annealing takes place in a conventional furnace, where samples are sealed in a crucible and buried in sacrificial powder (shown in greater detail in Section 6.2.4). The sacrificial powder is made of the same composition as the sample pellet to reduce the volatilisation and loss of lead from the samples. For each experiment the temperature and dwell time will differ and will be stated in the text.

6.2.4 Material Characterisation

To understand the structural changes that occur during the solid-state crystal growth procedure, microstructural analysis has been undertaken after each experiment. The techniques used here include optical microscopy, scanning electron microscopy and energy dispersive X-ray spectroscopy. These techniques are explained in detail in Section 4.5.

The preparation of materials, to enable the microstructural analysis, is also listed in Section 4.5. Samples have been set in resin and polished to a mirror finish, the polishing procedure is listed in Section 4.5.4, taken from the equipment provider Buehler's recommended polishing route for ceramic materials (Buehler. 2021).

6.2.5 Particle Size Analysis

The size distribution of the precursor PMN-PT powder particles is a factor in determining the density of ceramics formed. The particle size distribution establishes the packing of particles and flowability of the powder, which directly affects the density of green body and therefore sintered body of the samples. A particle size analysis was undertaken to establish the average size and distribution of the calcined PMN-PT powders prepared in this work.

Figure 79 shows the particle size analysis data obtained. The average size of particles was found to be 0.75 μm , this is confirmed by the SEM images shown in Figure 80.

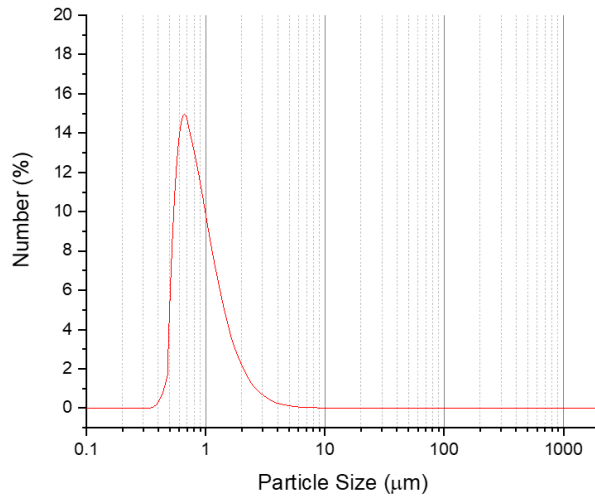


Figure 79. Particle size analysis of PMN-PT powders that have been prepared and calcined according to Section 4.2.

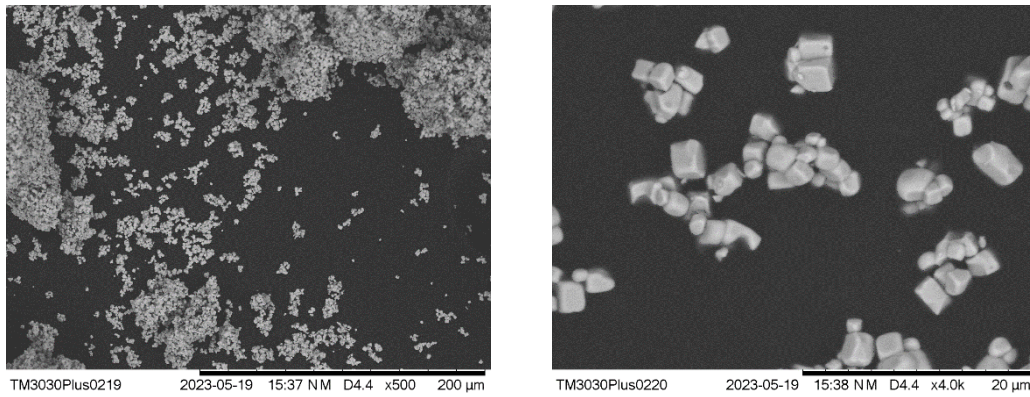


Figure 80. SEM images of PMN-PT powders that have been prepared and calcined according to Section 4.2.

6.2.6 Single Crystal Seed Properties

The XRD spectrum of the PMN-PT single crystal seed is shown in Figure 81. This confirms that the seed is [100] orientated.

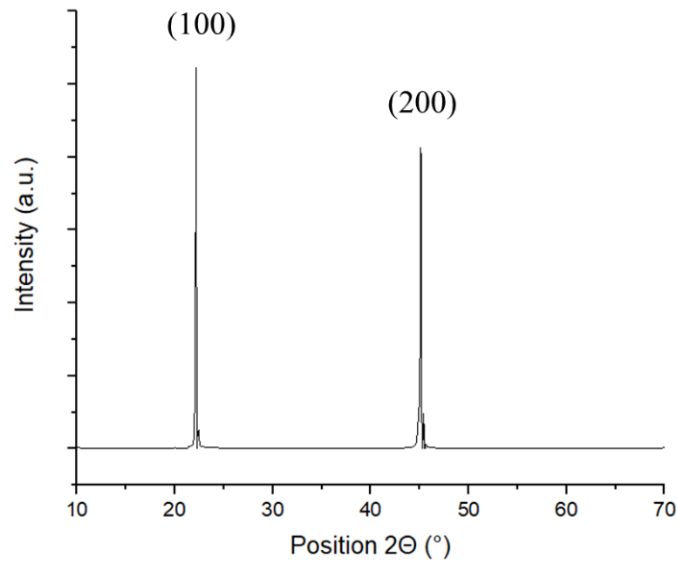


Figure 81. XRD Spectrum of PMN-PT single crystal seed.

6.3 Results and Discussion

6.3.1 Hot Press Unseeded Initial Trials

The first set of experiments were conducted without the implementation of single crystal seeds to understand how the microstructure of polycrystalline PMN-PT is effected when sintered in the hot press compared to sintering in a conventional furnace. Hot-pressing at various temperatures and pressures was explored as well as an annealing study to understand the effect of further heat treatment on the microstructural evolution of the hot-pressed samples.

The hot-pressed samples are compared to conventionally sintered counter parts. This is carried out by inspecting the microstructure of both samples and the electrical properties of the formed pellets. Sintering with the aid of a liquid phase by the addition of excess lead oxide to the materials is also explored in this section.

Results from this section aim to determine the optimal sintering conditions used during hot-pressing to produce ideal materials for solid state crystal growth experiments. The seeded growth trials are then explored in the next section of work, using the knowledge from the initial hot-pressing experiments.

6.3.1.1 Determining the Optimum Sintering Temperature

The first set of experiments aims to establish how hot-pressing with varying sintering temperature and pressure effects the microstructure of PMN-PT samples. The optimal sintering temperature here is defined as the temperature at which the highest density PMN-PT samples are obtained.

Samples were sintered in the hot press maintaining constant pressure of 20.4 MPa. The temperature at which the samples were held for sintering was varied in 50 °C increments from 1000 °C up to 1200 °C. A ramp rate of 300 °C/hour was used for all samples, and a dwell time of 5 hours was also kept consistent. Figure 82 shows the sinter profile used for materials hot-pressed at 1150 °C.

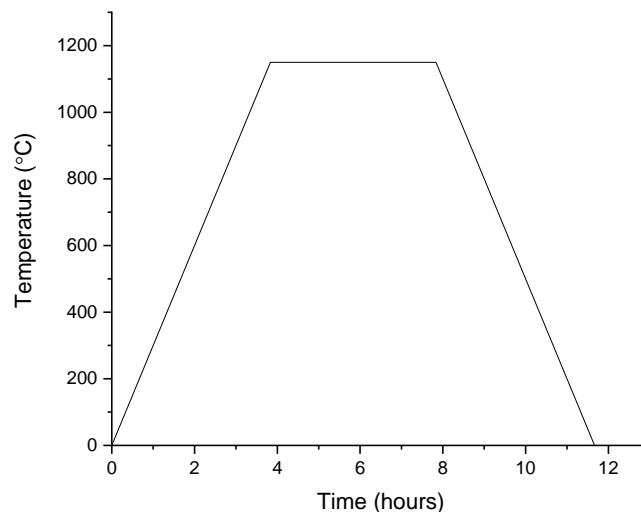


Figure 82. Sintering profile of PMN-PT in the hot press, dwelling temperature of 1150 °C.

Following hot pressing, the samples were cut as shown in Section 4.3.5. The newly exposed surfaces were then ground and analysed using X-ray diffraction. X-ray diffraction is used to identify the crystal phase and identify any impurities within the hot-pressed materials. The X-ray diffraction patterns of PMN-PT samples sintered for varying temperatures in the hot press, all at 20.4 MPa pressure, are shown in Figure 83.

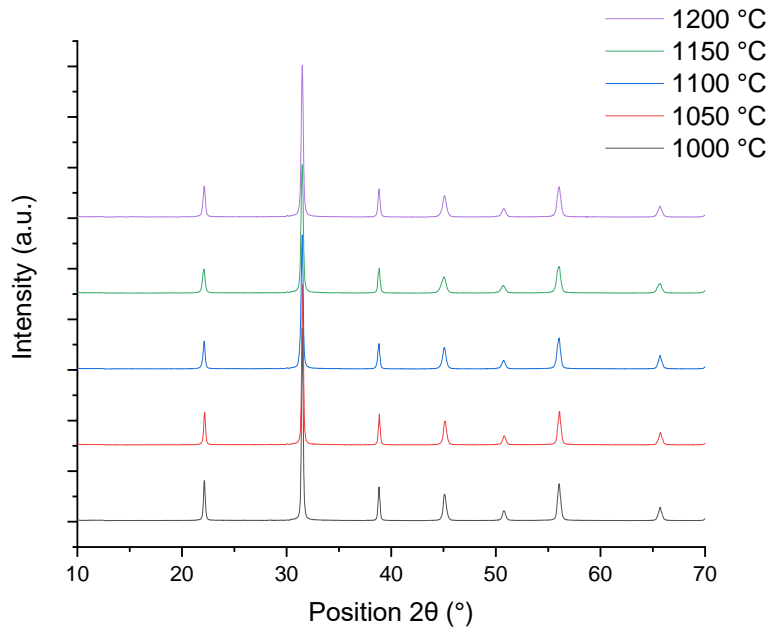


Figure 83. X-ray diffraction patterns of all samples sintered at a range of 1000°C - 1200°C.

The XRD spectra shown in Figure 83 exhibit the classic perovskite shape for all sintering temperatures analysed. They are all confirmed to be single phase with minimal differences seen in the peak positions. Closer inspection shows no peak splitting of the (002) peak, which would indicate a tetragonal phase present due to elongation of the unit cell along one direction. In the spectra shown in Figure 83, a single peak is observed indicating a rhombohedral phase where all unit cell edge lengths are equal. Each XRD spectrum shows no indication of impurity peaks. In the formulation of PMN-PT, a common impurity seen is the presence of a pyrochlore phase. The columbite method of synthesis was used to produce the PMN-PT here (detailed in Section 4.1.1.2) to reduce the presence of a pyrochlore phase. Figure 83 confirms this phase has been avoided and no other significant impurities can be seen.

The density of each sample was then measured using the Archimedes method (detailed in Section 4.5.1). The measured density of each sample as well as the % theoretical density, the percentage of which the measured sample density compares to the ideal PMN-PT unit cell, is shown in Table 6. The temperature at which the highest density of sintered pellet was achieved was at 1150 °C, at 8.10 g/cm³ which corresponds to a percentage theoretical density of 99.93%.

Table 6. Density of samples sintered in hot press at 10kN pressure for 4hours at varying temperatures.

Sinter Temperature (°C)	Density (g/cm ³)	Theoretical Density (%)
1000	6.97	87.59

1050	6.99	87.31
1100	7.24	90.75
1150	8.10	99.93
1200	7.98	98.80

The density of the samples is also displayed graphically in Figure 84. It is shown that as the temperature increases from 1000 °C up to 1150 °C the density of the sintered samples increases from a density of 6.97 g/cm³ up to 8.10 g/cm³. As the temperature continues to increase past 1150 °C the density of the samples decreases slightly to 7.98 g/cm³, this is thought to be due to excessive lead loss in the samples caused by the higher temperature, preventing further densification.

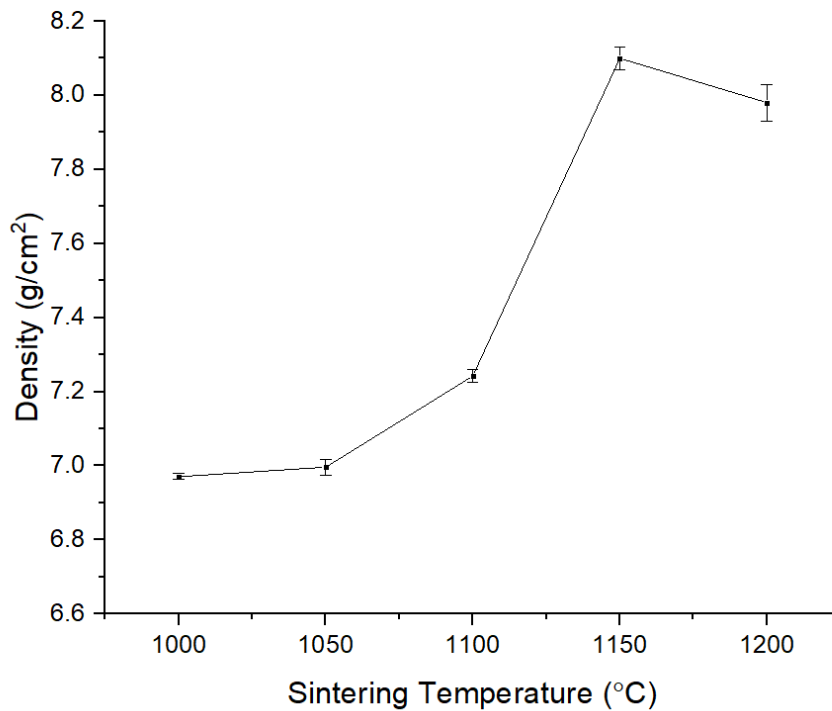


Figure 84. Density of PMN-PT samples sintered in the hot press at varying temperatures.

Figure 85 shows the microstructure of the sintered samples at temperatures varying from 1000 °C to 1200 °C. There is a high amount of porosity present in the samples sintered below 1100 °C

which is in agreement with the corresponding lower densities measured. It appears that full densification has not been achieved until the temperature is increased to 1150 °C.

The microstructure shown in Figure 85 shows that large amounts of intragranular porosity occur in samples sintered below 1100 °C and some porosity is still present at this temperature. Here the combination of 20.4 MPa pressure and 1100 °C is clearly not sufficient to drive mass transport at a rate fast enough to compact and densify the polycrystalline material. At 1150 °C the microstructure shows very little porosity, with minimal porosity existing within the grains rather than between them. The same is true for the PMN-PT sample hot pressed at 1200 °C, minimal porosity can be seen which is in agreement with the higher density value, 98.8% theoretical.

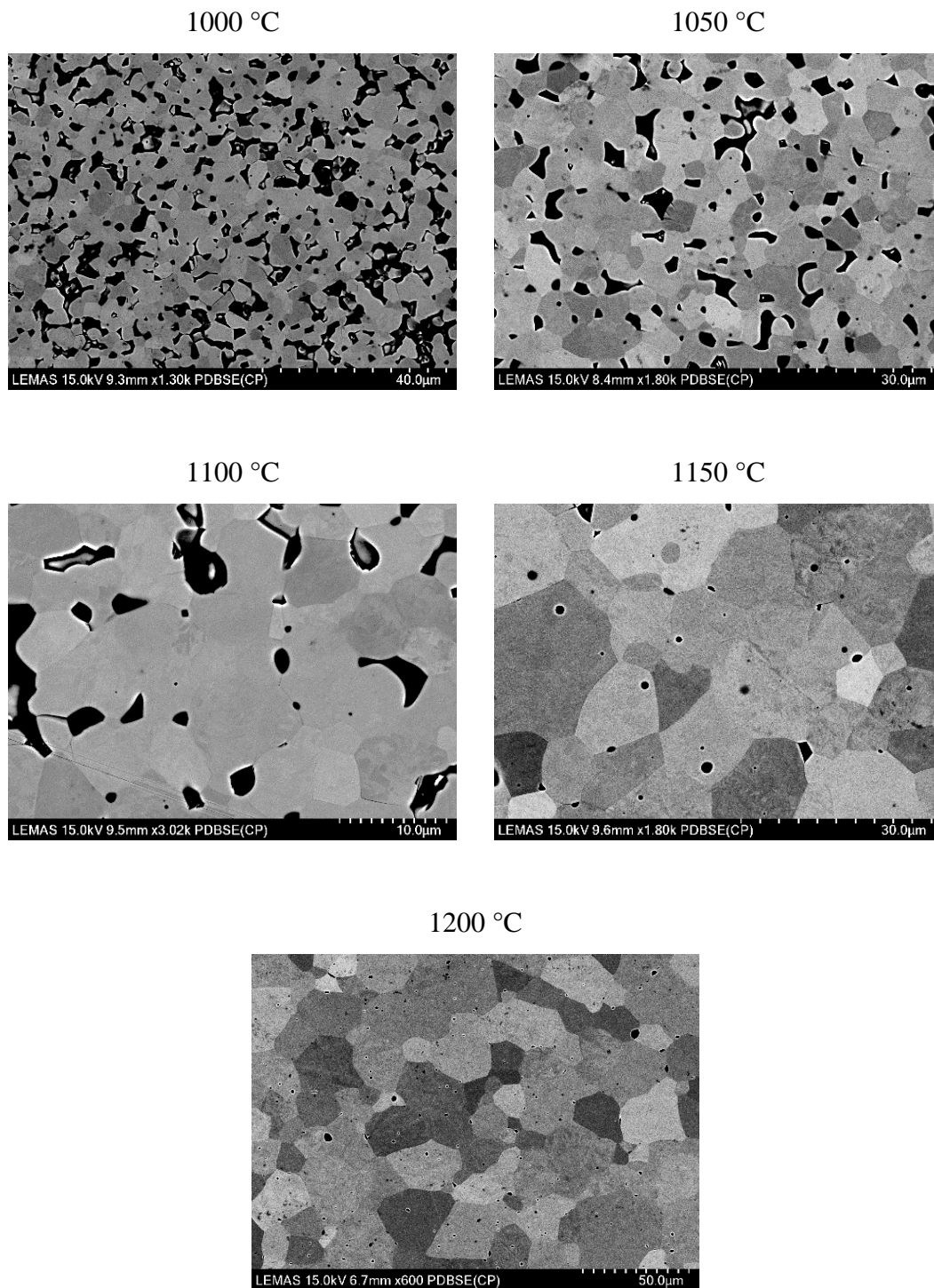


Figure 85. Scanning electron microscopy pictures showing the microstructure of sintered samples in the hot press at varying temperatures from 1000 °C to 1200 °C.

The average grain size of each sintered sample is shown in Figure 86, this is calculated using the linear intercept method, detailed in Section 4.5.4.4. From Figure 86 it can be seen that increasing the temperature from 1000 °C to 1050 °C has only a minor effect on increasing the grain size, with the average grain size remaining at approximately 4-6 μm. The average grain size then increases at 1150 °C to ~11 μm and further still at 1200 °C to ~25 μm.

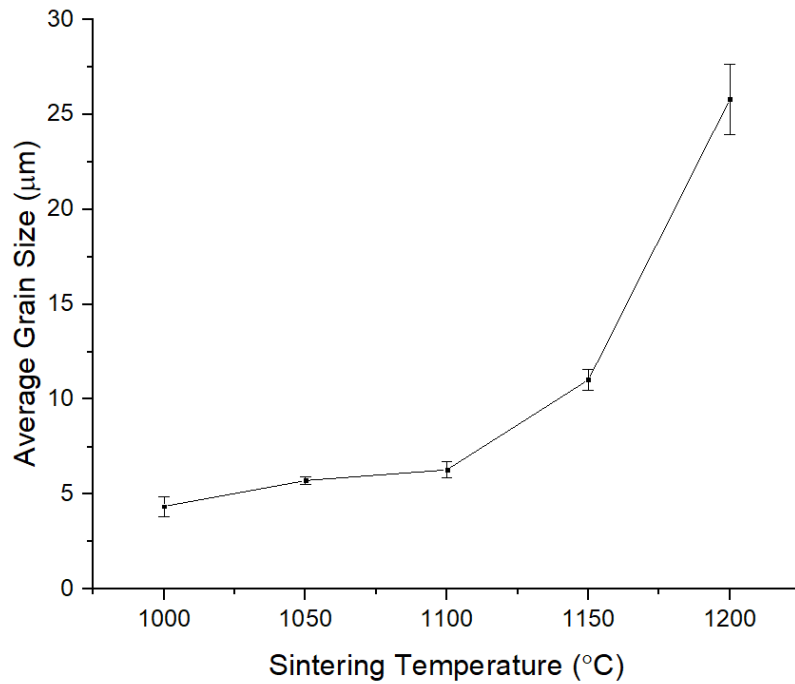


Figure 86. Average grain size vs sintering temperature of PMN-PT samples in the hot press.

The average grain size for each hot pressed PMN-PT sample is also shown in Table 7. The standard deviation of the average grain size measurements are displayed in Table 7 to give an idea of the variation of grain size in the materials. The biggest variation occurs in the sample sintered at 1200 °C, this is expected as any variation of grain sizes in the initial materials are exacerbated when the temperature is increased, and therefore the growth rate of the larger grains is higher. The variation of all other samples (sintered at 1150 °C and below) however is relatively low, less than 1 μm, indicating a unimodal distribution of grain sizes for all the initial samples.

Table 7. Average grain size of hot-pressed samples with varying sinter temperature from 1000 -1200 °C.

Sinter Temperature (°C)	Average Grain Size (µm)	Standard Deviation (µm)
1000	4.36	0.53
1050	5.72	0.18
1100	6.29	0.43
1150	11.03	0.55
1200	25.79	1.85

Figure 87 shows the average grain size and density of each sample as a function of sintering temperature. From this set of experiments, it can be seen that samples sintered below 1150 °C are less dense and although they have a finer grain structure, will not be suitable as precursors for solid state crystal growth. As the sintering temperature increases past 1100 °C, the density continues to increase, and the average grain size begins to increase up to a value of ~25 µm at 1200 °C. As the density at 1200 °C begins to decrease, possibly due to lead loss from the sample at high temperatures, sample sintering in the hot press will be conducted in further experiments at 1150 °C to produce highly dense samples.

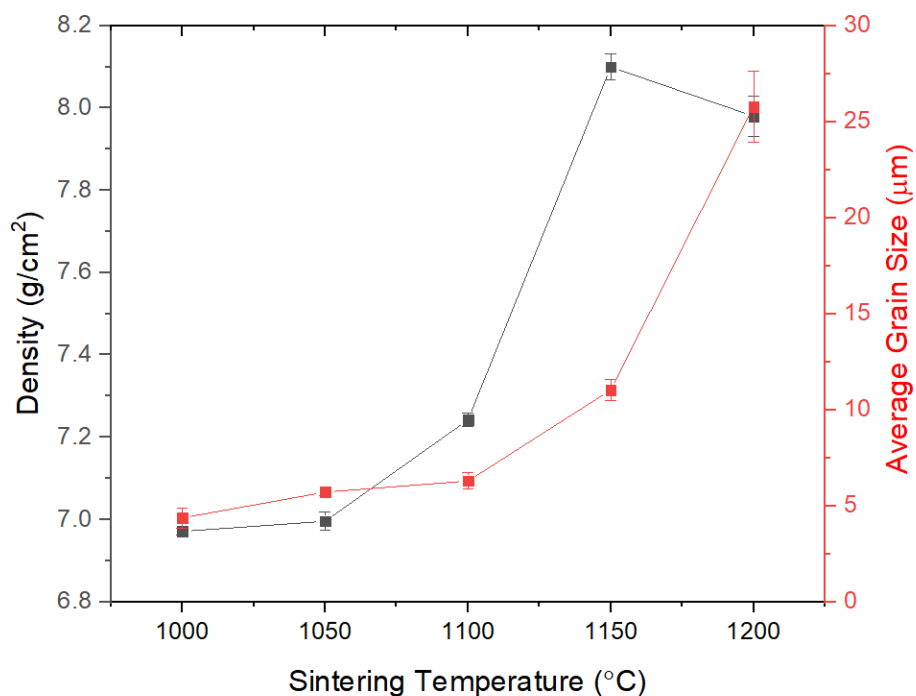


Figure 87. Density and average grain size plotted for hot-pressed PMN-PT samples sintered at varying temperatures.

6.3.1.2 Investigating the Effects of Sintering Pressure on Microstructure

The next set of experiments were conducted to investigate the effect of increasing the sintering pressure during hot pressing and observing what effect this had on the microstructure of the PMN-PT pellets. Samples were prepared as before and loaded into the hot press. The sintering temperature was kept constant at 1150 °C, determined in the previous section to be the optimal sintering temperature where the most dense samples were formed.

Figure 88 shows the microstructure of pellets sintered at 0 MPa, this sample was loaded into the hot press die surrounded by packing powder in conditions identical to the other samples tested but sintered in a conventional furnace where there is no external pressure applied to the sample during sintering. Samples sintered in the hot press at 20.4 MPa and 40.8 MPa are also shown.

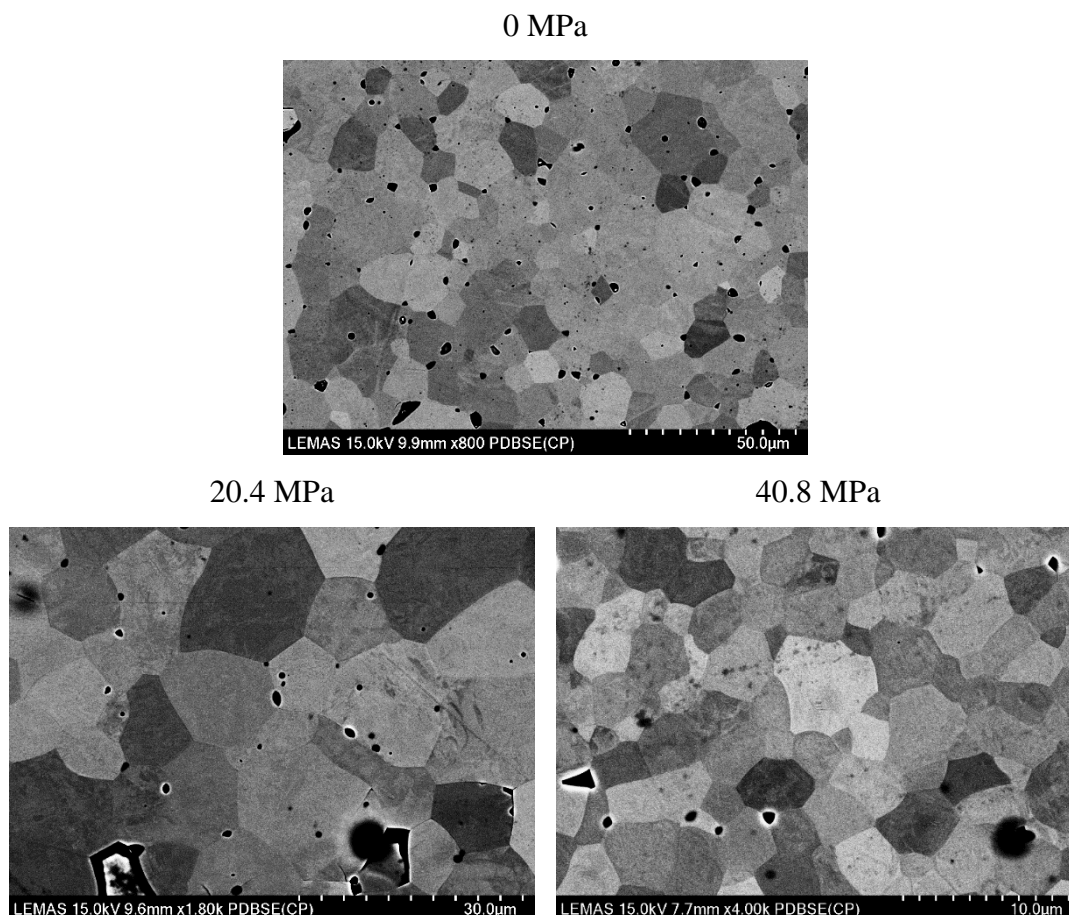


Figure 88. SEM images showing microstructure of sintered pellets of varying applied pressure; 0 MPa, 20.4 MPa and 40.8 MPa.

Figure 89 shows the effect of sintering pressure on the average grain size and the density obtained of each sample sintered at varying pressure, 0 MPa, 20.4 MPa and 40.8 MPa. It can be seen from Figure 89 that as the pressure is increased at sintering, the average grain size decreases. A conventionally sintered pellet has an average grain size of 22.9 μm , this decreases to 9.6 μm at 20.4 MPa and 3.9 μm for 40.8 MPa. It is therefore advantageous when sintering the precursor materials to use pressure of 40.8 MPa to obtain a fine grain structure.

The density of each pellet is also seen to vary with sintering pressure. A conventional sinter on average was shown to produce samples with density of 7.53 g/cm^3 , increasing the pressure to 20.4 MPa also increased the density to 8.10 g/cm^3 . Additional pressure up to 40.8 MPa resulted in a plateau of the achieved density and a minor reduction to 8.05 g/cm^3 . It seems the dominant effect of elevated pressure is a reduction in the grain size rather than further increased density, although as the sample is close to the 100% maximum theoretical density at 20.4 MPa this is to be expected.

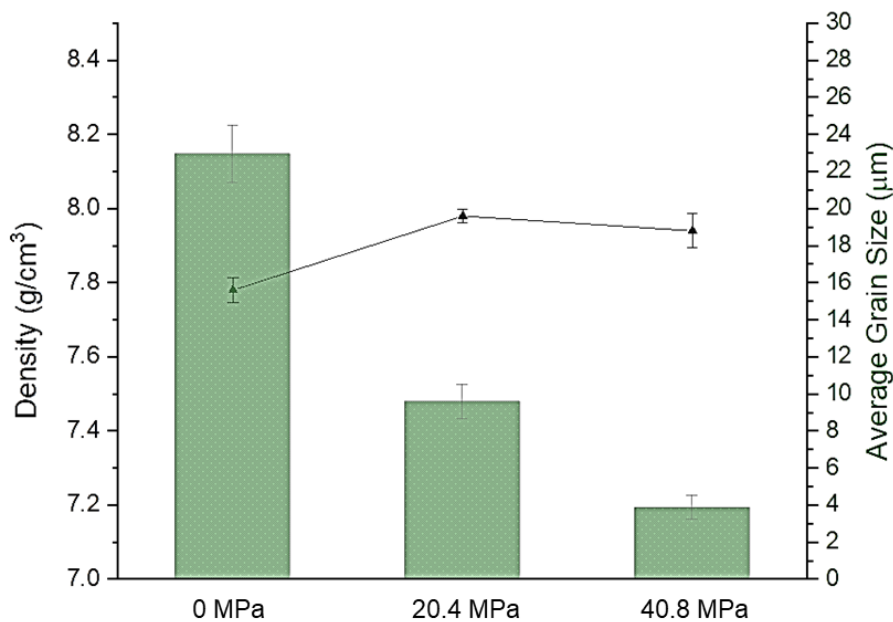


Figure 89. Effect of sintering pressure on average grain size and sample density.

A sample was also sintered at 61.2 MPa with the same hot press experimental set up. During this experimental run however, a pressure induced failure in the push rods caused immediate loss of pressure approximately 4 minutes after the hot press had reached sinter temperature 1150 $^{\circ}\text{C}$. From the experimental monitoring of the hot press explored in Section 5.5, it can be

inferred that the actual temperature of the die and sample was several degrees lower than the sinter temperature at the time of failure, as the time at which thermal expansion ceases in the push rods is approximately 20 minutes after the recorded temperature reaches the sintering temperature. It was concluded from inspecting the microstructure of this sample, shown in Figure 90, that full sintering had not occurred at the time of failure. The microstructure of the sample is extremely porous. Due to damage incurred from this by the heating elements of the furnace it was decided for the longevity of the equipment that samples would be run at a maximum of 40.8 MPa for the remainder of the project.

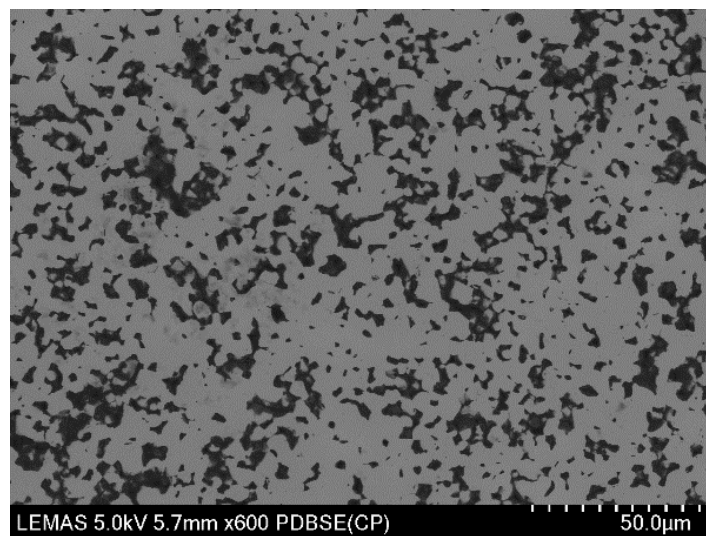


Figure 90. Hot press sample sintered at 61.2 MPa, push rod failure before sample had reached sintering temperature.

6.3.1.3 Comparison to Conventionally Sintered Pellet

To determine the effectiveness of the use of hot press, conventionally sintered samples that were prepared in identical conditions and sintered in a standard furnace to allow comparison between the sintering methods. It is first necessary to discuss how best to compare the sintering methods, as conventional sintering typically requires a binder be used in formulating the green material.

A binder is used in conventionally sintered pellets to aid the densification process, by facilitating closer packing of the particles, and is subsequently burned out of the final material during the sintering process. The addition of binder was initially explored when using the hot

press. The binder burn-out stage is more complex in the hot press as the sample packed in the die with applied pressure creates a sealed environment, limiting the outflow of binder from the sample. When 2% by mass Optapix binder was incorporated into green PMN-PT powder and then hot pressed, the elevated temperature created a reducing atmosphere in which the lead content in the PMN-PT powder was chemically reduced and the sample rendered un-usable.

Another trial was conducted where a PMN-PT pellet with 2% Optapix binder incorporated was first heated to 650 °C in a conventional furnace with the aim to burn out the binder before then transferring to the hot press and sintering. The sample that was produced in this way, shown in Figure 91, was found to be 2.8% less dense than the counterpart sample that was sintered in the hot press using only water as binder. It can be seen in Figure 91 that there is a large amount of porosity in the sintered pellet, and it was concluded that during the binder burn out in the conventional furnace some partial sintering had taken place. As the already partially sintered sample was transferred to the hot press, much more energy was required to drive the densification and shrinking process which resulted in the more porous and open structure.

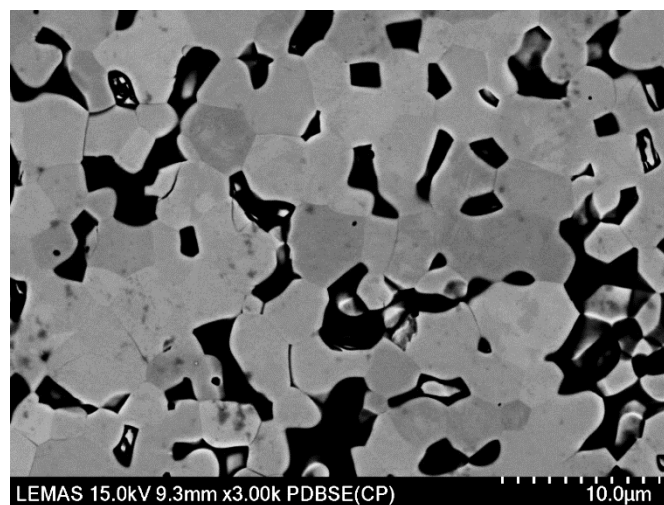


Figure 91. SEM image of sample sintered in the hot press at 1150 °C with 2% Optapix binder incorporated into PMN-PT powder.

To eliminate the porosity accrued during this two-step binder burnout and sintering process it was decided that the hot-pressed pellets would use water as a binder. This is a much smaller molecule that can escape during the sintering stage and does not produce a reducing atmosphere leading to compositional anomalies in the sample.

This binder addition stage is however necessary in conventionally sintered pellets. When a conventional PMN-PT pellet was sintered with water as binder, to replicate hot pressing conditions, the resulting pellets collapsed upon being removed from the crucible. The microstructure of the hot-pressed sample is therefore most accurately compared to the a conventionally sintered pellet with incorporated binder shown in Figure 92 The density of this conventionally sintered pellet was found to be 7.68 g/cm^3 , samples sintered in the hot press at $1150 \text{ }^\circ\text{C}$ have a measured density of 7.98 g/cm^3 . The average grain size has also been reported in Section 6.3.1.2, where the average grain size of a samples is seen to decrease with increasing pressure applied during sintering, from approximately $22 \text{ }\mu\text{m}$ to $5 \text{ }\mu\text{m}$. The use of the hot press is therefore more effective at producing highly dense samples than a conventional furnace.

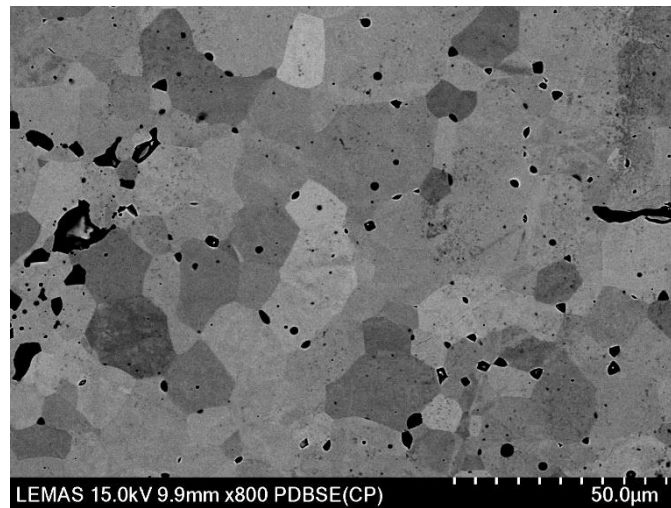


Figure 92. SEM image of conventionally sintered PMN-PT pellet with 2% Optapix binder, sintered at $1150 \text{ }^\circ\text{C}$ with a binder burnout stage of $650 \text{ }^\circ\text{C}$ for 2 hours preceding being heated to sintering temperature.

Both hot pressed samples and conventional samples were also compared using X-ray diffraction, this is shown in Figure 93. Both spectra show single phase PMN-PT without impurities, no strong peak splitting indicates the composition is within the morphotropic phase boundary where rhombohedral and tetragonal phases coexist.

In a study by Wang et al. (2021) conventionally sintered pellets and hot pressed PMN-PT counterparts were also analysed using XRD. It was found that when the (111) and (200) peaks in the XRD spectra are compared, (shown in Figure 94) there is a small shoulder on the (111) conventionally sintered ceramic peak. It was suggested in the work by Wang et al. (2021) that this indicated rhombohedral distortion of the perovskite structure, whereas the hot pressed

(111) and (200) peaks are symmetrical indicating high relaxation with weaker structural distortion.

It can be seen in Figure 94 that the XRD results indicated that there was less structural distortion in the hot pressed PMN-PT ceramic than in the conventionally sintered PMN-PT ceramic and the decreased grain size was considered the reason for the weaker structural distortion and induced high relaxation behaviour in perovskite ferroelectric oxides. Figure 94 indicates the same behaviour is seen in this work.

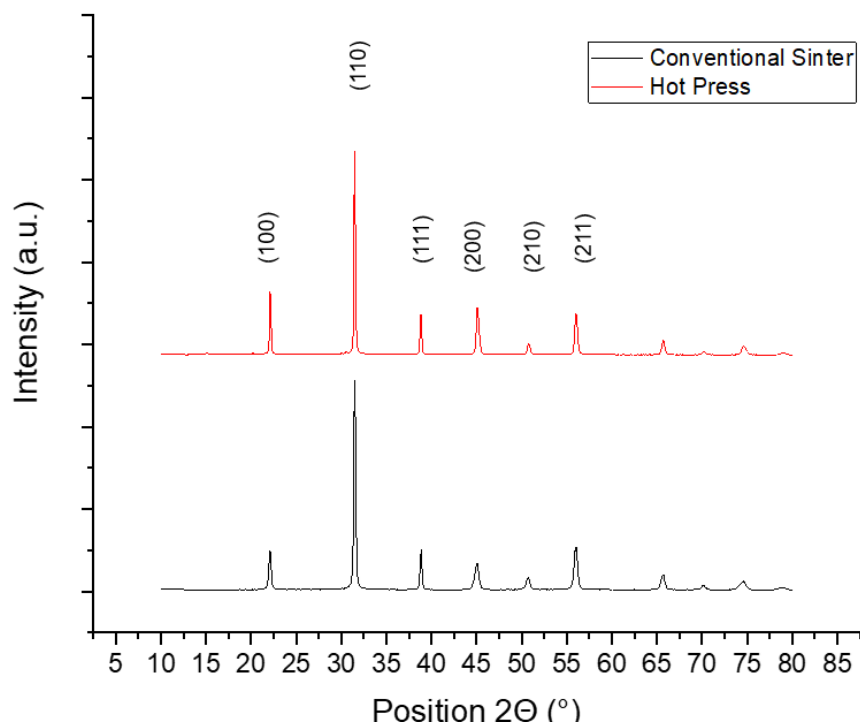


Figure 93. XRD spectra of conventionally sintered PMN-PT sample (1150 °C) and hot-pressed sample (1150 °C, 20.4 MPa).

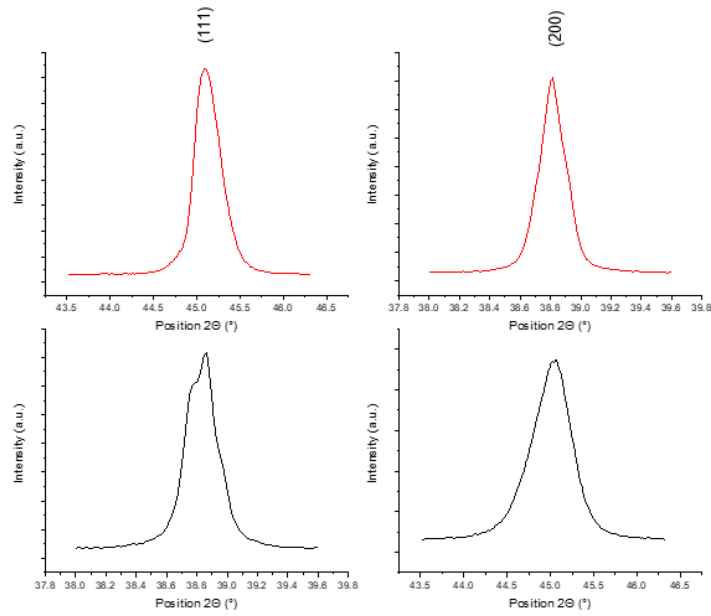


Figure 94. Enlarged (111) and (200) peaks in XRD spectra of conventionally sintered PMN-PT sample (1150 °C) and hot-pressed sample (1150 °C, 10 kN).

A conventionally sintered sample was also compared against a hot-pressed sample by examining the dependence of permittivity and dielectric loss with temperature, shown in Figure 95.

Figure 95 the Curie Temperature is shown to be at around 160 °C. These curves show frequency dispersion at T_C for the maximum permittivity, indicating that both samples exhibit relaxor ferroelectric behaviour. The hot-pressed sample data shows a sharper peak at around 170 °C. Both samples also display the characteristic rhombohedral to tetragonal crystal structure change represented by a ‘hump’ in the permittivity at around 125 °C.

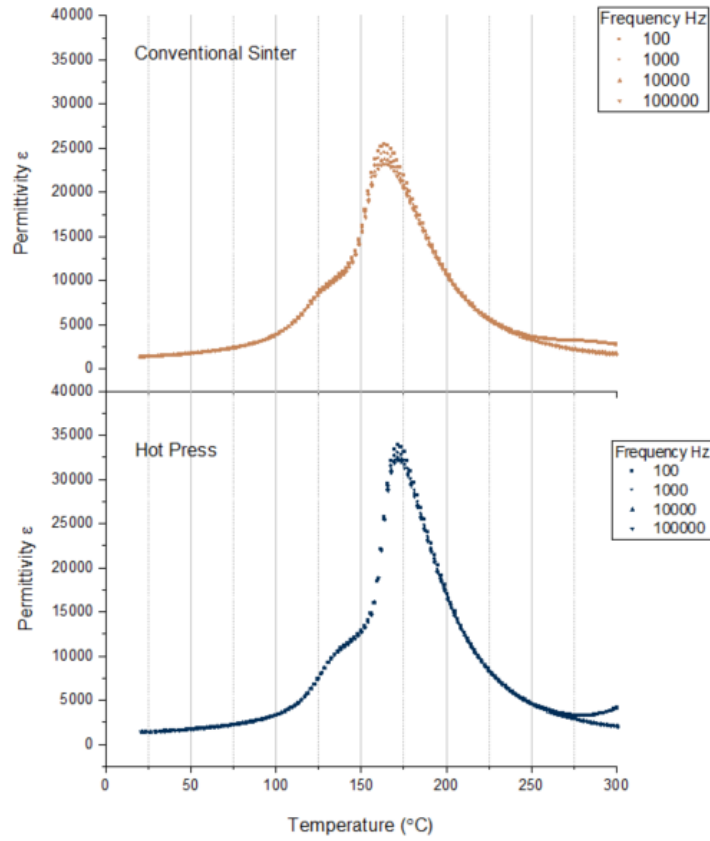


Figure 95. Permittivity vs temperature plot of conventionally sintered PMN-PT 1150 °C and hot pressed PMN-PT 1150 °C 20.4 MPa

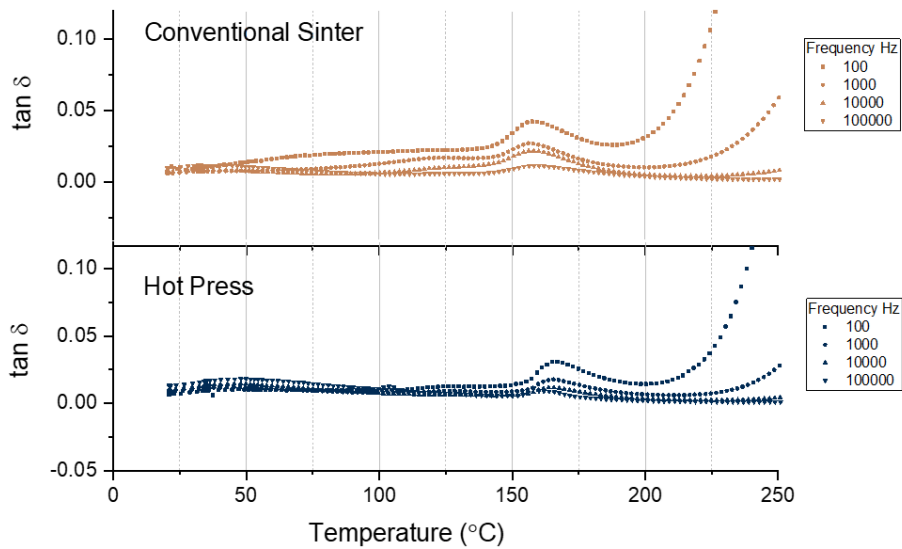


Figure 96. Losses vs temperature plot of conventionally sintered PMN-PT 1150 °C and hot pressed PMN-PT 1150 °C 20.4 MPa.

6.3.1.4 Excess Lead Incorporated Into PMN-PT Samples.

During this analysis the concept of incorporating excess lead oxide into the samples was explored. Excess lead oxide is used to introduce liquid phase at the grain boundaries to facilitate faster diffusion of ions across grain boundaries to enable movement of the grain boundaries. The faster rate of mass transport also enables a reduction of porosity as growing grains fill voids interstitially.

Excess lead oxide was incorporated into the precursor pellets to investigate how this effected the sintered microstructure. A matrix of samples was completed for comparison, where samples of PMN-PT were hot pressed at 1150 °C (as determined as the most effective temperature in Section 6.3.1.1). One set of samples was sintered at 20.4 MPa and one at 40.8 MPa. This will then be repeated with an addition of 2% excess PbO to create a matrix of 4 independent sets of samples as shown in Table 8.

Table 8. Matrix of samples investigated in hot press initial trials which incorporate addition of 2% excess lead oxide (PbO).

Sample details for Excess Lead Incorporation Trials (sinter temperature, pressure, and excess lead oxide content)	
20.4 MPa – 0% excess PbO	20.4 MPa – 2% excess PbO
40.8 MPa – 0% excess PbO	40.8 MPa – 2% excess PbO

Each of the samples shown in Table 8 was prepared according to the processing route outlines in Section 4.2. Excess lead oxide was added to the samples after the calcination stage of stoichiometric PMN-PT. The samples were then loaded into the hot press and then sintered at 1150 °C at either 20.4 MPa or 40.8 MPa of pressure. The microstructure of these samples in shown in Figure 97.

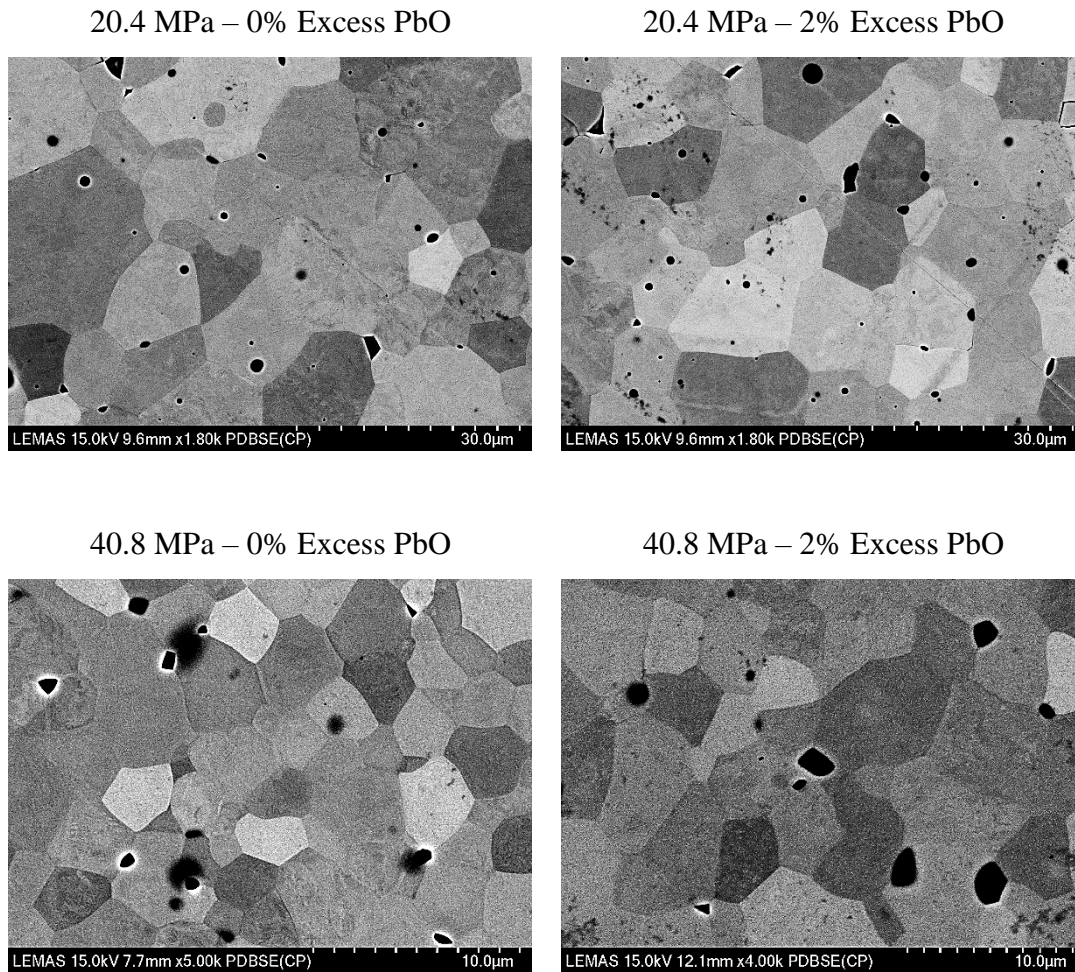


Figure 97. SEM images of sample matrix of initial lead incorporation trials. Samples were sintered in the hot press as specified, with varying excess lead oxide incorporated into green powder.

From the SEM images shown in Figure 97, the average grain size of each the polycrystalline samples were calculated using the linear intercept method. The average grain size and density of the samples is shown in Figure 98 and Table 9. The results for conventionally sintered samples are also included for comparison.

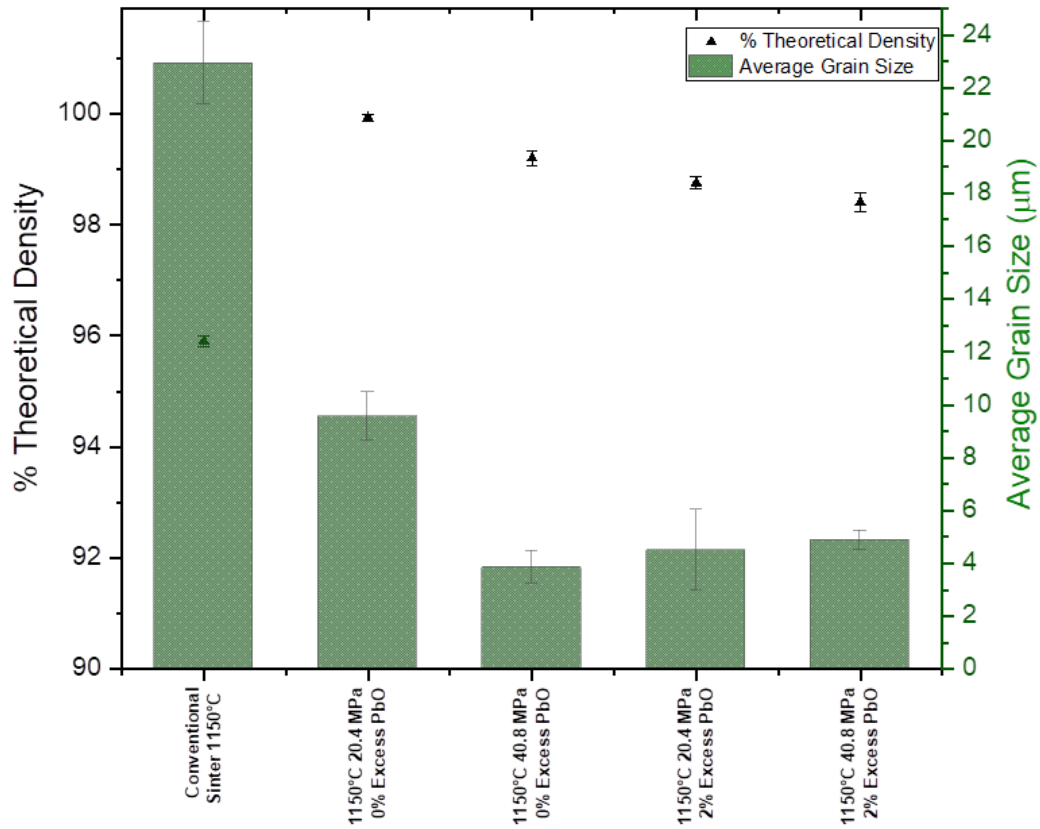


Figure 98. Summary of initial trials excess lead incorporated sample matrix and conventional sample comparison showing average grain size and density of each sample.

Table 9. Summary of initial trials excess lead incorporated sample matrix and conventional sample comparison showing average grain size and density of each sample.

Sample	Average Grain Size (μm)	Average Grain Size Standard Deviation (μm)	% Theoretical Density (%)	% Theoretical Density Error (%)
Conventional Sinter 1150°C	22.93	1.55	95.91	1.02
1150°C 20.4 MPa 0% Excess PbO	9.57	0.92	99.93	0.69
1150°C 40.8 MPa 0% Excess PbO	3.84	0.63	99.20	1.39
1150°C 20.4 MPa 2% Excess PbO	4.49	1.54	98.76	1.08
1150°C 40.8MPa 2% Excess PbO	4.87	0.36	98.41	1.77

It is clear from both Table 9 and Figure 98 that hot pressing of the polycrystalline ceramics increases the density of the formed pellet. All samples sintered in the hot press have a theoretical density above 98%, the conventionally sintered sample has a theoretical density of 95.9%. The samples that have been hot pressed with excess lead oxide content appear to have a slightly higher theoretical density than those sintered with excess lead, >99% compared to >98% respectively. This is attributed to increased lead loss of the samples with incorporated 2% excess PbO.

It can be seen from this data that a considerably finer grain structure is achieved in hot pressed samples, <9.57 μm , when compared to a conventional sinter, 22.9 μm . This confirms that the hot-pressing process has indeed suppressed some grain growth in the polycrystalline sample during sintering.

When comparing the stoichiometric samples without the incorporation of excess PbO, the grain size has decreased from 9.6 μm to 3.8 μm . The addition of excess PbO for samples hot-pressed at 20.4 MPa and 40.8 MPa results in polycrystalline where the average grain size is below 5.0 μm . The excess lead addition has had a more profound effect on samples sintered at 20.4 MPa of pressure, where the grain size reduced from 9.6 μm with 0% excess PbO to 4.5 μm with the addition of 2% PbO.

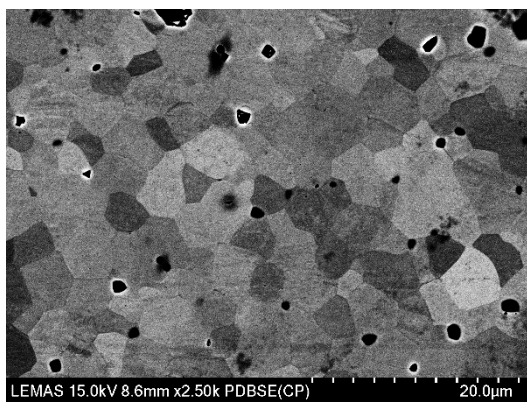
There is more spread of data around the average grain size of the samples sintered at 0.4 MPa, implying that the additional pressure in the hot press is more effective at suppressing grain growth in the polycrystalline matrix than lower pressure, resulting in a sharper unimodal grain distribution.

6.3.1.5 Annealing Study of Unseeded Compositions

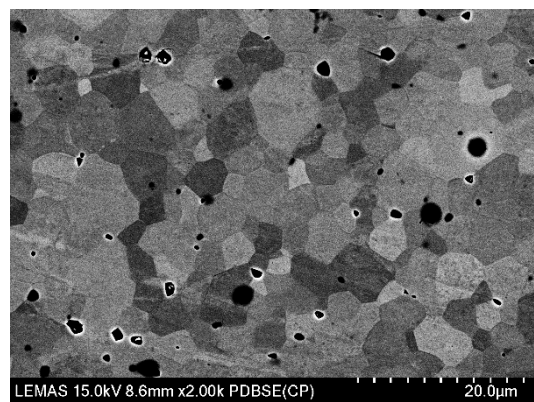
For this set of experiments, the four samples shown in Table 8 have been annealed in a conventional furnace after sintering in the hot press. The samples were all annealed at a temperature of 1150 °C. This was carried out to develop the understanding of how grain growth of the hot-pressed samples develops with further heat treatment with respect to time. After sintering in the hot press, the samples were annealed for a duration of 2, 4, 8 and 16 hours.

The microstructure of the sample hot pressed at 1150 °C 20.4 MPa containing no excess lead is shown in Figure 99. The average grain size for each annealing time is then shown in Figure 100.

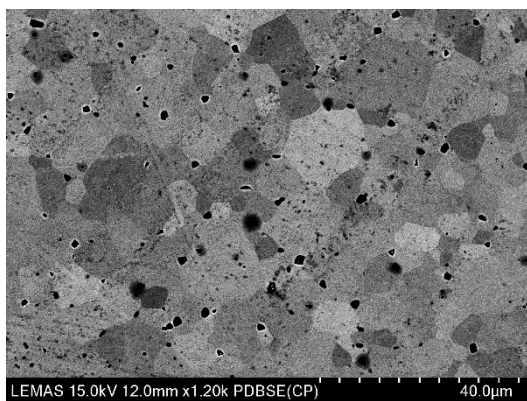
Figure 100 shows that with increasing annealing time the average grain size of the polycrystalline matrix has increased. The growth rate is generally higher up to 8 hours, after this time the rate of growth of grains begins to slow. There is some evidence of larger grains forming in the SEM images shown in Figure 99. This is seen most clearly in samples annealed for 16 hours where there are several larger grains forming.



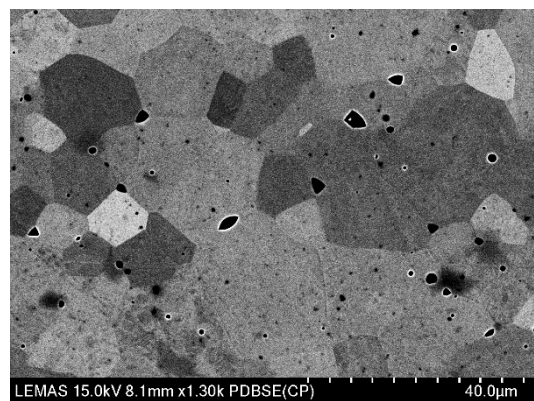
Annealed 2 Hours



Anneal 4 Hours



Anneal 8 Hours



Anneal 16 Hours

Figure 99, SEM images showing annealing of hot pressed (10kN 1150 °C) PMN-PT samples annealed at 1150 °C for 2, 4, 8 and 16 hours.

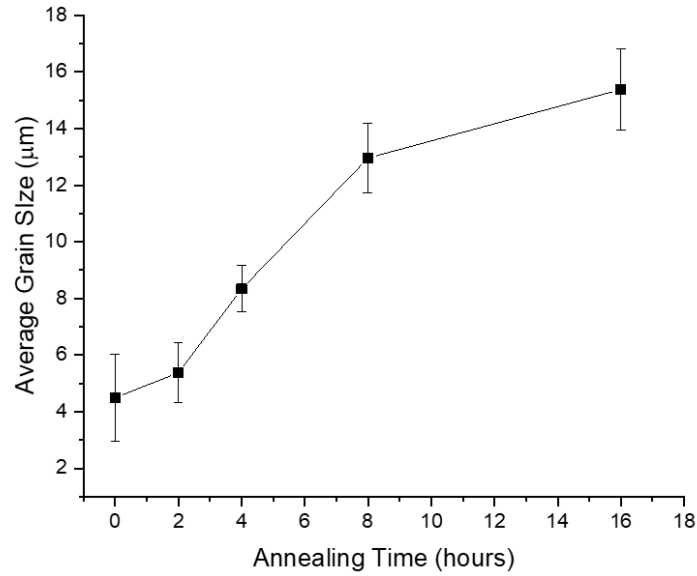
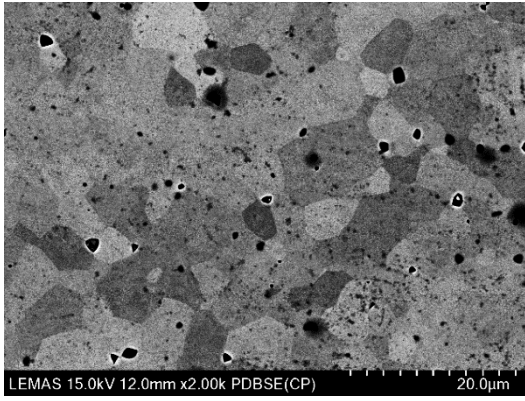


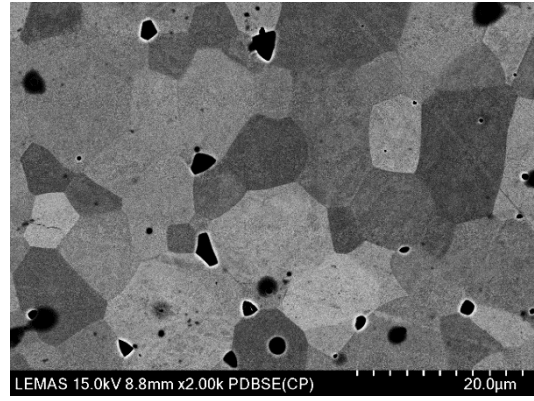
Figure 100. Annealing study of sample hot pressed at 10 kN, 1500 °C containing no excess PbO.

Figure 101 shows the SEM images of the polycrystalline matrix of sample hot pressed at 40.8 MPa and 1150 °C and then annealed at 1150 °C for varying times, 2, 4, 8 and 16 hours. Figure 102 shows the average grain size for each of these materials.

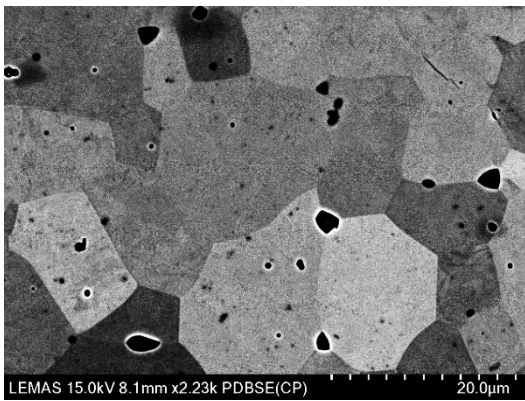
Figure 102 shows a similar gradient to that of Figure 100, where the fastest rate of grain growth is seen in the first 8 hours.



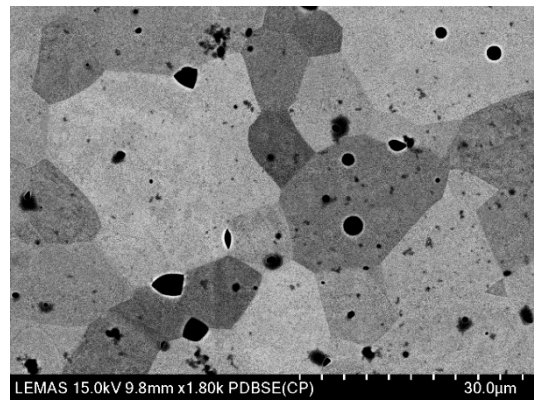
Anneal 2 Hours



Anneal 4 Hours



Anneal 8 Hours



Anneal 16 Hours

Figure 101, SEM images showing annealing of hot pressed (40.8 MPa, 1150 °C) PMN-PT samples annealed at 1150 °C for 2, 4, 8 and 16 hours.

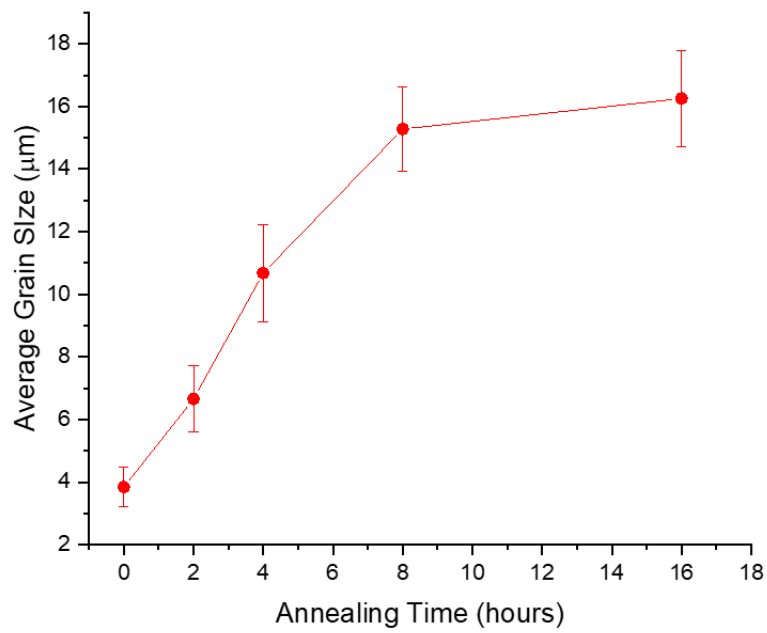
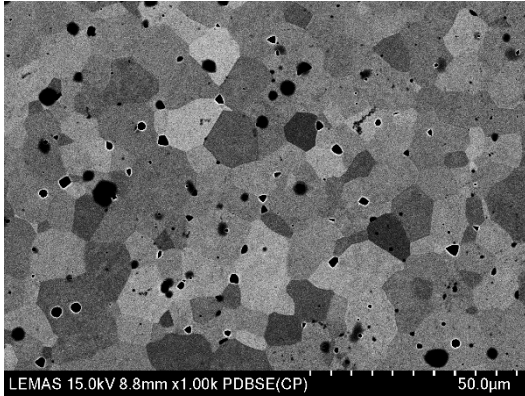
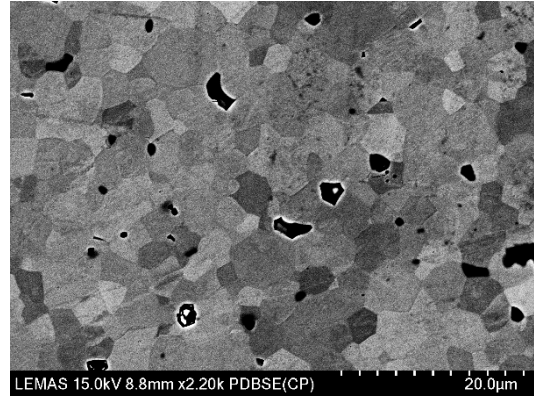


Figure 102. Annealing study of sample hot pressed at 20 kN, 150 °C containing no excess PbO.

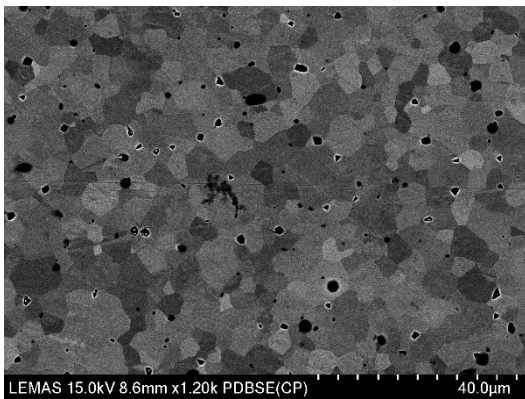
Figure 103 shows the SEM images of the polycrystalline matrix of sample hot pressed at 20.4MPa and 1150 °C and annealed at 1150 °C for varying times, 2, 4, 8 and 16 hours. This sample also contains 2% excess lead oxide. Figure 104 shows the average grain size for this sample at the various annealing times.



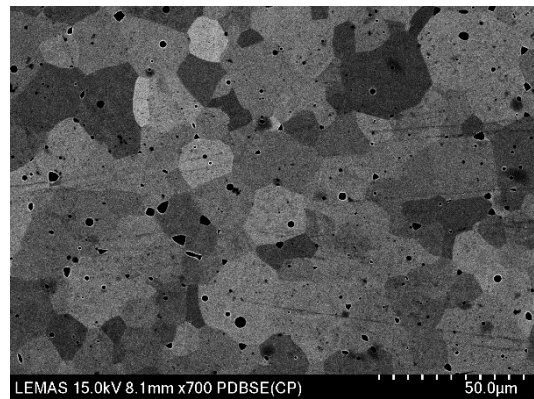
Annealed 2 Hours



Anneal 4 Hours



Anneal 8 Hours



Anneal 16 Hours

Figure 103, SEM images showing annealing of hot pressed (20.4 MPa 1150 °C) PMN-PT samples containing 2% excess PbO annealed at 1150 °C for 2, 4, 8 and 16 hours.

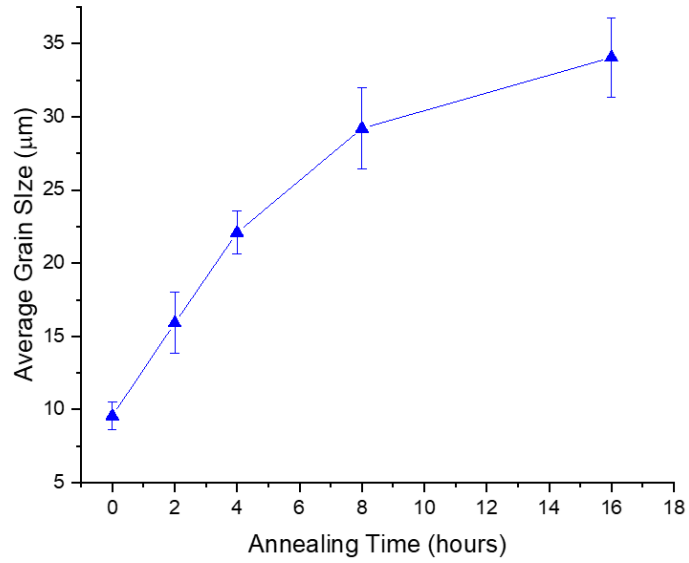
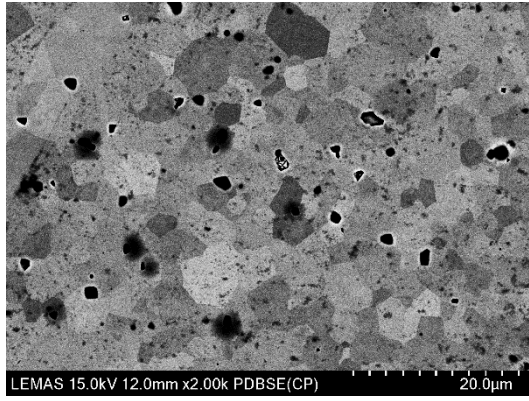
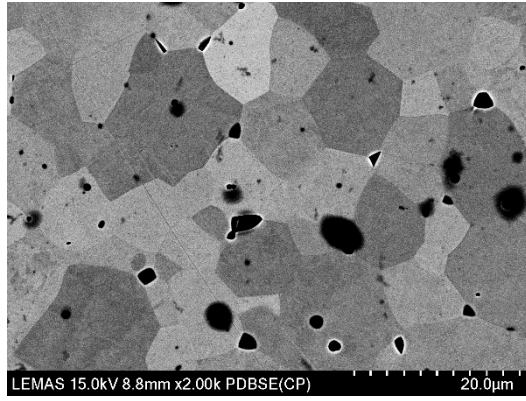


Figure 104. Annealing study of sample hot pressed at 20.4 MPa, 1150 °C containing 2% excess PbO.

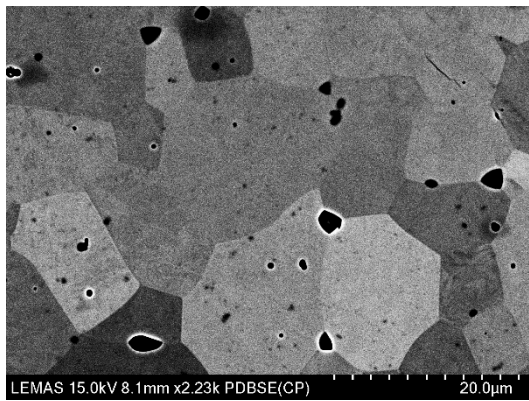
Figure 105 shows the SEM images of the polycrystalline matrix of sample hot pressed at 20 kN, 1150 °C and annealed at 1150 °C for varying times, 2, 4, 8 and 16 hours. Figure 106 shows the average grain size for each of these materials.



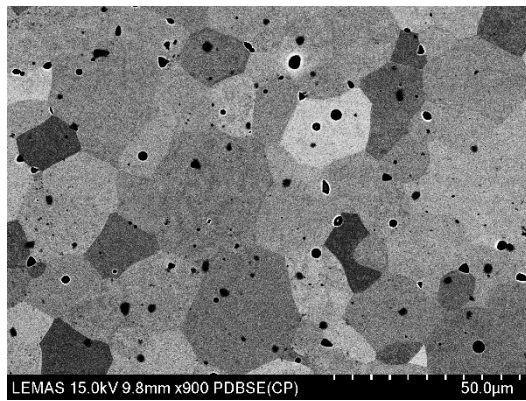
Annealed 2 Hours



Anneal 4 Hours



Anneal 8 Hours



Anneal 16 Hours

Figure 105, SEM images showing annealing of hot pressed (40.8 MPa 1150 °C) PMN-PT samples containing 2% excess PbO annealed at 1150 °C for 2, 4, 8 and 16 hours.

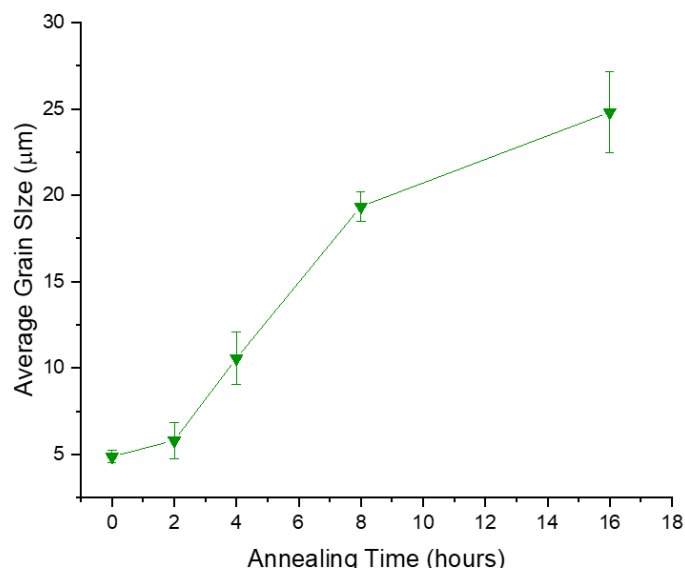


Figure 106. Annealing study of sample hot pressed at 40.8 MPa, 150 °C containing 2% excess PbO.

Figure 107 shows the collection of annealing results presented in this section to allow comparison between the four different samples. It can be seen that the sample that exhibited the most grain growth over the 16-hour period was hot pressed at 20 MPa containing 2% excess lead. The average grain size after 16 hours had increased from 9.6 μm to 34.0 μm . Samples containing 2% excess lead generally show more grain growth than counterparts hot-pressed without excess lead. The sample hot-pressed at 40.8 kN containing 2% excess lead showed a large amount of grain growth, increasing from 4.9 μm to 24.8 μm .

The rate of grain growth of both samples sintered without excess PbO are very similar. An increased amount of grain growth is seen during the start of annealing, particularly in the first 8 hours. A more significant plateau occurs in the grain growth of the non-excess lead samples after the 8-hour mark. Those samples containing excess lead appear to be experiencing a prolonged region of grain growth surpassing 8 hours.

Sample containing excess lead also show a higher degree of variation of grain size in the matrix. This is again indicating that the formation of liquid phase in the polycrystalline matrix has allowed for faster mass transport across boundaries and hence more growth is taking place. In this case the distribution of grain size in the matrix is becoming larger, however. The liquid phase content seems to have exacerbated the individual growth of grains resulting in a wider spread as larger grains grow at the expense of smaller, resulting in a more varied grain size distribution. Abnormal grain growth within the matrix is ideally minimal to reduce the chance of larger grains impinging on crystal seeds in the SSCG trials and reducing the rate of conversion to single crystal.

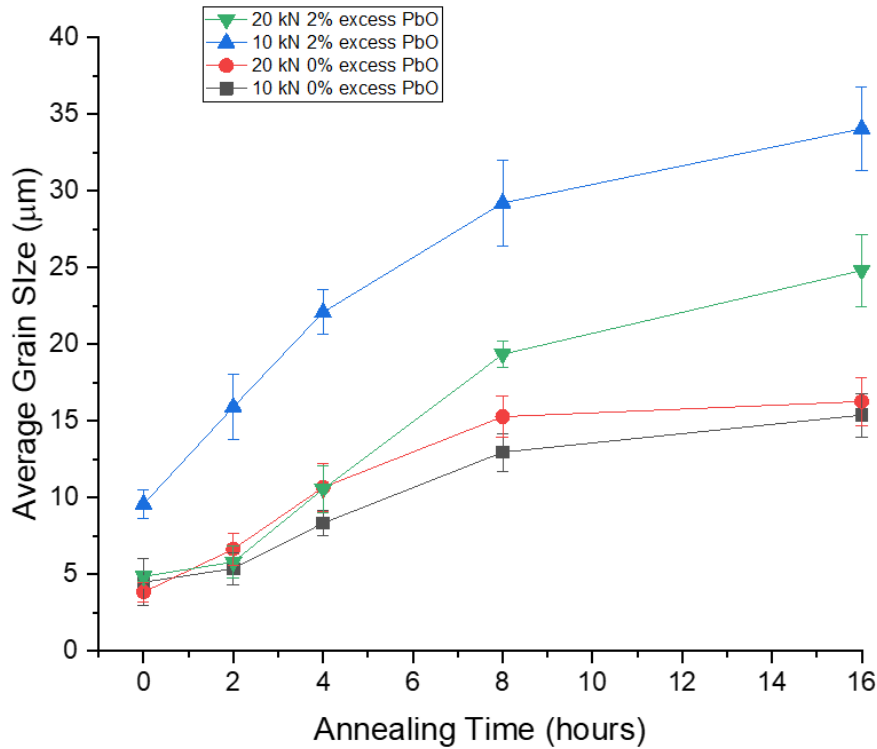


Figure 107. Comparison of all annealing trials carried out on annealing study. Samples show have been hot pressed and then annealed in a conventional furnace at 1150 °C for varying amounts of time, 2h, 4h, 8h and 16 hours.

Normal grain growth follows a parabolic law as a function of time. All annealing samples shown in Figure 108 show a good fit to the parabolic growth law exhibited in normal grain growth. From Figure 108, the highest grain growth rates occur in samples containing an excess of 2% PbO within the polycrystalline matrix. This implies that the grain boundary mobility samples with liquid phase or excess PbO has been increased. This is documented in other works where it is shown that presence of liquid phase PbO significantly impacts the grain boundary mobility.

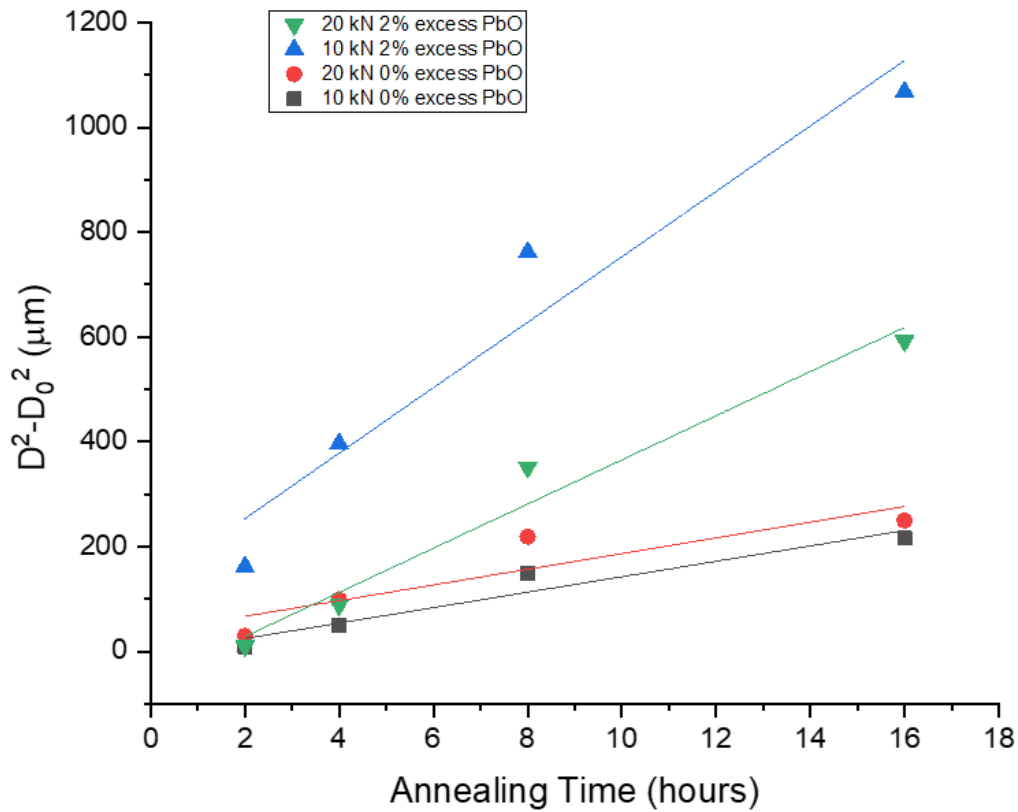


Figure 108. Plot of parabolic growth law for annealing trials.

6.3.2 Single Crystal Seeding

The next set of experiments carried out the solid state crystal growth process by sintering PMN-PT with an embedded single crystal seed in the hot press and then further heat treating to encourage growth from the seed.

The PMN-PT samples are prepared according to Section 6.2.1. The single crystal is embedded in the green powder at the cold pressing stage of the process, the pressed pellet is then transferred into the hot press to be sintered. After sintering, the materials are cut as shown in Section 6.2.5 and transferred to a conventional furnace where they are surrounded by atmospheric powder of the same composition in a sealed crucible and annealed for varying time and temperature.

This section explores the annealing process and how the duration and temperature of the further heat treatment effects the microstructure of the sample and growth from the seed.

6.3.2.1 Barium Titanate Single Crystal Seeding

To begin the solid-state crystal growth work, barium titanate single crystals were first used to seed the precursor ceramic material. Barium titanate has a similar lattice parameter to that of PMN-PT and so lattice strain is kept minimal. The lattice parameter of PMN-PT is 4.2 Å (Wang et al, 2004) and barium titanate 3.99-4.10 Å (Wang et al, 2010).

It has been shown in other work that BaTiO₃ can be used as an effective template for PMN-PT seeded growth, Kim et al, (2006) reported growth of 50 µm over 10 hours heat treatment for BaTiO₃-seeded polycrystalline PMN-35PT. Commercially, Ceracomp have reported growth of mm size PMN-PT single crystals formed from solid-state crystal growth method using BaTiO₃ seeds (Lee, 2003).

6.3.2.1.1 Experimental Procedure

To incorporate the single crystal seed into the polycrystalline matrix and initiate the solid-state crystal growth process, the seed crystal must have good contact with the polycrystalline material. Top seeded solid-state crystal growth was first explored in this work, where the seed single crystal was simply pressed onto the surface of the hot-pressed polycrystalline pellet and annealed in a conventional furnace. The surfaces of both the seed crystal and the polycrystalline pellet were first polished to a mirror finish to enable good contact. Figure 109 shows an SEM image of this set up. Here, a barium titanate single crystal seed has been pressed onto a previously hot-pressed stoichiometric PMN-PT pellet. The barium titanate single crystal seed was loaded on top of the hot-pressed pellet and then surrounded by PMN-PT green powder, to act as sacrificial powder to minimise volatilisation of PbO from the sample. This configuration can be seen in Figure 109. Figure 110 shows an enlarged view of interface between the seed crystal and matrix.

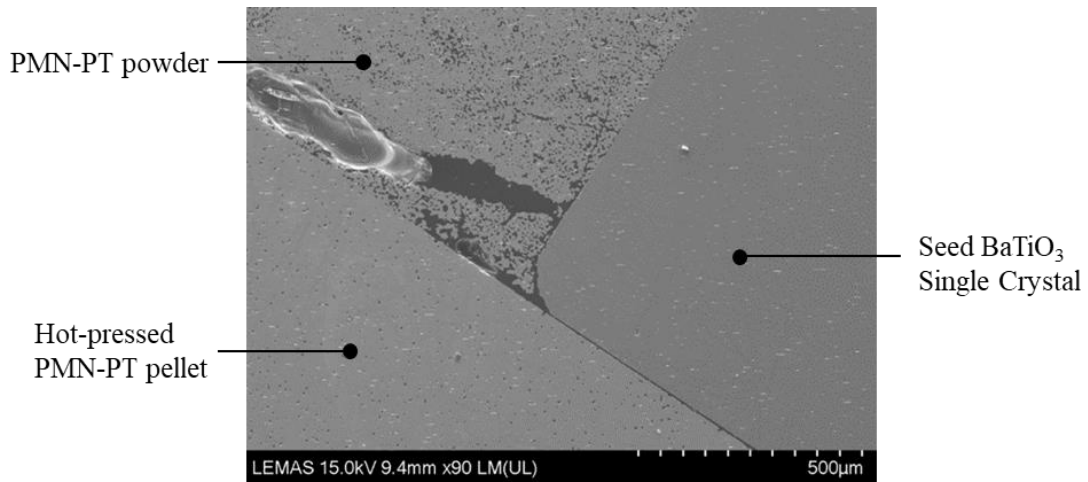


Figure 109. Polycrystalline PMN-PT pellet pre-sintered in the hot press at 40.8 MPa and 1150 °C in contact with BaTiO₃ single crystal seed. The set up has been annealed at 1150 °C for 50 hours.

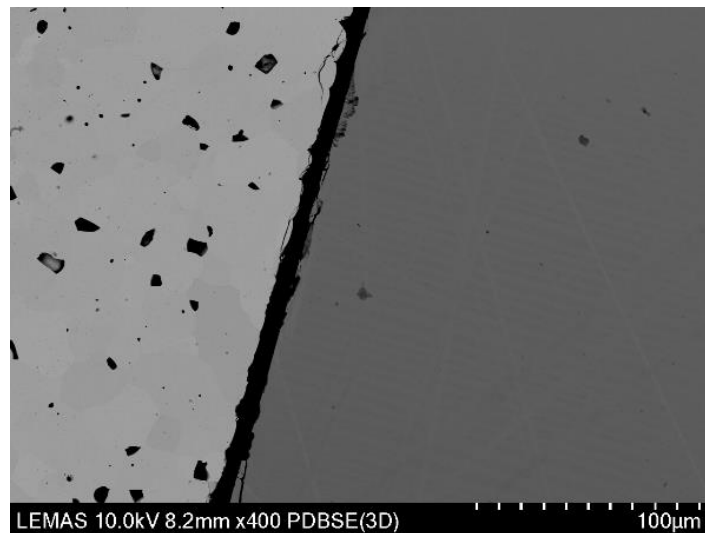


Figure 110. Polycrystalline PMN-PT pellet pre-sintered in the hot press at 40.8 MPa and 1150 °C showing lack of contact between BaTiO₃ single crystal seed and polycrystalline matrix. The set up has been annealed at 1150 °C for 50 hours.

The sample shown in Figure 109 has been annealed in a conventional furnace for 50 hours to induce solid-state crystal growth from the seed. It is clear from this image that contact between the seed crystal and the polycrystalline precursor is insufficient. Even with careful polishing and loading there is a clearly visible fissure between the surface of the seed and the hot-pressed pellet.

The next set of experiments therefore incorporated the single crystal seed as part of the hot-pressing procedure. The green PMN-PT powder was cold isostatically pressed at 20 MPa for 5 mins, this time with the single crystal seed embedded in the powder compact. This encouraged

better contact to the single crystal seed surfaces to facilitate solid-state crystal growth. The compacts containing the single crystal seed were then loaded into the hot press and sintered at pressure.

Figure 111 shows a PMN-PT polycrystalline matrix with BaTiO₃ single crystal seed. This SEM image was taken after hot pressing at 1150 °C 20.4 MPa. Figure 111 confirms that embedding the single crystal seed in the green powder prior to hot pressing is effective at facilitating contact between the seed and matrix.

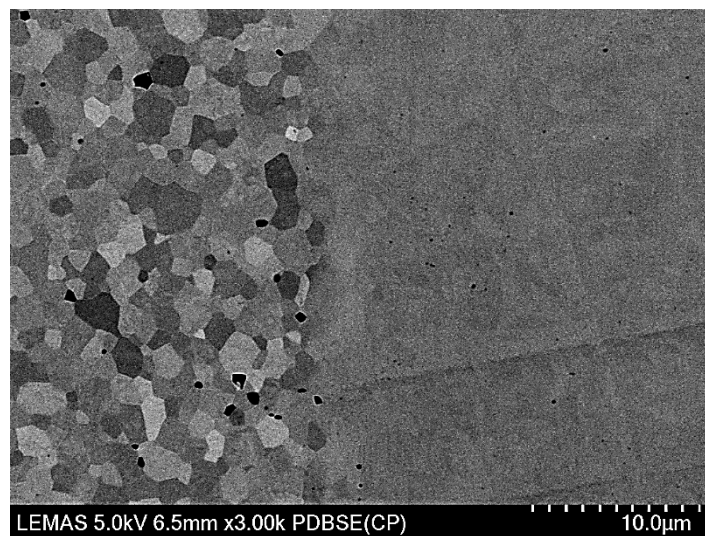


Figure 111. Barium titanate single crystal seed incorporated into PMN-PT polycrystalline matrix; this sample has been hot pressed at 1150 °C 40.8 MPa.

6.3.2.1.2 Results of Barium Titanate Single Crystal Seeding

Barium titanate single crystals were incorporated into PMN-PT powder and hot pressed at 1150 °C, as determined as the optimum sintering temperature to achieve most dense pellets in Section 6.3.1.1. Pressures of 20.4 MPa and 40.8 MPa were then used to study how this effected the solid-state crystal growth from the seed.

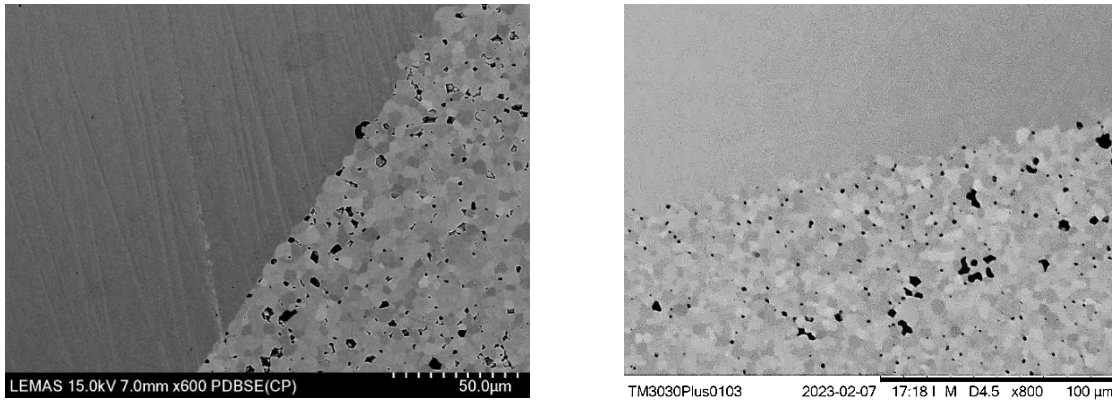


Figure 112. SEM image of microstructure of hot pressed PMN-PT pellet with barium titanate single crystal seed and annealed at 1150 °C for 20 hours. Hot pressing conditions – left 1150 °C 20.4 MPa, right 1150 °C 40.8 MPa.

No crystal growth was seen in the barium titanate seeded samples. Although barium titanate has been shown to be an acceptable substrate on which to grow PMN-PT previously, the results seen in this section do not indicate any growth has taken place from the barium titanate single crystal seed.

Contrary to findings published by Kim et al (2006) and Lee (2003), no grain growth from the seed has occurred in these barium titanate-seeded samples. The findings of these conducted experiments imply that the activation energy for growth of the single crystal seed is too high for growth to occur in this case.

A possible theory of why this has occurred uses the perspective of the solute drag mechanism. Solute drag is often used as a technique of limiting grain growth. Where interaction potential exists between an impurity and a grain boundary in a ceramic matrix, the solute will be either attracted to or repelled from the boundary, resulting in a spatial concentration profile. In each case, whether the solute segregates towards the grain boundary or away, movement of the grain boundary changes the spatial distribution of dopants on either side of the boundary requiring longer range diffusion to maintain the equilibrium concentration distributions and so drag will arise (Powers and Glaeser, 1998). Dopants or other impurities can also change boundary lattice and surface diffusivities, thereby altering the mobility of boundaries and pores. They can, by segregation to the boundary, create a drag force on boundary motion, or, if enough impurity is present, form precipitates that can pin the boundary (Powers and Glaeser, 1998).

If the barium titanate is viewed as a solute in the PMN-PT system, the solution precipitation route dissolving part of the seed crystal and then reprecipitation in matrix has been slowed

down by the solute drag incurred. Overall limiting the grain boundary movement from barium titanate seed into the polycrystalline matrix.

It is also possible that as a result of pressure and temperature used in the hot-pressing procedure, a small amount of secondary phase has been formed at the interface of the seed crystal and polycrystalline matrix. In Section 7.3.1, texturing work is carried out that studies barium titanate platelets distributed in a PMN-PT polycrystalline sample. A secondary phase was formed and identified as $(\text{Pb}_{0.8}\text{Ba}_{0.2})(\text{Mg}_{0.167}\text{Nb}_{0.333}\text{Ti}_{0.5})\text{O}_3$ using XRD and EDX analysis.

The same experimental conditions as are used here are performed on the textured samples (hot pressing at 20.4 MPa 1150 °C and then further annealed at 1150 °C). It is possible therefore that a small amount of that same secondary phase has been produced here at the interface of the barium titanate single crystal seed and PMN-PT polycrystalline matrix. With the result of further solute drag hindering the solid-state crystal growth process.

6.3.2.1.3 Conclusions of Barium Titanate Single Crystal Seeding

Although no crystal growth has been observed in this section of seeding with single crystal barium titanate, there has been an important finding in the experimental procedure of these crystal growth experiments. Pressing the single crystal seed to the surface of the polycrystalline material was found to be much less effective than embedding the seed in the green powder compact. Contact between the seed and polycrystalline matrix is vital and this is best achieved by burying the seed prior to hot-pressing in the un-sintered ceramic powder, cold pressing the pellet with embedded seed and then hot pressing.

Lack of growth from the seed has been attributed to a combination of solute drag and secondary phase formed. In section 7.3.1 where experimental conditions are very similar, a secondary phase produced around barium titanate platelets in a PMN-PT matrix was identified as $(\text{Pb}_{0.8}\text{Ba}_{0.2})(\text{Mg}_{0.167}\text{Nb}_{0.333}\text{Ti}_{0.5})\text{O}_3$. This formation of secondary phase is thought to be causing a solute drag effect and severely limiting the amount of grain boundary mobility and therefore growth from the single crystal seed.

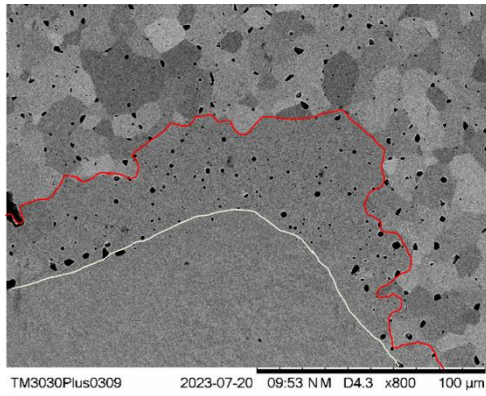
6.3.2.2 PMN-PT Single Crystal Seeding

This set of experiments uses single crystal PMN-PT seed for solid-state crystal growth experiments. Following on from work carried out previously, where single crystal growth was not seen when using barium titanate seed, PMN-PT is used here instead to minimise any hinderance to SSCG process. Knowledge from the prior sections on experimental conditions, procedure and material have been applied in this section.

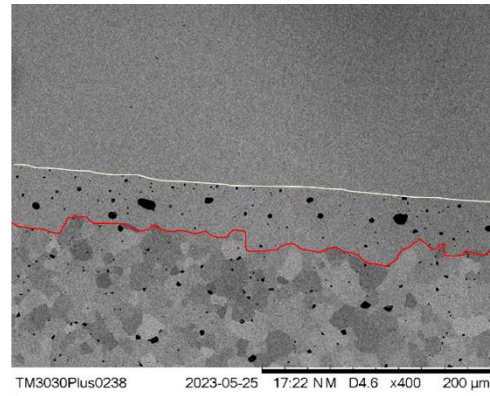
6.3.2.2.1 Annealing Time Analysis for SSCG Trials

PMN-PT single crystal seeds were embedded in PMN-PT green powder and then cold uniaxially pressed at 20 MPa as before. Stoichiometric composition PMN-PT was used in this study without the addition of any excess lead oxide. The pressed powder compact containing the PMN-PT single crystal seed was loaded into the hot press and sintered for 4 hours at 1150 °C and 40.8 MPa of pressure. The resulting sintered pellets were annealed in a conventional furnace at 1150 °C for varying amounts of time to study the progression of growth from the seed and grain growth of the matrix. The samples were annealed in a sealed crucible arrangement buried in sacrificial powder of the same composition as the PMN-PT pellet to minimise lead loss in the system. The samples were then cut and polished to be analysed using SEM as shown in Section 4.5.4.

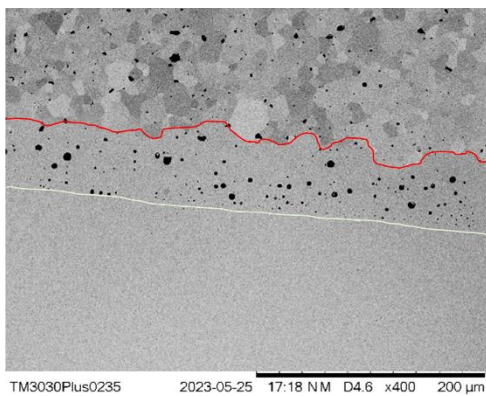
The samples of PMN-PT were annealed at 1150 °C for a duration of 10, 20, 50 and 100 hours. The growth resulting from solid-state crystal growth of the seed in these samples is shown in Figure 113. The white line drawn in the SEM images is to indicate the boundary of the single crystal seed. The red line indicates the amount of grain growth and is drawn at the interface of the growth area and the polycrystalline matrix.



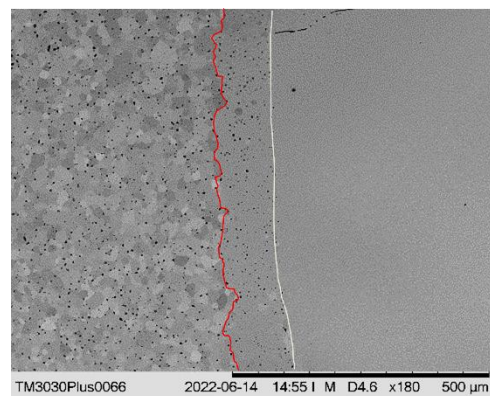
Annealed 10 hours



Annealed 20 hours



Annealed 50 hours



Annealed 100 hours

Figure 113. SEM images of for stoichiometric PMN-PT pellets that have a PMN-PT single crystal seed embedded. The powder compacts have been hot pressed at 1150 °C 40.8 MPa for 4 hours and then annealed for varying times at 1150 °C.

Figure 113 shows that there has been solid-state crystal growth taking place in the stoichiometric hot-pressed PMN-PT samples seeded with single crystal PMN-PT. The areas of crystal growth can be distinguished in the SEM images as some porosity is left behind in the area of single crystal growth. Figure 114 summarised the amount of single crystal growth observed over time. It can be seen from Figure 114 that the growth rate of the seed crystal is fastest before 20 hours. The growth rate at each time stage is reported in Table 10.

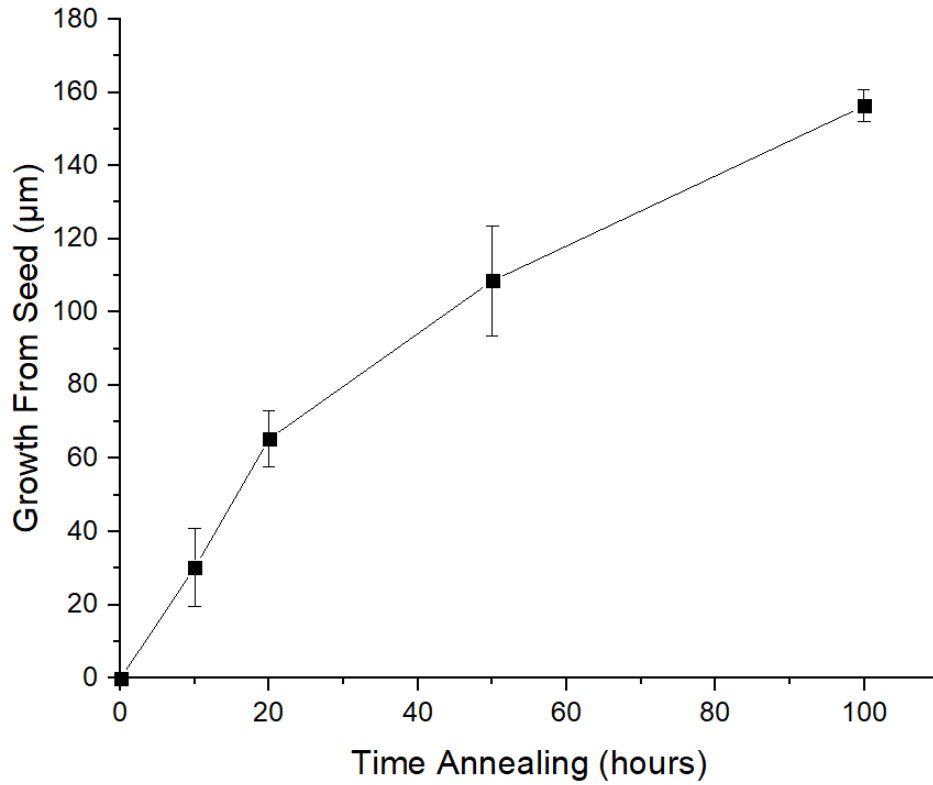


Figure 114. Average solid-state crystal growth from seed for stoichiometric PMN-PT pellets that have a PMN-PT single crystal seed embedded. The powder compacts have been hot pressed at 1150 °C 20 kN for 4 hours and then annealed for varying times at 1150 °C.

Table 10. Growth rate observed in PMN-PT seeded PMN-PT matrix hot-pressed at 1150 °C 40.8 MPa and further annealed at 1150 °C.

Experiment Time (hours)	Growth Rate µm/h	Error (± µm)
0-10	3.03	0.53
10-20	3.51	0.35
20-50	1.44	0.05
50-100	0.96	0.09

The maximum growth rate observed in this experiment was 3.5 µm/hour. This is comparable to results achieved by Li et al (1998) who reported growth rate of 6 µm/hour of PMN-35PT. Khan et al. (1999) and Kim et al. (2006) reported growth rates of 0.14 µm/hour and 5-20 µm/hour respectively for PMN-35PT. Higher growth rates were reported however by King et al (2003) of 20 µm/hour where excess lead was added to the PMN-35PT polycrystalline matrix.

6.3.2.2.2 Comparison to Conventional Sinter

A solid-state crystal growth experiment was conducted on a conventionally sintered sample to allow for comparison to hot-pressed samples. In this instance, PMN-PT green powder has been cold pressed at 20 MPa for 5 mins with an embedded PMN-PT single crystal seed. The procedure for sample loading has been kept identical to the hot-pressing experiments. The compacted powder with embedded seed are then transferred to the hot press die and surrounded by packing powder. This die set up is then loaded instead into a conventional furnace to sinter for 4 hours at 1150 °C. Figure 115 shows the microstructure of the polycrystalline matrix after sintering and growth from the single crystal seed. A larger amount of porosity is immediately evident in the polycrystalline matrix. Growth of the single crystal seed has taken place, again outlined for clarity with red (interface of matrix and growth area) and white (interface between growth area and single crystal seed).

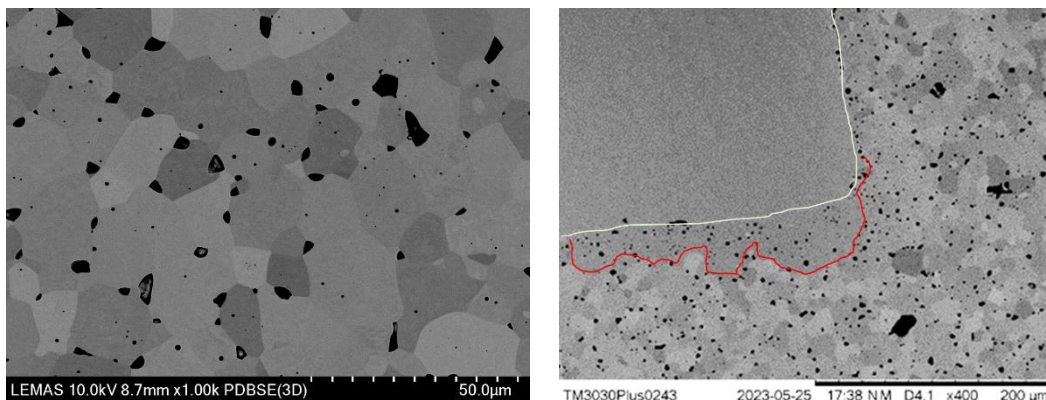


Figure 115. Solid-state crystal growth of conventionally sintered PMN-PT pellet with embedded PMN-PT single crystal seed.

The growth area around the single crystal seed shown in Figure 115 is sporadic and does not occur continuously at the interface between the seed and polycrystalline matrix. Figure 115 shows growth from the seed along one edge of the seed but no growth experienced on the adjacent side.

It can be seen in Table 11, where the grain growth data for conventionally sintered PMN-PT and hot pressed PMN-PT are recorded, that the grain growth achieved was significantly less after conventional sintering followed by 100 hours annealing at 1150 °C. The average growth

from the seed of the conventional sinter was recorded as 16.7 μm whereas the counterpart hot-pressed pellet achieved single crystal growth of up to 108.5 μm . The error associated with the crystal growth is much higher in the conventional sinter due to the sporadic nature of the growth, at some lengths of the seed/matrix interface no growth was seen, whereas the hot-pressed sample exhibited consistent growth around the single crystal seed.

The average grain size of the conventionally sintered sample increased from 22.9 μm before annealing to 29.3 μm after. This is a similar to the rate of grain growth that is seen from the hot-pressed sample, from 9.57 μm to 18.36 μm , although the hot-pressed samples, polycrystalline matrix is finer to begin with. The largest difference between the two samples is in the rate of single crystal growth.

Table 11. Comparison of solid-state crystal growth achieved from PMN-PT polycrystalline with embedded PMN-PT single crystal seed that have been sintered in the hot press or conventionally sintered.

Sample	Conventional Sinter		Hot Press	
	Value (μm)	Standard Deviation (μm)	Value (μm)	Standard Deviation (μm)
Average grain size prior to annealing	22.9	1.55	9.57	0.41
Average grain size post annealing	29.3	3.71	18.36	0.56
Average growth from seed	16.74	10.86	108.54	4.29

6.3.3 Solid State Crystal Growth Results

The next set of experiments builds on the SSCG work achieved with PMN-PT-seeded samples. The hot-pressing procedure has been kept the same and annealing temperature has been varied to encourage faster growth rate of the single crystal seed. The addition of excess PbO into the PMN-PT polycrystalline matrix has also been explored in this section, samples have been prepared with 2% and 5% excess lead oxide to produce liquid phase presence in the polycrystalline matrix.

6.3.3.1 Stoichiometric PMN-PT

Solid-state crystal growth has been shown to occur in PMN-PT seeded samples as shown in the previous sections. To optimise the solid-state crystal growth process, the temperature at which the annealing takes place is varied here with a view to increase the rate of growth obtained.

The optimal hot-pressing conditions have been established previously in this work. For this set of experiments the green PMN-PT powders are therefore be seeded with a PMN-PT crystal seed, using deionised water as binder, and hot pressed at 1150 °C and 40.8 MPa for 4 hours before being removed from the hot press and annealed in a conventional furnace at varying temperature. The annealing temperatures to be analysed vary in increments of 50 °C from 950 °C up to 1200 °C. All samples were sintered for 100 hours.

Figure 116 shows the microstructure of the hot pressed PMN-PT polycrystalline matrix before annealing has taken place. The average growth from the PMN-PT single crystal seed and average grain size calculated for each sample are reported in Figure 122 and Figure 123 respectively.

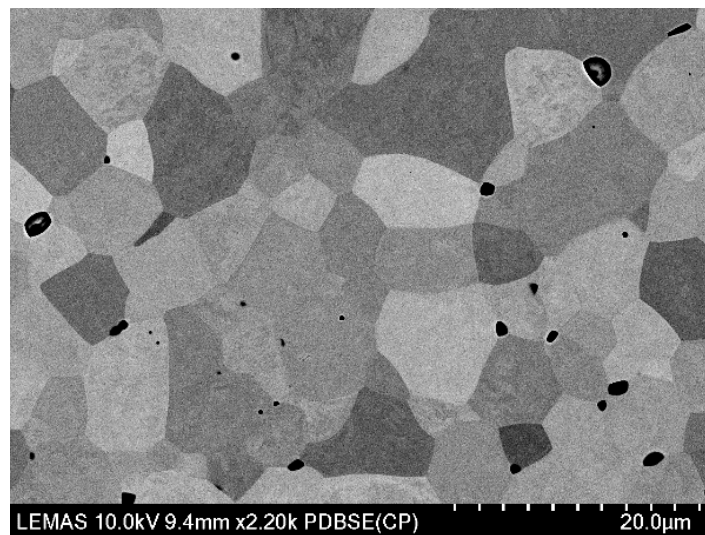


Figure 116. SEM image of polycrystalline matrix of sample PMN-PT with 0% excess lead oxide, sintered in the hot press at 1150 °C 20 kN/

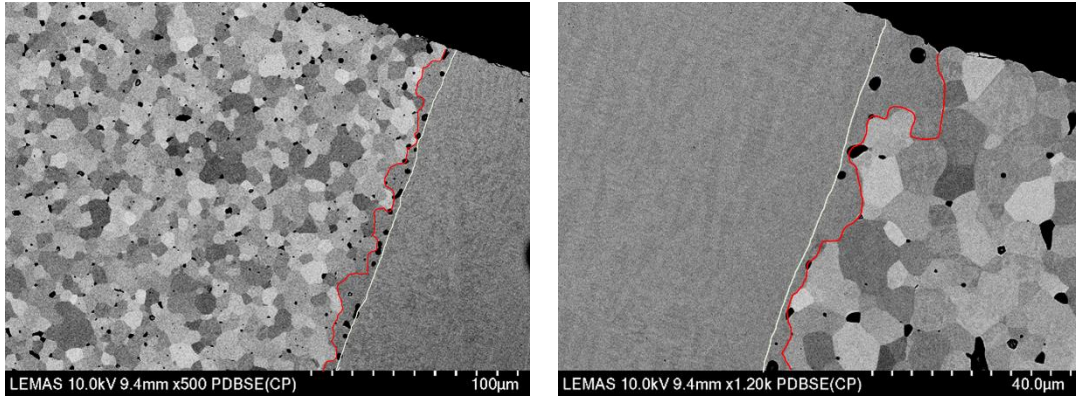


Figure 117. SEM images of single seed growth and polycrystalline matrix of sample PMN-PT with 0% excess lead oxide, sintered in the hot press and annealed for 100 hours at 950 °C.

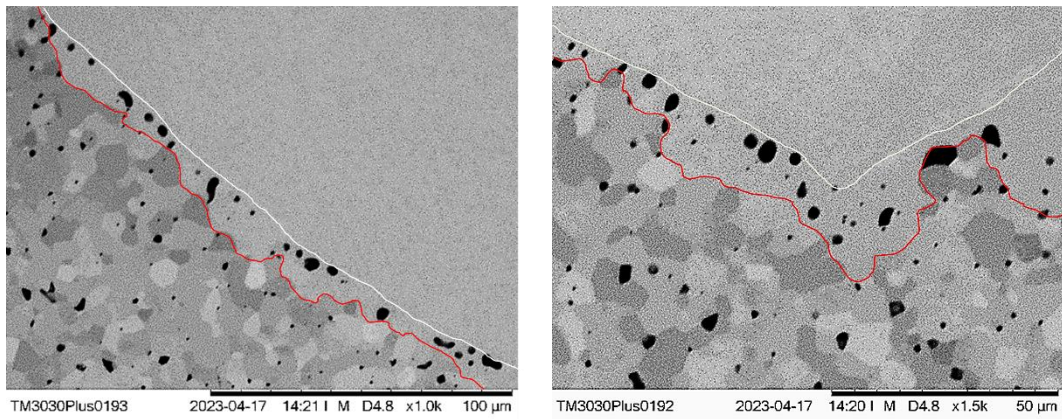


Figure 118. SEM images of single seed growth and polycrystalline matrix of sample PMN-PT with 0% excess lead oxide, sintered in the hot press and annealed for 100 hours at 1000 °C.

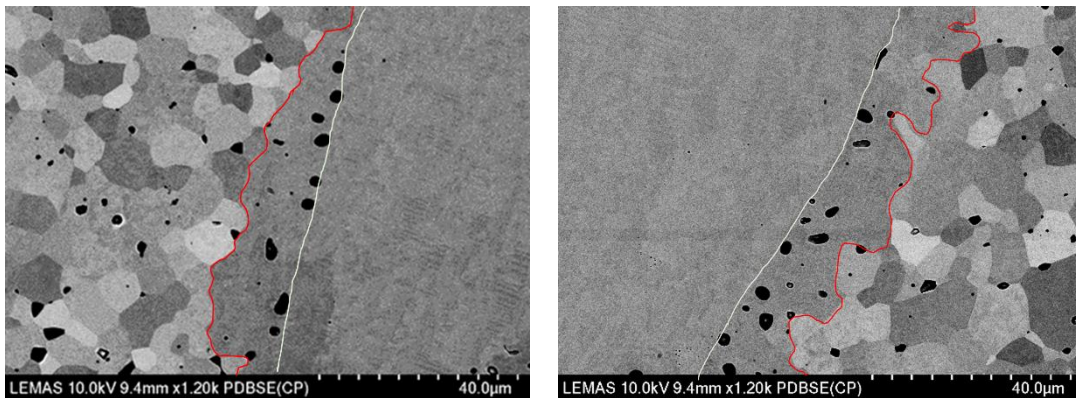


Figure 119. SEM images of single seed growth and polycrystalline matrix of sample PMN-PT with 0% excess lead oxide, sintered in the hot press and annealed for 100 hours at 1050 °C.

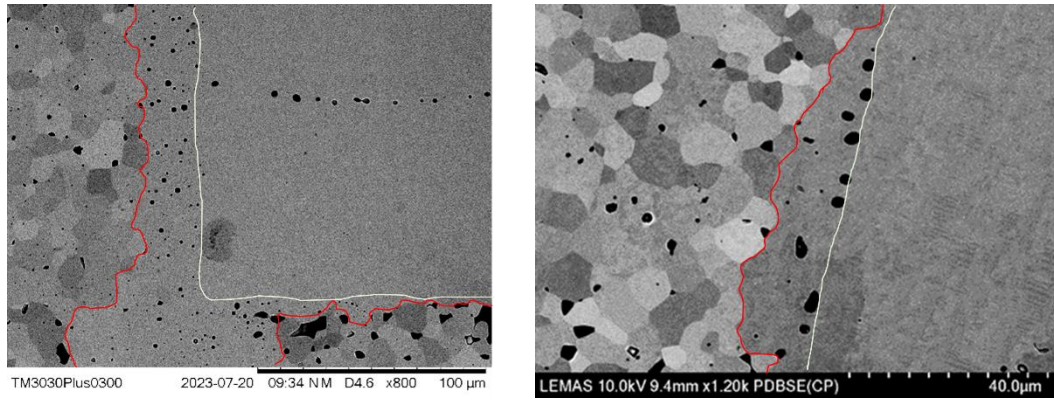


Figure 120. SEM images of single seed growth and polycrystalline matrix of sample PMN-PT with 0% excess lead oxide, sintered in the hot press and annealed for 100 hours at 1100 °C.

Some SSCG crystal growth is present in samples annealed at 950 °C, 1000 °C and 1050 °C (Figure 117, Figure 118 and Figure 119 respectively) but is very limited, all under 10 μm. However, growth is consistent around the whole seed. At 1100 °C the amount of growth increases to 38 μm, shown in Figure 120. The maximum amount of growth is seen at 1150 °C. Growth from the seed on average into the polycrystalline matrix reaches a value of 108 μm at this temperature. With the annealing temperature increasing again to 1200 °C the amount of growth exhibited from the seed is 79 μm, slightly less than the value observed at 1150 °C.

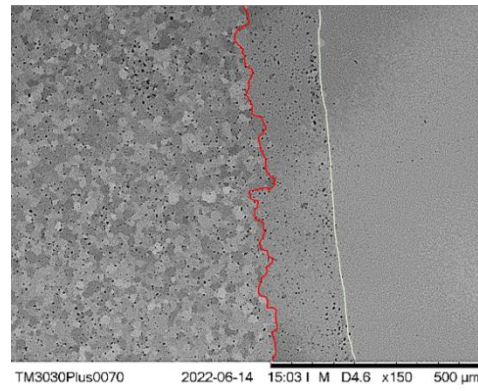
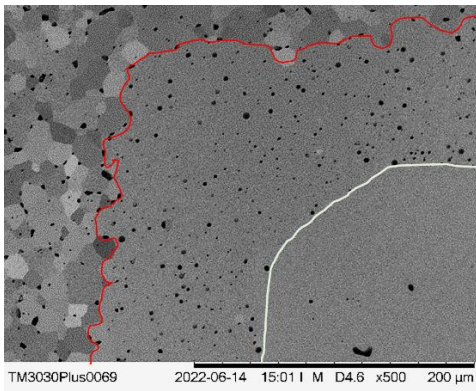
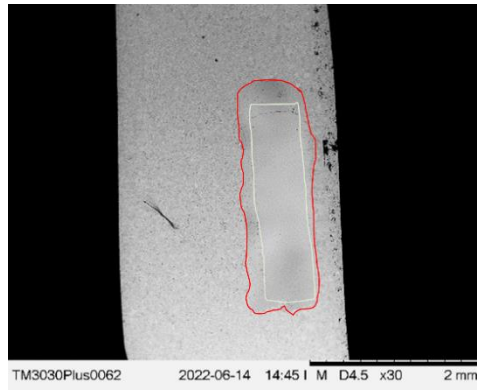


Figure 121. SEM images of single seed growth and polycrystalline matrix of sample PMN-PT with 2% excess lead oxide, sintered in the hot press and annealed for 100 hours at 1150 °C.

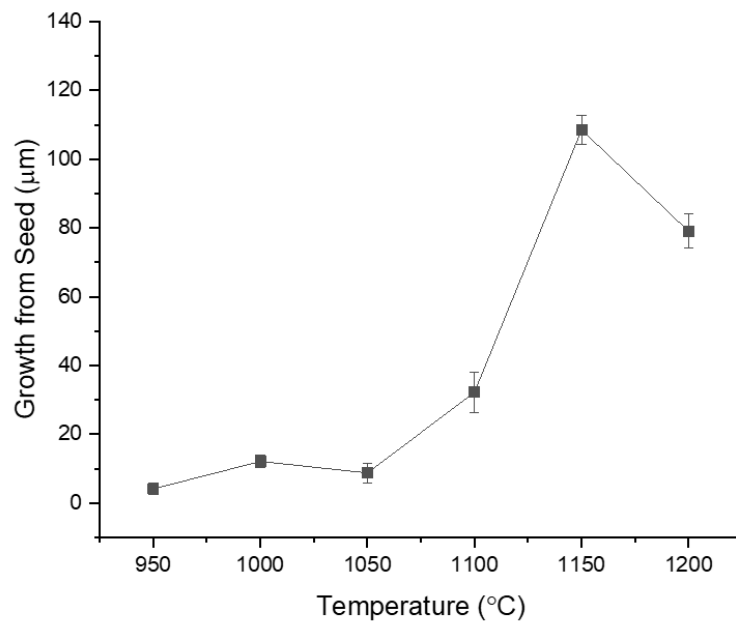


Figure 122. Summary of solid-state crystal growth experiments for stoichiometric PMN-PT. The average growth from seed is recorded for each of the PMN-PT samples with embedded PMN-PT seed. The samples are hot pressed and then annealed in a conventional furnace for 100 hours at varying temperature.

The average grain size of the polycrystalline matrix for each annealing temperature is also recorded in Figure 123. The average grain size did not increase substantially until a temperature of 1150 °C was reached. The grain size increased from approximately 10 μm up to 18 μm and then a slight increase to 19 μm at 1200 °C. The spread of average grain size also appears to increase with annealing temperature according to Figure 123.

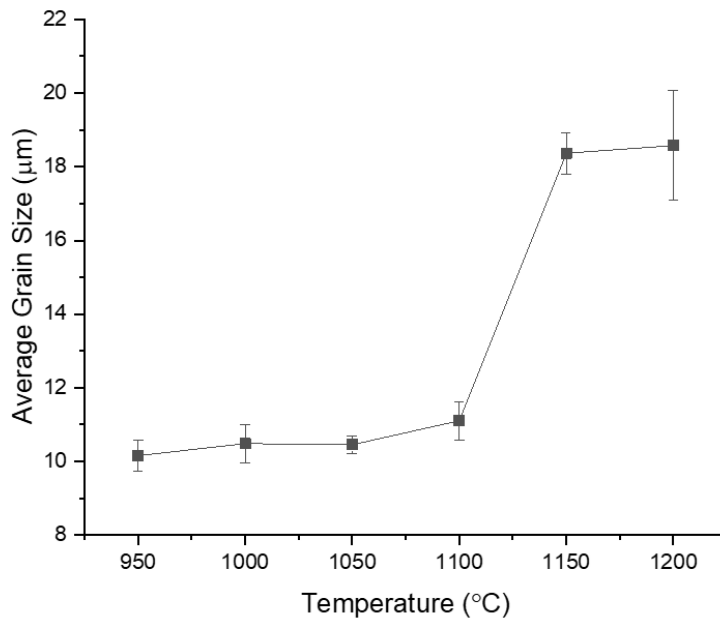


Figure 123. Summary of solid-state crystal growth experiments for stoichiometric PMN-PT. The average grain size is recorded for each of the PMN-PT samples with embedded PMN-PT seed. The samples are hot pressed and then annealed in a conventional furnace for 100 hours at varying temperature.

6.3.3.2 PMN-PT with 2% Excess PbO

The set of experiments performed in Section 6.3.3.1 were then replicated here with a PMN-PT matrix containing 2% excess PbO to produce liquid phase in the sample. The annealing times were again varied after hot-pressing had taken place with the 2% PbO excess PMN-PT and single crystal PMN-PT seed.

Figure 124 shows the hot-pressed polycrystalline PMN-PT with 2% excess PbO matrix. The average grain size of this pellet starts slightly lower than that of stoichiometric PMN-PT at 4.5 μm compared to 9.6 μm.

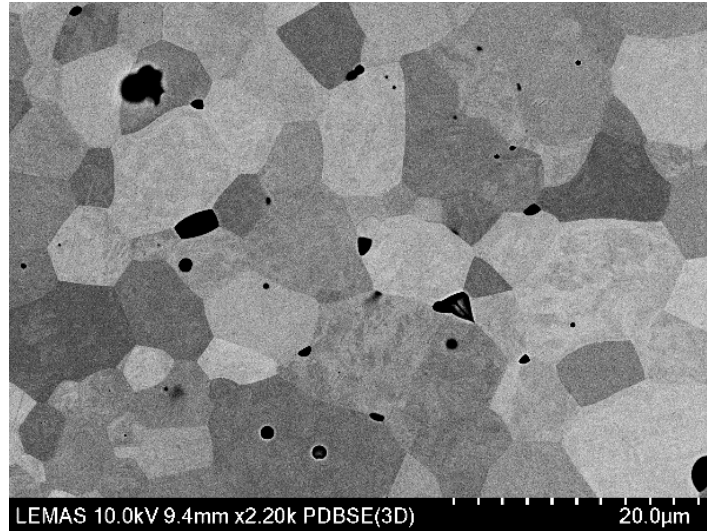


Figure 124. Microstructure of PMN-PT hot pressed pellet with 2% excess lead oxide,

Immediately at an annealing temperature of 950 °C there is substantial solid-state crystal growth of 86 μm had taken place, shown in Figure 125. The excess PbO and therefore larger amount of liquid phase increased the grain boundary mobility compared to the PMN-PT sample without excess PbO. Figure 126 shows SSCG of 93 μm obtained when the annealing temperature used was 1000 °C. The amount of growth from the single crystal seed peaks at 1050 °C, shown in SEM images in Figure 127 and graphically in Figure 130.

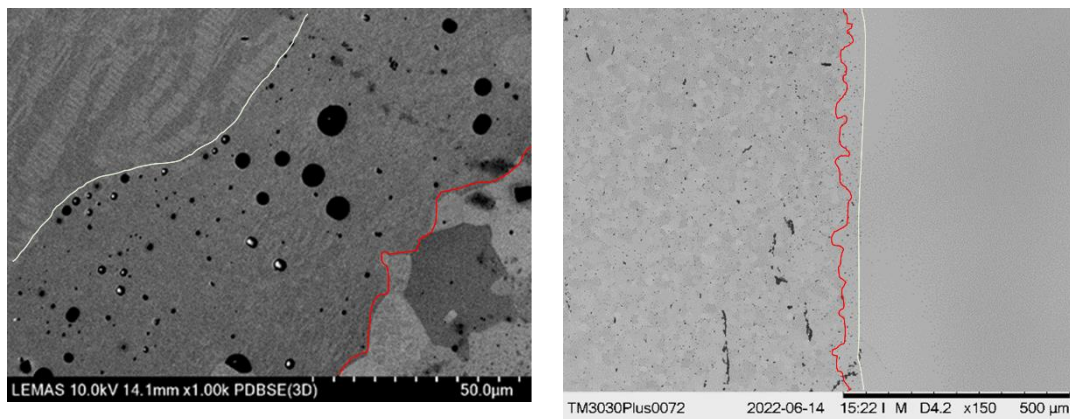


Figure 125. SEM images of single seed growth and polycrystalline matrix of sample PMN-PT with 2% excess lead oxide, sintered in the hot press and annealed for 100 hours at 950 °C.

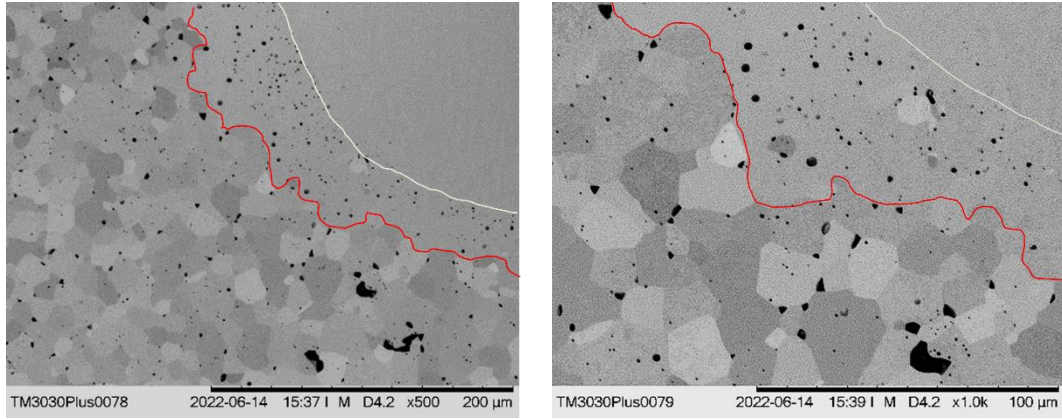


Figure 126. SEM images of single seed growth and polycrystalline matrix of sample PMN-PT with 2% excess lead oxide, sintered in the hot press and annealed for 100 hours at 1000 °C.

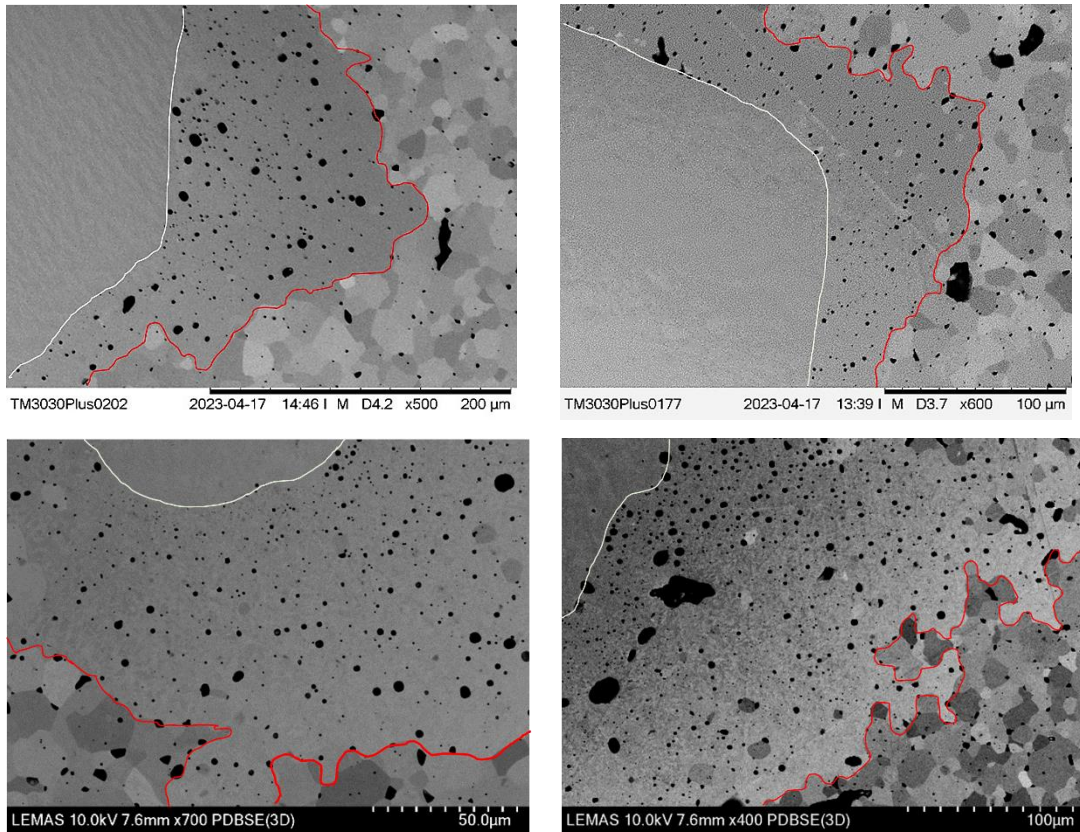


Figure 127. SEM images of single seed growth and polycrystalline matrix of sample PMN-PT with 2% excess lead oxide, sintered in the hot press and annealed for 100 hours at 1050 °C.

It can be seen in Figure 127 that a large amount of porosity is present in the grain growth area of the PMN-PT with 2% excess PbO samples. This is particularly visible in the large growth areas where the sample is annealed at 1050 °C. The porosity in the growth area is far higher than that of the polycrystalline matrix. This implies that porosity is forming as a consequence

of the growth of the single crystal seed and not simply originating from the polycrystalline matrix.

Figure 128 and Figure 129 still show SSCG evidence at higher annealing temperatures but the growth from seed is reported at only approximately 70 μm , much less than at 1050 $^{\circ}\text{C}$. Further increase in annealing temperature up to 1200 $^{\circ}\text{C}$ results in growth from seed of just 33 μm .

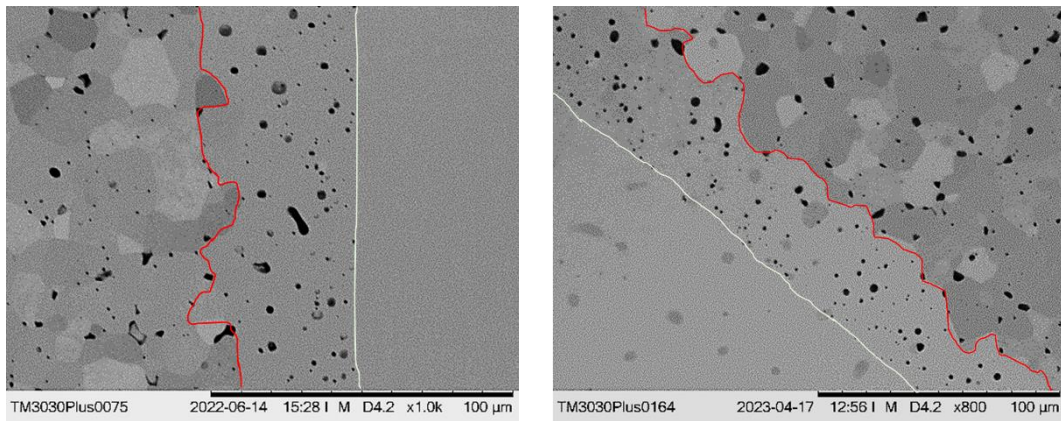


Figure 128. SEM images of single seed growth and polycrystalline matrix of sample PMN-PT with 2% excess lead oxide, sintered in the hot press and annealed for 100 hours at 1100 $^{\circ}\text{C}$.

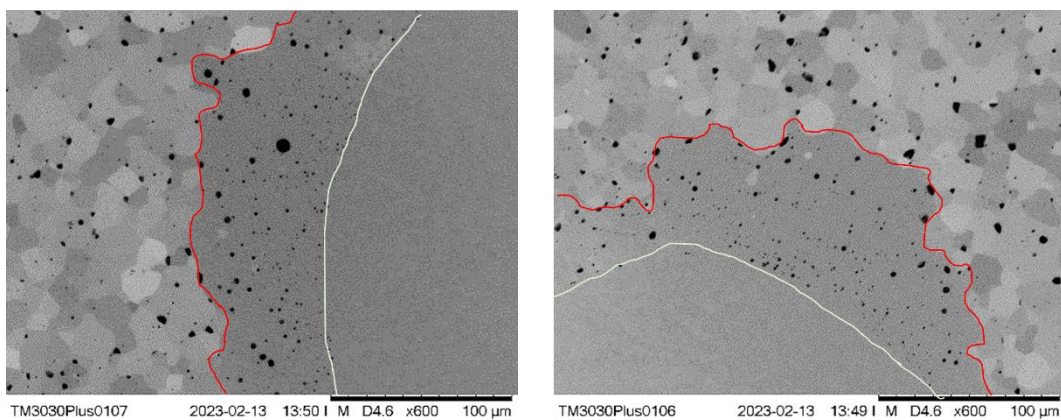


Figure 129. SEM images of single seed growth and polycrystalline matrix of sample PMN-PT with 2% excess lead oxide, sintered in the hot press and annealed for 100 hours at 1150 $^{\circ}\text{C}$.

Figure 130 and Figure 131 show the average growth from the seed and average grain size calculated for each annealing temperature respectively. It can be seen here that there is a peak of growth from the seed at annealing temperature 1050 $^{\circ}\text{C}$ at 156 μm . Growth from the seed as the annealing temperature continues to increase above 1050 $^{\circ}\text{C}$ but the rate is reduced. The lead loss experienced in the sample at higher temperatures is thought to be the cause of this.

Likewise for average grain growth at varying annealing temperature, there is steady growth up to 1050 °C and then a reduction in the average grain size after annealing at the higher temperatures.

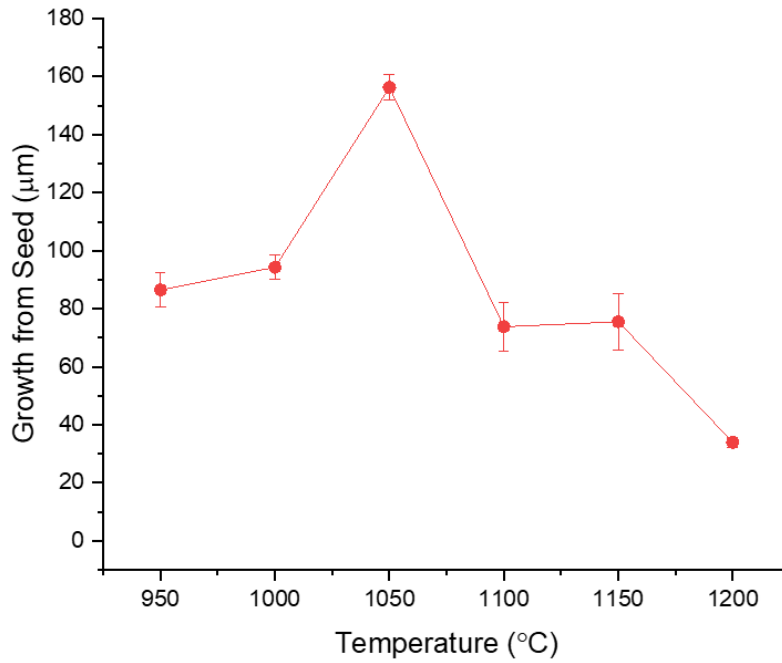


Figure 130. Summary of solid-state crystal growth experiments for PMN-PT with 2% excess lead oxide. The average growth from the seed is recorded for each of the PMN-PT + 2% PbO samples with embedded PMN-PT seed. The samples are hot pressed and then annealed in a conventional furnace for 100 hours at varying temperature.

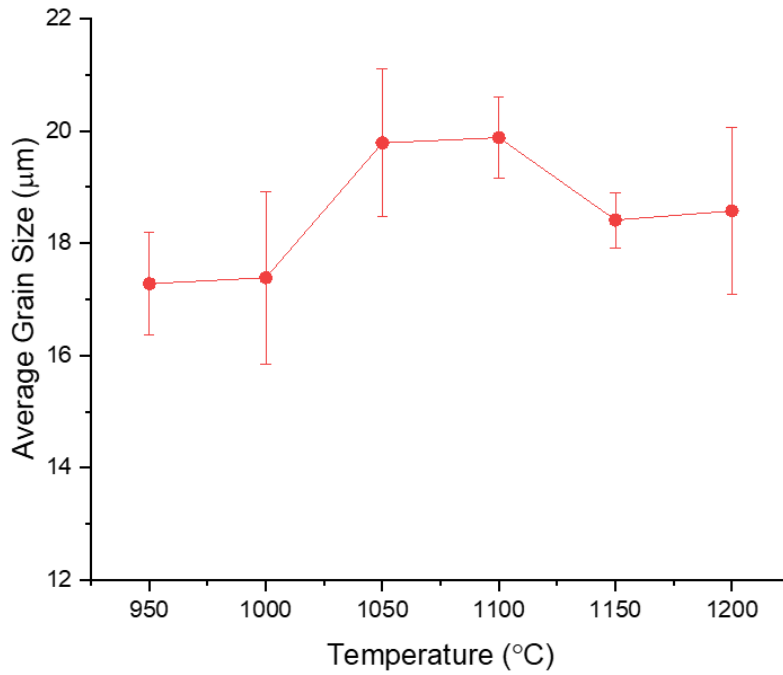


Figure 131. Summary of solid-state crystal growth experiments for PMN-PT with 2% excess lead oxide. The average grain size is recorded for each of the PMN-PT + 2% PbO samples with embedded PMN-PT seed. The samples are hot pressed and then annealed in a conventional furnace for 100 hours at varying temperature.

As stated previously one of the main advantages of the SSCG process is that the segregation of material is eliminated in this process, whereas in traditional methods, such as Bridgman, a concentration gradient throughout the grown crystal is formed. EDX was therefore performed on these areas of highest growth rate, annealed at 1050 °C, to analyse whether any segregation of ions throughout the growth area had occurred. The EDX results are presented in Figure 132.

There is no segregation apparent in Figure 132. The EDX compositional maps show an even spread of PMN-PT components across the seed, growth area and polycrystalline matrix.

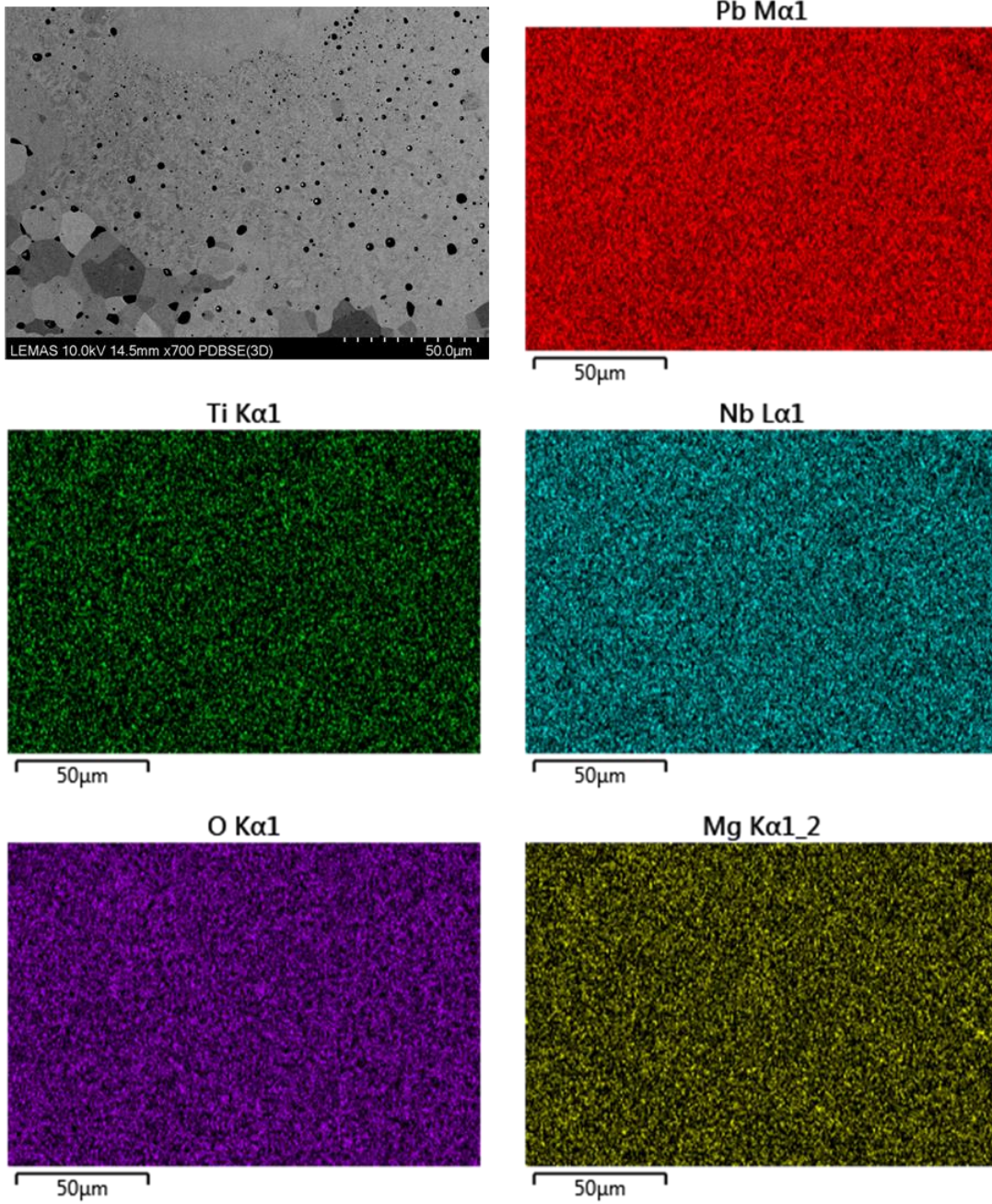


Figure 132. EDX analysis of single seed growth and polycrystalline matrix of PMN-PT sample with 2 % excess lead oxide, hot pressed and then annealed at 1050 °C for 100 hours.

6.3.3.3 PMN-PT with 5% PbO

The SSCG experiments with varying annealing temperature are replicated here with a PMN-PT matrix containing 5% excess PbO. The annealing times were again varied after hot pressing had taken place with the 5% PbO excess PMN-PT and single crystal PMN-PT seed. Figure 133 shows the microstructure of the PMN-PT sample with 5% excess PbO prior to hot pressing. The average grainsize was initially 6.8 μm .

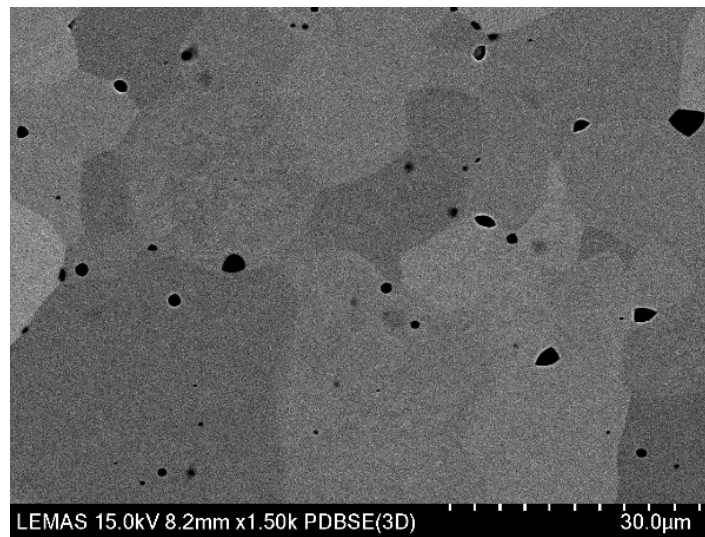


Figure 133. Microstructure of PMN-PT hot pressed pellet with 5% excess lead oxide,

Figure 134 and Figure 135 show the SEM images of growth from the seed obtained where the annealing temperatures used are 950 $^{\circ}\text{C}$ and 1000 $^{\circ}\text{C}$. The average amount of grain growth observed was 48 μm increasing to 99 μm at 1000 $^{\circ}\text{C}$.

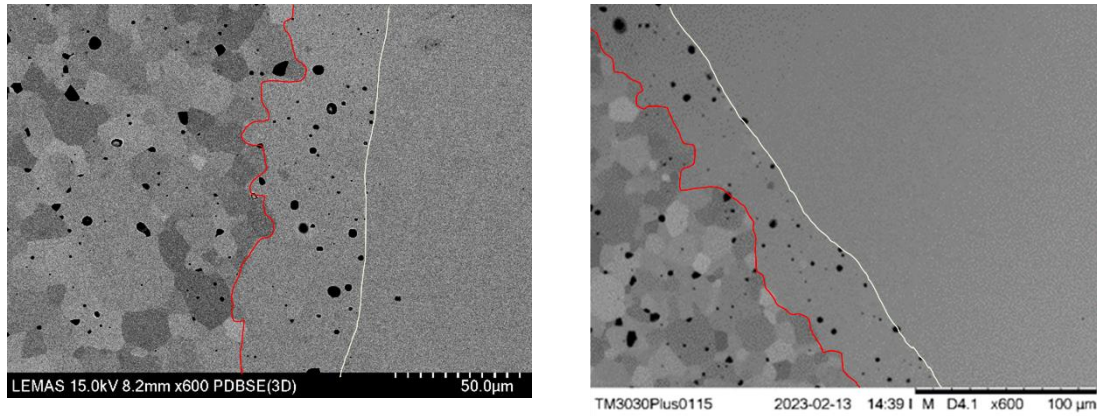


Figure 134. SEM images of single seed growth and polycrystalline matrix of sample PMN-PT with 5% excess lead oxide, sintered in the hot press and annealed for 100 hours at 950 °C.

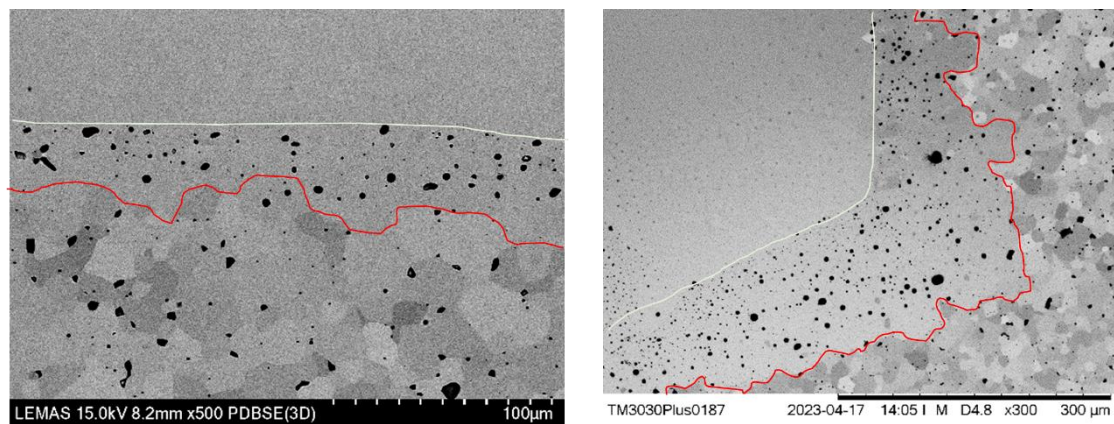


Figure 135. SEM images of single seed growth and polycrystalline matrix of sample PMN-PT with 5% excess lead oxide, sintered in the hot press and annealed for 100 hours at 1000 °C.

As in the PMN-PT samples with 2% excess lead, samples with 5% excess lead exhibited the most amount of growth from the crystal seed when annealing took place at a temperature of 1050 °C, as shown in Figure 136, where the growth from the grain reached 125 μm. The same phenomena of porosity appearing in the single crystal growth area is also apparent, as it was in the PMN-PT with 2 % excess lead. Again at temperatures higher than 1050 °C there was less growth observed from the single seed as shown in Figure 136 and Figure 137 and represented in Figure 138.

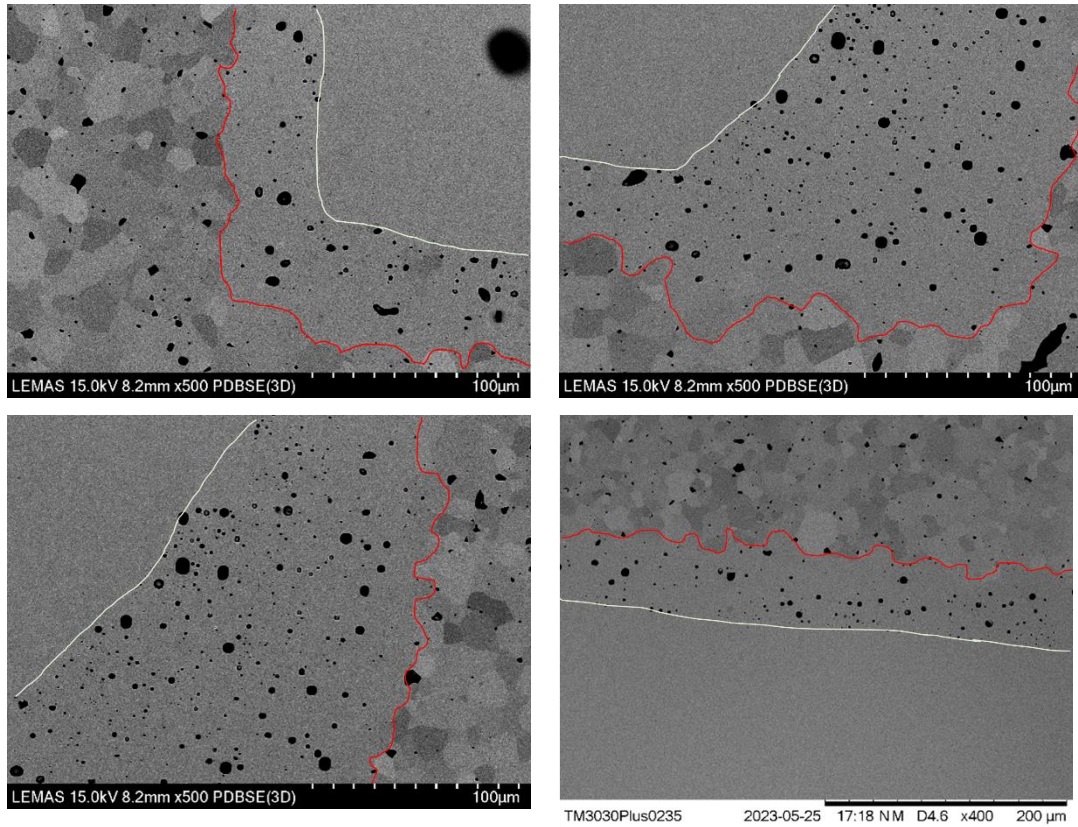


Figure 136. SEM images of single seed growth and polycrystalline matrix of sample PMN-PT with 5% excess lead oxide, sintered in the hot press and annealed for 100 hours at 1050 °C.

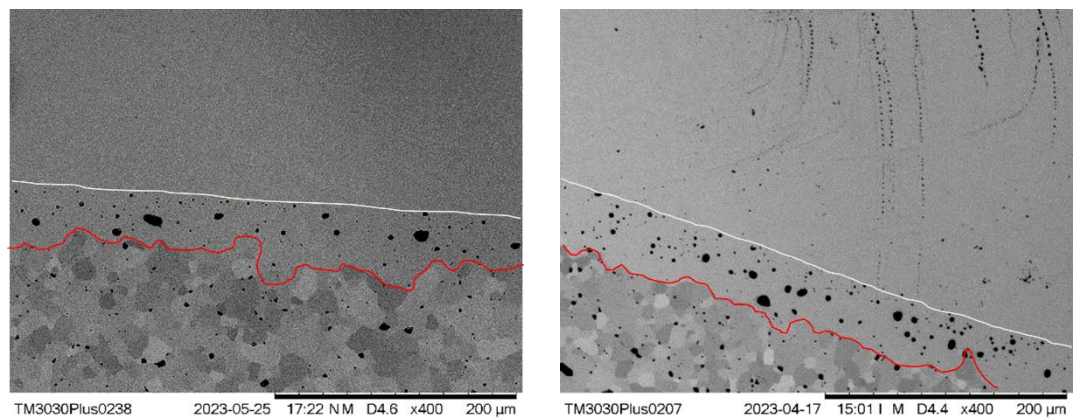


Figure 137. SEM images of single seed growth and polycrystalline matrix of sample PMN-PT with 5% excess lead oxide, sintered in the hot press and annealed for 100 hours at 1100 °C.

The average growth from the seed for each of the annealing temperatures has been reported in Figure 138 and average grain size is reported in Figure 139. The average growth from the seed shows a very similar pattern to the PMN-PT sample with 2% excess lead, with a clear peak in growth from the seed at 1050 °C. The average grain size appears to increase rapidly at 1000 °C increasing from 14 µm to 17µm and then plateauing between 17 and 18 µm. The standard

deviation of grain sizes calculated is also greater, implying that there is more of a spread of grain sizes within the matrix.

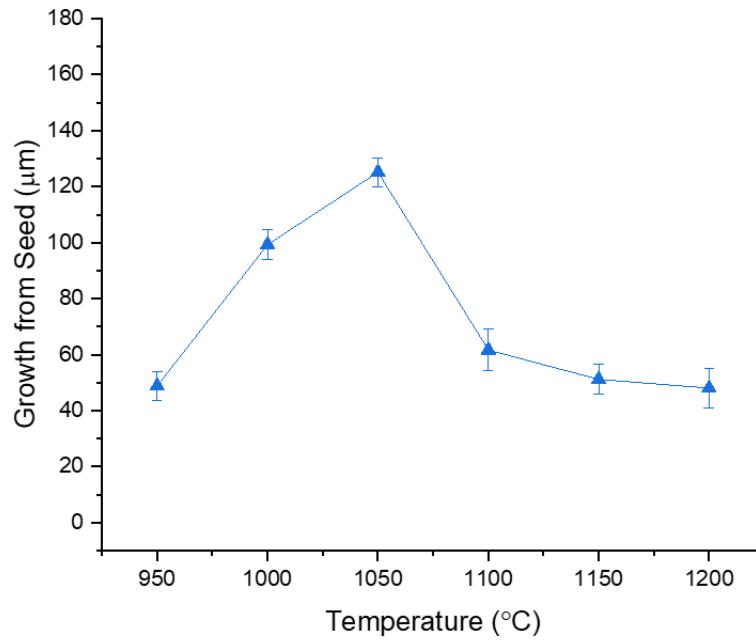


Figure 138. Summary of solid-state crystal growth experiments for PMN-PT with 5% excess lead oxide. The average grain size is recorded for each of the PMN-PT + 5% PbO samples with embedded PMN-PT seed. The samples are hot pressed and then annealed in a conventional furnace for 100 hours at varying temperature.

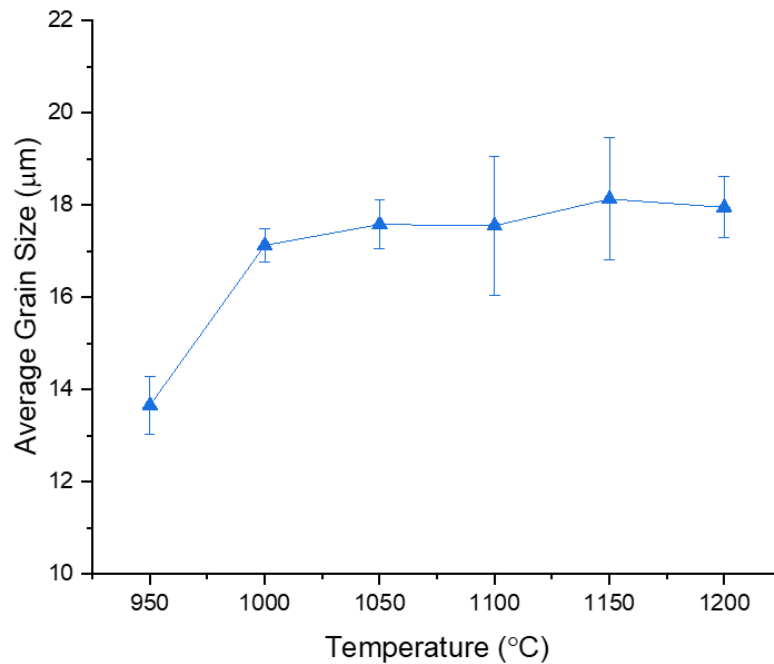


Figure 139. Summary of solid-state crystal growth experiments for PMN-PT with 5% excess lead oxide. The average grain size is recorded for each of the PMN-PT + 5% PbO samples with embedded PMN-PT seed. The samples are hot pressed and then annealed in a conventional furnace for 100 hours at varying temperature.

Again, EDX has been performed on the large growth areas to determine if any segregation has occurred within the growth area. It is clear from Figure 140 that this is not the case, there is an even spread of PMN-PT components throughout the seed crystal, growth area and matrix as expected.

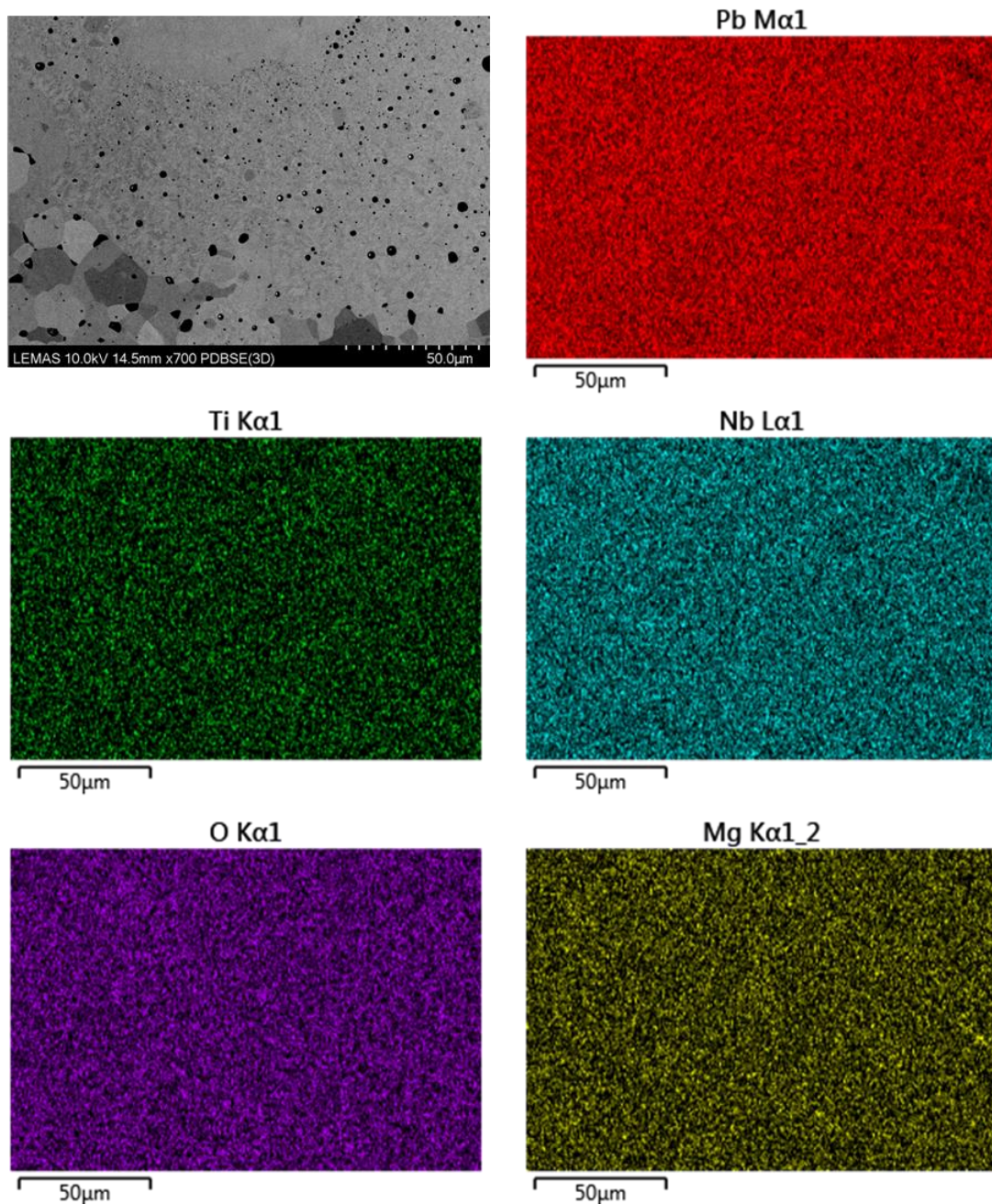


Figure 140. EDX analysis of single seed growth and polycrystalline matrix of PMN-PT sample with 5 % excess lead oxide, hot pressed and then annealed at 1050 °C for 100 hours.

6.3.3.4. Summary and Conclusions of Solid-State Crystal Growth Trials

The results from the SSCG experiments undertaken, where hot pressed pellets of PMN-PT containing 0%, 2% and 5% excess PbO have been further heat treated to induce SSCG at varying annealing temperatures. The amount of growth observed from the PMN-PT seed single crystal for each set of samples has been presented in Figure 141.

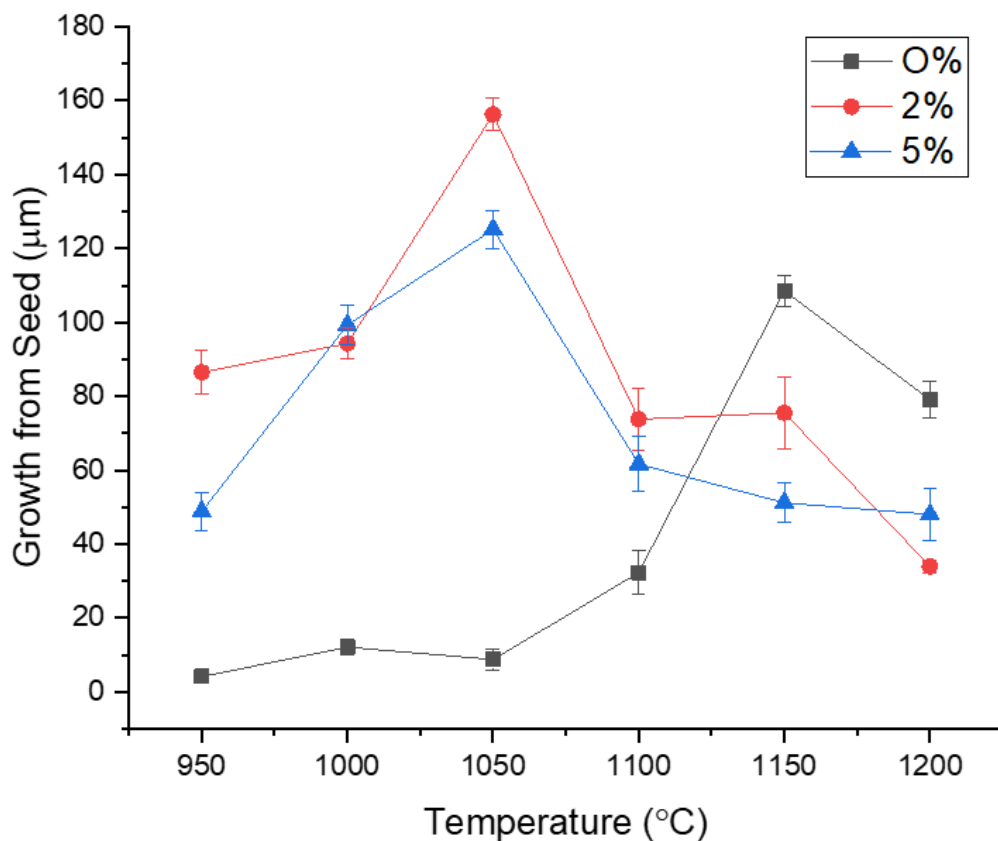


Figure 141. Summary of SSCG experiments showing growth from seed obtained at varying annealing temperatures for PMN-PT samples containing 0%, 2% and 5% excess PbO.

Solid-state crystal growth of a PMN-PT single crystal seed into a PMN-PT polycrystalline matrix has been achieved for samples containing 0%, 2% and 5% excess PbO. The maximum amount of crystal growth for each sample is shown in Table 12.

This rate of growth is reported after an annealing time of 100 hours, however in previous Section 6.3.2.2.1 it was estimated that the rate of growth from the seed is increased at the onset of annealing. For PMN-PT not containing excess lead, the growth rate from the seed at between

0-10 hours of annealing was approximately 3 $\mu\text{m}/\text{h}$. As previously discussed in Section 6.3.2.2.1 this is comparable to results achieved by Li et al (1998) who reported growth rate of 6 $\mu\text{m}/\text{hour}$ of PMN-35PT. Khan et al (1999) and Kim et al (2006) reported growth rates of 0.14 $\mu\text{m}/\text{hour}$ and 5-20 $\mu\text{m}/\text{hour}$ respectively for PMN-35PT. Higher growth rates were reported however by King et al (2003) of 20 $\mu\text{m}/\text{hour}$.

Table 12. Summary of grain growth from SSCG experiments.

Sample Excess PbO	Maximum growth from seed (μm)	Growth from seed standard deviation (μm)	Growth rate ($\mu\text{m}/\text{h}$)
0%	108.5	4.3	1.1
2%	156.3	4.4	1.6
5%	125.2	5.2	1.3

The addition of liquid film in the polycrystalline matrix by incorporating an excess of lead oxide in the samples is shown to increase the amount of growth achieved by the single crystal seed. It has been reported in other works such as King et al. (2003) that both the matrix and single crystal growth constants increased with increasing PbO content This was attributed to an increase in pore mobility, where in this PMN-35PT system pore drag inhibits grain growth. As the volume fraction of liquid was increased, it is believed that the pore surfaces became coated with a very thin liquid film, thereby allowing for a faster atomic flux and increased pore mobility (King et al, 2003).

It is also noted that the growth rate continued to increase with increasing film thickness (proportional to volume fraction) until an equilibrium thickness was reached, at which point the growth rate achieved a maximum value. For this study by King et al. (2003) it is also noted that the maximum growth rate achieved was at 3 mol % excess PbO. Khan et al. (1999) also report in their experiments that for PMN-35PT grown via SSCG, increased growth occurs due to boundary-wetting where the PbO-based phase increased boundary mobility considerably, and thus promoted single-crystal growth.

This is consistent with results displayed here, growth rate for the seed appears to be fastest in samples with 2% excess PbO. Samples with excess 5% PbO still exhibit a higher growth rate than those without excess PbO however not as fast as those with 2% excess PbO. This result

implies that the increased rate of mass diffusion has been accelerated by the liquid film, but as this film increases in thickness, the actual amount of distance travelled becomes limiting.

From the SEM images presented in Section 6.3.3 where SSCG is shown, the formation of porosity in the area of single crystal growth is prevalent particularly in samples with incorporated excess PbO. Li et al. (1998) also report pore formation in growth area of SSCG trials on PMN-35 PT system. They attribute a slowing in growth rate to pore coarsening, and compositional degradation during the anneal being responsible. This was also noted in the work by King et al. (2003), the cause of the large amount of porosity developed when PMN-35PT was said to be a consequence of series of complex phase transformations undergone by the PbO which result in the evolution of oxygen.

The results highlight in Figure 141 show that for samples of PMN-PT containing both 2% and 5% excess lead, grain growth from the seed is inhibited after 1050 °C. This is thought to be caused by excessive PbO volatilisation and loss from the system, resulting in a slower rate of mass transfer due to loss of liquid phase. Loss of PbO from the liquid film at grain boundaries may be resulting in pore formation as grain boundaries move.

For future work, an investigation into sintering in different atmospheres should be undertaken in attempt to control the amount of porosity formed during grain growth. Some progress in reducing porosity of PMN-32PT has been carried out by sintering in an oxygen atmosphere (Richter et al, 2009).

6.3.3.5 Arrhenius Calculations of SSCG Experiments

Progress of grain growth during isothermal annealing can be analysed using the general equation for grain growth and the Arrhenius Equation. This is shown in Equation (24), where d is the average grain size, n is the growth exponent (Stráská et al, 2015). The activation energy (Q) is then determined as the slope of dependence of $\ln(d^n - d_0^n)$ on $1/\text{temperature}$ (T).

$$d^n - d_0^n = k_0 \exp\left(-\frac{Q}{RT}\right) \quad (24)$$

This method of determining the activation energy for grain growth has been used previously in the by Stráská et al. (2015) where it was applied to annealed ultra fine grain magnesium alloy. The value of $n = 2$ was used in this study following on from model of normal grain growth and grain boundary migration. This has been found in Section 6.3.1.5 to hold true for the grain growth seen here in hot-pressed PMN-PT.

This is then applied to growth from the seed single crystal by assuming the initial grain size is equal to zero and the growth from the seed becomes the grain size after annealing has taken place.

The Arrhenius plot for PMN-PT sample without excess lead is shown in Figure 142. Where $\ln(\text{seed growth})$ is plotted against Temperature^{-1} . It can be seen here that there is a good linear fit to the results.

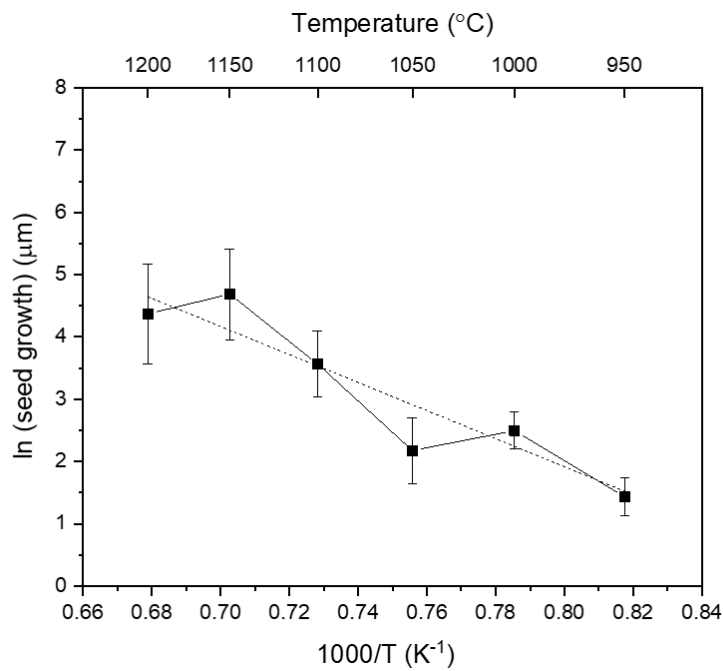


Figure 142. Arrhenius plot of seed growth obtained in stoichiometric PMN-PT solid-state crystal growth experiments.

The same analysis was plotted for the annealed samples containing 2% and 5% excess PbO. This is shown in Figure 143 and Figure 144 respectively.

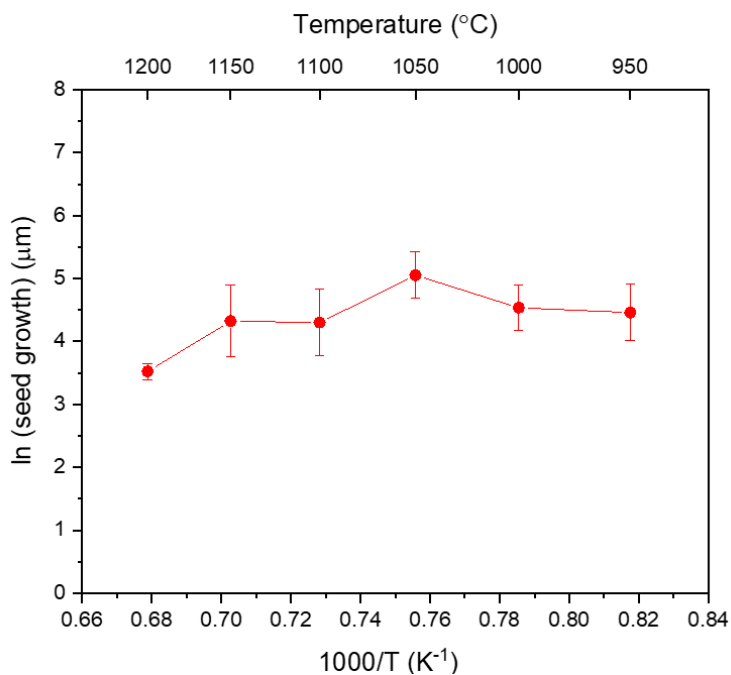


Figure 143. Arrhenius plot of seed growth obtained in stoichiometric PMN-PT with 2% excess PbO solid-state crystal growth experiments.

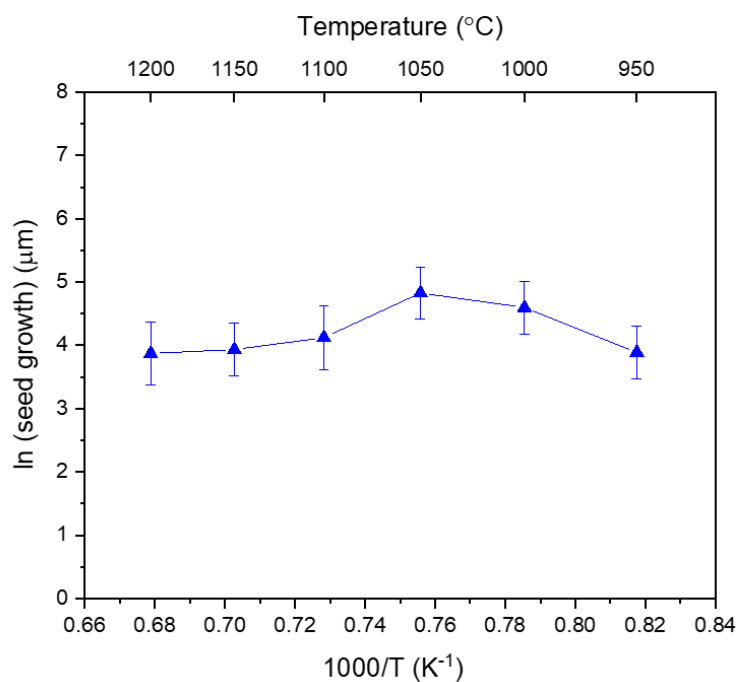


Figure 144. Arrhenius plot of seed growth obtained in stoichiometric PMN-PT with 5% excess PbO solid-state crystal growth experiments.

Initial inspection of Figure 143 and Figure 144 implies that these samples containing excess PbO do not appear to follow the Arrhenius law. There is no clear linearity across all

temperatures. However, it has been concluded in Section 6.3.3.4 that excessive lead loss in the 2% and 5% excess PbO samples when annealed at 1100°C and above severely restricts the single crystal growth process. If annealing temperatures above 1100 °C are considered to be un-effective for crystal growth and not included in the Arrhenius analysis, the resulting plot is shown in Figure 145.

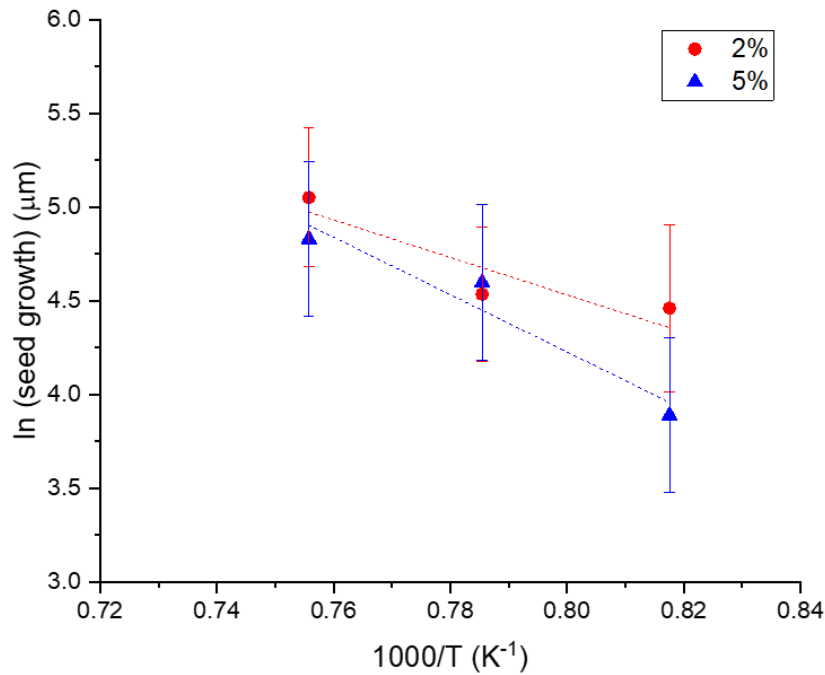


Figure 145. Arrhenius plot of seed growth obtained in PMN-PT with 2% and 5% excess lead oxide solid-state crystal growth experiments.

It is apparent in Figure 145 that there is Arrhenius behaviour occurring in the temperature range where growth from the seed is uninhibited by excess lead oxide loss (950 °C – 1050 °C). A linear fit can be applied here for the samples containing 2% and 5% excess PbO.

The values of activation energy of each PMN-PT sample containing 0%, 2% and 5% excess PbO are reported in Table 13. The activation energy for grain growth in the PMN-PT polycrystalline matrix has also been calculated again using Arrhenius Law. The gradient of $\ln(d^n - d_0^n)$, where ‘d’ is the average grain size after annealing and ‘d₀’ is the grain size of the hot-pressed samples prior to annealing, is plotted against 1/temperature (T). The activation energy calculated for grain growth for each set of PMN-PT samples, containing 0%, 2% and 5% excess PbO and is reported in Table 14.

Table 13. Calculated activation energy for single crystal growth from the seed for PMN-PT samples containing 0%, 2% and 5% excess PbO.

Sample excess PbO	Activation Energy (kJ/mol)	Error	R ²
0%	193.9	±6.3	0.86
2%	79.8	±7.3	0.83
5%	127.4	±6.4	0.93

Table 14. Calculated activation energy for polycrystalline grain growth rate for PMN-PT samples containing 0%, 2% and 5% excess PbO.

Sample excess PbO	Activation Energy (kJ/mol)	Error	R ²
0%	166.8	±9.2	0.62
2%	23.8	±5.3	0.76
5%	61.6	±6.3	0.83

Table 13 shows the calculated activation energy values for each PM-PT sample with various amount of excess PbO are all within the same order of magnitude and show a consistent pattern of results to that of the activation energy required for grain growth.

Table 13 shows that the value of activation energy calculated for each set of PMN-PT samples, is smallest where 2% excess PbO is present at 79.8 kJ/mol, followed by 5% excess PbO where activation energy is 127.4 kJ/mol and finally PMN-PT without the addition of excess PbO at 193.9 kJ/mol. This is consistent to the data shown in Table 14 where the activation for grain growth showed the same trend happening where $Q_{2\% \text{ excess PbO}} < Q_{5\% \text{ excess PbO}} < Q_{0\% \text{ excess PbO}}$.

It is clear that the presence of liquid film in the samples has increased the rate of atomic diffusion in samples containing 2% and 5% excess PbO. The activation energy for both single crystal growth and seeded growth is lower than that of PMN-PT with no excess PbO incorporated. The reason for the lower activation energy of 2% excess PbO compared presence of PbO liquid layer at 5% is that enough liquid phase is present to increase the atomic diffusion rate however the larger thickness of the film (at 5% PbO) may be inhibiting the rate of diffusion in absolute terms as there is more distance for the atoms to actually move between grains.

It would be tempting to conclude that when comparing Table 13 to Table 14 the higher activation energy between the growth from single crystal seed and activation energy of growth in the matrix implies that growth from the seed requires more energy and is hence more difficult to achieve. Grain growth in the matrix is always competing against growth from the single

crystal seed. There are too many unknowns at this point to definitively determine whether this is the case, more work should be conducted establishing k_0 constants and increase amount of data collected within the range of temperatures where Arrhenius behaviour is clearly exhibited.

6.3.3.5.1 Conclusions and Further Work of Arrhenius Calculations

It can be shown from this section of work that the PMN-PT samples do exhibit Arrhenius behaviour during annealing to induce single crystal growth. Samples sintered with excess PbO show Arrhenius behaviour at temperatures between 950 °C – 1050 °C, where there is not excessive lead loss from the system.

The activation energy for single crystal growth of PMN-PT is not reported in other literature. To give a comparison to other materials, BaTiO₃ grain growth activation energy has been reported as 19.7 kJ/mol (Clabel et al, 2021). The values of activation energy calculated here fall within the reasonably expected order of magnitude of grain growth and single crystal growth behaviour.

The activation energies calculated are consistent with a pattern established where $Q_{2\% \text{ excess PbO}} < Q_{5\% \text{ excess PbO}} < Q_{0\% \text{ excess PbO}}$ holds true for both single crystal growth from the seed and grain growth in the matrix. This has been explained by the presence of liquid film at the grain boundaries in samples containing 2% and 5% excess lead, but the thickness of the liquid film at 5% hindering mass diffusion due to the increased distance required for diffusion across the film.

6.3.4 Manganese Doped PMN-PT Solid State Crystal Growth

6.3.4.1 Introduction to Manganese-Doped PMN-PT Work

This section of work is intended to investigate whether the SSCG technique can be effective at inducing single crystal growth in manganese doped PMN-PT, which is not well documented in other literature. Manganese doped single crystals are of significant interest due to low mechanical loss properties and performance in high power applications. They are currently

limited to manufacture by modified Bridgman method (Luo et al, 2009). Melt-growth methods will always result in segregation of the manganese and so a concentration gradient is formed through the grown single crystal. SSCG could be used as an alternative to mitigate this problem.

Although commercial company Ceracomp offer mm size Mn-doped PMN-PT crystals grown by solid state crystal growth, any published works are limited to determining performance properties of the crystals, there is a significant gap in literature of processing manganese doped PMN-PT via SSCG method. This study was therefore carried out to determine the feasibility of SSCG method for production of Mn-doped PMN-PT.

In this study the manganese dopant is added to the stoichiometric PMN-PT powder at 2% by mass. Manganese is assumed here to substitute for $Mg_{1/3}Nb_{2/3}$. Deficiency of the $Mg_{1/3}Nb_{2/3}$ has been calculated to ensure the charge neutrality of the overall compound is maintained.

6.3.4.2 XRD manganese doped PMN-PT

The XRD spectrum shown in Figure 146 shows single phase perovskite structure with no significant impurities seen. This is XRD of calcined powder Mn-PMN-PT powder, no differences in peak position or splitting are seen when compared to stoichiometric PMN-PT.

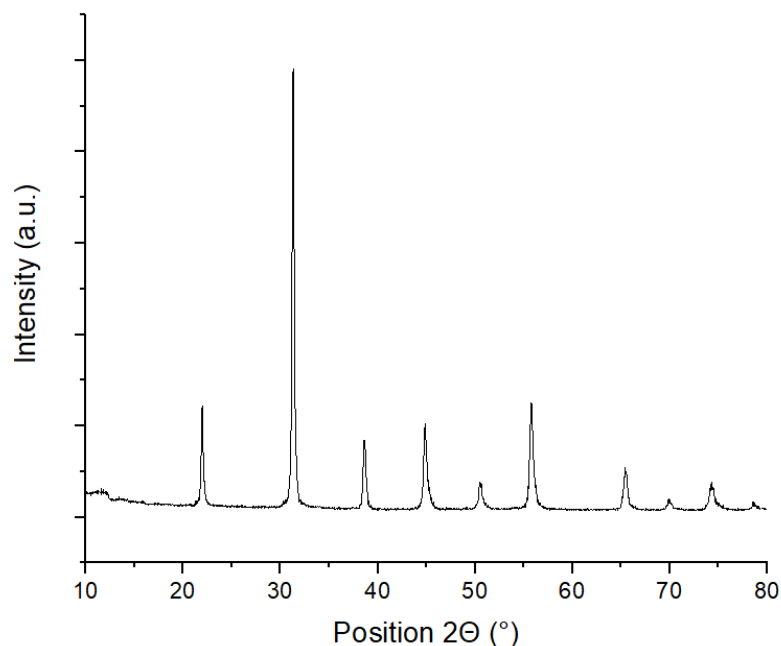


Figure 146. XRD Spectra of PMN-PT with 2% manganese doping.

6.3.4.3. Microstructure of hot-pressed manganese doped PMN-PT

The manganese doped PMN-PT powder was sintered in the hot press at 1150 °C. This temperature was selected as it was determined in Section 6.3.1.1 as the optimum sintering temperature for stoichiometric PMN-PT in the hot press. The green Mn- doped PMN-PT powders were seeded prior to sintering with a PMN-PT single crystal seed. This was kept the same as previous experimental procedures, the seed and green pellet were uniaxially cold pressed at 20 MPa for 5 mins with deionised water as a binder. They were then transferred to the hot press ceramic die, surrounded with yttria stabilised zirconia packing powder and loaded into the hot press for sintering.

Two different sintering pressures were used, 20.4 MPa and 40.8 MPa to determine what effect this would have on the microstructure of the sintered Mn-doped PMN-PT ceramics. After hot-pressing both samples were then annealed in a conventional furnace at 1150 °C for 100 hours to carry out solid-state crystal growth.

Figure 147 and Figure 148 show the microstructure of hot-pressed manganese doped PMN-PT samples both sintered at 1150 °C, at a pressure of 20.4 MPa and 40.8 MPa respectively. For both sintering regimes the ceramics produced were both in excess of 98.9% theoretical density (as shown in Table 15).

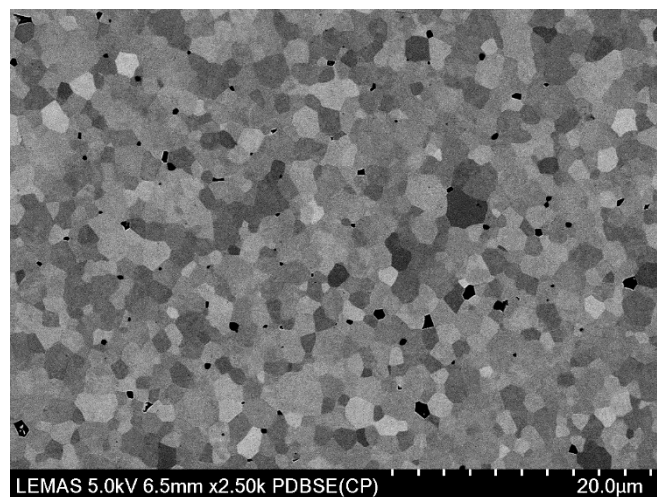


Figure 147. SEM image of polycrystalline matrix of Mn doped PMN-PT sample hot-pressed at 20.4 MPa and 1150 °C.

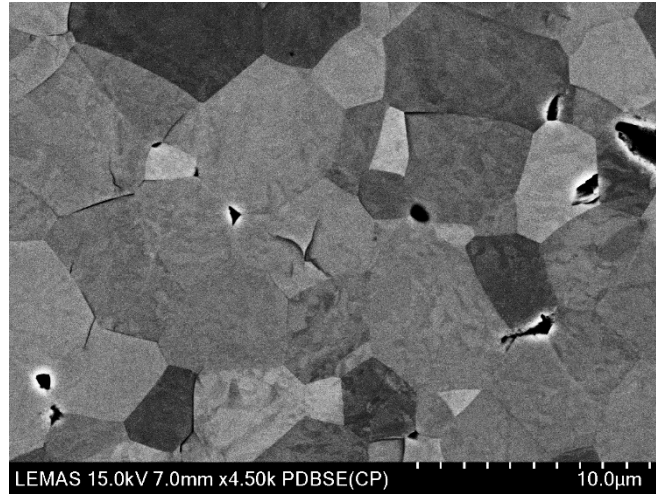


Figure 148. SEM image of polycrystalline matrix of Mn doped PMN-PT sample hot-pressed at 40.8 MPa and 1150 °C.

6.3.4.4 Solid-State Crystal Growth of Manganese-Doped PMN-PT

The manganese doped PMN-PT sintered ceramics were then annealed in a conventional furnace for 100 hours at 1150 °C. Figure 147 and Figure 148 show the grain growth achieved from this annealing process for 20.4 MPa and 40.8 MPa sintering pressure respectively. Here the white lines represent the boundary of the single crystal seed, and the red line indicates the boundary of the polycrystalline matrix. The area enclosed between the 2 lines is therefore the area of single crystal growth.

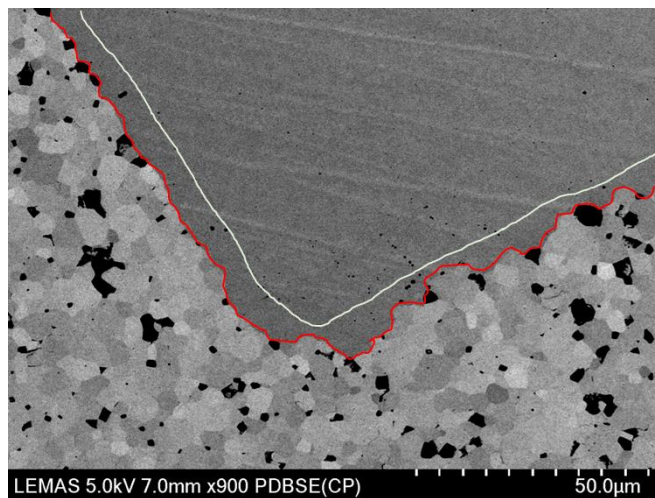


Figure 149. SEM image of solid-state crystal growth of Mn doped PMN-PT hot pressed at 20.4 MPa 1150 °C and annealed at 1150 °C for 100h.

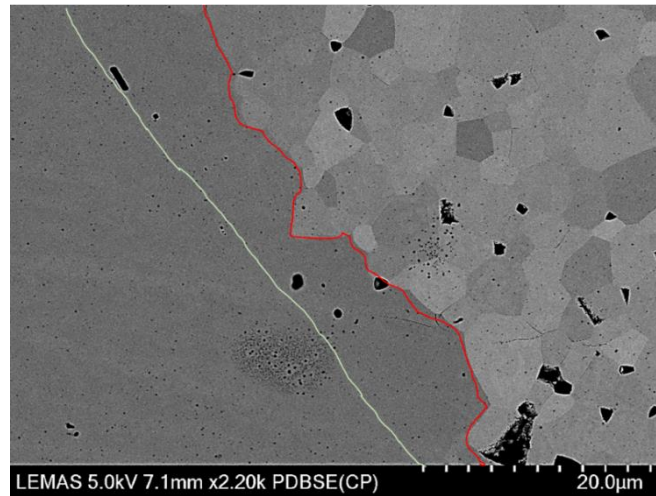


Figure 150. SEM image of solid-state crystal growth of Mn doped PMN-PT hot pressed at 40.8 MPa 1150 °C and annealed at 1150 °C for 100h.

This section of work was initially intended to be a feasibility study of SSCG of Mn-doped PMN-PT, which has been proved possible in the Figure 149 and Figure 150, where single crystal growth of up to ~25 μm is achieved.

From the SEM images shown in Figure 149 and Figure 150 it is apparent that there is much less visible porosity in the growth area than results shown in the previous section where undoped PMN-PT is studied (Section 6.3.3). This result is a significant finding regarding porosity reduction of the grown single crystal.

To explain the lack of porosity in the SSCG growth area it is suggested that if the Mn is incorporated with an average valence state of $<4+$ (assumed to be $2+$) then a likely compensation mechanism is the formation of excess oxygen vacancies. This facilitates an increase in oxygen diffusion in the matrix and thereby helps to eliminate the porosity in the grown area of the crystal.

A summary of the growth parameters of the Mn-doped PMN-PT samples are shown in Table 15. It can be seen here that the grain size of samples sintered at both sintering temperatures is comparable to that of stoichiometric PMN-PT previously presented.

Table 15. Summary of solid-state crystal growth trials for manganese doped PMN-PT samples.

Sample Property - Mn doped PMN-PT	10 kN		20 kN	
	Value	Standard Deviation	Value	Standard Deviation
% Theoretical Density	98.94	0.01	99.26	0.03
Average grain size pre annealing (μm)	3.02	0.44	5.70	0.39
Average grain size post annealing (μm)	6.36	0.47	6.87	0.40
Average growth from seed (μm)	5.92	2.34	6.91	1.91

The average growth from the seed is lower than that experienced by un-doped PMN-PT (Section 6.3.3). Growth of undoped samples reached a maximum of 108 μm after the same conditions in the hot press; 1150 °C and 40.8 MPa, and then annealing in a conventional furnace for 100 h at 1150 °C. The manganese doped sample however only exhibited growth from the seed of 7 μm in the same conditions, reducing the growth rate significantly. This is theorised to be because of the effects of solute drag mechanism, where interaction between the manganese and the grain boundary occurs, resulting in the segregation of manganese within the grain and changes of the spatial distribution of manganese on either side of the grain boundary incurring drag on the grain boundary (Powers and Glaeser, 1998). This drag force appears to reduce the amount of growth from the seed by such an amount that the amount of manganese present may be pinning the grain boundary.

6.3.4.5 EDX Analysis Manganese Doped PMN-PT

One of the advantages of using the solid-state crystal growth technique is chemical homogeneity of the grown crystal. To determine if this is the case EDX has been used to analyse the composition of the crystal seed.

From the EDX data in Figure 151, it can be seen that there is no compositional change between the seed crystal growth area and the polycrystalline matrix. Although the amount of

incorporated manganese is small enough to be missed by the detector, there is no evidence to show high concentrations of manganese at the interface which implies lack of manganese build up in the system.

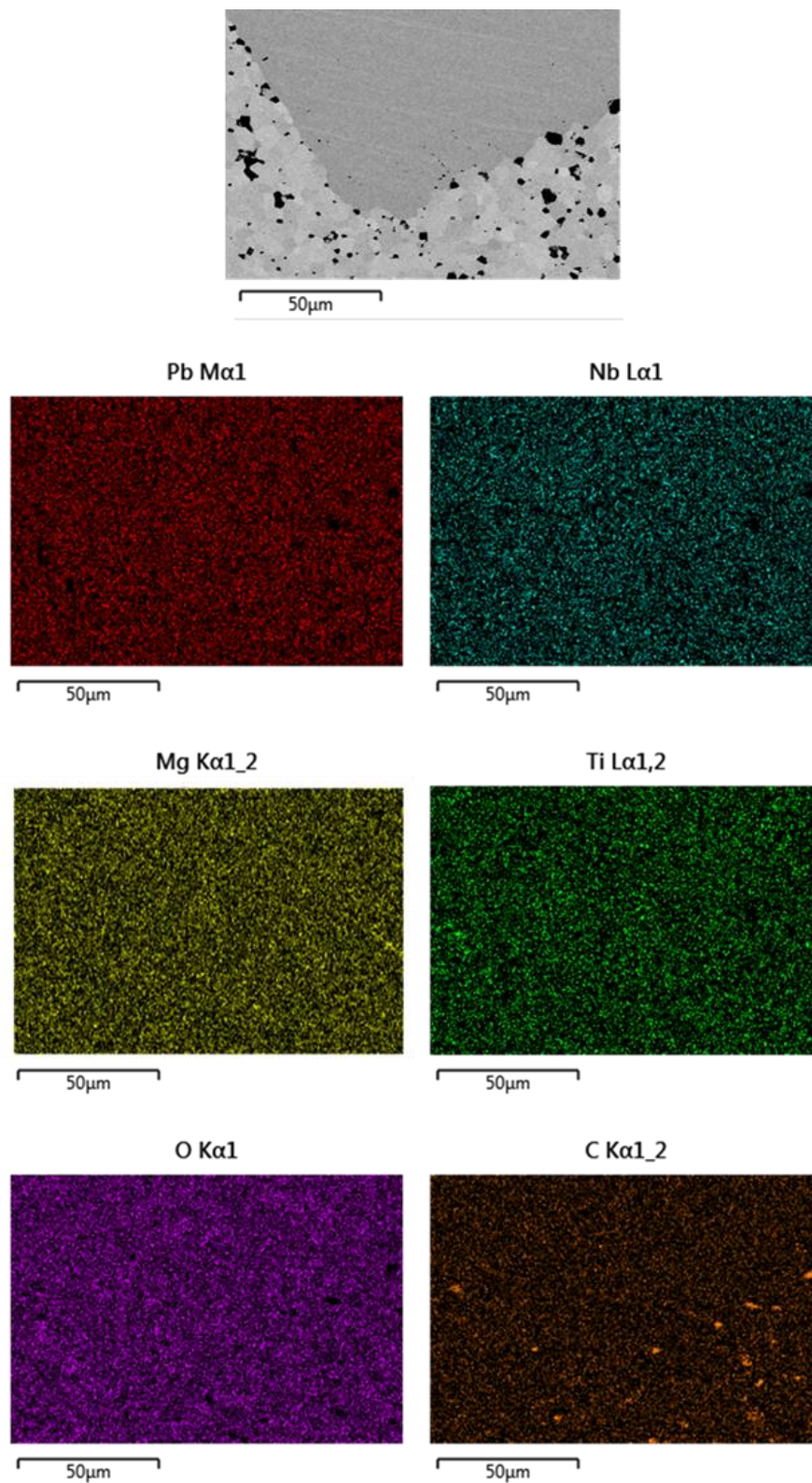


Figure 151. EDX analysis of manganese doped PMN-PT

6.3.4.6 Conclusions and Future Work of Manganese-Doped PMN-PT

This section of work has shown that it is indeed feasible to grow Mn-doped PMN-PT single crystals via the SSCG method. The rate of which growth from the seed occurred in this instance was seen to be lower than that of undoped PMN-PT. This is theorised to be caused by solute drag mechanisms acting within the PMN-PT matrix.

Interestingly, the manganese doping appears to have a profound effect on the porosity incurred in areas of solid-state crystal growth. The amount of porosity seen in the Mn-doped experiments is significantly lower than that of PMN-PT. This is suggested to be caused by the valence state of incorporated manganese being compensated by formation of excess oxygen vacancies, facilitating an increase in oxygen diffusion in the matrix and thereby helping to eliminate the porosity.

This interesting set of results forms an ideal basis for further work. Firstly, to accelerate growth rate, a higher temperature sinter and finer initial particle size should be used. Transmission electron microscopy would give more insight into the interface of the seed crystal to growth area and the growth area to the polycrystalline matrix. A series of experiments should also be conducted to investigate the growth rate of Mn-PMN-PT with annealing time to gain more knowledge in the nature of the growth mechanism. The role of atmosphere during the annealing of both doped and undoped matrices, including oxygen, nitrogen and argon atmospheres should also be analysed.

6.4 SSCG Summary and Conclusions

This section of work has given an in-depth study of solid-state crystal growth carried out in hot-pressed PMN-PT ceramics. The initial aim of this chapter was to establish the hot-pressing procedure by undertaking a series of experiments to establish the optimum sintering conditions to produce highly dense PMN-PT samples. Samples of highest density >99.9% theoretical density were produced in the hot press when sintered at 1150 °C and 40.8 MPa. This was then compared to a conventional sinter to highlight how hot-pressing could achieve higher density samples with smaller average grain size, producing ideal precursor materials for SSCG.

The implementation of excess lead oxide into the PMN-PT samples was also explored and a study conducted on single crystal growth achieved using liquid film enhanced sintering. Annealing studies on PMN-PT samples with and without 2% excess lead were carried out. It was seen that growth of the grains followed the parabolic growth law and liquid phase presence encouraged a faster rate of grain growth.

Solid-state crystal growth trials with single crystal seeding was then be explored. The seed embedding technique was first established, it was found that embedding the single crystal seed in the green powder compact gave much better contact between the seed and matrix grains. Barium titanate single crystal seeds, contrary to other works, were found to not induce any grain growth into the PMN-PT matrix. This was attributed to the formation of a secondary phase identified in texturing work (Chapter 7) resulting in inhibited grain growth.

PMN-PT single crystal seeding was shown to be effective at inducing solid-state crystal growth for hot pressed PMN-PT samples containing 0%, 2% and 5% excess lead oxide, growth of was seen of 108 μm , 156 μm and 125 μm respectively. These results were comparable with the growth rates calculated for 100 hours annealing to other works of SSCG of PMN-PT. It was shown that the growth rate was enhanced by liquid film presence, as seen in the literature, an addition of 2% excess lead was found to produce the highest rate of grain boundary mobility resulting in more grain growth.

Porosity was seen to form in the areas of single crystal seed growth, particularly in samples containing excess PbO. It was also noted that the growth of single crystal seed is inhibited after the annealing temperature surpasses 1050 °C for both samples containing excess PbO. This is thought to be caused by excessive PbO volatilisation and loss from the system, resulting in a slower rate of mass transfer due to loss of liquid phase. Loss of PbO from the liquid film at grain boundaries may be resulting in pore formation as grain boundaries move.

Arrhenius plots have then been produced to calculate the activation energy for single crystal growth of each PMN-PT composition as a function of annealing time. The value of activation energy calculated for each set of PMN-PT samples, is smallest where 2% excess PbO is present at 79.8 kJ/mol, followed by 5% excess PbO where activation energy is 127.4 kJ/mol and finally PMN-PT without the addition of excess PbO at 193.9 kJ/mol. This is consistent to calculated activation energy of grain growth which follows the same trend: $Q_{2\% \text{ excess PbO}} < Q_{5\% \text{ excess PbO}} < Q_{0\% \text{ excess PbO}}$.

Solid state crystal growth trials of manganese doped PMN-PT was then carried out to determine the feasibility of production of manganese doped PMN-PT in this way. Initial trials determined that solid-state crystal growth was evident in the samples, although at a slower rate than that of un-doped PMN-PT, attributed to solute drag inhibiting grain growth.

Interestingly it was also apparent that there is much less visible porosity in the growth area than un-doped PMN-PT. To explain the lack of porosity in the SSCG growth area it is suggested that if the Mn is incorporated with an average valence state of $<4+$ (assumed to be $2+$) then a likely compensation mechanism is the formation of excess oxygen vacancies. This may facilitate an increase in oxygen diffusion in the matrix and thereby help to eliminate the porosity.

6.5 SSCG Future Work

There are several opportunities for further work to improve the depth of this study. Firstly, conducting additional SSCG experiments to determine grain growth as a function of time would give better understanding of the grain growth mechanisms taking place in the PMN-PT samples. Also, additional annealing temperatures should be studied to improve the reliability of the Arrhenius work in determining activation energy.

There is great scope for carrying out SSCG experiments in different sintering atmospheres. In external work, some progress in reducing porosity of PMN-32PT by sintering in an oxygen atmosphere has already been seen. This would be particularly interesting to compare to the SSCG trials of PMN-PT with incorporated excess PbO in attempt to control the amount of porosity formed during grain growth.

Further work should be pursued in the manganese-doped PMN-PT section of this work. Transmission electron microscopy should be used to give more insight of the interface of the seed crystal to growth area and the growth area to the polycrystalline matrix. A series of experiments should also be conducted to investigate the growth rate of Mn-PMN-PT with annealing time to give more insight into the growth mechanism. The role of atmosphere during the annealing of both doped and undoped matrices, including oxygen, nitrogen and argon atmospheres should also be analysed.

The hot pressing and SSCG techniques investigated in this work could also be applied to other material formulations of interest including PIN-PMN-PT, PMN-PZT and samarium doped compositions.

Chapter 7 Texturing of Piezoelectric Ceramics using Uniaxial Hot-Press

7.1 Introduction

Crystallographic texturing of polycrystalline ceramics is a method of achieving significant enhancements in the piezoelectric properties. Templated grain growth (TGG) enables the fabrication of textured ceramics with single crystal-like properties. The intrinsically high cost and complexity of single crystal growth techniques has created significant interest in the processing and properties of textured piezoelectric ceramics as an alternative.

In principle, poled polycrystalline perovskites oriented in the [001] direction have nearly the same macroscopic symmetry as [001]-poled single crystals (Messing et al, 2001) and therefore textured ceramics with the same material anisotropy should have similarly high piezoelectric response of single crystals. Ceramics that show texture levels up to 90%, show significant enhancements in the piezoelectric properties relative to randomly oriented ceramics with comparable densities. Piezoelectric coefficients of textured piezoelectrics are from 2 to 3 times higher than polycrystalline ceramics and as high as 90% of the single crystal values. In textured PMN-PT, a low field (<5 kV/cm) piezoelectric coefficient (d_{33}) of ~ 1600 pC/N was obtained (Messing et al, 2001).

The TGG process is similar to that of solid-state crystal growth, where the TGG of textured materials takes advantage of the preferred growth of large particles, or seed crystal in the case of SSCG, oriented in a dense microstructure. When heated, the boundary between the single crystal template and the polycrystalline migrates into the matrix. The thermodynamic driving force for this boundary migration is driven by the reduction of overall free energy in the system. In almost all cases of TGG, the kinetics of boundary migration is increased by purposely introducing a grain boundary liquid (Seabaugh et al, 2000).

To fabricate textured materials, larger template particles are dispersed in a matrix of relatively finer grains. Initially, the template particles are randomly oriented but are then aligned during processing. To facilitate orientation by shear forming techniques such as tape casting and extrusion, the template particles should be anisometric (Seabaugh et al, 2000). The template

particles must also have a lattice parameter similar to that of the matrix grains and sufficient thermal stability to withstand the growth process; and remaining inert in the presence of liquid phase to prevent formation of secondary phases decreasing growth rate. Growth can also be slowed by impingement of growing templated grains.

Several processing routes have been shown to induce texture development in ceramics. Shear forming of slurries that contain anisotropically shaped seed templates, results in highly oriented green bodies that produce strongly textured electronic ceramics and composite materials when sintered (Watanabe et al, 1989). Shear forming processes such as tape casting and extrusion are generally used in the processing of textured ceramics to induce orientation in the anisometric seed particles. The TGG process is shown schematically in Figure 152.

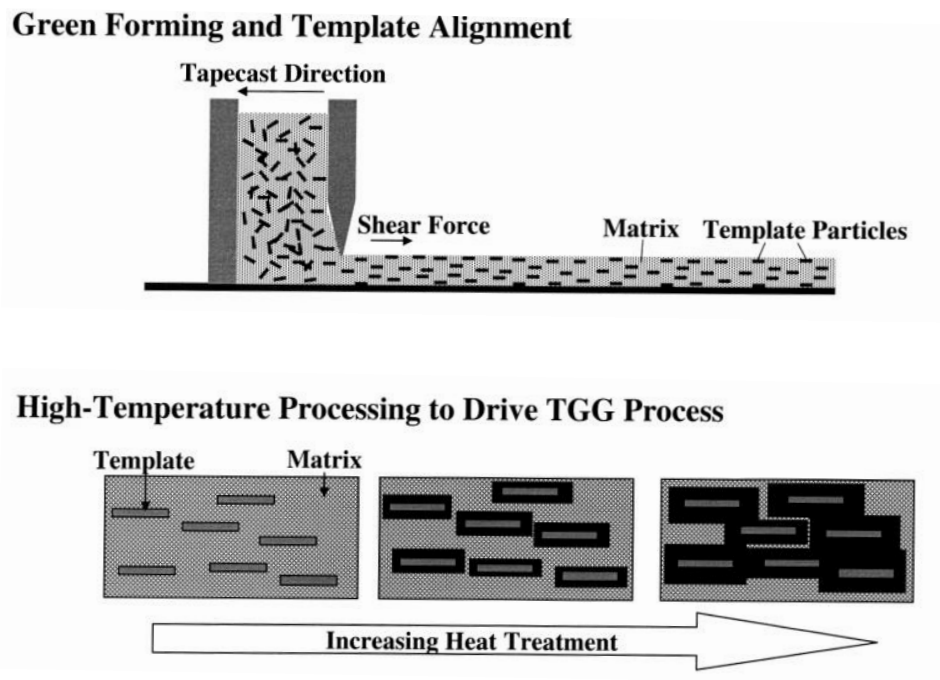


Figure 152. Schematic of template alignment by tape casting and the texture fraction increase with heating. (Messing et al, 2001).

This piece of exploratory work was conducted to determine the feasibility of hot-pressing PMN-PT and BaTiO₃ piezoelectric ceramics as a means of texturing, without the use of a shear forming stage.

7.2 Experimental Procedure

This section of work details the experiments undertaken to evaluate the effectiveness of hot-pressing as a means of producing textured piezoelectric ceramics. Anisometric platelets are used as the seed growth templates, these are orientated in the polycrystalline body using the uniaxial pressure generated by the hot press.

BaTiO₃ platelets are incorporated into green ceramic powders at varying volume percentage, from 5-15 %. In the first set of experiments PMN-PT is used as the ceramic powder, as prepared according to Section 4.2. To accelerate grain growth, an excess of 2% by mass lead oxide has been added to the powders prior to hot pressing.

The BaTiO₃ platelets are incorporated into the ceramic powder by manual stirring. As the pellets are much larger with greater mass compared to the individual ceramic particles, segregation issues are prevalent with other mixing methods. Ball milling in this case is unsuitable as the high shear will damage the BaTiO₃ platelets. As the platelets anisometric property controls their ability to orientate under pressure, this high energy mixing method is too destructive to use. Platelets are therefore incorporated manually with a spatula with continuous stirring for 5 mins.

After the pellets are incorporated, they are cold uniaxially pressed at 20 MPa for 5 mins to form pellets which can then be transferred to the hot press ceramic die for loading into the hot press. This is carried out as explained in Section 4.3.2 where the sample pellet is surrounded by yttria stabilised zirconia packing powder to protect both the pellet and die, and to distribute pressure evenly to the sample.

Samples are then sintered in the hot press at 1150 °C at a pressure of either 20.4 or 40.8 MPa. A full summary of the experimental procedure is outlined in Section 4.4.

7.2.1 Barium Titanate Platelets

The barium titanate platelets sourced from Entekno Materials, (Eskisehir, Turkey) are shown in Figure 153, this image highlights the anisometric shape of the platelets. The platelets are barium titanate material with a quoted value of up to 10% bismuth impurity.

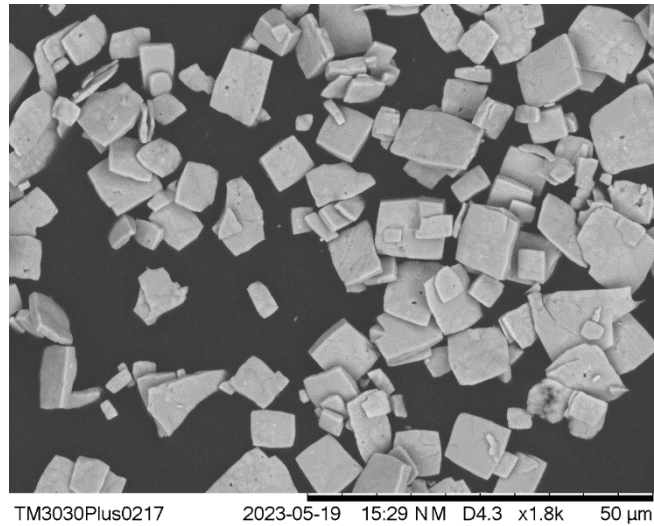


Figure 153. Barium titanate platelets.

7.2.1.1 Platelet Particle Size

Using the SEM images, the average size of the BaTiO₃ platelets has been determined. The average length, in this case defined as the longest length of flat surface of the platelet, was found to be 7.5 μm with a standard deviation of 2.81 μm. The thickness of the platelets was found to be 0.6 μm with a standard deviation of 0.12 μm. The aspect ratio of the platelets, defined as the ratio of the longest length: the thickness of the platelets, is an average of 12.5:1. Figure 154 shows SEM images displaying platelet shape and size and a summary of the determined values are displayed in Table 16.

Table 16. Summary of barium titanate platelet properties.

Dimension	Value (μm)	Standard Deviation (μm)
Size (characteristic length)	8.5	±2.8
Aspect Ratio (long length: thickness)	12.5:1	12.5 (±5.4) :1

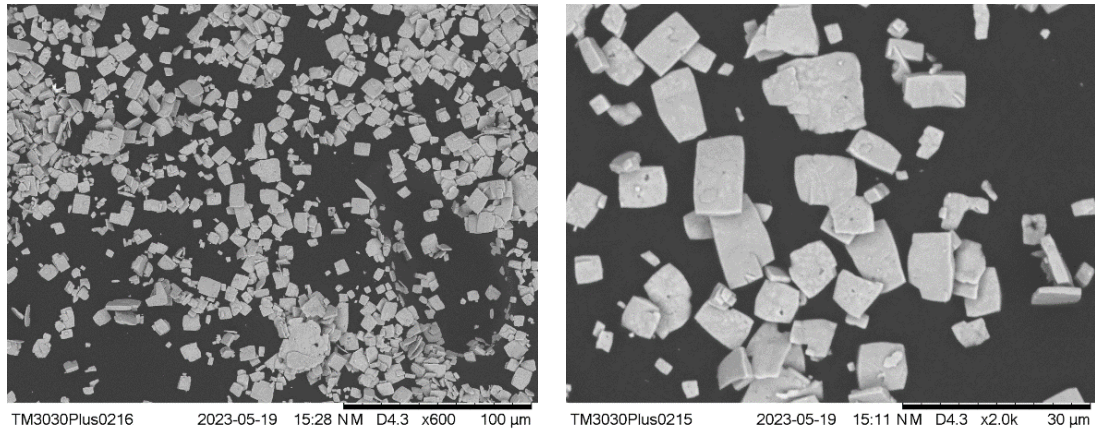


Figure 154. SEM image of barium titanate platelets used in texturing process.

As shown previously for the growth of single crystals by templated grain growth, matrix grain growth can reduce the thermodynamic driving force enough that template growth stops. A large size difference between the template particles and matrix grains is therefore preferred (Seabaugh et al, 2000).

7.2.1.2 XRD Analysis of Barium Titanate Platelets

The platelets were also characterised using XRD, this is shown in Figure 155. The XRD confirms the perovskite phase of BaTiO_3 platelets. The small impurity peak at $2\theta = 27$ is due to impurity content of Bismuth, this peak is characteristic of bismuth oxide in form Bi_2O_3 (Niveditha and Sindhu, 2015).

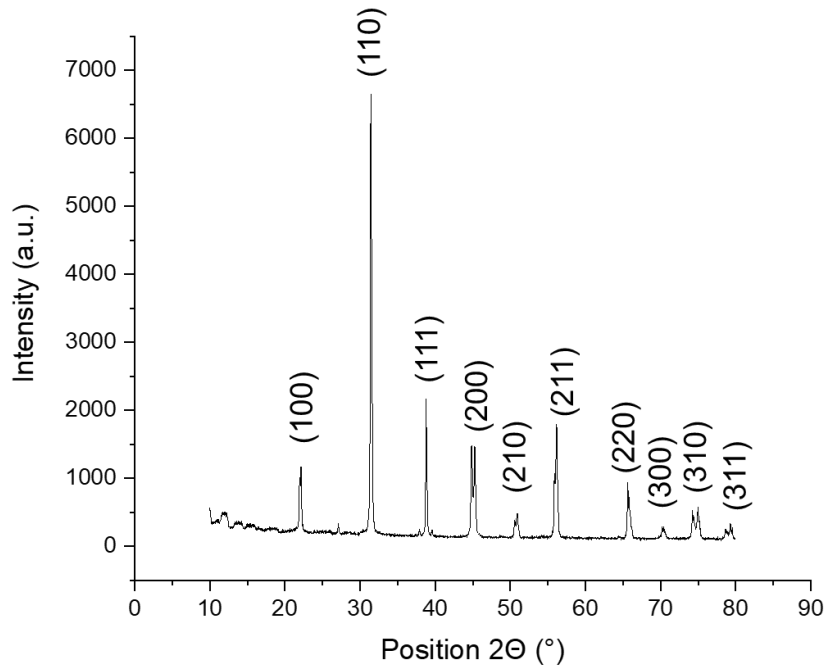


Figure 155. XRD spectra of barium titanate platelets.

7.2.1.3 Volume Fraction of Platelets

The volume fraction of barium titanate templates to be incorporated into the ceramic powder for these experiments was based on the literature survey conducted. In the work by Messing et al (2001), the function of volume percent templates for a range of template sizes for 100% textured material is calculated theoretically. To estimate the effect of template size and concentration on microstructure during texturing, the average centre-to-centre distance for neighbouring template particles, based on template loading and size, is calculated according to Equation (25) (Messing et al, 2001).

$$x_T = \left(\frac{6}{\pi f_T} \right)^{1/3} \quad (25)$$

Assuming complete growth of a textured material, the final grown grain size will be the same as the spacing of templates X_T , which depends on the number frequency of the templates f_T . Figure 156 then shows the templated grain size for a 100% textured material as a function of volume percent templates for a range of template sizes.

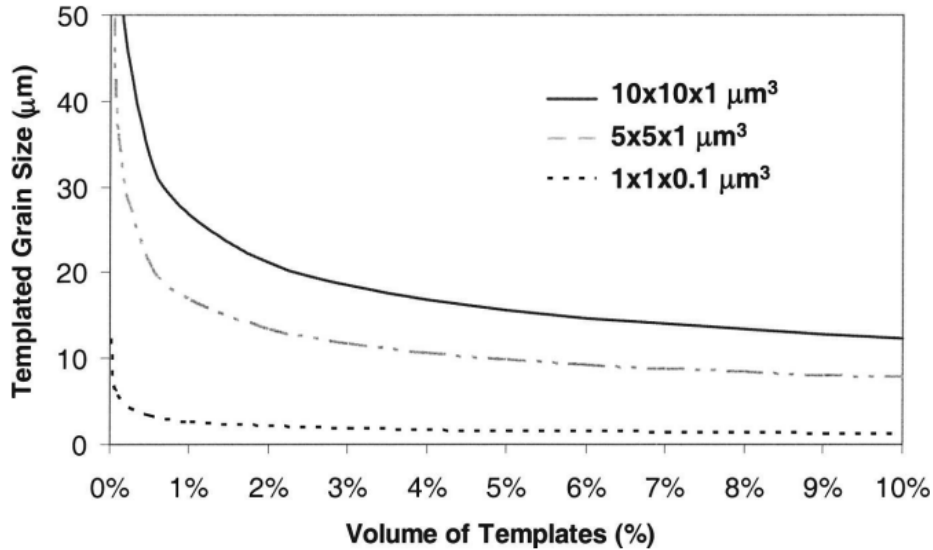


Figure 156. Calculated templated grain size as a function of template concentration and template size for a 100% textured material.

7.2.2 Material Characterisation

The materials characterisation techniques used in this section are SEM, EDX and XRD. These techniques are explained in detail in Sections 4.5.4, 4.5.5 and 4.5.2 respectively. Textured samples are taken from the hot-press and prepared for analysis by cutting into sections, as shown in Section 4.5.4.3, setting in resin and polishing according to Section 4.5.4.2.

7.2.2.1 Lotgering Factor

Further analysis using XRD spectra is used in this section of work to quantify the amount of orientation in the produced textured pellets. The Lotgering Factor (LF) is a simple method used to calculate the degree of orientation in a sintered ceramic by comparing relative peak densities of the resulting XRD spectrum. This uses the assumption that changes of the relative intensity of Bragg peaks are the result of a preferred grain alignment. The Lotgering Factor is calculated using this relationship Equation (26) and Equation (27) (Francher, 2021). Where P denotes the fraction of the summation of the peak intensities corresponding to the preferred orientation axis (001), to that of the summation of all diffraction peaks in oriented materials. P_0 is P of a

material with a random particle distribution. The LF varies between 0 and 1; LF = 0 corresponds to random orientation, and LF = 1 to perfect orientation. (Furushima et al, 2010).

$$LF_{(001)} = \frac{P_{(001)} - P_0}{1 - P_0} \quad (26)$$

$$P_{(001)} = \frac{\sum I_{(001)}}{\sum I_{(hkl)}} \quad (27)$$

$$P_{(0)} = \frac{\sum I_{0(001)}}{\sum I_{0(hkl)}}$$

7.3 Results and Discussion

7.3.1 PMN-PT Texturing

The first set of results show the SEM images of textured PMN-PT ceramic with BaTiO₃ platelets. The pellets were produced with 10% volume platelets of BaTiO₃, and hot-pressed at 1150 °C 20.4 MPa. Images have been taken on the surface of sample normal to pressure and as a cross section aligned with the pressure axis as shown in Figure 157.

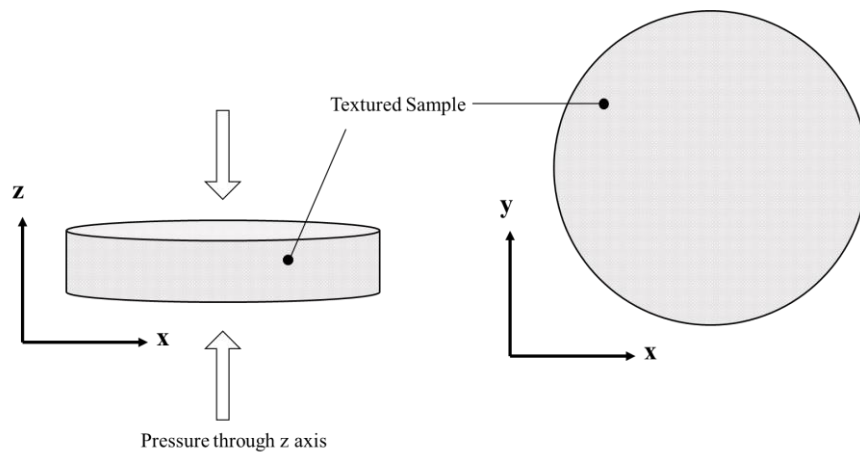


Figure 157. Schematic of pressure axis on textured sample showing cross section view (left) and surface view (right).

Figure 158 shows an SEM image of the overall sample, showing the cross section of a divided pellet. The axis of pressure is indicated in the Figure and the orientation is kept constant for all SEM images where cross section is presented.

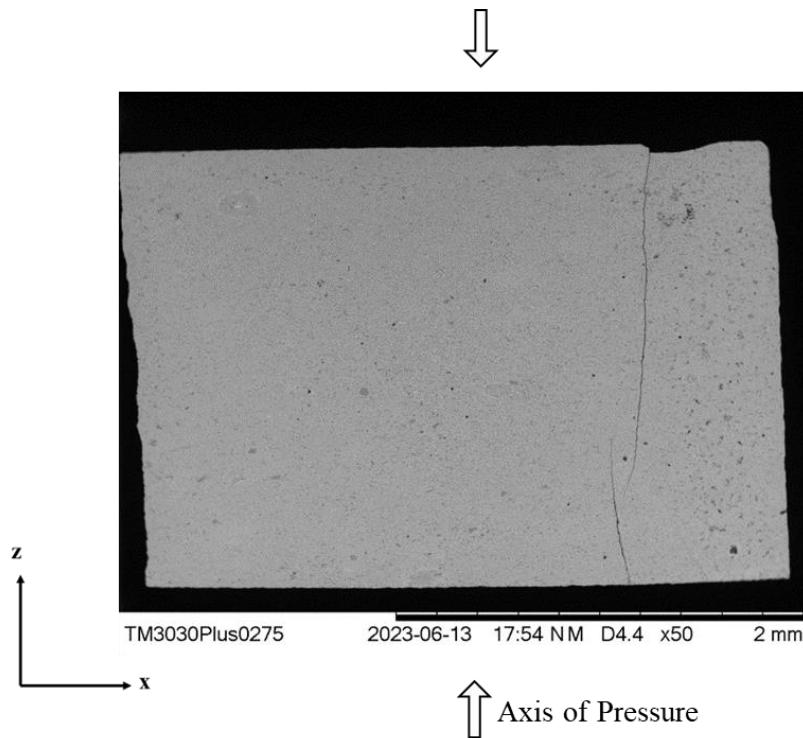


Figure 158. SEM image of cross section PMN-PT textured sample 10% volume platelets, hot pressed at 20.4 MPa 1150 °C. Pressure applied during sintering is through the top and bottom of the image.

Figure 159 shows a collection of SEM images taken of the cross sections of the hot-pressed PMN-PT pellets with BaTiO_3 platelets. The axis of pressure runs from the top to bottom of all images as in Figure 158. Visual inspection of these shows some evidence of orientation. The platelets are the darker rectangular shapes contrasted against the PMN-PT matrix. Particularly in images C and D of Figure 159, the platelets can be seen to consistently orientate in the z direction, where the long edge of the platelets aligns normal to the direction of pressure.

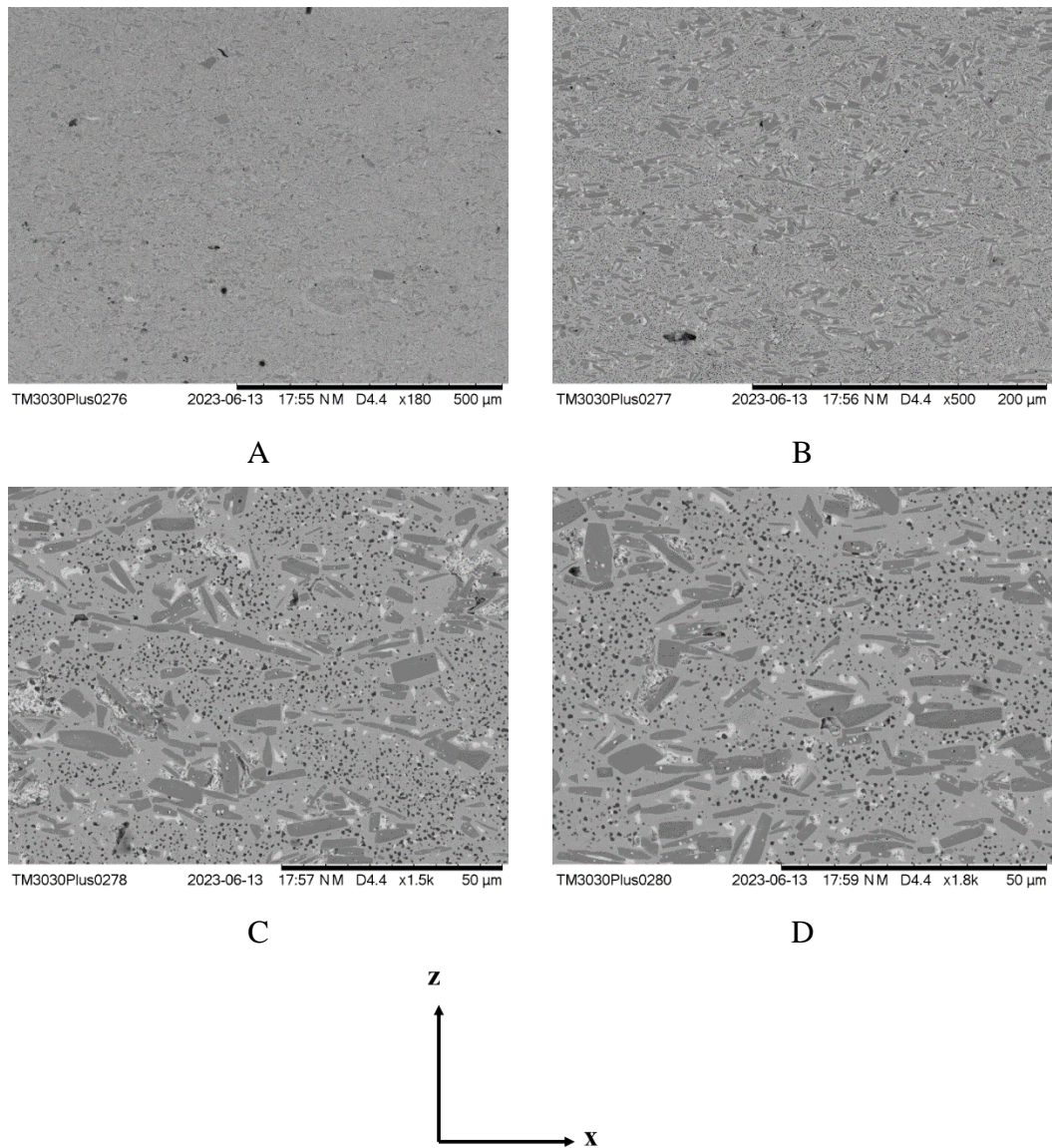


Figure 159. SEM images of cross section PMN-PT textured sample 10% volume platelets, hot pressed at 20.4 MPa 1150 °C. Pressure applied during sintering for all samples is through the top and bottom of the images.

This orientation evidence is also seen in Figure 160, which shows SEM images of the sample surface. This view shows the top face of the pellet where the pressure has been applied directly to the surface. It can be seen in these images, particularly in image F that the large surface of platelets appears to be visible, shown by the large dark rectangular shapes. These rectangular shapes have no angle of orientation as far as rotation in the x and y direction, which is to be expected as the force causing the anisometric shapes to orientate is not in this plane, but instead in the z direction. The platelets do appear to have orientated in the z plane, the large surface of the platelets are exposed, implying the platelets have rotated due to the pressure acting through the z axis.

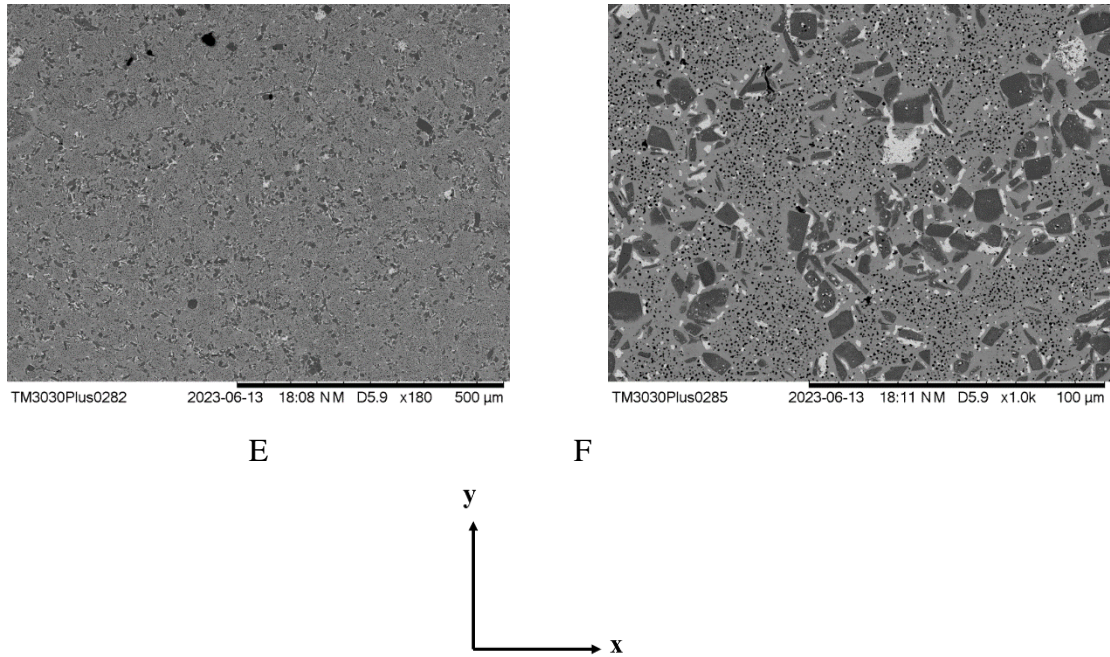


Figure 160. SEM image of surface PMN-PT textured sample 10% volume platelets.

An exaggerated schematic of the platelet expected alignment with this pressure is shown in Figure 161, to make the arguments made in this section about platelet alignment clearer. This is an exaggerated schematic of orientation of platelets that is expected to be see at the two different view of SEM images: cross sectional and surface.

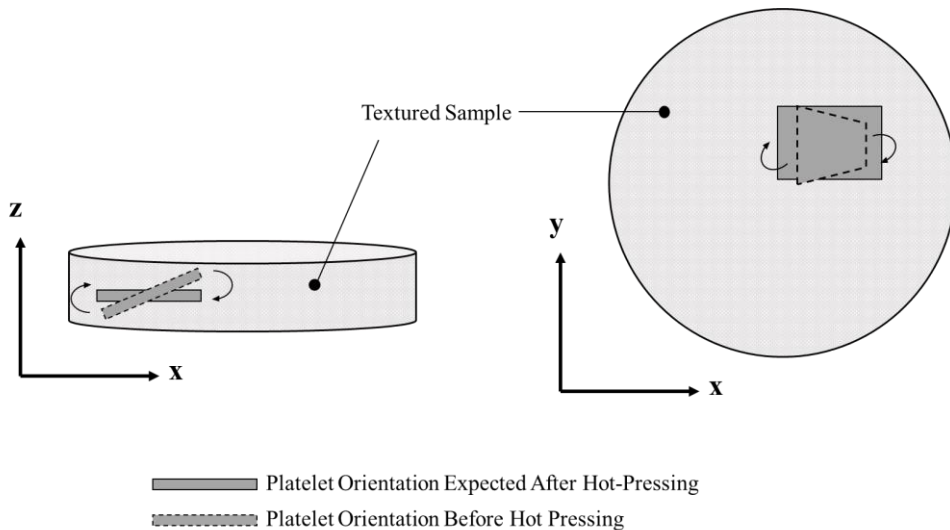
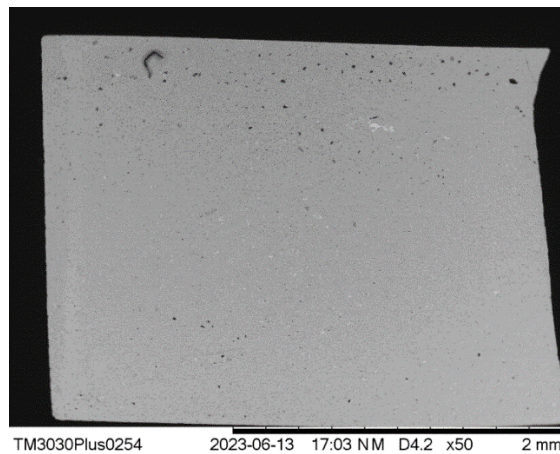


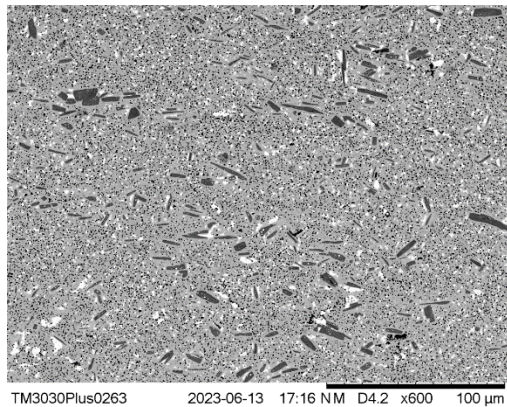
Figure 161. Schematic of exaggerated platelet orientation expected in cross sectional view and surface view of samples.

It is also clear in these images that there is some formation of secondary phase, shown by the white sections around the BaTiO₃ platelets. Figure 160 F shows very clearly the formation of a secondary phase around the platelets.

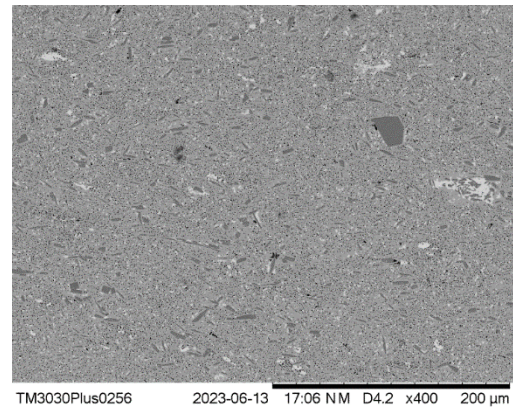
A second set of samples were also produced in the same way, PMN-PT powder with 10% by volume platelets was hot-pressed at 1150 °C, this time at a pressure of 40.8 MPa. Figure 162 shows the SEM images of the cross-section view of the textured pellet. Again here, with inspection of the SEM images, the evidence of orientation of the platelets can be seen.



G



H



I

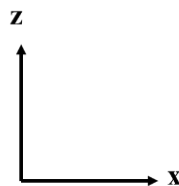


Figure 162. SEM images of cross section PMN-PT textured sample 10% volume platelets, hot pressed at 40.8 MPa 1150 °C. Pressure applied during sintering for all samples is through the top and bottom of the images.

Figure 163 shows the surface perspective of textured samples hot pressed at 20 kN 1150 °C.

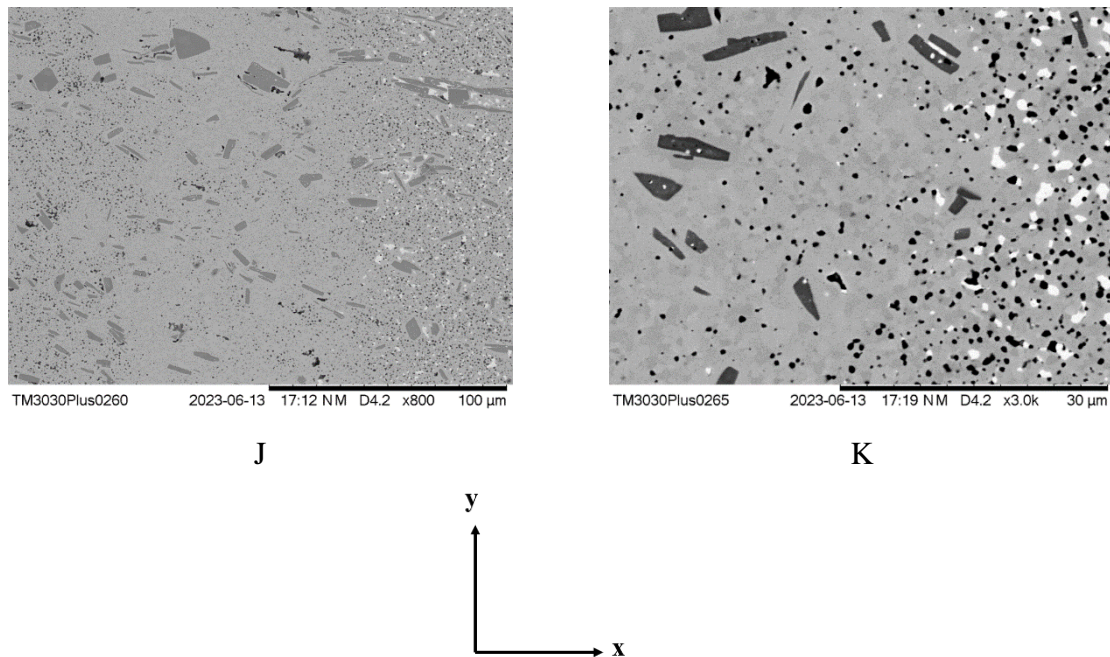


Figure 163. SEM images of cross section PMN-PT textured sample 10% volume platelets, hot pressed at 40.8 MPa 1150 °C.

The PMN-PT samples with incorporated BaTiO₃ show promising initial orientation occurring within the polycrystalline matrix. To analyse further and determine the composition of the secondary phase formed, XRD and EDX analysis was performed on the textured pellets.

7.3.1.1 Textured PMN-PT Analysis Using XRD and EDX

Figure 164 shows the XRD of starting PMN-PT calcined powder without the addition of platelets or hot pressing, which confirms single phase perovskite structure. Figure 165 shows the XRD spectra of the PMN-PT powder with 10% volume BaTiO₃ platelets incorporated and hot-pressed at 1150 °C 20.4 MPa. There are multiple peaks corresponding to a secondary phase displayed in this spectrum. Using HighScore XRD analysis software, the measured pattern can be matched with International Centre for Diffraction Data (ICDD) in a search and match algorithm. After identification of peaks, the best match found to account for the impurity phase was a barium lead magnesium titanium niobium oxide, with chemical formula

$(\text{Pb}_{0.8}\text{Ba}_{0.2})(\text{Mg}_{0.167}\text{Nb}_{0.333}\text{Ti}_{0.5})\text{O}_3$ (ICCD 01-076-6500). This is a tetragonal crystal system with similar lattice parameters to PMN-PT; $a \& b = 3.9921 \text{ \AA}$, $c = 4.0435 \text{ \AA}$.

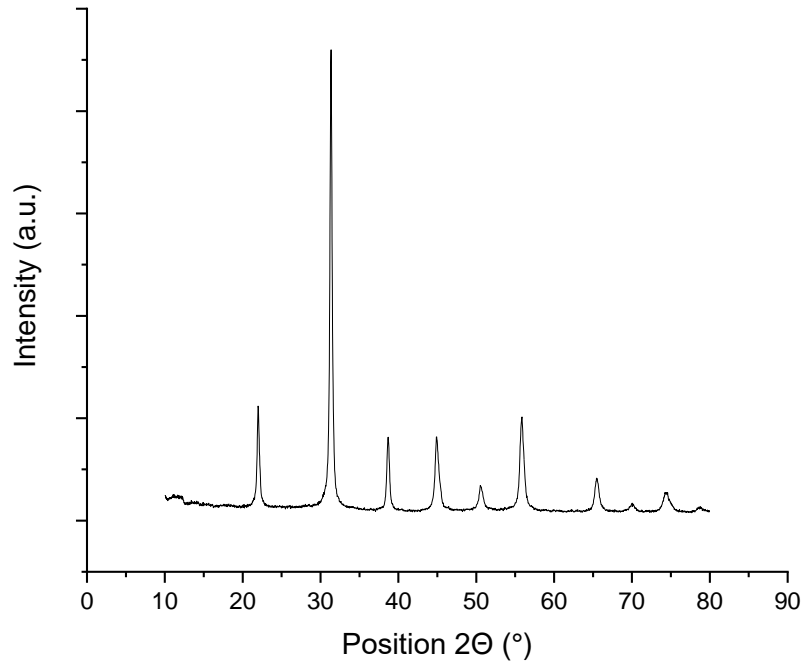


Figure 164. XRD spectra of PMN-PT powder used in texturing trials.

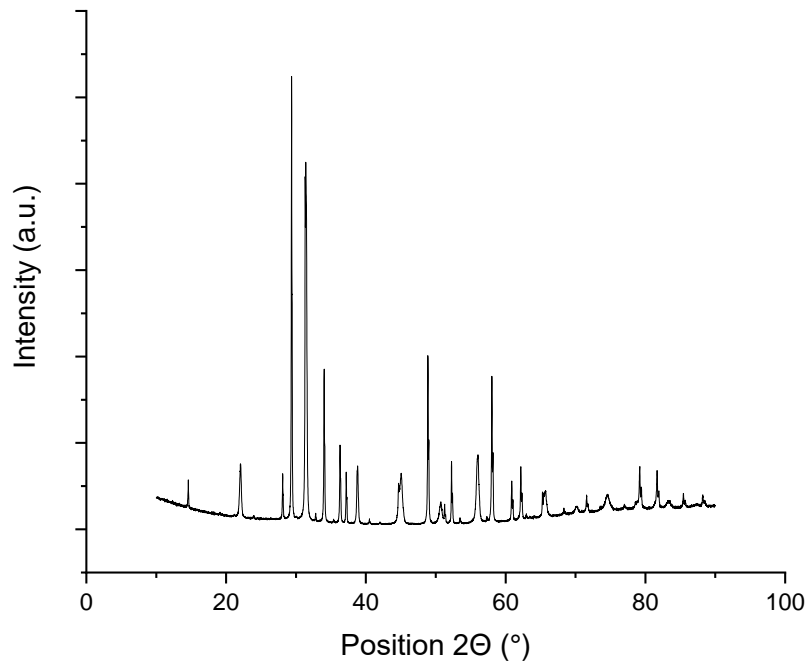


Figure 165. PMN-PT with 10% platelet BaTiO₃ hot-pressed at 1150 °C 20.4 MPa XRD spectra.

This secondary phase is also be confirmed by EDX data shown in Figure 166.

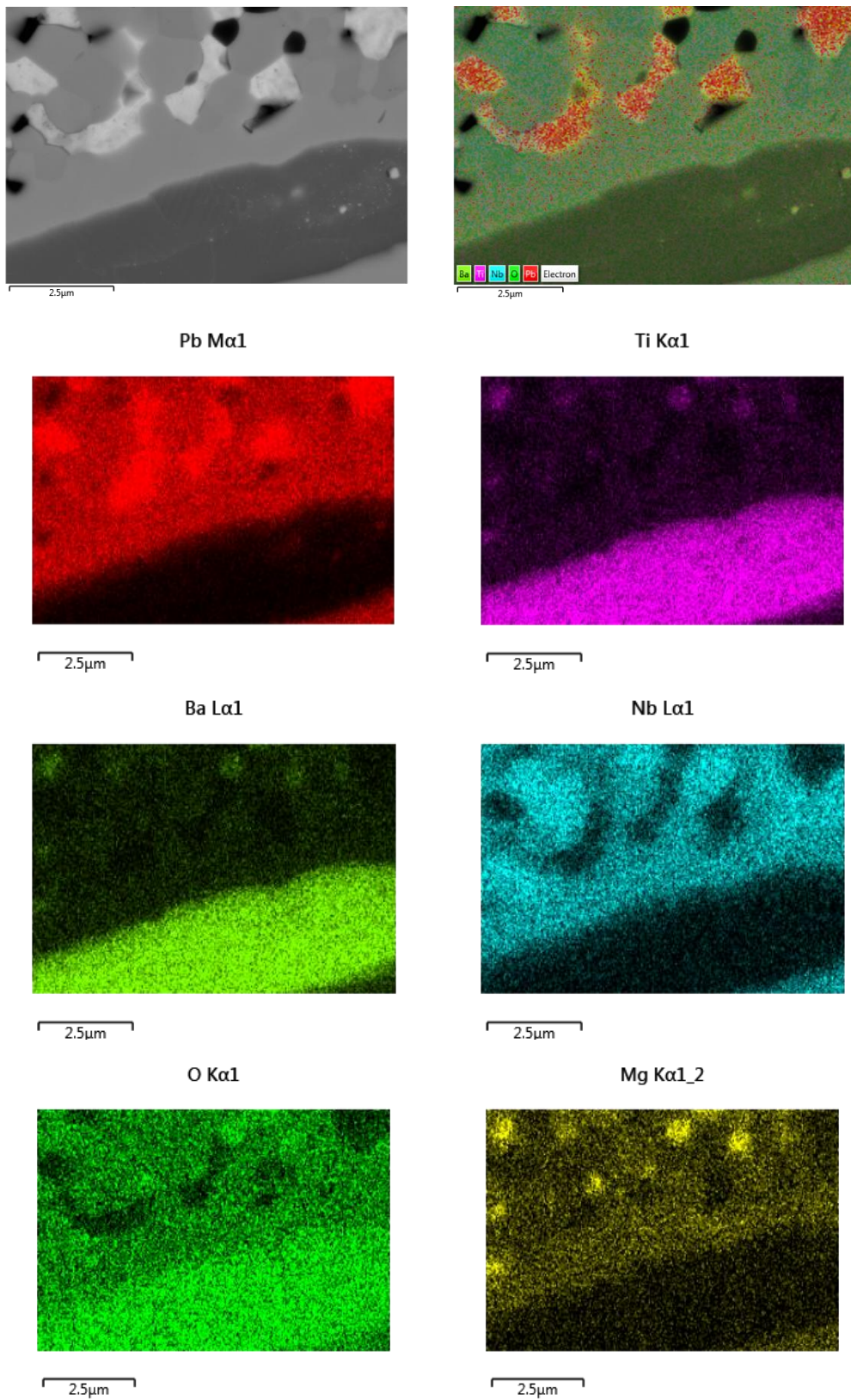


Figure 166. EDX images of PMN-PT textured sample 10% volume platelets, hot pressed at 20.4 MPa.

It can be seen in Figure 166 that there is actually 4 phases present, the barium titanate platelets (dark grey large rectangular area), PMN-PT grain (light grey surrounding), impurity phase rich in lead (light coloured), and dark sections that could be mistaken as pores but are in fact areas rich in titanium, barium, niobium, oxygen and magnesium, and with some lead content. This is the secondary phase $(\text{Pb}_{0.8}\text{Ba}_{0.2})(\text{Mg}_{0.167}\text{Nb}_{0.333}\text{Ti}_{0.5})\text{O}_3$ identified by the XRD spectrum in Figure 165. Bismuth was not detected in the EDX analysis, implying that the bismuth impurity content is too small, around 1%, to be seen with EDX.

The pressure delivered by the hot press and therefore increased energy in the system during sintering is suggested to have altered the thermodynamics of the system, inducing the formation of impurity phases. The increased energy is sufficient to allow diffusion of barium out of the platelets and into concentrated phases in the PMN-PT matrix.

7.3.1.2 Conclusions of PMN-PT Texturing

The pellets produced incorporating barium titanate platelets into PMN-PT show good signs of initial texturing. The platelets are seen in SEM images to orientate with the axis of pressure. It is worth pursuing texturing in this way to understand and quantitatively analyse the degree of texturing in the sample taking place.

However, large amounts of impurity phases are found when hot-pressing BaTiO_3 platelets with PMN-PT matrix. The impurity phases have been identified using EDX and XRD as $(\text{Pb}_{0.8}\text{Ba}_{0.2})(\text{Mg}_{0.167}\text{Nb}_{0.333}\text{Ti}_{0.5})\text{O}_3$ and a lead rich impurity phase.

The next phase of this work is to therefore continue the texturing work with BaTiO_3 polycrystalline ceramic instead of PMN-PT to avoid formation of any secondary phases and to enable quantification of orientation.

7.3.2 Texturing of Barium Titanate

Following from the previous texturing work, where secondary phases were formed in the PMN-PT matrix (Section 7.3.1) it was decided that texturing experiments would be undertaken with

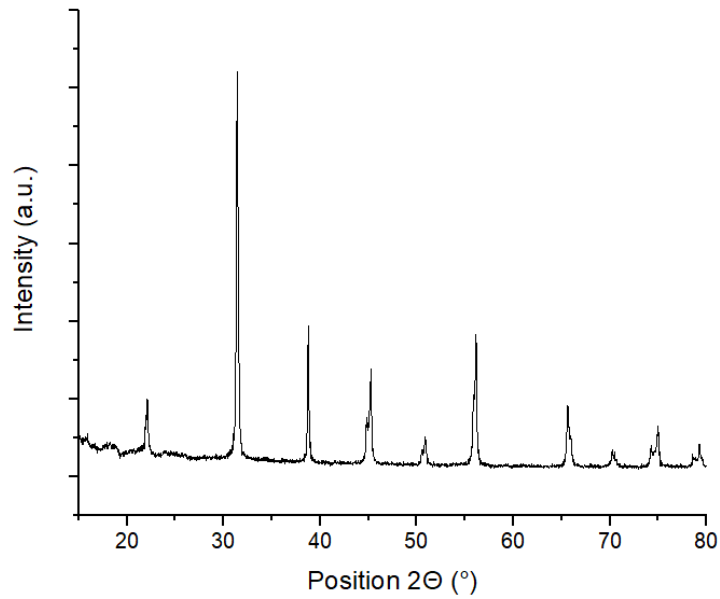
barium titanate polycrystalline ceramic with the inclusion of barium titanate platelets. The homogeneity of the seed templates and polycrystalline matrix reduces the chance of formation of any impurity phases and allows for quantitative analysis of texturing fraction achieved.

Barium titanate green powder is manufactured by the solid oxide processing route as detailed in Section 4.4.2. Using an excess of titanium oxide (TiO_2) has in external works, been reported to incur a liquid phase and facilitate grain boundary movement. In the work by Hennings et al, (1987) BaTiO_3 sintered with an excess of 2% TiO_2 , gave rise to the fastest growing grains upon sintering at 1330 °C. This composition was therefore used in these experiments to maximise the amount of orientation and growth from platelets.

The barium titanate texturing pellets were prepared in the same way as PMN-PT texturing experiments as outlined in Section 7.21. After the barium titanate green powder and platelets had been cold isostatically pressed at 20 MPa for 5 mins, they were transferred to the hot press die, surrounded by yttria stabilised zirconia packing powder and sintered at 1200 °C 20 MPa. 1200 °C was used in this case as this is the upper limit of the hot press furnace. The samples were then taken out of the hot press and transferred to a sealed crucible surrounded by sacrificial powder of the same composition in a sealed crucible and annealed at 1330°C for times 5, 10, 15 and 20 hours.

The volumetric content of platelets was also varied in this work to analyse the impact this would have on final texturing fraction. Volumetric percentages of 5, 10 and 15% were used in this set of experiments.

Figure 167 shows the XRD spectrum of calcined barium titanate with 2% mol excess TiO_2 as prepared for these experiments. This XRD spectrum forms the basis of the untextured comparison of peak intensities for later analysis using Lotgering Factor.



• *Figure 167. XRD spectra of untextured barium titanate.*

XRD of the prepared texturing samples after hot-pressing were first inspected to ensure no impurity phases were formed during this process. Figure 168, Figure 169 and Figure 170 show the XRD spectra of texturing samples produced in the hot press (1200 °C, 20.4 MPa) for volume percentage content of platelets 5, 10 and 15% respectively. Figure 168, Figure 169 and Figure 170 all show single phase barium titanate with no evidence of secondary phases or impurities with the expected tetragonal structure expected at room temperature.

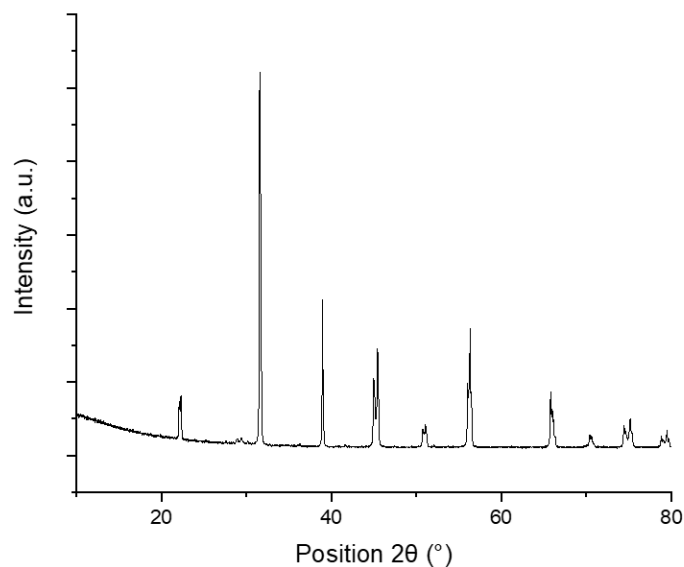


Figure 168. XRD Spectrum of barium titanate sample with 5% volume of platelets hot pressed at 1200 °C 20.4 MPa.

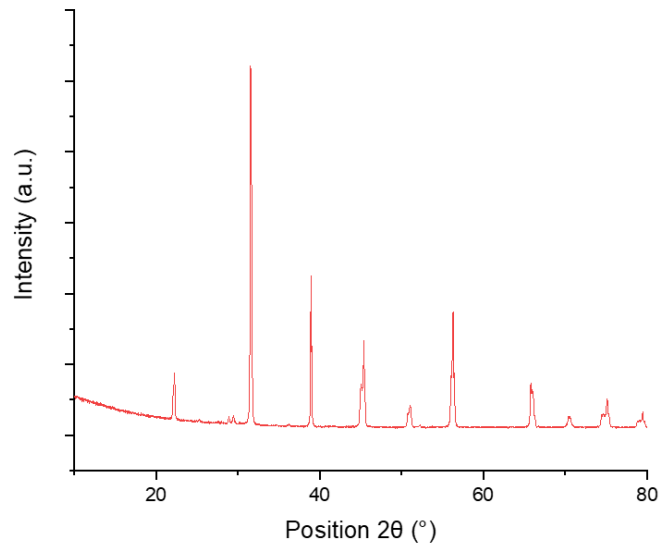


Figure 169. XRD Spectrum of barium titanate sample with 10% volume of platelets hot pressed at 1200 °C 20.4 MPa.

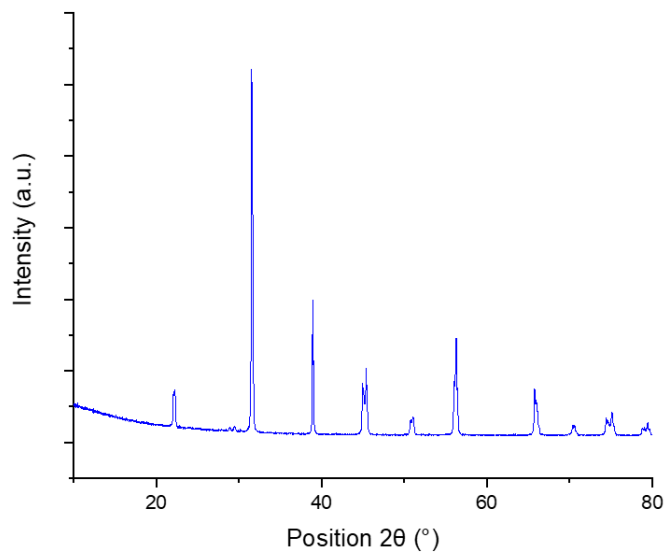


Figure 170. XRD Spectrum of barium titanate sample with 15% volume of platelets hot pressed at 1200 °C 20.4 MPa.

The Lotgering Factor, detailed in section 7.2.2.1, is then used to determine the overall texturing fraction of the annealed samples. The relative peak intensities of the preferred orientation axis (001) are calculated and compared to that of an untextured sample to produce a value for Lotgering Factor of each sample, this is displayed in Figure 171.

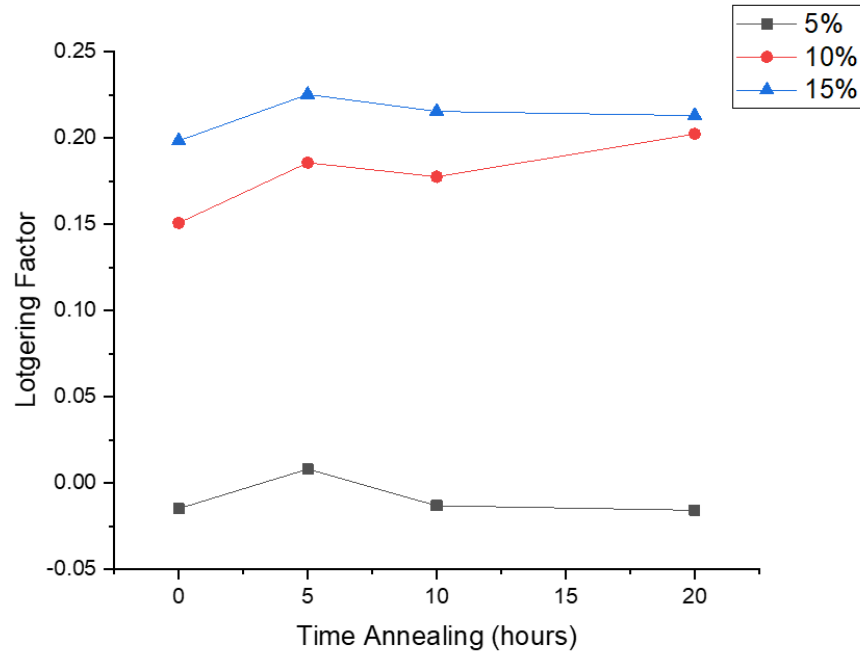


Figure 171. Lotgering Factor analysis of barium titanate ceramic with varying volumetric content of barium titanate platelets (5, 10 and 15%) annealed at 1330 °C for varying times (0, 5, 10, 15 hours).

It can be seen in Figure 171 that Lotgering factors of approximately 0.20, 0.15 and 0 for the barium titanate textured samples have been obtained for a platelet fraction of 15%, 10% and 5% respectively. The addition of 5 volume % platelet fraction appears to be insufficient to incur orientation and produce textured samples. This sample exhibits the same degree of texture as the randomly orientated sample across all annealing times.

The 10% volumetric percent platelet addition has induced an orientation in this sample, initially 15.1% degree of texturing was seen after hot pressing (before annealing has taken place). The fraction of orientation then increases with increasing annealing time up to a value of 20.2%. This implies that the platelets in the barium titanate matrix have induced orientation in the polycrystalline structure with further heat treatment.

A similar discovery is seen for the 15% volumetric content of platelets. Initial orientation is higher, as expected as there are more orientated platelets in the sample, initially the fraction of orientated material is 19.8% and with further heat treatment this increases up to 21.3%. This result also shows that the platelets are inducing orientation in the polycrystalline matrix as they are heated, the increase in energy to the system allows grains surrounding the platelets to orientate along the (001) favourable orientation.

7.3.2.1 Conclusion of Barium Titanate Texturing

The use of barium titanate polycrystalline powder with barium titanate platelets eliminated the formation of impurity phases seen in the textured samples. The degree of texturing could then be calculated using the Lotgering Factor, where the relative intensities XRD peaks are compared for randomly orientated samples and the preferred crystallographic direction. Overall, the Lotgering Factors presented in Figure 171 show that a maximum of approximately ~ 20% textured fraction that was obtained using this set-up and experimental method.

7.4 Texturing Summary and Conclusions

The amount of texturing observed with analysis of barium titanate textured pellets using Lotgering factor, approximately 20%, is insufficient without further work to produce highly orientated textured ceramics. However, the key conclusions that have come from this section of work is that there is evidence of texturing from hot-pressing of the samples which increases with further heat treatment. There is orientation observed in the barium titanate texture samples before annealing, which then increases with annealing. This implies that there is orientation of the polycrystalline grains being induced by the platelets. This was mostly seen in samples with higher volume fraction of pellets. A volume fraction of 5% was insufficient to produce any significant fraction of texturing.

It is also important to note that impurity phases are incurred in this method when hot-pressing is applied to barium titanate platelets incorporated into a PMN-PT matrix. The impurity phases have been identified using EDX and XRD as $(\text{Pb}_{0.8}\text{Ba}_{0.2})(\text{Mg}_{0.167}\text{Nb}_{0.333}\text{Ti}_{0.5})\text{O}_3$. It can be seen that the pressure supplied by the hot press has changed the thermodynamics of the system sufficiently to produce this secondary phase, limiting the orientation achieved using this method. The small amount of bismuth content in the barium titanate platelets may also catalyse a change in the phase equilibria resulting in production of secondary phases.

7.5 Texturing Further Work

Further work is needed in this area to improve the amount of orientation seen in the hot press textured samples. It has been shown to be possible to orientate barium titanate platelets with the pressure in the hot press and induce orientation into the matrix with further annealing.

The presence of bismuth in the system is the greatest unknown factor in this work. BaTiO₃ platelets with less impurity content should be used in future work to determine to what extent bismuth has altered the phase stability of the PMN-PT matrix with incorporated barium titanate platelets.

To improve the amount of orientation achieved initially without annealing it is important to study more the effects of pressure and particle size of the matrix material and platelets have on the resulting orientation of the sample. Increasing the ease of which the platelets can move within the powder about the axis of pressure is vital and particle size will affect this.

To incur more growth after hot pressing it is important to study the role of liquid phase in facilitating grain orientation within the textured samples. A series of experiments should be undertaken where the amount of excess TiO₂, and therefore liquid phase, concentration in the barium titanate polycrystalline is studied.

This process could also be looked at as a secondary stage for texturing after a shear forming process such as tape casting has taken place. As the density of the ceramics is essential in determining the piezoelectric properties, the use of the hot press could aid in the densification process whilst providing some further orientation of anisotropic particles within the matrix.

Summary and Conclusions

The initial aims of this work were to establish the hot-pressing process to produce ideal precursor candidates for solid-state crystal growth. It has been shown, by conducting a study of processing conditions, that samples of >99.9% theoretical density can be produced in the hot press when sintered at 1150 °C and 40.8 MPa. after a. A full set of conclusions is given in Section 6.4.

The next aim of the work was to carry out the SSCG process with the hot-pressed samples and investigate how single crystal growth rate was changed as a function of further heat treatment conditions. The solid-state crystal growth trials were then carried out using single crystal seeding of both BaTiO₃ and PMN-PT. It was found when using barium titanate single crystal seeds, contrary to other works, no single crystal growth was induced in the PMN-PT matrix. This was attributed to the formation of a secondary phase, identified later in texturing work (Chapter 7), that resulted in grain growth being inhibited.

PMN-PT single crystal seeding was shown to be effective at inducing solid-state crystal growth for hot-pressed PMN-PT samples containing 0%, 2% and 5% excess lead oxide, growth of 108 μm, 156 μm and 125 μm was seen respectively. These results were comparable with the growth rates stated in other works of SSCG of the PMN-PT system. It was shown that the growth rate was enhanced by liquid film presence, an addition of 2% excess lead was found to produce the highest rate of grain boundary mobility resulting in more grain growth.

Arrhenius plots have then been produced to calculate the activation energy for single crystal growth of each PMN-PT composition as a function of annealing time. The value of activation energy calculated is smallest where 2% excess PbO is present at 79.8 kJ/mol, followed by 5% excess PbO where activation energy is 127.4 kJ/mol and finally PMN-PT without the addition of excess PbO at 193.9 kJ/mol. This is consistent to calculated activation energy of grain growth which follows the same trend: $Q_{2\% \text{ excess PbO}} < Q_{5\% \text{ excess PbO}} < Q_{0\% \text{ excess PbO}}$.

The next aim of this work was to carry out manganese doped PMN-PT SSCG experiments and conduct some exploratory work using knowledge gained in previous chapters. Initial trials determined that solid state crystal growth was evident in the samples, although at a slower rate than that of un-doped PMN-PT, attributed to solute drag inhibiting grain growth.

Interestingly it was also apparent that there is much less visible porosity in the growth area than un-doped PMN-PT. To explain the lack of porosity in the SSCG growth area it is suggested to be the product of oxygen vacancy mobility.

The final aim of this work was to carry out a feasibility study of hot-pressing as a tool for orientating textured ceramics. The amount of texturing observed with analysis of barium titanate textured pellets using Lotgering factor, was found to be approximately 20% which is presents a good opportunity for further work to produce highly orientated textured ceramics.

The key conclusions that have come from this short section of work is that there is evidence of texturing from hot pressing of the samples which increases with further heat treatment. Also the identification of the impurity phases using EDX and XRD as $(\text{Pb}_{0.8}\text{Ba}_{0.2})(\text{Mg}_{0.167}\text{Nb}_{0.333}\text{Ti}_{0.5})\text{O}_3$ provided valuable insight into the SSCG trials seeded with barium titanate single crystal seed.

Further Work

Further work has been summarised after each corresponding chapter, the main areas of future work are presented here. The most promising avenues using the knowledge gained in this work fall into 2 main categories; investigation into manganese doped PMN-PT formed by SSCG and use of different annealing/sintering atmospheres to further SSCG work.

Further work should be carried out in the manganese doped PMN-PT, the results presented where the porosity incurred in the single crystal growth area is limited by the presence of Mn in the system is a critical result. Transmission electron microscopy should be used to give more detailed insight of the interface of the seed crystal to growth area and the growth area to the polycrystalline matrix. A series of experiments should also be conducted to investigate the growth rate of Mn-PMN-PT with annealing time to gain more information about the growth mechanism.

There is great scope for carrying out SSCG experiments in different sintering atmospheres as a means of reducing porosity in the grown crystal. In external work, some progress in reducing porosity of PMN-32PT by sintering in an oxygen atmosphere has already been seen. This would be particularly interesting to compare to the SSCG trials of PMN-PT with incorporated excess PbO where there is a larger fraction of porosity formed during single crystal growth. The role of atmosphere during the annealing of both doped and undoped matrices, including oxygen, nitrogen and argon atmospheres should be analysed.

Application of the knowledge gathered in this work would be very interesting on different Pb-based systems including PIN-PMN-PT, PMN-PZT and samarium doped compositions.

References

- Asadikiya, M., Sabarou, H., Chen, M. and Zhong, Y. 2016. Phase diagram for a nano-yttria-stabilized zirconia system. *RSC Advances*. **6**(21),pp.17438–17445.
- Atkins, P.W. and Julio De Paula 2010. *Physical chemistry*. 9th ed. New York: W.H. Freeman And Co.
- Atkinson, H.V. and Davies, S. 2000. Fundamental aspects of hot isostatic pressing: An overview. *Metallurgical and Materials Transactions A*. **31**(12), pp.2981–3000.
- Baasandorj, L. and Chen, Z. 2021. Recent Developments on Relaxor-PbTiO₃ Ferroelectric Crystals. *Crystals*. **12**(1), p.56.
- Buehler. 2021. Grinding and polishing guide - buehler - metallography equipment & supplies for sample preparation. *Buehler*. [Online]. [Accessed 15 September 2023]. Available from: <https://www.buehler.com/blog/grinding-and-polishing-guide/>.
- Cady, W.G. 2018. *Piezoelectricity : an introduction to the theory and applications of electromechanical phenomena in crystals*. Mineola, New York: Dover Publications, Inc.
- Clabel H., J.L., Nazrin, S.N., Lozano C., G., Pereira da Silva, M., Siu Li, M. and Marega Jr., E. 2021. Activation energy and its fluctuations at grain boundaries of Er³⁺:BaTiO₃ perovskite thin films: Effect of doping concentration and annealing temperature. *Vacuum*. **194**(2), p.110562.
- Cross, L E. 1994. Relaxor ferroelectrics: an overview. *Ferroelectrics*. **151**(1) pp.305– 320,
- Djordjevic, N. 2005. Influence of charge size distribution on net-power draw of tumbling mill based on dem modelling. *Minerals Engineering*. **18**(3),pp.375–378.
- K. Echizenya and Matsushita, M. 2011. Continuous feed growth and characterization of PMN-PT single crystals. JFE MINERAL COMPANY.
- E. M. Sabolsky, A. R. James, S. Kwon, S. Trolier-McKinstry, and G. L. Messing, Piezoelectric Properties of 001 Textured Pb(Mg_{1/3}Nb_{2/3})O₃-PbTiO₃ Ceramics, *Applied Physics Letters* 78(17), 2551–2553 (2001).

- E. M. Sabolsky, S. Kwon, E. Suvaci, A. R. James, G. L. Messing, and S. Trolier-McKinstry, Dielectric and Electromechanical Properties of 001 - Textured (0.68)Pb(Mg_{1/3}Nb_{2/3})O₃ - (0.32)PbTiO₃, vol. 1, Proceedings of the 2000 IEEE International Symposium on Applications of Ferroelectrics, Honolulu, HI, (S. K. Streiffer, ed., Institute of Electrical and Electronics Engineers, New York, NY, 2000), pp. 393–396.
- E. M. Sabolsky, S. Trolier-McKinstry, and G. L. Messing, Dielectric and Piezoelectric Properties of 001Fiber-Textured 0.675Pb(Mg_{1/3}Nb_{2/3})O₃-0.325PbTiO₃ Ceramics, *Journal of Applied Physics* 93(7), 4072–4080 (2003).
- ENERPAC 2019. Hydraulic Cylinders, Jacks, Rams | Enerpac. *www.enerpac.com*. [Online]. [Accessed 19 October 2019]. Available from: <https://www.enerpac.com/en-au/cylinders-and-jacks/AUCylinders>.
- Fancher, C.M. 2021. Diffraction Methods for Qualitative and Quantitative Texture Analysis of Ferroelectric Ceramics. *Materials*. **14**(19), p.5633.
- G. S. Smolensky and A. Agronovskaya. 1960. *Soviet Physics Solid State*, 1 pp.1429,
- Guo, R. 2012. *Morphotropic phase boundary perovskites, high strain piezoelectrics, and dielectric ceramics: proceedings of the dielectric materials and multilayer electronic devices symposium and the morphotropic phase boundary phenomena and perovskite materials symposium held at the 104th annual meeting of the American Ceramic Society, April 28-May 1, 2002 in St. Louis, Missouri. Westerville, Ohio: American Ceramic Society.*
- Guo, Y., Luo, H., Ling, D., Xu, H., He, T. and Zhang, Y. 2003. The phase transition sequence and the location of the morphotropic phase boundary region in (1-x)[Pb(Mg_{1/3}Nb_{2/3})O₃]-xPbTiO₃ single crystal. *Journal of Physics: Condensed Matter*. **15**(2), pp.L77–L82.
- Hammond, C. 2009. *The Basics of Crystallography and Diffraction*. OUP Oxford.
- Hennings, D., Janßen, R. and Reynen, P. 1987. Control of Liquid-Phase-Enhanced Discontinuous Grain Growth in Barium Titanate. *Journal of the American Ceramic Society*. **70**(1), pp.23–27.

- Holterman, J. and Groen, P. 2012. *An introduction to piezoelectric materials and components*.
Stitching Applied Piezo.
- Jona, F. and G. Shirane 1962. *Ferroelectric Crystals*. Pergamon.
- K. T. Zawilski, M. C. C. Custodio, R. C. DeMattei, S. G. Lee, R. G. Monteiro, H. Odagawa,
and R. S. Feigelson. 2003. Segregation During the Vertical Bridgman Growth of Lead
Magnesium Niobate/Lead Titanate Single Crystals. *Journal of Crystal Growth* 258(3–
4), pp.353–367
- KJN 2005. 90 x 90 H Aluminium profile. *www.aluminium-profile.co.uk*. [Online]. [Accessed
23 October 2019]. Available from: [https://www.aluminium-profile.co.uk/90x90-
heavy-aluminium-profile-kjn990500](https://www.aluminium-profile.co.uk/90x90-heavy-aluminium-profile-kjn990500).
- Lee, H. Y., Lee, J. B., Hur, T. M. and Kim, D.H. 2009 Method for Solid-State Single Crystal
Growth. (US 2009/0211515 A1).
- Liebertz, J. 1987. Uniaxial hot-pressing of fine-particle, pure barium titanate without die.
International Journal of High Technology Ceramics. 3(2), pp.153–163.
- Marakhovsky, M.A., Панич, А.Е., Таланов, М.В. and Marakhovskiy, V.A. 2021.
Comparative study of the hard and soft PZT-based ceramics sintered by various
methods. *Ferroelectrics*. 575(1), pp.43–49.
- Mendelson, M I. 1969. Average Grain Size in Polycrystalline Ceramics. *Journal of the
American Ceramic Society*. 52(8),pp 443-446.
- Messing, G.L., Sabolsky, E.M., Kwon, S. and Trolier-McKinstry, S. 2001. Templated Grain
Growth of Textured Piezoelectric Ceramics. *Key Engineering Materials*. 206-213,
pp.1293–1296.
- Mojca Otoničar, Andraž Bradeško, Samir Salmanov, Chung, C., Jones, J.L. and Tadej Rojac
2021. Effects of poling on the electrical and electromechanical response of PMN–PT
relaxor ferroelectric ceramics. *Open ceramics*. 7(7), pp.100140–100140.
- Nanoscience Instruments 2018. Scanning electron microscopy - nanoscience instruments.
Nanoscience Instruments. [Online]. Available from:
<https://www.nanoscience.com/techniques/scanning-electron-microscopy/>.

- Niveditha, C.V. and Sindhu, S. 2015. α - Bi_2O_3 photoanode in DSSC and study of the electrode–electrolyte interface. *RSC Advances*. **5**(95), pp.78299–78305.
- Patil, R.P., Gaikwad, S.S., Karanjekar, A.N., Khanna, P.K., Jain, G.H., Gaikwad, V.B., More, P.V. and Bisht, N. 2020. Optimization of strontium- doping concentration in BaTiO_3 nanostructures for room temperature NH_3 and NO_2 gas sensing. *Materials Today Chemistry*. **16**(2), p.100240.
- Remeika, J.P. and W. Morrison Jackson 1954. A Method for Growing Barium Titanate Single Crystals. *Journal of the American Chemical Society*. **76**(3), pp.940–941.
- Ryoichi Furushima, Tanaka, S., Kato, Z. and Keizo Uematsu 2010. Orientation distribution–Lotgering factor relationship in a polycrystalline material-as an example of bismuth titanate prepared by a magnetic field. *Journal of the Ceramic Society of Japan*. **118**(1382), pp.921–926.
- S Park and Thomas R Shrout. (1997) Ultrahigh strain and piezoelectric behaviour in relaxor based ferroelectric single crystals. *Journal of Applied Physics*, 82(4),
- Salma, U., Hasanuzzaman, M., Bhuiyan, I.U. and Hashmi, S. 2022. High strength alumina composite for protective armors: A review. *Reference Module in Materials Science and Materials Engineering*.
- Sasaki, H. 1965. Growth of BaTiO_3 Crystals from TiO_2 -Rich Melt. *Japanese Journal of Applied Physics*. **4**(1), pp.24–24.
- Shimanuki, S. Saito, S. and Yamashita, Y. 1998. Single crystal of the $\text{Pb}(\text{Zn}_{1/3}\text{Nb}_{2/3})\text{O}_3$ – PbTiO_3 system grown by the vertical Bridgeman method and its characterization, *Jpn. J. Appl. Phys.* **3**(7), pp.3382.
- Swartz, S L and Shrout, T R. (1982) Fabrication of perovskite lead magnesium niobate. *Materials Research Bulletin*, **17**(10) pp.1245–1250.
- T, Takenaka and K. Sakata. 1980. Grain Orientation and Electrical Properties of Hot-Forged $\text{Bi}_4\text{Ti}_3\text{O}_{12}$ Ceramics. *Japanese Journal of Applied Physics*. 19(10), pp.31–39.
- Tadej Rojac 2023. Piezoelectric response of disordered lead-based relaxor ferroelectrics. *Communications materials*. **4**(1).

- V.L. Balkevich and C.M. Flidlider 1976. Hot-pressing of some piezoelectric ceramics in the PZT system. *Ceramurgia International*. **2**(2), pp.81–87.
- Wang, F., Wang, H., Yang, Q., Zhang, Z. and Yan, K. 2021. Fine-grained relaxor ferroelectric PMN-PT ceramics prepared using hot-press sintering method. *Ceramics International*.
- Watanabe, H., Kimura, T. and Yamaguchi, T. 1989. Particle Orientation During Tape Casting in the Fabrication of Grain-Oriented Bismuth Titanate. *Journal of the American Ceramic Society*. **72**(2), pp.289–293.
- Yamamoto, T. and Sakuma, T. 1994. Fabrication of Barium Titanate Single Crystals by Solid-State Grain Growth. *Journal of the American Ceramic Society*. **77**(4), pp.1107–1109.